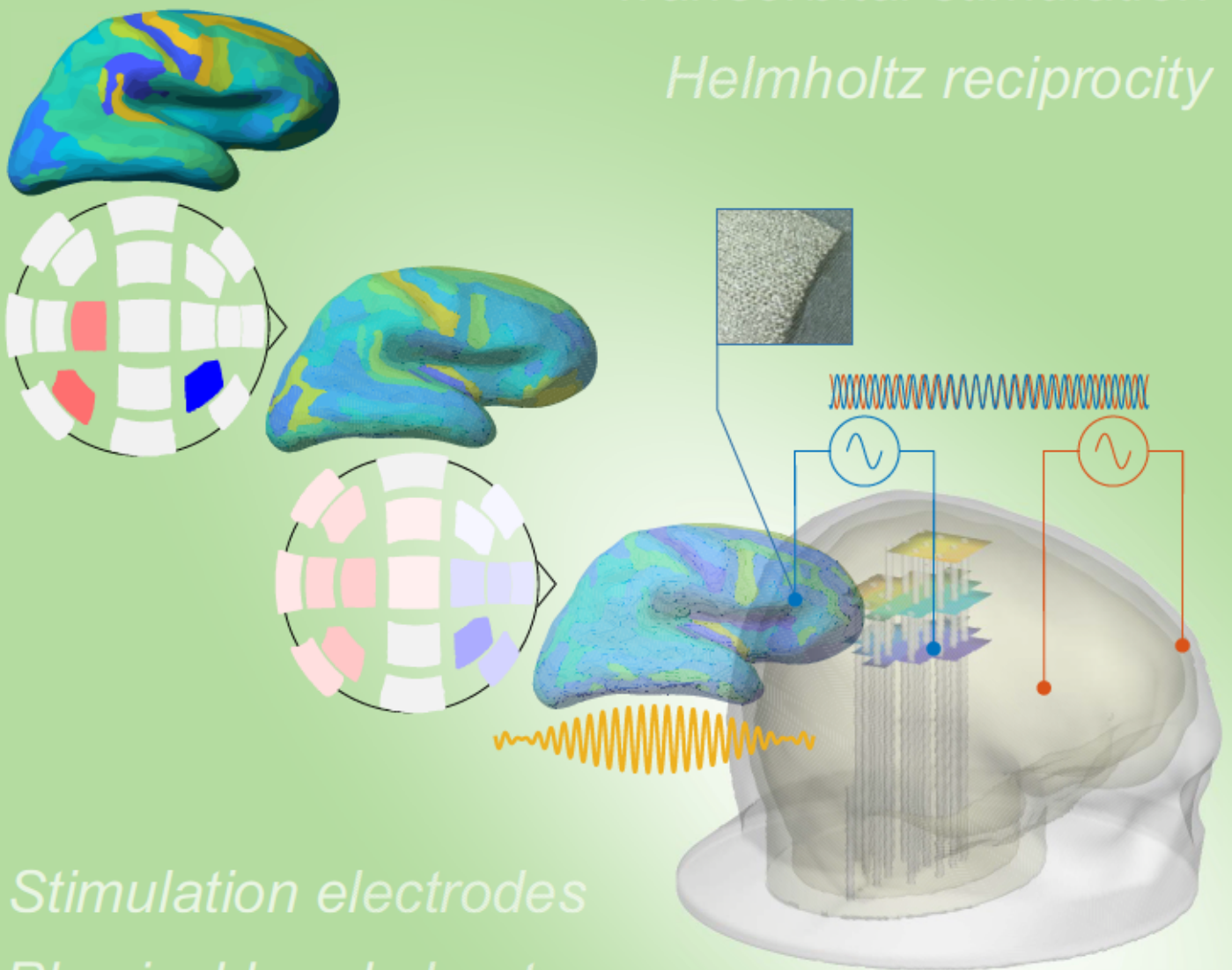


Transcranial electric stimulation — modeling, application, verification

Alexander Hunold

Transorbital stimulation

Helmholtz reciprocity



Stimulation electrodes
Physical head phantom

Transcranial electric stimulation

—
modeling, application, verification

by

Alexander Hunold

Born on June 3rd, 1988

Technische Universität Ilmenau
Department of Computer Science and Automation

Submitted in partial fulfillment of the requirements for the
Doctor engineer (Dr.-Ing.)
degree

Focus topics: Computational & Interventional Neuroscience, Modeling

Doctoral supervisor: Univ.-Prof. Dr.-Ing. habil. Jens Haueisen

Reviewers : Prof. D.Sc. Jari Hyttinen
Asst.-Prof. Dr. rer. nat. Alexander Opitz

Prior degrees: B.Sc and M.Sc in Biomedical Engineering

Submission: November 26, 2020

Presentation: June 9, 2021

DOI: 10.22032/dbt.49291

URN: urn:nbn:de:gbv:ilm1-2021000170



This work is licensed under Creative Commons Attribution 4.0 International (CC BY 4.0).

Preface

This thesis is based on my research activities conducted at the Institute of Biomedical Engineering and Informatics (BMTI), and in research visits. I am most grateful for the chance to learn from and work with many partners contributing to my knowledge, skills and experience. In these ways many people have contributed to this thesis, to whom I am deeply obliged, and I would like to thank some of them here.

My greatest thanks go to my scientific supervisor, Prof. Dr.-Ing. habil. Jens Haueisen, for opening up the perspective of a doctorate and for offering a position in academia to me, for supporting the development of my skills and providing advice in countless discussions, for promoting my scientific progress, for strategic mentoring and especially for the freedom to create and pursue my own ideas.

For generating a positive work environment leading to innovative developments resulting in joint publications arising from multiple research projects, and valuable discussions, I thank all my former and present colleagues and friends at the BMTI, especially Dr.-Ing. Roland Eichardt, Dr.-Ing. Lorenz Esch, Dr. rer. nat. Uwe Graichen, Dr.-Ing. René Machts and Dr.-Ing. Daniel Strohmeier. For their additional encouragement on a very personal level, I gratefully thank Dr.-Ing. Christoph Dinh and Dr.-Ing. Patrique Fiedler.

I deeply thank all my collaborators for supporting my scientific advancement in joint publications. I especially thank Assoc.-Prof. M.D. Ph.D. Michael Funke and Sen.-Lec. D.Sc. Matti Stenroos for motivating and promoting me already at a very early stage, as well as Prof. Dr. Andrea Antal and Prof. Dr. Marcus Meinzer for highlighting the neurosciences to me and advancing my scientific contributions.

I also thank my industrial partners Klaus Schellhorn and Sebastian Berkes from neuroConn GmbH for their valuable advice with direct practical relevance in the application field and comprehensive support with equipment, which also holds for Gerald Rosner and Christoph Müller from warmX GmbH.

I thank all my friends, especially Philipp, Ivonne and Steffen, for cheering me up in joyful sessions. I gratefully thank my relatives, especially my parents Christine and Mathias, for promoting my development with unconditional support and ongoing motivation. Last but not least, I express my most exceptional gratitude to my family, I thank my wife Daniela for her encouragement in difficult times, for grounding me in times of heights, and for always covering my back, and I thank my children Hanna and Paul for their understanding and for cheerfully inspiring me with their own development.

Abstract

Electric manipulation of neuronal activity gathered interest in neuroscientific research and showed therapeutic effects throughout past centuries. The non-invasive application of weak currents with a few milliamperes to the head, called transcranial electric stimulation (tES), captured manifold applications in neuroscience and clinical research in the last decades. The conventionally cumbersome and rather unspecific administration of the stimulation current with respect to its distribution for targeting and the electrode interface desire further innovation and verification.

The present thesis addresses current flow modeling for targeted stimulation, electrode developments for current administration and measurement approaches verifying stimulation configurations.

Simulated transorbital stimulation gave rise to current density distributions in the retina demonstrating distinct hot spots depending on the electrode montage. Similarly, simulations of multi-electrode configurations on the head addressed location and orientation specific targets in the cortex. These simulations indicate the feasibility of specific stimulation configurations for targets in the retina and the cortex.

For stimulation application, new concepts for stimulation application based on textile electrodes with integrated electrolyte reservoir and additive manufactured dry electrodes embodied in a textile cap have been introduced. These newly developed electrodes demonstrated functionality by replicating previously described effects of current stimulation and increased stimulation precision, reproducibility and lowered the preparation effort.

A homogeneous volume conductor and a realistically shaped three-compartment head phantom have been physically implemented for technical verification experiments. Metrological experiments in these phantoms demonstrated feasibility of multi-electrode stimulation configurations, especially the approach of temporal interference, and verified the stable performance of new electrode concepts.

Concluding, the present thesis contributes innovations in the field of tES with a new approach for targeting cortical areas by multi-electrode stimulation, new compliant electrode concepts and physical phantoms for metrological verification.

Zusammenfassung

Die Verwendung von Elektrizität zur Beeinflussung neuronaler Aktivität weckte das Interesse neurowissenschaftlicher Forschung und zeigt bereits seit einigen Jahrhunderten therapeutische Wirkungen. In den letzten Jahrzehnten fand die nicht-invasive Anwendung schwacher Ströme von wenigen Milliampere am Kopf, bezeichnet als transkranielle Elektrostimulation (tES), in den Neurowissenschaften und der klinischen Forschung vielfältige Anwendungen. Die konventionell aufwendige implementierte Elektrodenansatzstelle und eher unspezifische Verteilung der Stimulationsströme benötigen jedoch weitere Innovationen und Verifikationen.

Die vorliegende Arbeit befasst sich mit der Modellierung des Stromflusses für die gezielte Elektrostimulation, mit der Entwicklung von Elektrodenkonzepten für die Stromeinprägung, sowie mit messtechnischen Ansätzen zur Verifikation von Stimulationskonfigurationen.

Simulationen transorbitaler Stromstimulationen zeigten Stromdichteverteilungen in der Netzhaut, die in Abhängigkeit von der Elektrodenmontage deutlich unterschiedliche lokale Maxima aufwiesen. In ähnlicher Weise wurden orts- und orientierungsspezifische Ziele im Kortex mit Simulationen von Konfigurationen mehrerer Elektroden auf dem Kopf adressiert. Diese Simulationen zeigten die Realisierbarkeit zielgenauer Stimulationskonfigurationen für die Retina und Zielgebiete im Kortex.

Für die Stimulationsanwendung wurden neue Konzepte auf Basis von textilen Elektroden mit integriertem Elektrolytreservoir und gedruckten Trockenelektroden eingeführt, die in flexiblen Hauben eingearbeitet sind. Diese neu entwickelten Elektroden zeigten ihre Funktionalität in Studien, die zuvor beschriebenen Effekte der Stromstimulation reproduzierten, wobei sie die Präzision und Reproduzierbarkeit der Stimulation erhöhten und den Vorbereitungsaufwand verringerten.

Für technische Verifikationsexperimente wurden ein homogener Volumenleiter und ein realistisch geformtes dreischichtiges Kopfphantom physikalisch realisiert. Messtechnische Experimente an diesen Phantomen zeigten die Machbarkeit von Stimulationskonfigurationen mit mehreren Elektroden, insbesondere den Ansatz der zeitlichen Interferenz, und verifizierten die Stabilität der neuen Elektrodenkonzepte.

Zusammenfassend trägt die vorliegende Arbeit zu Innovationen auf dem Gebiet der tES bei, indem ein neuer Multi-Elektroden-Ansatz für die Adressierung kortikaler Ziele, neuen angepassten Elektrodenkonzepte und physikalische Phantome für die metrologische Verifikation beschrieben werden.

Contents

Preface	i
Abstract	iii
Zusammenfassung	v
Contents	viii
Nomenclature	ix
1 Introduction	1
1.1 Transcranial electric stimulation	1
1.2 TES from an engineering perspective	3
1.2.1 Current flow modeling	3
1.2.2 Stimulation electrodes and their applications	4
1.2.3 Verification of stimulation concepts	5
2 Modeling of stimulation schemes	7
2.1 Transorbital electric stimulation	7
2.1.1 Introduction	7
2.1.2 Material and Methods	8
2.1.3 Results	12
2.1.4 Discussion	22
2.2 Reciprocity in targeting transcranial electric stimulation	26
2.2.1 Introduction	26
2.2.2 Material and Methods	27
2.2.3 Results	35
2.2.4 Discussion	49
3 Application systems for transcranial electric stimulation	53
3.1 Textile stimulation cap	53
3.1.1 Introduction	53
3.1.2 Material and Methods	54
3.1.3 Results	58

3.1.4	Discussion	67
3.2	Dry stimulation electrodes	72
3.2.1	Introduction	72
3.2.2	Material and Methods	72
3.2.3	Results	75
3.2.4	Discussion	79
4	Verification of transcranial electric stimulation concepts	83
4.1	Temporal interference TES	83
4.1.1	Introduction	83
4.1.2	Material and Methods	84
4.1.3	Results	89
4.1.4	Discussion	94
4.2	TES applied to a head phantom	97
4.2.1	Introduction	97
4.2.2	Material and Methods	98
4.2.3	Results	106
4.2.4	Discussion	114
5	Significance and prospect	119
	Bibliography	121
	Appendix	A
	Curriculum vitae	I
	List of publications	VII
	Declaration of authorship	XVII
	Erklärung	XIX

Nomenclature

ABS	Acrylonitrile Butadiene Styrene
Ag/AgCl	Silver / Silver Chloride
AM	Amplitude Modulation
AM-tES	Amplitude Modulated tES
CAD	Computer Aided Design
CDI	Current Density Imaging
COS	Cosine of angle between vectors
CSF	Cerebro Spinal Fluid
CT	Computer Tomography
DLP	Digital Light Processing
EEG	Electroencephalography
EIT	Electrical Impedance Tomography
EMD	Earth Movers Distance
ERG	Electroretinography
FDM	Fused Deposition Modeling
FFT	Fast Fourier Transform
FWHM	Full Width Half Maximum
HD-tES	High Definition tES
IAF	Individual Alpha (α) Frequency
IMD	Intermodulation Distortion
IQR	Interquartile Range
MAG	Magnitude Ratio
MAG _{rel}	Relative Magnitude Difference
MRI	Magnetic Resonance Imaging
NaCl	Sodium Chloride
NCI	Neural Current Imaging
NIRS	Near-Infrared Spectroscopy
OCP	Open Circuit Potential
PLA	Polylactic Acid
RDM	Relative Distance Measure
RPC	Reproducibility Coefficient
SB	Sphenoid Bone

SNR	Signal-to-Noise Ratio
tACS	Transcranial Alternating Current Stimulation
tDCS	Transcranial Direct Current Stimulation
tES	Transcranial Electrical Stimulation
TI	Temporal Interference
TI-tES	Temporal Interference tES
tRNS	Transcranial Random Noise Stimulation
ULF-MRI	Ultra-Low-Field MRI

1 Introduction

1.1 Transcranial electric stimulation

The human brain is one of the most complex systems known. It represents a network in the order of 10^{12} neurons, with each establishing $10^3 - 10^4$ connections to other neurons via 10^{15} synapses exchanging 10^{18} neuro-transmitters per second (Faugeras et al., 1999). This network enables the human's brain capabilities.

Investigations and manipulations of the human brain have been approached since ancient times, starting with the description of euphoric effects of poppy plants in Sumerian records (around 4000 B.C.) and the introduction of acupuncture by Shennong (around 2700 B.C.). Since the study by Jean-Baptiste Le Roy (1726-1779) on treating blindness by electroshock (Le Roy, 1755) and the investigation of bioelectromagnetism in 1790 by Luigi Alisio Galvani (1737-1798) (Galvani, 1791), research in electrophysiology gained high impact from the 19th century onwards. Galvanic currents were used to relate structure and function in the brain (Rolando, 1809) in studies by Luigi Rolando (1773-1831). Therapeutic applications of electric currents evolved until their establishment in the mid of the 19th century leading to the valuation by Guillaume-Benjamin-Amand Duchenne (1806-1875) that 'no sincere neurologist could practice without using electrotherapy' (Duchenne (de Boulogne), 1855; Harms, 1955). With Hans Berger (1873-1941) discovering the human electroencephalography in 1924 (Berger, 1929), the field of neurophysiology achieved a breakthrough for diagnosis. In the field of stimulation, animal models were often utilized to investigate effects of electrical stimulation in the 20th century. In this line Creutzfeldt et al. (1962) stimulated the exposed cortex of a cat reporting neuron excitation and inhibition for surface positive and negative currents. Further Bliss and Lømo (1973) revealed long-lasting potentiation as result of increased efficiency of synaptic transmission satisfying criteria for synaptic memory mechanisms proposed by Hebb (1949). In this time, electric stimulation in humans was used to investigate neurophysiological systems and in clinical applications. The visual system was investigated via electric stimulation of the eye, which evoked electrically induced phosphenes (Brindley, 1955). The electroconvulsive therapy was clinically applied in the treatment of schizophrenia and depression (Cerletti, 1954).

With the beginning of the 21st century, Michael Nitsche and Walter Paulus pioneered the non-invasive application of weak direct currents to modulate neuronal activity in the brain. In their first publication Nitsche and Paulus (2000) demonstrated motor excitation

by anodal and inhibition by cathodal stimulation with intensities up to 1 mA applied via a pair of electrodes with areas of 35 cm².

The field of transcranial electrical stimulation (tES) applying weak currents (few mA) to the head has evolved regarding applied current waveforms and intensities, electrode configurations and fields of application.

With respect to the current waveforms, mainly four types (Moreno-Duarte et al., 2014) have been applied for tES: transcranial direct current stimulation (tDCS), transcranial pulsed current stimulation (tPCS), transcranial alternating current stimulation (tACS), and transcranial random noise stimulation (tRNS).

A tDCS scenario is fully described by the current intensity (mA) delivered for the stimulation duration (minutes) via an electrode configuration with their size and placement description. Optionally, fade-in and fade-out intervals can be specified at the beginning and the end of the stimulation to prevent transient onset or offset stimulation. The electrode positions determine the addressed cortical areas. Anodal current flowing inward to the local cortex, is anticipated to depolarize the soma of pyramidal neurons and hyperpolarize their apical dendrites, whereat cathodal current flowing outward the local cortex is expected to provoke the opposite (Moreno-Duarte et al., 2014). These changes in the membrane potential alter the level of neuronal excitability.

In tACS, sinusoidal waves introduce their frequency and potential amplitude offset as additional parameters compared to tDCS. Rather than modulating neuronal excitability, tACS affects the neuronal transmembrane potential to enforce neural firing with the stimulation frequency. For the course of action in tACS, two explanatory tracts are followed (Tavakoli and Yun, 2017). On the one hand tACS is thought to act via entrainment of the exogenous stimulation frequency on the neuronal firing (Krause et al., 2019). On the other hand tACS is thought to establish plasticity changes affecting neuronal spike timing (Vossen et al., 2015).

The stimulation with pulse sequences can be considered as hybrid of tDCS and tACS with on- and off-times as adjustable parameters in case of monophasic stimulation or biphasic rectangular pulses with potentially varying duty cycles. Pulsed current stimulation increased the degree of freedom in waveform design compared to tACS used in dosage optimization (Moreno-Duarte et al., 2014) or to elicit transient stimulation effects, e.g. phosphenes in transorbital stimulation (Freitag et al., 2019).

Similarly to tACS, random noise stimulation (tRNS) facilitates alternating currents but with randomly distributed frequencies and amplitudes. Normally distributed frequencies in the range from 0.1 Hz to 640 Hz are used in tRNS, whereat low- (0.1 Hz–100 Hz) and high- (101 Hz–640 Hz) frequency ranges are distinguished (Reed and Cohen Kadosh, 2018). Applications of tRNS showed high efficacy in modulation of motor cortex excitability, likely moderated via voltage-gated sodium channels (Chaieb et al., 2015).

The initial tDCS montages incorporated exact two current terminals, an anode and a cathode (Nitsche and Paulus, 2000). At these terminals, the stimulation current was administered via patch rubber electrodes placed in saline soaked sponges and fixated via rubber bands. The stimulation montages with electrodes of several square centimeters in area resulted in rather diffuse current distributions in the brain. Attempts to focalize the stimulation current in the brain resulted in the introduction of smaller electrodes combined in more diverse configurations with respect to number of electrodes and their positioning (Datta et al., 2009a).

With these degrees of freedom originating from the applicable waveforms and stimulation configuration, tES entered multiple fields of application. In neuroscience research, tES contributes to the understanding of physiological mechanisms (Fregni et al., 2005b; Antal et al., 2004b) and has therapeutic applications to neurological and psychiatric disorders such as stroke (Fregni et al., 2005a; Baker et al., 2010), epilepsy (Fregni et al., 2006; San-Juan et al., 2015), depression (Palm et al., 2012; Padberg et al., 2017) and chronic pain (Antal et al., 2017b; Pinto et al., 2018).

Despite manifold applications of tES in neuroscience and clinical research, several aspects regarding stimulation dose, application and verification desire further developments (Woods et al., 2016; Antal et al., 2017a).

The present thesis aims to shed light onto current flow modeling to guide stimulation protocols addressing specific targets, advances in administration of current stimulation via novel electrodes, and verification of stimulation configurations in physical volume conductor setups, from an engineering perspective.

1.2 TES from an engineering perspective

1.2.1 Current flow modeling

Initial tES montages incorporated a, so called, active electrode above the addressed cortical target region and a distant return electrode (Nitsche and Paulus, 2000). This approach was based on the simplified assumption, the active electrode would mainly affect the underlying cortical region in a rather homogeneous manner.

Further, applications of tES mostly use fixed regimes to all participants within a respective study (Karabanov et al., 2016). This disrespects individual differences, such as anatomical features (Moliadze et al., 2018) and thus potentially contributes to the inter-individual variability in tES effects (Li et al., 2015).

Simulating the current flow in realistic volume conductor models can clarify misconceptions on the current distribution in tES studies (Bikson et al., 2010) and account for individual anatomical structures (Datta et al., 2012).

Modeling the head as volume conductor for simulations of bio-electromagnetic field distributions in the regime of quasi-stationary approximation of Maxwell's equations (Plonsey and Heppner, 1967) builds on a long tradition in the fields of sensitivity analysis and source localization to electroencephalography (EEG) and magnetoencephalography (MEG) (Hunold et al., 2016, 2014). Spherical head models provided the starting point for analytic solutions (Sarvas, 1987). Increasing degrees of detail and complexity to multi-compartment head models (Vorwerk et al., 2014; Puonti et al., 2020) incorporating anisotropic conductivity parameterizations (Güllmar et al., 2010) demanded numerical boundary (Stenroos et al., 2007) and finite (Buchner et al., 1997) element solvers.

Early approaches of current flow modeling for tES also relied on spherical head models (Miranda et al., 2006; Bikson et al., 2008) and advanced to highly realistic volume multi-compartment models incorporating anisotropic white matter conductivity (Ramperasad et al., 2014; Wagner et al., 2014). The software toolboxes SimNIBS (Windhoff et al., 2013; Thielscher et al., 2015) and ROAST (Huang et al., 2019) have been introduced to provide integrated solutions for head modeling, current flow simulation and outcome analysis. Further pipelines, relying on more user interactions or custom code, include COMETS2 (Lee et al., 2017), SCIRun (Dannhauer et al., 2012) and SimBio (Wagner et al., 2014). Current flow modeling for tES supports safety analysis of current density distributions (Bikson et al., 2016) and tissue temperature due to impressed electric energy (Datta et al., 2009b). Computational analysis assist dosage considerations (Peterchev et al., 2012; Evans et al., 2020), especially for vulnerable populations e.g. patients with implants (Datta et al., 2010) or children (Kessler et al., 2013). Further, new electrode configurations and layouts have been investigated based on computational models (Datta et al., 2009a; Martin et al., 2017). More precisely, current flow modeling provides the basis for tES optimization to focus the stimulation to target brain regions (Dmochowski et al., 2011; Wagner et al., 2016; Guler et al., 2016) and to investigate tES effects on particular subsystems, e.g. the visual system (Laakso and Hirata, 2013).

This thesis contributes to the field of current flow modeling in chapter 2 with a simulation study focusing on non-invasive electrical stimulation of the retina in section 2.1 and a targeting approach based on Helmholtz reciprocity in section 2.2.

1.2.2 Stimulation electrodes and their applications

Conventional setups for tES application involve carbon doped rubber electrodes, either inserted in saline soaked sponge pockets (Nitsche and Paulus, 2000) or coated with adhesive electrolyte paste (Moliadze et al., 2010) fixated by rubber bands. Advances in the fixation of this type of electrodes include head gears (Seibt et al., 2015) and caps (Mansour et al., 2020). The head gear supported electrode positioning to target the left dorsolateral pre-frontal cortex with decreased inter-individual variability in e.g. depression treatment

(Seibt et al., 2015). The electrolyte layer between the stimulation electrode and the scalp mitigates effects from electro-chemical processes carried out at the interface between the stimulation electrode as electron conductor and the scalp as ion conductor. More precisely, the electrolyte layer provides ions lowering the overpotential to prevent irreversible Faradaic reactions in the scalp (Merrill et al., 2005). Even though, chemical processes at rubber electrodes are poorly described, in conjunction with multiple electrolyte gels, conductive rubber was characterized as applicable in tES (Minhas et al., 2010).

In the same study, silver/silver chloride (Ag/AgCl) ring and disc electrodes with diameters of around 10 mm were characterized with respect to their electrode potential, pH-value and temperature changes and introduced for use in targeted high definition tES (HD-tES) (Minhas et al., 2010). Applicable in multi-electrode configurations for targeted tES, such small electrodes are incorporated in cap systems integrating electrolyte reservoirs (Nikolin et al., 2015; Sprugnoli et al., 2019).

Other electrode concepts focus on geometric adaptations for current spread reduction and apply concentric configurations with a disc electrode in the center surrounded by four return electrodes (Datta et al., 2009a; Edwards et al., 2013) or a concentric ring as return electrode (Bortoletto et al., 2016; Martin et al., 2017).

Comparable to the development of pasteless EEG electrodes (Pedrosa et al., 2018), in tES, the utilization of stimulation electrodes with pre-configured electrolytes was introduced for applications below the hair line (Khadka et al., 2018).

This thesis contributes to the field of application systems for tES in chapter 3 introducing a flexible cap with integrated textile stimulation electrodes 3.1 and a concept study introducing real dry electrodes for tES 3.2.

1.2.3 Verification of stimulation concepts

Stimulation configurations calculated via current flow modeling to achieve a distinct stimulation desire verification with respect to the predicted current distribution in the head as volume conductor. Similarly, stimulation systems require performance evaluations prior to initial applications in humans. These purposes aspire metrological approaches allowing the inclusion of real-world environmental influences.

Physical head phantoms implementing the ground truth for source and volume conductor configurations have been realized based on synthetic structures and human skulls for measurement modalities, i.e. magnetocardiography (Tenner et al., 1999; Wetterling et al., 2009) and MEG/EEG (Leahy et al., 1998; Baillet et al., 2001). Such phantoms also incorporated structures, modeling anisotropic conductivity (Liehr and Haueisen, 2008).

For tES verification, synthetic hydrogel phantoms with incorporated stimulation electrodes were introduced (Jung et al., 2013; Kim et al., 2015). Verification measurements of the electric field distributions for realistic tES setups were performed in human cadaver (Vöröslakos

et al., 2018; Liu et al., 2018) and in surgical patients during stereotactic EEG interventions (Opitz et al., 2016; Huang et al., 2017). These measurement highlighted the merely ohmic conduction character and the shunting of current within the scalp and the reduction of current flow by the skull layer resulting in field strength around 0.5 V/m for 1 mA stimulation intensity (Opitz et al., 2016; Huang et al., 2017; Vöröslakos et al., 2018). This intensity is within the range calculated in modeling studies (Datta et al., 2009a; Miranda et al., 2013) and reflects a lower bound for stimulation effects shown *in vitro* (Radman et al., 2007). Where results from measurements in the human cadaver were limited by the degrading electric conductivity in postmortem tissue (Vöröslakos et al., 2018), measurements in human patients were limited by temporal dynamics of the utilized setups as voltage drops in the order of 10 % – 20 % were found in the range from 1 Hz – 20 Hz (Opitz et al., 2016; Huang et al., 2017).

This thesis contributes to the field of verification approaches for tES in chapter 4 demonstrating the performance of temporal interference tES in a large scale homogeneous volume conductor in section 4.1 and the realization of a three compartment physical head phantom for testing tES stimulation and application concepts in section 4.2.

2 Modeling of stimulation schemes

2.1 Transorbital electric stimulation

2.1.1 Introduction

Transorbital electric current stimulation targeting the retina involves electrodes placed in the vicinity of the eye (possibly involving a distant return electrode) to administer current intensities of a few hundred μA . Such stimulation reduced the defect depth or enlarged the visual fields in patients with optic neuropathy as reported in clinical single case observations (Fedorov et al., 2011; Gall et al., 2011, 2010). Further, prospective, double blind, randomized, placebo-controlled clinical trials assessing the efficacy of transorbital electric current stimulation also suggest that visual field perception can be improved in patients with optic nerve damage (Sabel et al., 2011) and glaucoma (Gall et al., 2016).

In basic research, transorbital electric current stimulation was applied to investigate neurovascular coupling in the retina (Freitag et al., 2019) and the characteristics of phosphenes (light perceptions without light entering the eye) depending on the stimulation montage (Sabel et al., 2020a).

In most applications of transorbital electric current stimulation, the induced current in the eye, or more precisely, the retina, is inaccessible. However, having insights on the current distribution in the retina could help to interpret experimental observations and to design stimulation schemes for specific pathologies. Current flow modeling by means of simulating the current density distribution in volume conductor models can provide such information on the current pattern for the modeled stimulation configurations.

One example for using current flow modeling in relation to experimental observations is a study on phosphene characteristics (Sabel et al., 2020a), in which the spatial distribution of phosphene perception was correlate to amplitude hot spots in the current density distribution. Since early applications of transcutaneous alternating current stimulation of the visual system (Antal et al., 2003), the origin of such phosphenes has been questioned.

Origins in the cortex and the retina or interactions of both areas have been proposed (Paulus, 2010). On the one hand, a modeling study indicated current density amplitudes in the eyes resulting from visual cortex stimulation as likely high enough to elicit retinal phosphenes (Laakso and Hirata, 2013). On the other hand, a study comparing stimulation montages in left-right and anterior-posterior direction, indicating higher current densities in the eye to be associated with decreased phosphene generation for montages with anterior-

posterior current alignment. For both montages phosphene perceptions was positively coupled to current densities in the occipital lobe (Indahlastari et al., 2018).

In the above mentioned studies, standard stimulation electrode montages were used for all participants, irrespective of the location and size of the individual anatomical damage or functional lesion.

Current flow modeling is a prerequisite for determining electrode configurations leading to targeted stimulation. Targeted subject-specific multi-electrode stimulation is already applied in transcranial electric brain stimulation (Antal et al., 2017a; Bikson et al., 2016) but less considered in electric stimulation of the eye. However, it is conceivable that transcorneal electric stimulation of the retina targeting the area of the visual impairment can potentially increase the specificity of the stimulation and improve the outcome. Anatomical inter-subject variability is less pronounced in the eye compared to the brain. Therefore, specific stimulation montages to target retinal regions might be more universally valid across subjects compared to target montages for the brain.

Here, the current density distributions for electrode montages used in transorbital stimulation studies are investigated by means of simulating the transorbital direct current stimulation. Qualitative and quantitative descriptions of the vectorial current density are provided with respect to their amplitude and orientation. Further, the amplitude and orientation differences originating from different stimulation montages are analyzed in comparison to a reference montage.

Parts of this chapter have been previously presented as part of a review (Sabel et al., 2020b) and in abstract form (Hunold et al., 2015, 2018a).

2.1.2 Material and Methods

A structural T1-weighted magnetic resonance imaging (MRI) dataset from a 22 years old male volunteer was segmented using the FreeSurfer (FS) software (<http://surfer.nmr.mgh.harvard.edu>) (Fischl, 2012). Binary masks for white and gray matter, cerebrospinal fluid, skull and scalp were extracted from the FS outcome using a segmentation approach (Perdue and Diamond, 2014) facilitating the Matlab (The Mathworks Inc., Natick, USA) toolbox iso2mesh (Fang and Boas, 2009). The eye compartments (vitreous and aqueous humor, lens, retina, sclera, cornea and base of the optic nerve) as well as muscles and fat surrounding the eye were segmented semiautomatically using own Matlab scripts applying iso2mesh functions. The freely available SimBio-Vgrid software (<http://vgrid.simbio.de/>) meshed the combined binary masks to hexahedral elements (Berti, 2004) keeping the voxel geometry from the MRI data with an isotropic resolution of 1 mm. The resulting finite element method (FEM) model comprised 4.3 million hexa-

hedral elements with 4.4 million nodes. Conductivity values as indicated in Table 2.1 were assigned to the tissue compartments .

Table 2.1: Tissue conductivity values in S/m according to respective literature references.

Tissue	Conductivity in S/m	Reference
White matter	0.14	(Ramon et al., 2004)
Gray matter	0.33	(Ramon et al., 2004)
Cerebrospinal fluid	1.79	(Baumann et al., 1997)
Skull	0.01	(Tang et al., 2008)
Scalp	0.435	(Burger and Milaan, 1943)
Vitreous humour	1.55	(Lindenblatt and Silny, 2001)
Lens	0.32	(Lindenblatt and Silny, 2001)
Aqueous humour	1.8	(Gabriel et al., 1996)
Retina	0.7	(Gabriel, 1996)
Sclera	0.56	(Lindenblatt and Silny, 2001)
Cornea	0.5	(Lindenblatt and Silny, 2001)
Optic nerv	0.03	(Gabriel et al., 1996)
Muscle	0.35	(Gabriel, 1996)
Fat	0.04	(Gabriel et al., 1996)

The volume conductor model of the head was extended with stimulation electrodes as 4 mm thick compartments (cf. Figure 2.1). The electrodes were modeled as one compartment reflecting the Ten20 (D.O. Weaver and Company, Aurora, CO, USA) conductive paste. Therefore, its conductivity was set to 8 S/m (Saturnino et al., 2015). Electrodes with 3 cm \times 3 cm side length were positioned at O2, Cz, Fp2, F8 and F7 according the international 10–20 system (Jasper, 1958; Klem et al., 1999), right infraorbital, above the temples, and above the sphenoid bones (SB) at the level of the lateral palpebral ligaments. Further a ring electrode with inner and outer diameters of 40 mm and 56 mm surrounding the right eye and a 10 cm \times 10 cm electrode over Oz were modeled. The simulations were performed considering two electrodes at a time using the SimBio software (https://www.mrt.uni-jena.de/simbio/index.php/Main_Page), applying the adjoint approach (Wagner et al., 2014). The scalar electric potential at each node of the mesh was obtained solving the Laplace equation with in-homogeneous Neumann boundary conditions at electrode nodes summarizing to a current intensity of 1 mA and homogeneous Neumann boundary conditions at the scalp nodes not shared with an electrode compartment. The electric field was obtained as gradient of the scalar electric potential in each finite element. The current density was calculated as electric field scaled by the tissues’ conductivity value.

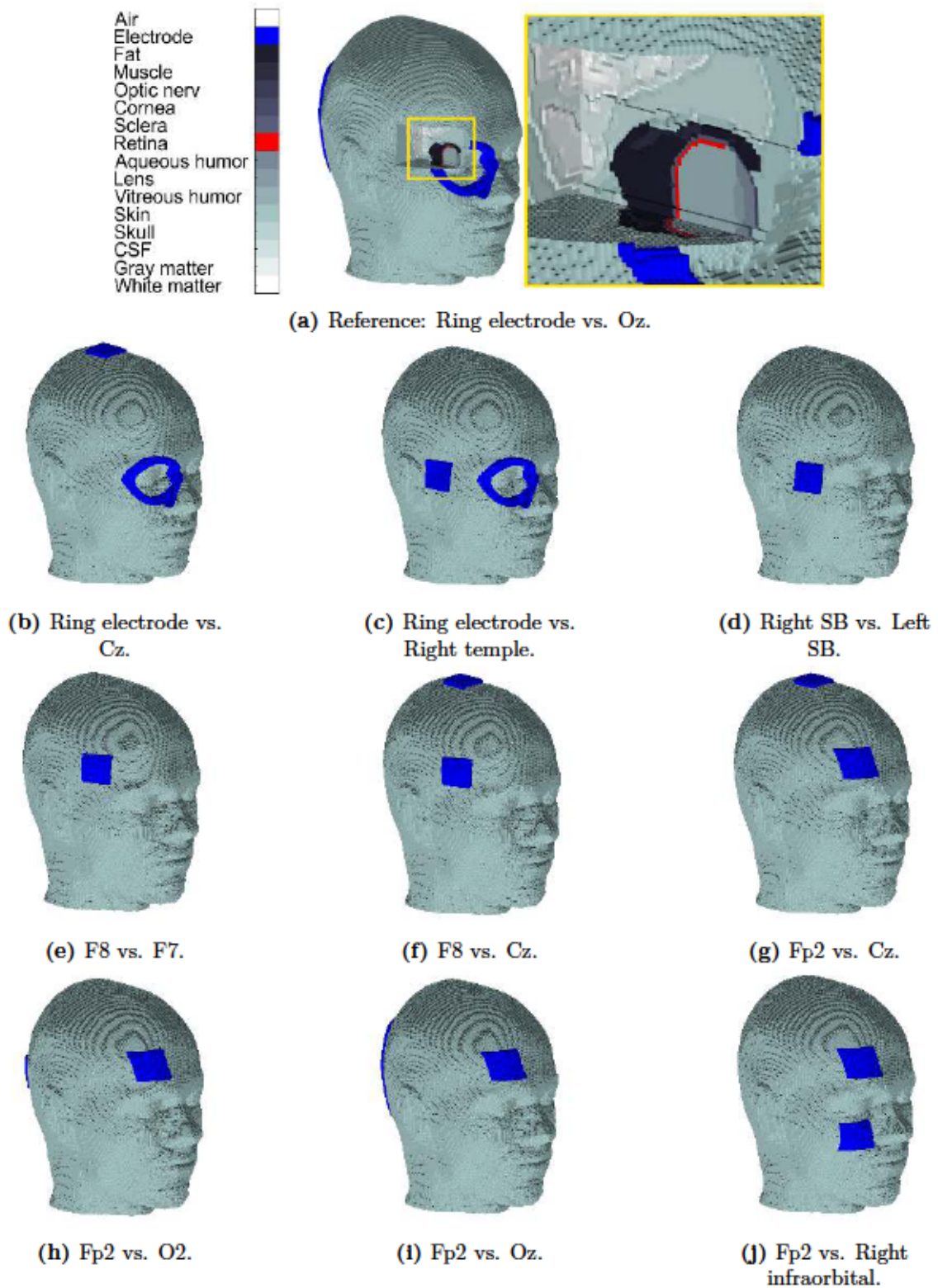


Figure 2.1: Simulation models according to montages described in Table 2.2. Colors code conductivity compartments (a).

The stimulation intensity in the retina of the right eye was evaluated qualitatively by visualizing the current density as vectors with orientation and amplitude.

For quantitative analysis, the total current density J_{tot} in the retina was considered according to equation 2.1 with i integrating over the $n = 917$ elements of the retina.

$$J_{tot} = \sum_{i=1}^n |\vec{J}_i| \quad (2.1)$$

Comparisons of test montages to a distinct reference montage were analyzed in order to evaluate differences in the current density distributions originating from different stimulation montages. The montage comprising the ring electrode and the electrode at Oz led to full field phosphene perception as described in Freitag et al. (2019) and thus motivated its use as reference montage. The test montages reflect montages applied in Sabel et al. (2020a). Montages as described in Table 2.2 were chosen for this comparison.

Figure 2.1 presents the model with an incision in the eye region in the reference montage (a) and all test montages (b-j).

Table 2.2: Simulated montages of transorbital electric stimulation targeting the retina.

Role	Anode	Cathode
Reference	Ring electrode	Oz
Test	Ring electrode	Cz
	Ring electrode	Right temple
	Right SB	Left SB
	F8	F7
	F8	Cz
	Fp2	Cz
	Fp2	O2
	Fp2	Oz
Fp2	Right infraorbital	

The current density distributions of the test montages were compared to the current density distribution from the reference montage based on intensity and directionality measures. The magnitude ratio (MAG), according to equation 2.2, evaluated variations in the current density amplitudes generated by the different test montages with respect to the reference montage.

$$MAG = \frac{|\vec{J}_{test}|}{|\vec{J}_{ref}|} \quad (2.2)$$

Deviations in directionality were evaluated by the cosine of angles between current density vectors (COS) from simulations of reference and test montages in each element of the right retina, according to equation 2.3.

$$COS = \frac{\vec{J}_{ref} \cdot \vec{J}_{test}}{|\vec{J}_{ref}| |\vec{J}_{test}|} \quad (2.3)$$

Further, the earth movers distance (EMD) was calculated according to equation 2.4.

$$EMD = \frac{\sum_{i=1}^n \sum_{j=1}^n d_{ij} f_{ij}}{\sum_{i=1}^n \sum_{j=1}^n f_{ij}} \quad (2.4)$$

with i and j integrating over the n elements of the retina in the reference (i) and test (j) montage models, d symbolizing the distance between \vec{J}_{ref} and \vec{J}_{test} and f being the flow which is minimized to determine the EMD, as conceivable from Rubner et al. (2000). The EMD represents a distance between the three dimensional current density distributions in the retina from reference and test montages and thus incorporates both amplitude and orientation features.

2.1.3 Results

The simulations of transorbital electric stimulation using the models introduced in subsection 2.1.2 resulted in current density distributions in the volume conductor models. Figure 2.2 illustrates an example of the current density vector distribution with color-coded amplitudes. The image shows the current density vectors superimposed to the volume conductor model for the region of interest at and around the eye in the reference model.

The total current density J_{tot} integrated over all elements in the retina varied from 147.1 A/m² (Fp2 vs. Right infraorbital) to 35.6 A/m² (F8 vs. Cz). Total and mean current density maximized for the montage Fp2 vs. Right infraorbital ($J_{tot} = 147.1$ A/m², $J_{mean} = 0.16$ A/m²) followed by the montages involving the ring electrode surrounding the eye ($J_{tot} \approx 105.5$ A/m², $J_{mean} \approx 0.115$ A/m²) with large electrode areas near the right eye. In contrast, montages involving the electrode F8 or the electrode at the right SB with their return electrodes rather distant to the right eye, resulted in lowest current density values in the right retina (J_{tot} : 35.56 A/m² - 57.59 A/m², J_{mean} : 0.04 A/m² - 0.06 A/m²). Intermediate current density intensities with $J_{tot} \approx 86$ A/m² ($J_{mean} \approx 0.08$ A/m²) were generated by montages incorporating the electrode at Fp2 close to the right eye and rather distant return electrodes at Cz, Oz or O2. Table 2.3 provides an overview of quantitative measures with the mean current density amplitude J_{mean} , its standard deviation J_{std} , the

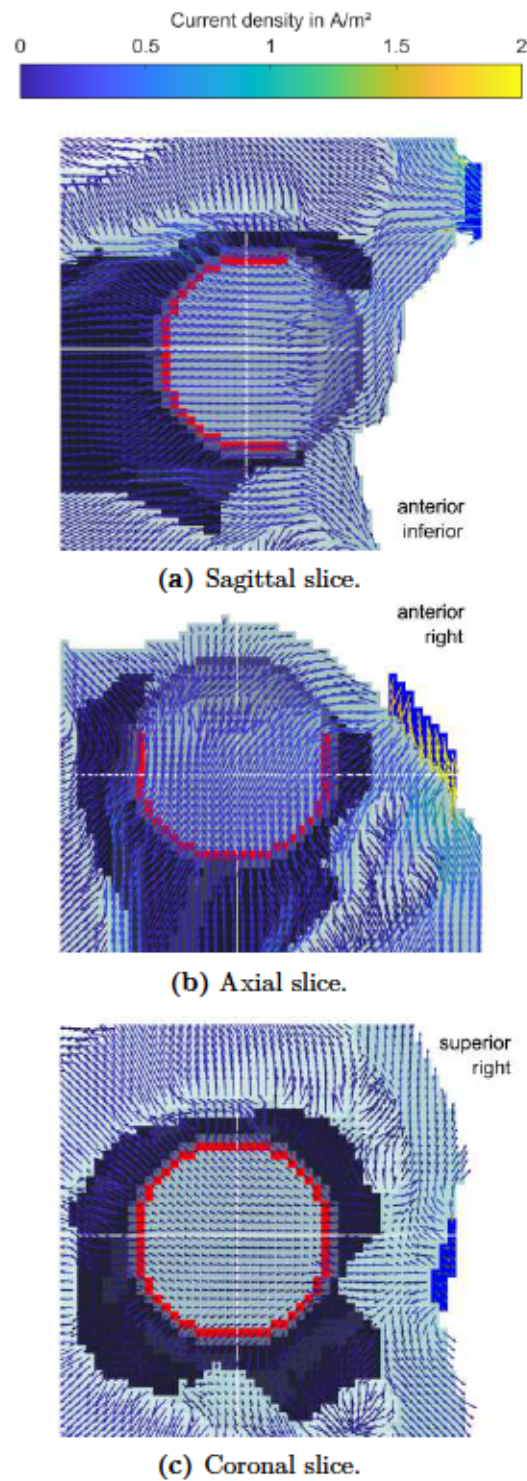


Figure 2.2: Current density vector distributions with color-coded amplitudes in the region of interest of the right eye and its vicinity simulated in the reference model (Table 2.2) superimposed on model sections. Tissue compartments are color-coded as introduced in Figure 2.1a. White lines indicate cut-planes in the three interrelated sub-figures (a) to (c).

Table 2.3: Quantitative measures of current density amplitudes derived from the retina of the different models.

Model	J_{tot}	J_{mean}	J_{std} in A/m ²	J_{min}	J_{max}
Ring electrode vs. Oz	105.14	0.11	0.03	0.06	0.35
Ring electrode vs. Cz	105.75	0.12	0.03	0.06	0.36
Ring electrode vs. Right temple	105.52	0.11	0.03	0.05	0.32
Right SB vs. Left SB	57.56	0.06	0.04	0.03	0.28
F8 vs. F7	42.08	0.05	0.02	0.02	0.14
F8 vs. Cz	35.56	0.04	0.02	0.02	0.11
Fp2 vs. Cz	81.62	0.09	0.03	0.04	0.23
Fp2 vs. O2	88.44	0.10	0.03	0.04	0.25
Fp2 vs. Oz	88.14	0.10	0.03	0.04	0.25
Fp2 vs. Right infraorbital	147.13	0.16	0.10	0.06	0.60

minimal value J_{min} and maximal value J_{max} of the current density amplitude occurring in the right retina of the simulation models introduced in Table 2.2.

For visualization purposes, the model elements of the retina were projected on a 2D plane in polar coordinates. The amplitude distributions of the current densities for the different montages are depicted in Figure 2.3. The montages incorporating the ring electrode generated current density distributions peaking in the superior section with intermediate eccentricity and providing current density values in the order of 0.1 A/m² in the central section. The return electrodes demonstrated minor influences on the current density distributions in these montages as conceivable from Figure 2.3a-c. Similarly, the electrode Fp2 dominated the appearance of the current density distributions depicted in Figure 2.3g-i with a hot spot in the superior right periphery irrespective of the return electrode at Cz, O2 or Oz. In contrast the Right infraorbital electrode introduced a even more dominant hot spot, both with respect to intensity and extend, in the inferior section from intermediate to maximal eccentricity in combination with the electrode Fp2 (cf. Figure 2.3j). The montages incorporating electrodes lateral to the eyes, i.e. F7, F8 and SB electrodes, generated current density distribution with lower amplitudes compared to the other montages (cf. Figure 2.3d-f). With the electrode F8, relative hot spots in the right eye occurred lateral and nasal with slightly larger extent and intensity in the lateral location. In contrast, the electrode at the right SB clearly induced a current density hot spot in the right lateral periphery of the right retina.

The orientation of the current density vectors along the anatomical axes, in anterior-posterior, medial-lateral and inferior-superior directions, is depicted in Figure 2.4. The montages incorporating the ring electrode generated current density distributions predom-

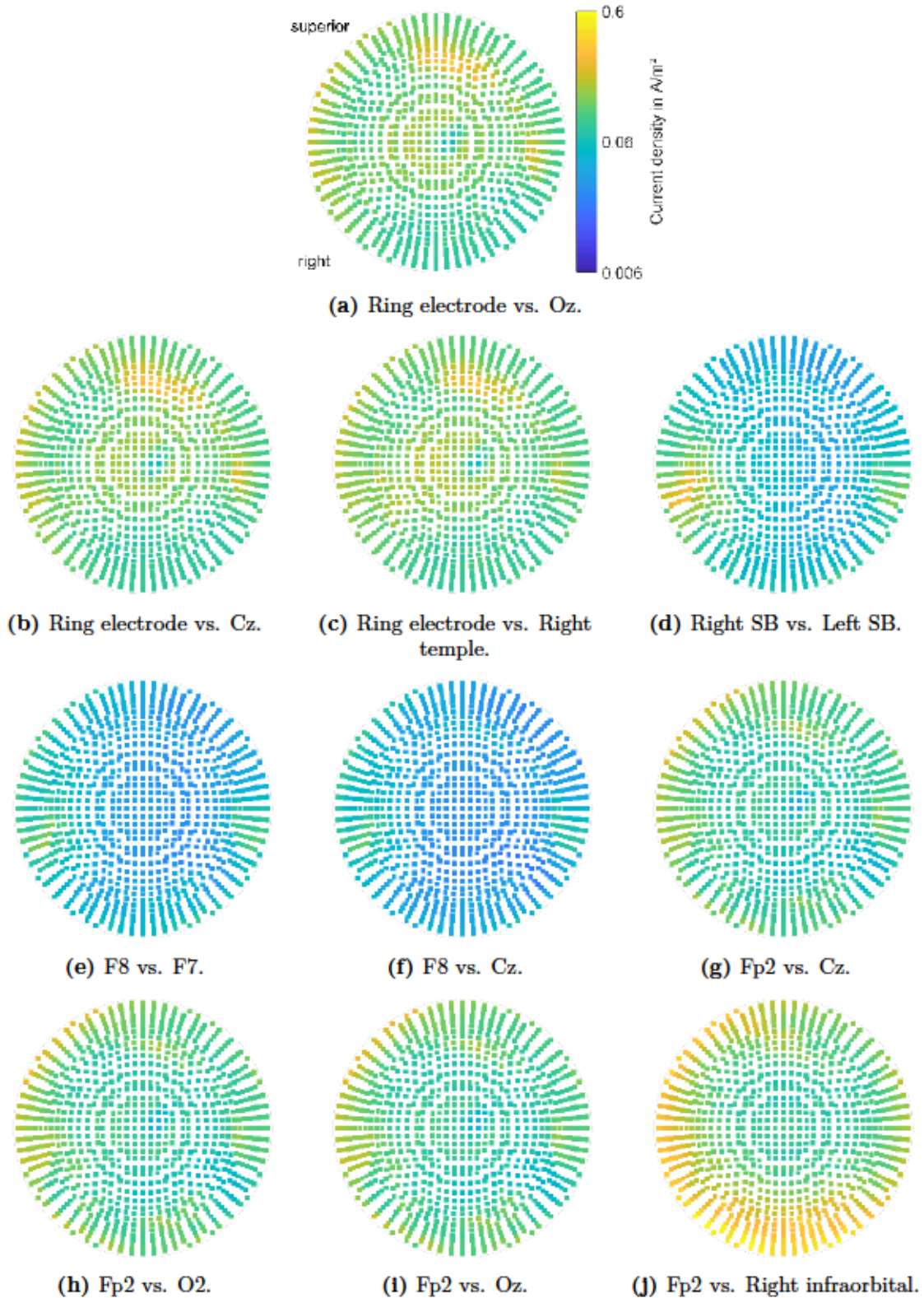


Figure 2.3: Current density amplitude distributions in the right retina of models introduced in Figure 2.1 projected on a plane in polar coordinates. Colors code current density amplitudes on a logarithmic scale as introduced in (a).

inantly orientated along the anterior-posterior axis 2.4a-c. The return electrodes demonstrated minor influences on the current density orientation in these montages. Montages with lateral electrode positions, on the SBs or F8 and F7, generated current density distribution with major medial-lateral orientation (cf. Figure 2.4d-f). The electrode Fp2 dominated the direction of the current density vectors along the anterior-posterior axis in central and superior areas as depicted in Figure 2.4g-i, and with inferior-superior orientation in the frontal inferior part. In all these montages, the return electrodes demonstrated minor influences on the current density orientations. In contrast the Right infraorbital electrode introduced a change in orientation to predominantly inferior-superior direction in combination with the electrode Fp2 (cf. Figure 2.4j).

The magnitude ratio (MAG) of the current density amplitudes in the retina reflected amplitude differences between each test model and the reference model.

As conceivable from the current density amplitude evaluations above, montages incorporating the ring electrode and the electrode Fp2 generated current density amplitudes similar to the reference montage, reflected in mean MAG values around 1 (0.08 - 1.57). However, the deviating morphologies of hot spots in the current density distributions from montages with electrode Fp2 resulted in $MAG_{min} \approx 0.43$ and $MAG_{max} \approx 3.4$, considerably deviating from 1. Especially, the Fp2 vs. Right infraorbital montage with the dominant inferior hot spot generated highest deviations from the $MAG = 1$ in the extreme values with $MAG_{min} = 0.39$ and $MAG_{max} = 7.39$. The current densities from montages with lateral electrodes generated less intense current density distributions resulting in average MAG values below 1 with $MAG_{mean} \approx 0.4$ for F8 montages and even lower with $MAG_{mean} \approx 0.1$ for SB electrodes. Due to the disjoint positions of hot spots in the reference montage and the test montages with lateral electrodes, the average MAG_{max} was around 1.1. Table 2.4 provides an overview of the MAG quantities, i.e. the mean magnitude ratio MAG_{mean} , its standard deviation MAG_{std} , the minimal value MAG_{min} and the maximal value MAG_{max} for the test models introduced in Table 2.2.

The MAG value distribution on the right retina for the test montages are depicted in Figure 2.5. The montages incorporating the ring electrode generated homogeneous MAG distributions with values around 1 (cf. Figure 2.5a,b) reflecting the similarities in current density distributions in Figure 2.3a-c. The MAG distributions from montages with electrode Fp2 and cephalic return electrodes (cf. Figure 2.5f-h) indicated relatively small deviations from 1 in the periphery towards smaller values (dark blue rim) and in areas with intermediate eccentricity towards larger values (light blue areas). The MAG distribution from montage Fp2 vs. Right infraorbital electrode (cf. Figure 2.5i) indicated very low MAG values in the very dark blue area reflecting the dominant inferior hot spot in Figure 2.3j). The MAG distributions from montages with lateral electrodes (cf. Figure 2.5c-e) indicated most prominent deviations from 1 with larger MAG values in the central region and in a superior area with intermediate eccentricity. These reflected the current density hot spots from the

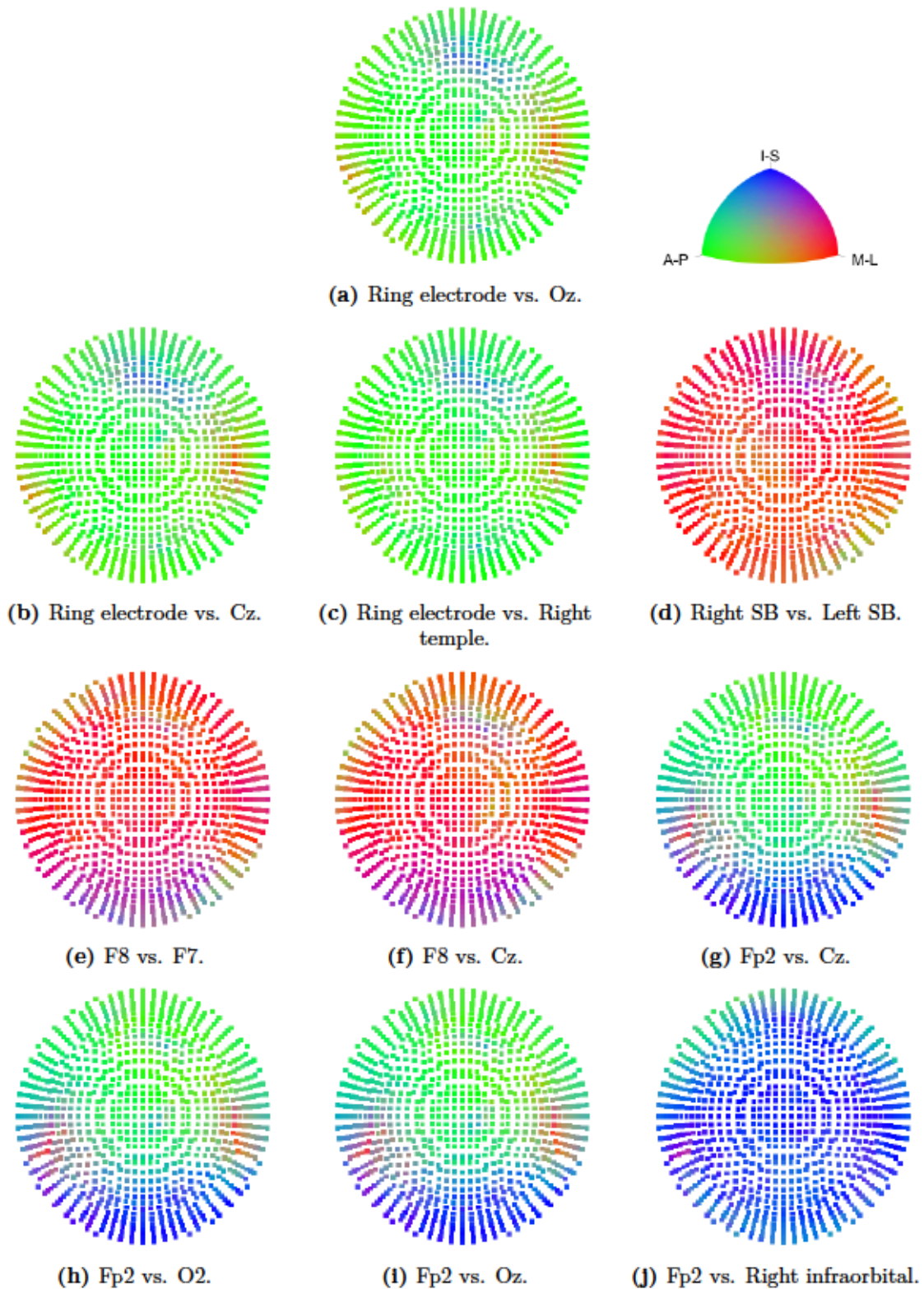


Figure 2.4: Current density orientation in elements depicted in Figure 2.3 with color-coded vector components along the anatomical axis, in anterior-posterior (A-P), medial-lateral (M-L) and inferior-superior (I-S) direction.

Table 2.4: Quantitative measures of the magnitude ratio (MAG) derived from the retina of the different test models with respect to the reference model.

Model	MAG_{mean}	MAG_{std}	MAG_{min}	MAG_{max}
Ring electrode vs. Cz	1.00	0.02	0.92	1.08
Ring electrode vs. Right temple	1.02	0.09	0.81	1.37
Right SB vs. Left SB	0.07	0.31	0.17	2.31
F8 vs. F7	0.42	0.18	0.12	1.22
F8 vs. Cz	0.35	0.13	0.16	0.96
Fp2 vs. Cz	0.80	0.22	0.45	1.83
Fp2 vs. O2	0.87	0.27	0.43	2.10
Fp2 vs. Oz	0.87	0.27	0.43	2.10
Fp2 vs. Right infraorbital	1.57	1.19	0.39	7.39

reference montage in the areas of low current density amplitudes from these test montages.

The cosine of angles (COS) between current density vectors in the retina from each test model with respect to the reference model evaluated the orientation differences. Table 2.5 provides an overview of the COS quantitative, i.e. the mean COS_{mean} , its standard deviation COS_{std} , the minimal value COS_{min} and the maximal value COS_{max} for the test models introduced in Table 2.2. The qualitative distributions depict changes in current density orientation as shown in Figure 2.6.

Similar to the current density amplitude distributions, the current density orientation was marginally affected by the return electrode in montages incorporating the ring electrode. This resulted in homogeneous COS distributions with values around 1 as depicted in Figure 2.6a,b. Montages with electrode Fp2 and cephalic return electrodes introduced interior peripheral orientation changes (cf. Figure 2.6f-h) up to approximately 120 degrees with $COS_{min} \approx -0.5$. However, major central and superior parts of the current density orientation indicated orientation deviations smaller than 45 degrees, resulting in a $COS_{mean} \approx 0.7$. In contrast, the montage Fp2 vs. Right infraorbital electrode introduced orientation changes of 75 degrees and above for most parts of the retina, resulting in a $COS_{mean} \approx 0$. Only a superior peripheral rim indicated relatively small orientation of around 30 degrees changes with $COS_{max} = 0.88$. The current density orientation distributions from montages with lateral electrodes revealed complex pattern in Figure 2.6c-e and a wide range between $COS_{min} \approx -0.7$ and $COS_{max} \approx 0.9$. The lateral electrodes close to the right eye (F8, Right SB) resulted moderate orientation changes up to approximately 60 degrees with orange or yellow colored COS values in a right lateral rim of the retina. A left superior lateral area with intermediate eccentricity, most prominent in the montages with Cz, indicated small to moderate orientation changes, with $COS_{max} \approx 0.9$. An inferior

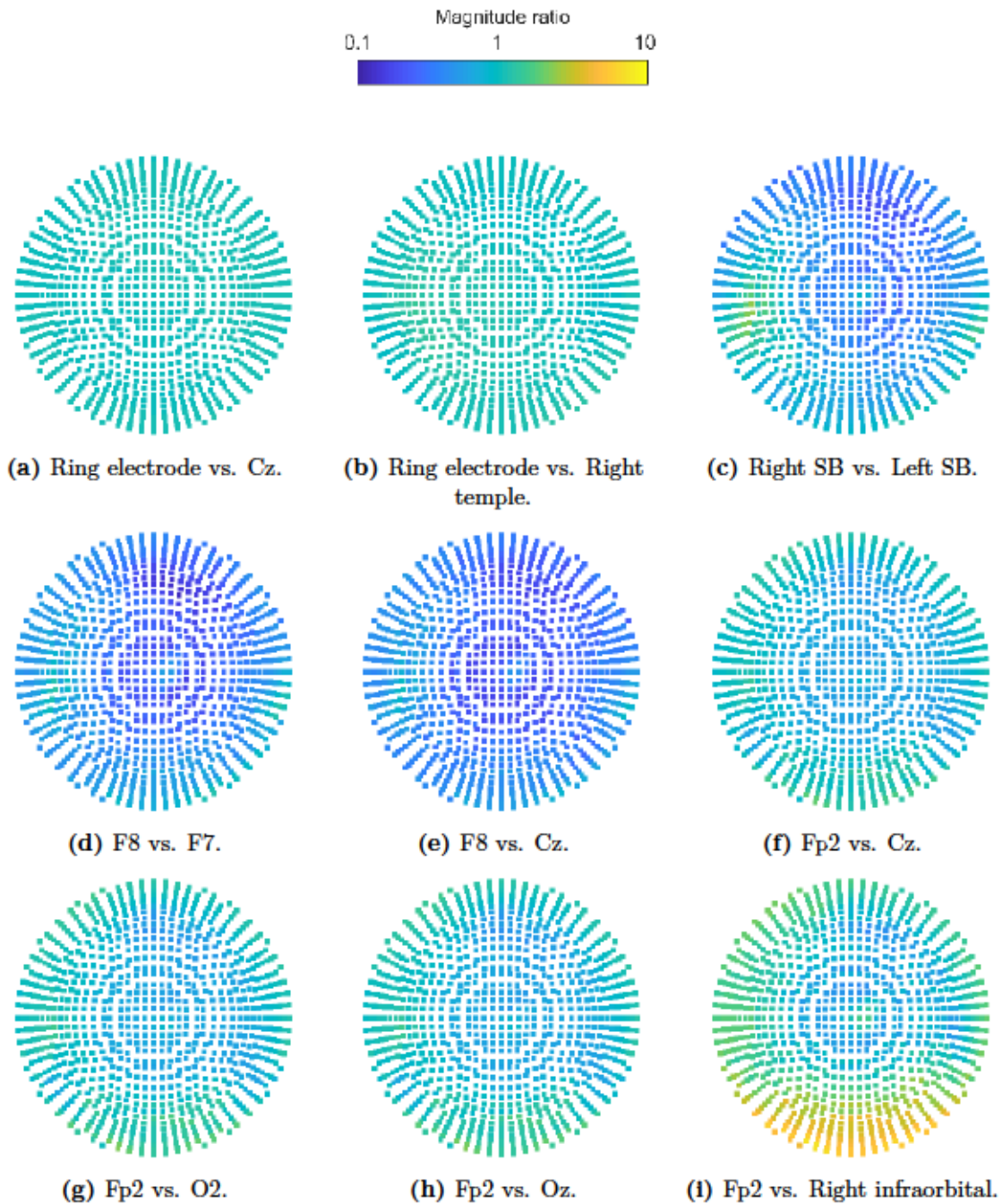


Figure 2.5: Magnitude ratio (MAG) distributions in the right retina of the test models introduced in Figure 2.1 projected on a plane in polar coordinates. Colors code the MAG as introduced above the sub figures.

Table 2.5: Quantitative measures of the cosine of angles (COS) between current density vectors from the retina of the different test models with respect to the reference model.

Model	COS_{mean}	COS_{std}	COS_{min}	COS_{max}
Ring electrode vs. Cz	1.00	0.001	0.99	1.00
Ring electrode vs. Right temple	0.98	0.017	0.84	1.00
Right SB vs. Left SB	0.12	0.353	-0.75	0.91
F8 vs. F7	0.22	0.347	-0.75	0.92
F8 vs. Cz	0.35	0.368	-0.71	0.95
Fp2 vs. Cz	0.71	0.302	-0.47	0.98
Fp2 vs. O2	0.68	0.305	-0.49	0.97
Fp2 vs. Oz	0.68	0.306	-0.48	0.97
Fp2 vs. Right infraorbital	-0.06	0.347	-0.84	0.88

nasal and a right central region consistently demonstrated strongest orientation changes for these montages of around 120 degrees and above, with $COS_{min} \approx -0.7$.

The earth movers distance (EMD) quantified the dissimilarity, considering amplitude and orientation features, between the current density distributions in the retina from test models and the reference model. Across all test model – reference model comparisons, the average EMD was 0.0789 A/m^2 with a standard deviation of 0.0513 A/m^2 . The minimal EMD was 0.006 A/m^2 and the maximal EMD was 0.186 A/m^2 , which occurred for the test models Ring electrode vs. Cz and Fp2 vs. Right infraorbital. Table 2.6 provides an overview of the EMDs for all test models.

Table 2.6: Earth movers distance (EMD) derived from the current density in the retina between the different test models and the reference model.

Model	EMD in A/m^2
Ring electrode vs. Cz	0.006
Ring electrode vs. Right temple	0.025
Right SB vs. Left SB	0.081
F8 vs. F7	0.088
F8 vs. Cz	0.109
Fp2 vs. Cz	0.062
Fp2 vs. O2	0.076
Fp2 vs. Oz	0.077
Fp2 vs. Right infraorbital	0.186

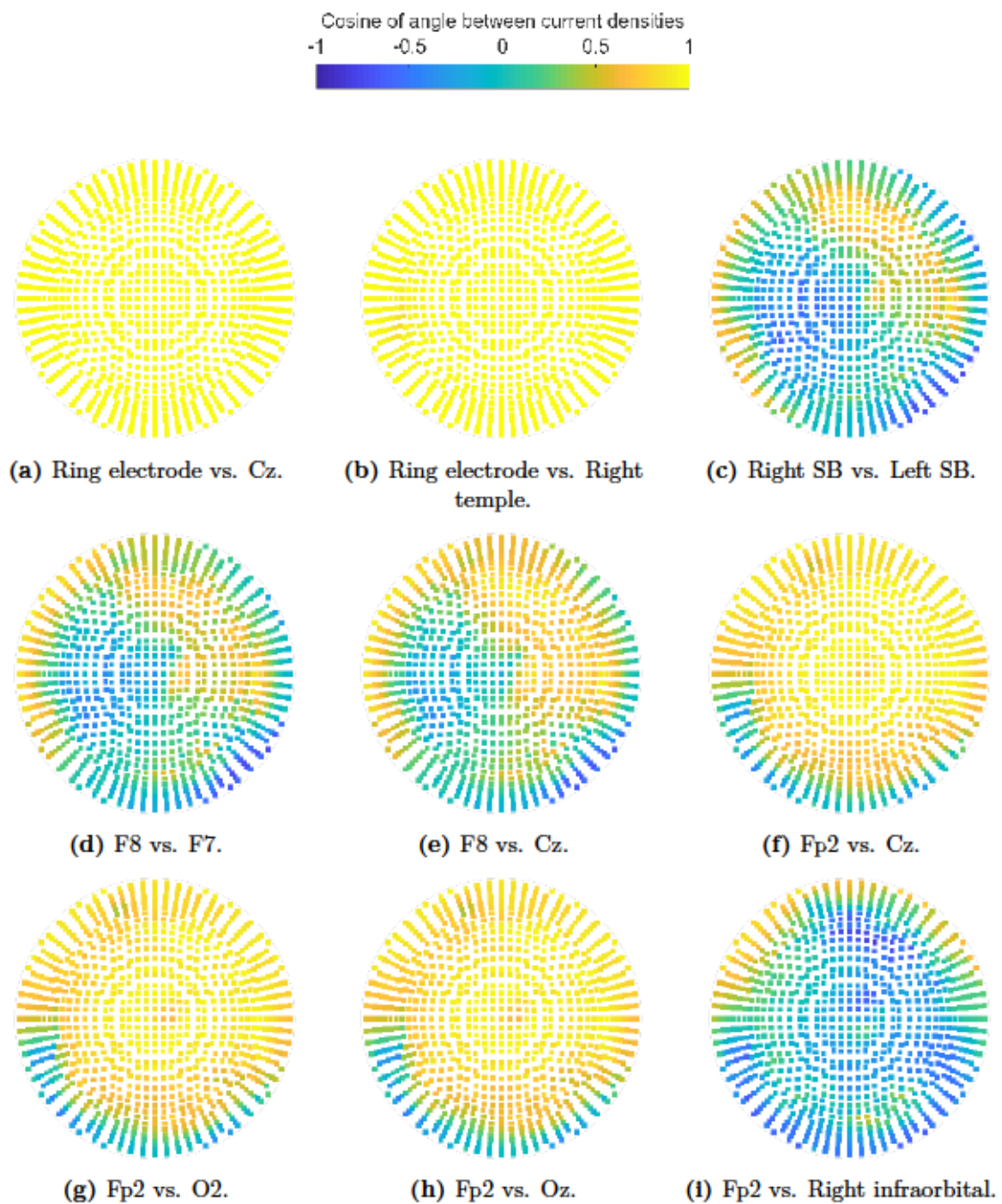


Figure 2.6: Cosine of angle (COS) distributions in the right retina of the test models introduced in Figure 2.1 projected on a plane in polar coordinates. Colors code the COS as introduced above the sub figures.

2.1.4 Discussion

The models representing transorbital electric stimulation montages involved electrodes in the eye vicinity and at standard positions derived from the 10–20 system. A ring electrode surrounding the eye and patch electrodes at Fp2, F8 and over the right sphenoidal bone centered at the height of the lateral palpebral ligament served as stimulation electrodes. The stimulation montage comprising the ring electrode and a large return electrode over the occiput, as used in (Freitag et al., 2019), served as reference montage for model comparisons. The various test montages were derived from experimental phosphene investigations, among other pilot studies utilized in (Sabel et al., 2020a).

The resulting current density amplitude in the retina varied by a factor of 4 to 5 for the quantitative measures of the totally impressed current density, the mean and the maximal current density.

The maximal value in these quantitative measures of the current density occurred for the montage Fp2 vs. Right infraorbital, which incorporated two electrodes close to the eye, followed by the montages incorporating the ring electrode. However, the ring electrode ensured a more homogeneous activation of the retina on this high intensity level with a slight focus in central regions. In contrast the Fp2 vs. Right infraorbital montage demonstrated a more peripheral activation of the retina.

The minimal values in amplitude measures of the current density were consistently provided by the montage F8 vs. Cz involving the most distant stimulation electrode with respect to the right eye and a cephalic return electrode. The amplitude distributions for montages incorporation F8 as stimulating electrode were rather homogeneous on a low intensity level without strong hot spots.

The most focal stimulation of a lateral spot in the right periphery of the right retina was provided by the montage right SB vs. left SB. Montages incorporating Fp2 as stimulating electrode led to dominant right upper peripheral activation of the retina, except for the montage with the infraorbital return electrode, where the periphery was almost completely activated and the hot spot occurred in the inferior hemisphere.

Interpreting the MAG distributions for the test montages incorporating the stimulation electrodes at F8 and at the infraorbital position, it seemed conceivable that the distance of the stimulation electrode strongly influence the stimulation intensity in central regions of the retina. Further, alterations in the positioning of a single stimulation electrode close to the eye rather strongly influences the hot spot location as derivable from the montage right SB vs. left SB.

The COS quantities measured the orientation deviation from the test montages with respect to the reference model. Stimulating the retina as half-spherical structure, the orientation of the current density might represent an essential parameter when targeting

specific regions. The ring electrode ensured a rather homogeneous orientation of the impressed current in anterior-posterior direction, even when the return electrode was changed in extent and location. Only a small spot in the right periphery demonstrated a orientation shift of up to 30 degrees with the return electrode at the right temple. Similarly, the montages incorporating the electrode at Fp2 and a distant return electrode (Cz, Oz, O2) provided rather homogeneous direction profiles in a similar direction as in the reference montage. Just the inferior frontal part of the retina indicated an orientation change up to 90 degrees for those montages with respect to the reference current density. In contrast, the montage of Fp2 vs. the right inferiororbital electrode changed the predominant orientation to inferior-superior direction, which resulted in changes up to 180 degrees in the inferior frontal part, in central regions around 90 degrees and kept the reference orientation in the superior frontal periphery. The montages incorporating laterally positioned electrodes changed the orientation in medial-lateral direction predominantly affecting right central and left peripheral regions with rather similar variations from the reference distribution.

In contrast to MAG and COS as distinct quantitative measures for amplitude and orientation comparison, the EMD represented an overall measure accounting for amplitude and orientation aspects. The EMD indicated largest dissimilarity from the reference model for montage Fp2 vs. right infraorbital, since this model impressed stronger currents with rather different overall orientation compared to the reference. The montages of the ring electrode and Cz or the right temple electrode showed the smallest EMD values. However, the small orientation changes due to the return electrode at the right temple introduced a factor of around 4 between the EMD values of these two montages.

The transorbital stimulation with stimulation electrodes close to the eye as presented here, provided current density distributions with maximal amplitudes in the retina from $0.11 \text{ A/m}^2 - 0.6 \text{ A/m}^2$ for a stimulating current intensity of 1 mA. Maximal current density amplitudes in the range of $0.008 \text{ A/m}^2 - 0.04 \text{ A/m}^2$ have been estimated to be sufficient to evoke retinal phosphenes and therefore stimulate the retina (Laakso and Hirata, 2013). Thus each montage incorporated in the present study qualified for phosphene provocation in the retina. The current density in the retina simulated with the montages incorporating a stimulation electrode close to the eye appeared around a factor of 10 stronger compared to simulation studies investigating phosphenes evoked by transcranial electric stimulation, which considered electrodes distant to the eye (Indahlastari et al., 2018; Laakso and Hirata, 2013). This might enable a dynamic range of stimulation intensities below 1 mA, enabling partial retinal stimulation at montage specific hot spots. When incorporating a frontal stimulation electrode at Fpz in tES montages, the mean current density amplitude in the eye were around 0.2 A/m^2 (Indahlastari et al., 2018) and thus in the range of the results presented here. Therefore, such tES montages likely induce retinal phosphenes.

The current density amplitudes of maximal 0.6 A/m^2 simulated here (equivalent to $(0.6 \text{ A/m}^2)/(0.7 \text{ S/m}) = 0.9 \text{ V/m}$) for the retina, were in well agreement with the estimated dosage for two electrode stimulation delivered to the brain in the range from $0.2 \text{ V/m} - 1.6 \text{ V/m}$ (Datta et al., 2009a; Parazzini et al., 2011). The intensities calculated here were an order of magnitude smaller than the current intensities of 6.3 A/m^2 at which brain injury could occur as derived from animal studies (Antal et al., 2017a).

Simulating the current density distribution in volume conductor models is essential to design electrode montages targeting specific areas. Especially when aiming at sub-regions of the retina to address individual failure symptoms and functional lesions, electrode montages stimulating the target with desired orientation and amplitude, are desired. The here presented simulations demonstrate the possibility to target specific regions of the retina, by the use of various electrode configurations for transorbital electric stimulation. Due to the relative consistent anatomy of the eye across subjects, individual volume conductor models as for the brain might not be necessary. However, in case of anatomical abnormalities in the eye, e.g. retinal detachment, or its vicinity, the volume conductor model would need to reflect the patient specific anatomy.

The above mentioned studies used eye models with significant simplifications. Depending on the desired degree of detail, very simple approaches, such as modeling the eye as one compartment (Hauelsen et al., 1995) might be sufficient. In studies investigating the current distribution in the eye impressed by electrical stimulation, the eye models were embedded in realistic finite element models of the head, in which up to 15 different tissue types were considered. These included nine major eye compartments (cornea, sclera, lens, vitreous humor, aqueous humor, retina, optic nerve, muscles, fat tissue) and six major head compartments (white matter, gray matter, cerebrospinal fluid, skull compacta, skull spongiosa, skin), where the white matter compartment might incorporate anisotropic conductivity (Güllmar et al., 2010). Subsets of these compartments were used in the modeling studies of retinal electrical stimulation (Indahlastari et al., 2018; Hunold et al., 2018a, 2015; Gall et al., 2016; Laakso and Hirata, 2013).

The degree of detail in the eye model used in the present study introduced deviations from anatomy, especially in sub-millimeter structure. Such, the retina was modeled as one-element-layer over estimating its thickness by a factor of around three (Myers et al., 2015). The approximation of thin structures in the eye by model layers incorporating only one element in thickness also introduced a charge leakage issue, when the layer is bend (Sonntag et al., 2013). However, since the conductivity gradients across eye tissues were less pronounced as compared to the conductivity differences between CSF and skull, the leakage artifacts were less severe.

Given the availability of MRI data with sub-millimeter spatial resolution and applicable processing tools, the level of detail in the model should be improved in future studies. A

higher resolution in the FEM models will allow more realistic modeling of the eye anatomy, e.g. the retina, and grant the inclusion of more tissue types, e.g. the choroid. With those extensions, conductivity values for eye tissue types are desired and should be investigated in future experimental studies.

The present study incorporated different montages for transorbital electric stimulation to address current density distributions in the retina. The results provide a proof of concept for the stimulation of retinal regions with different current intensities and orientations. Extending this approach with variations of subject's viewing direction can increase the degrees of freedom yielding pathology specific stimulation. Further, the concept of targeting regions of interest by specific stimulation configurations can be transferred to transcranial electric stimulation.

2.2 Reciprocity in targeting transcranial electric stimulation

2.2.1 Introduction

Conventional stimulation setups of tES typically involve two rubber electrodes (anode, cathode) of several square centimeters, as introduced by Nitsche and Paulus (2000). The rubber electrodes are inserted in sponge pockets soaked with saline solution to establish a safe low impedance of the electrode–skin interface (Antal et al., 2017a). The electrodes are attached to the human head by rubber bands, which surround the head and hold the electrodes in place at pre-defined positions. This complicated and time-consuming procedure demands specifically trained personnel and is error-prone to electrode misplacement and variations in the effective electrode area. These drawbacks might contribute to a lack of reproducibility in longitudinal studies stimulating a specific participant, group studies involving different participants and comparability of stimulations across multiple sites involving different operators (Padberg et al., 2017). Further, fastening patch electrodes by rubber bands limits the number of electrodes in use, as well as the positions that can be addressed (Klein et al., 2013).

New applications of tES request reproducible dosage (Peterchev et al., 2012) which fundamentally relies on electrode positioning and placement especially in longitudinal studies, and across multiple subjects, as well as multiple centers. Further, stimulation schemes which target specific brain areas with predefined intensity and orientation at the target, and preserve non-target areas from external electric field desire individualized tES setups and stimulation current distributions across available electrodes. In this line, multi-channel tES can address distinct cortical targets (Dmochowski et al., 2011; Sadleir et al., 2012), and nodes in neuronal networks (Jefferys et al., 2003). However, the optimization of stimulation currents among the electrodes to address a distinct target in the brain is an ill-posed problem (cf. duality to source localization). Constrained solutions can be found in optimization for intensity, directionality or focality (Dmochowski et al., 2011; Wagner et al., 2016; Sadleir et al., 2012), but need to be compromised among these criteria. So far introduced multi-channel stimulation setups involve small electrodes with diameters up to 2 cm (Minhas et al., 2010) and electrode patches with an area of approximately 22 cm² (Sadleir et al., 2012). Previously introduced stimulation caps are based on electrode arrays (Park et al., 2011), and arrangements of small electrodes in an electroencephalography cap (Dmochowski et al., 2011). These approaches facilitate predefined layouts of small electrodes, but might introduce restrictions with respect to current density on the scalp and thus might raise safety concerns. Further, such setups limit individual fits since pre-assembled semi-rigid or rigid caps are used.

In order to overcome the limitations in the application of tES adherent to the conventional approach and to fulfill the needs in advanced tES application, the goal is to introduce an individualized cap based solution. A flexible cap with integrated large textile electrodes

based on light-weight and flexible fabric of silver-coated fibers was introduced (Fiedler et al., 2015a; Wunder et al., 2018). Enhancing this bipolar cap to a multi-channel stimulation cap raises the question how to distribute the stimulation current across electrodes to target a distinct area in the brain. Such a distribution of stimulation currents at multiple electrodes should ensure a physiologically effective electric field at the target brain region but not at other places in the brain. Model free approaches based on EEG setups (Cancelli et al., 2016) and Helmholtz reciprocity (Helmholtz, 1853; Fernández-Corazza et al., 2016; Dmochowski et al., 2017) have been proposed for setups involving more than hundred small electrodes.

Here Helmholtz reciprocity (Helmholtz, 1853) is applied to compute the distribution of stimulation currents for tES on a multi-channel stimulation cap incorporating textile electrodes of several square centimeters.

Parts of this chapter have been previously presented in talks at DGKN and BMT conferences in 2018.

2.2.2 Material and Methods

The volume conductor model described in section 2.1.2 was utilized for this targeting study as well. Table 2.1 provides a summary of the represented tissue compartments and the assigned conductivity values.

To define targets in the cortical compartment, the Destrieux atlas (Destrieux et al., 2010) was considered, which parcels the gray matter surface in gyri and sulci. The FreeSurfer (FS) software (<http://surfer.nmr.mgh.harvard.edu>) (Fischl, 2012) output incorporated the labeling of the gray matter surface for 74 parcels per hemisphere according to the Destrieux atlas. The gray matter surface nodes of each parcel were used to calculate their medoid as representative position for the parcel. To ensure the target position to be within the gray matter compartment of the FEM model, the medoid positions were projected on the Euclidean closest element center of a gray matter element. In each target position, four dipoles were defined: three along the main anatomical axes (anterior-posterior, medial-lateral, inferior-superior) and one in direction of the mean surface normal of the gray matter surface parcel. Figure 2.7 illustrates the Destrieux atlas parcels and a sample representation of the target definition.

Thus, the target definition for 74 atlas labels times two hemispheres times four directions resulted in 592 dipole targets in 148 positions throughout the entire gray matter.

In preparation of the Helmholtz reciprocity approach, forward simulations of the scalar electric potential were performed for each of the 592 target dipoles with a dipole strength of 100 nAm. The partial integration direct approach (Schimpf et al., 2002) as implemented

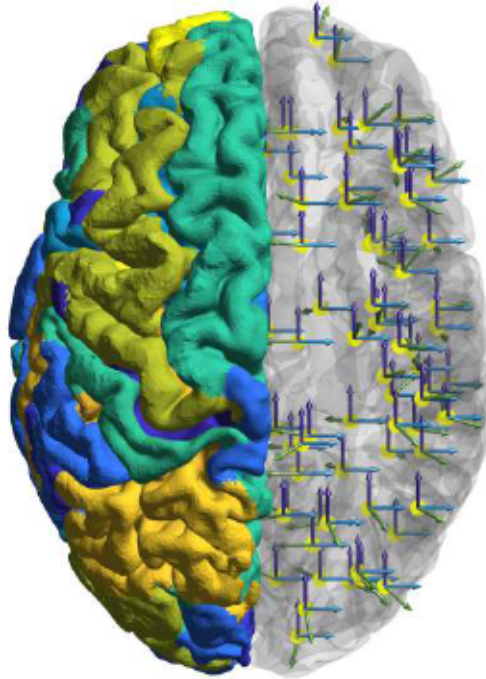


Figure 2.7: Target definition based on Destrieux atlas parcels of the gray matter surface (left hemisphere) with four dipoles in the medoid position of each label (right hemisphere). Colors code Destrieux labels (left hemisphere) and dipole directions (right hemisphere): anterior – dark blue, lateral – light blue, superior – yellow, parcel’s mean surface normal – green.

in the SimBio software was used for the forward solution. Therein, an algebraic multigrid preconditioned conjugate gradient (AMG-CG) iterative solver method (Lew et al., 2009) provides an efficient solution of the Laplace equation for the scalar electrical potential arising from the quasi-stationary approximation of Maxwell’s equations.

Here, the volume conductor model of the head was extended with 19 stimulation electrodes at positions according to an adapted layout of the international 10–20 system (Jasper, 1958; Klem et al., 1999). Electrodes were modeled as patches with dimensions of $4\text{ cm} \times 4\text{ cm}$ and 4 mm thickness as depicted in Figure 2.8. This electrode configuration reflected a layout for a flexible textile stimulation cap with integrated electrodes of silver-coated polyamide threads. Such textile stimulation electrodes incorporate a textile pocket for saline soaked sponges as electrolyte reservoir. Thus, the electrodes were modeled as one compartment reflecting the sponges soaked with 0.9 % sodium chloride solution. Therefore, their conductivity value was set to 1.4 S/m (Datta et al., 2011). Euclidean centers of each stimulation electrode were calculated and used to derive a triangulated mesh representation of the stimulation cap. The base functions of the SPHARA spatial Fourier analysis

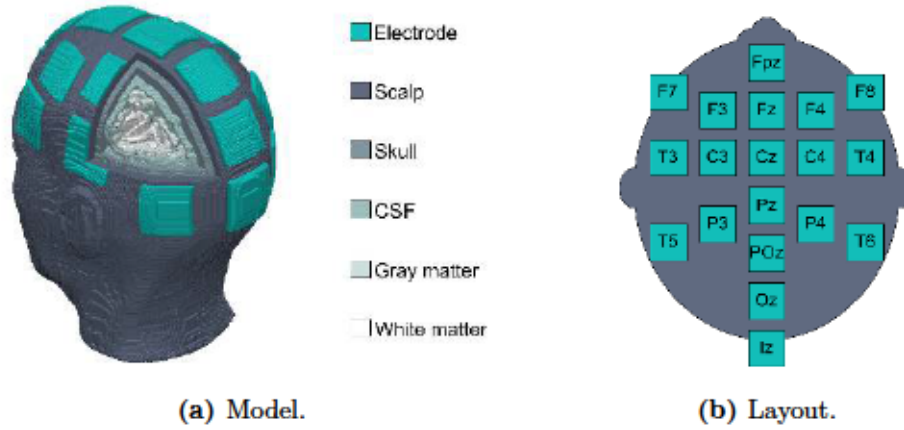


Figure 2.8: Volume conductor model with cutlet to visualize brain compartments (a) and the stimulating electrode layout (b).

(Graichen et al., 2015) were calculated based on the triangular mesh. Figure 2.9 shows the first four base function (sC) of the SPHARA spatial Fourier analysis for the stimulation cap.

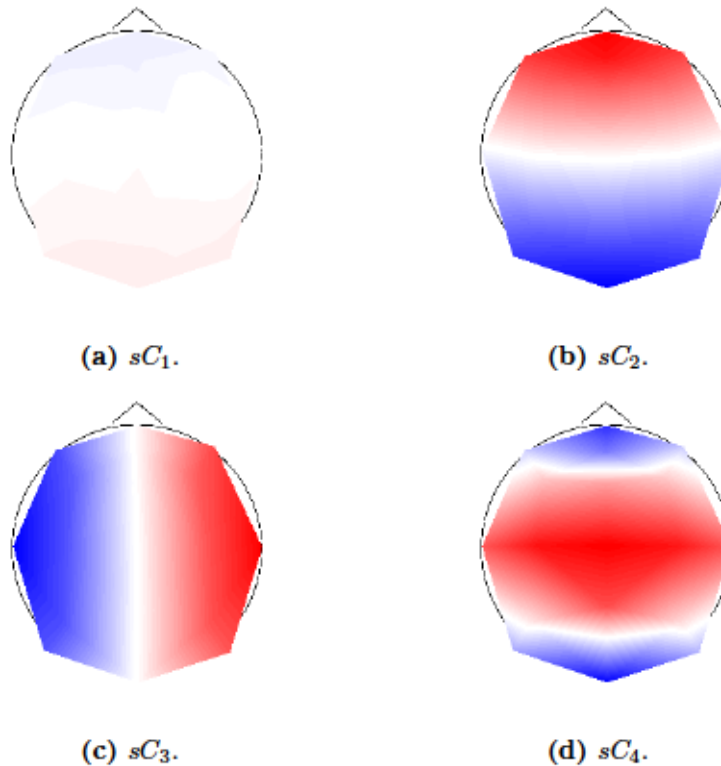


Figure 2.9: Topographies of the first four base function (sC) of the SPHARA spatial Fourier analysis for the stimulation cap.

The scalar electric potential from the forward simulations were evaluated at the foot nodes of the stimulation electrodes. The foot nodes of the stimulation electrodes mutually belong to the scalp and electrode compartments. The simulated scalar electric potential was integrated over the foot nodes belonging to one of the 19 stimulation electrodes, which resulted in one electric potential value per stimulation electrode. Evaluating the potential distributions across the stimulation electrodes which resulting from the forward simulations revealed predominantly dipolar, and predominantly monopolar potential distributions, the latter occurred from spatial subsampling due to the limited coverage of the head. The degree of dipolarity was computed according to equation 2.5 as radius r_d of a circle spanned over the second $sC_{d,2}$ and third $sC_{d,3}$ spatial components of the SPHARA decomposition of the scalar electric potential distributions simulated from the 592 dipoles d :

$$r_d = \sqrt{sC_{d,2}^2 + sC_{d,3}^2}. \quad (2.5)$$

Ideal dipolar pattern would provide a radius of 1. For predominantly dipolar potential distributions a deviation of 20 % from the ideal radius, was permitted. All configurations with a $r_d < 0.8$ were categorized as predominantly monopolar.

In case of a predominantly dipolar electric potential distribution, the electric potential at each electrode i was sign-dependently normalized according to equations 2.6 and 2.7:

$$u_p = \frac{u_{i,p}}{\sum_p u_{i,p}} \quad (2.6)$$

$$u_n = \frac{u_{i,n}}{\left| \sum_n u_{i,n} \right|} \quad (2.7)$$

Where p indicates electrodes with positive and n indicates electrodes with negative electric potential value u . Implementing two stimulation configurations, first a single electrode was assigned as current source for a *narrow* configuration. The source electrode src_{dn} was the electrode with the maximal absolute normalized electric potential according to equation 2.8:

$$src_{dn} = \max([u_p] \mid [|u_n|]) \quad (2.8)$$

Second, all electrodes of one sign subset were assigned to the current source for a *wide* configuration. The source electrodes src_{dw} incorporated all electrodes belonging to the subset with minimal integrated electric potential over the sign subset as stated in equation 2.9:

$$src_{dw} = \min \left(\sum_p u_{i,p} \mid \left| \sum_n u_{i,n} \right| \right) \quad (2.9)$$

Consequently, src_d originated from either of the subsets u_p or u_n . The current sink for each source src_d was generated by the set of electrodes snk_d with the largest absolute electric potential values best approximating src_d according to equations 2.10 and 2.11:

$$\min \left(\left[\sum_s \text{sort}([u_p] | [|u_n|]) \right] - |src_d| \right) \quad (2.10)$$

$$snk_d = \sum_s \text{sort}([u_p] | [|u_n|]) \quad (2.11)$$

This ensured src_d and snk_d to originate from different subsets u_p or u_n for both, *narrow* and *wide* configurations.

In case of a predominantly monopolar electric potential distribution, a reference electric potential u_{ref} was determined as maximal absolute integrated electric potential over one sign subset as stated in equation 2.12:

$$u_{ref} = \max \left(\sum_p u_{i,p} \mid \left| \sum_n u_{i,n} \right| \right) \quad (2.12)$$

The electric potential at each electrode i was normalized with respect to u_{ref} as indicated in equation 2.13:

$$o_i = \frac{u_i}{u_{ref}} \quad (2.13)$$

The electrode with the maximal absolute normalized electric potential served as source electrode src_m according to equation 2.14:

$$src_m = \max(|o|) \quad (2.14)$$

The remaining electrodes according to equation 2.15 were used to determine the current sink cs configuration:

$$cs = [|o|] \setminus src_m \quad (2.15)$$

Implementing again a *narrow* and a *wide* configuration, first src_m was approximated with the k largest elements in cs (cf. equation 2.16) for a *narrow* configuration of the current sink as snk_{mn} defined in equation 2.17:

$$\min \left(\left[\sum_k \text{sort}_{desc}([cs]) \right] - |src_m| \right) \quad (2.16)$$

$$snk_{mn} = \left[\text{sort}_{desc}([cs]) \right]_{1..k} \quad (2.17)$$

Second, approximating src_m with the l smallest elements in cs (cf. equation 2.18) resulted in a *wide* configuration as snk_{mw} according to equation 2.19:

$$\min\left(\left[\sum_l sort_{asc}([cs])\right] - |src_m|\right) \quad (2.18)$$

$$snk_{mw} = \left[sort_{asc}([cs])\right]_{1..l} \quad (2.19)$$

In summary, the above introduced approach provided signed ratios, which represented the activation of stimulation electrodes based on forward simulations of single current dipoles in target areas. Ultimately each current source or sink of a *narrow* or *wide* configuration was sign-preserving normalized to a sum of 1 with a precision of 2 decimals, such that these normalized values at each electrode could be directly transferred into stimulation current values with switched sign.

Figures 2.10 and 2.11 provide visual summaries of this procedure, called SPHARecip, which describe the spatial harmonic analysis based reciprocity approach.

The *max intensity* approach, described by Dmochowski et al. (2011), was used to compare the SPHARecip approach presented here to an often applied technique for tES optimization to a target. The stimulation electrode at Iz served as common return electrode in 18 bipolar tES simulations with each one of the remaining electrodes active. A mixing matrix with 18 columns from the bipolar simulations in the FEM model was generated for optimization towards *max intensity* in each of the 592 targets.

Over all, three targeting simulations were performed for each of the 592 targets, two (*narrow* and *wide*) using SPHARecip and one *max intensity* optimization.

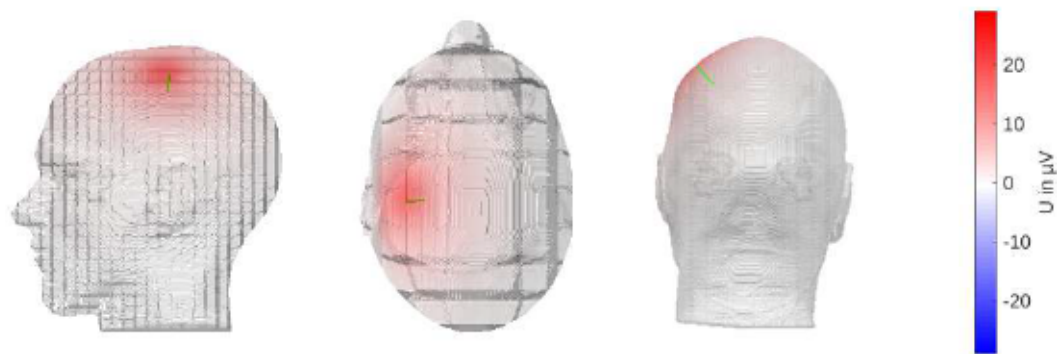
The *max intensity* approach provided a reference solution for the target stimulation. The electric field distributions of the *narrow* and *wide* configurations as test solutions were qualitatively compared to this reference based on distributions of the amplitude, its correlation coefficient CC (cf. equation 2.20) and its relative error RE (cf. equation 2.21):

$$CC = \frac{E_{ref} - \bar{E}_{ref}}{|E_{ref} - \bar{E}_{ref}|} \cdot \frac{E_{test} - \bar{E}_{test}}{|E_{test} - \bar{E}_{test}|} \quad (2.20)$$

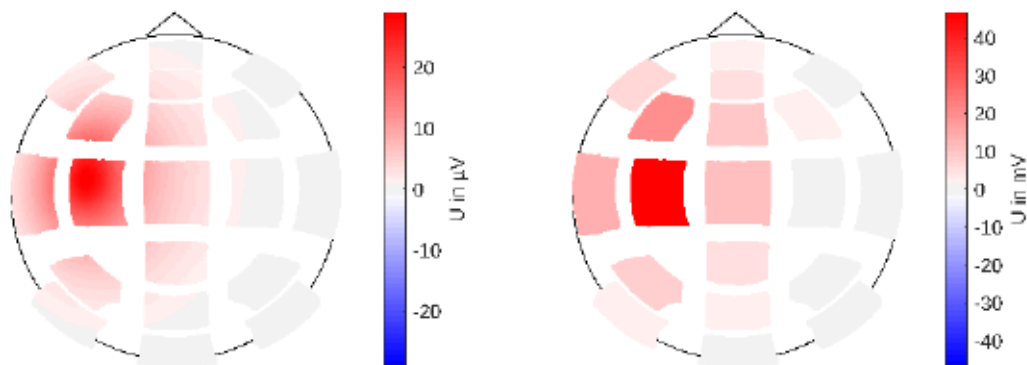
$$RE = \frac{|E_{ref} - E_{test}|}{|E_{ref}|} \quad (2.21)$$

with E denoting the electric field, *ref* and *test* labeling the reference and test solutions and \bar{E} marking the mean of E (Stenroos et al., 2014).

Quantitatively, the reference and test solutions were compared based on figures of merit, evaluating their distributions based on statistical comparisons. The figures of merit in-

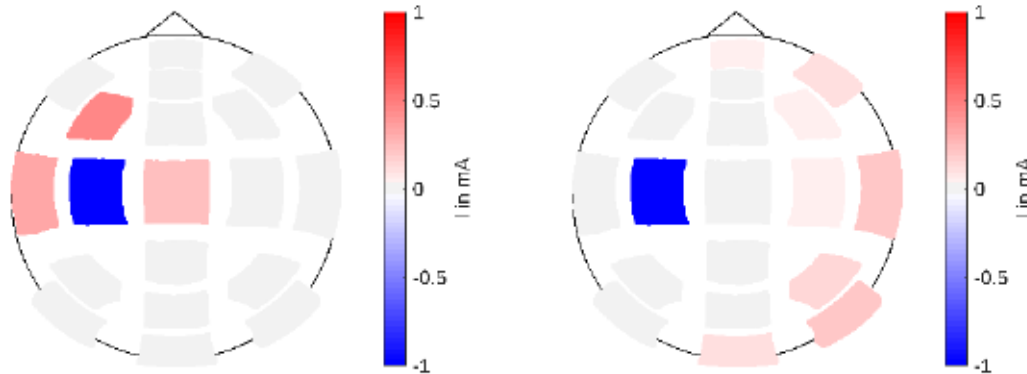


(a) Electric potential on model surface for target dipole (green arrow) simulation.



(b) Electric potential at electrodes.

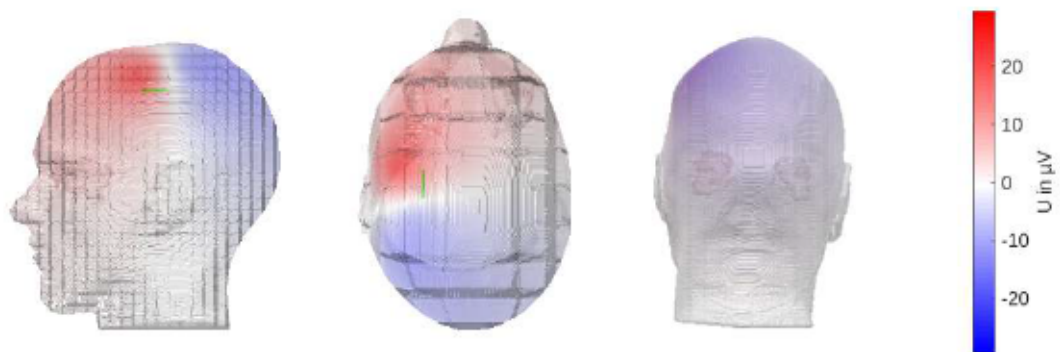
(c) Integrated electric potential at electrodes.



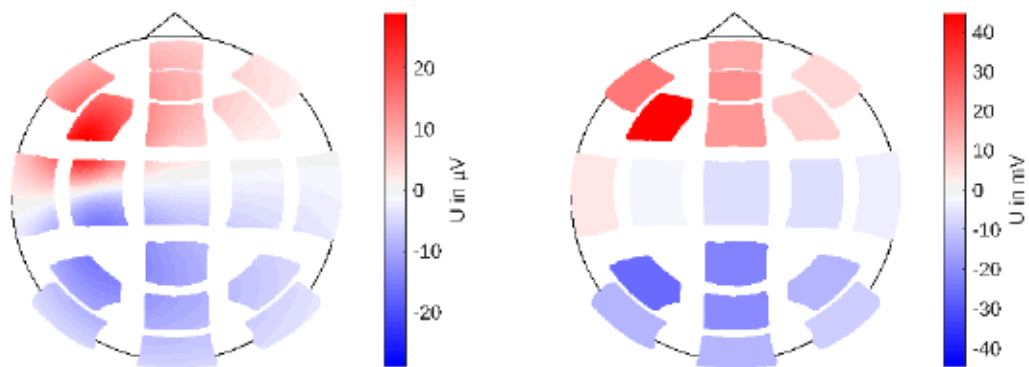
(d) Stimulation currents at electrodes for *narrow* configuration.

(e) Stimulation currents at electrodes for *wide* configuration.

Figure 2.10: SPHARecip approach for a target in the left precentral gyrus in direction of the mean surface normal of the gray matter surface in the parcel. Electric potential, originating from the target dipole, at the transparent scalp surface (a). Stimulation electrodes projected in a 2D plane in polar coordinates (b – e): Simulated scalar electric potential (b), Integrated electric potential per electrode (c), Stimulation current intensities for *narrow* (d) and *wide* (e) configurations.

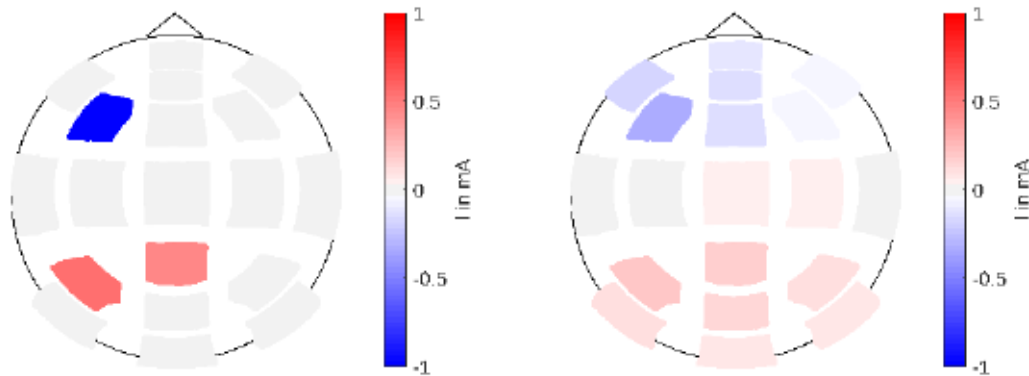


(a) Electric potential on model surface for target dipole (green arrow) simulation.



(b) Electric potential at electrodes.

(c) Integrated electric potential at electrodes.



(d) Stimulation currents at electrodes for *narrow* configuration.

(e) Stimulation currents at electrodes for *wide* configuration.

Figure 2.11: SPHARecip approach for a target in the left precentral gyrus in anterior direction. Electric potential, originating from the target dipole, at the transparent scalp surface (a). Stimulation electrodes projected in a 2D plane in polar coordinates (b – e): Simulated scalar electric potential (b), Integrated electric potential per electrode (c), Stimulation current intensities for *narrow* (d) and *wide* (e) configurations.

incorporated the following measures: the electric field amplitude at the target position as measure of intensity, the cosine COS of the angle between the target dipole moment and the electric field vector in the target position as measure of directionality, the fraction of gray matter volume in % containing more than 50 % of the maximal electric field in gray matter \hat{E} (cf. Full Width Half Maximum $FWHM$) as measure of focality, and the number of activated electrodes, as the amount of stimulation electrodes subjected to a stimulation current. Further, hot spots were evaluated as gray matter elements with an electric field amplitude higher than 90 % of \hat{E} . Hot spot clusters with 10 mm mutual distance were considered separately. For each hot spot, its center distance to the target position ($D_{cent-tar}$), its mean intensity (E_{mean}), the COS of the angle between the target dipole moment and the mean of the electric field vectors within the hot spot, and the fraction of electric field amplitude integrated within the 10 mm vicinity of the hot spot center compared to the electric field amplitude in the entire gray matter (E_{frac}) were evaluated.

The named figures of merit were investigated using descriptive statistics. The distributions from the three configurations, reference (*ref*), *narrow*, and *wide*, were compared based on the Wilcoxon rank sum test (equivalent to Mann-Whitney U-test) on a significance level of 5 %, and their confidence intervals. The 95 % confidence intervals of the sample's mean values were calculated based on 100,000 bootstrap samples.

2.2.3 Results

Evaluating the electric field distributions for specific targets, the Figures 2.12 and 2.13 show the comparison of reference and test solutions for the samples introduced in section 2.2.2 (cf. Figures 2.10 and 2.11). Both targets are located in the left precentral gyrus with an Euclidean distance of 22.16 mm to the closest vertex in the scalp surface.

For the target with direction of the mean surface normal of the gray matter surface in the parcel, the *ref* configuration incorporated the electrodes F3 as anode and C3 as cathode. Table 2.7 summarizes the quantitative comparison of the three stimulation configurations. The test configurations provided more specific stimulation to the target as the COS values were higher than for the reference configuration and the E_{target} values were comparable across all configurations. However, the reference configuration appeared overall more intense (\hat{E}) and more focal ($FWHM$).

Also the hot spots, distant to the target, appeared less pronounced for the test configurations compared to the reference configuration. Table 2.8 summarizes the quantities derived for the hot spots with amplitudes higher than 90 % of \hat{E} for each of the three stimulation configurations.

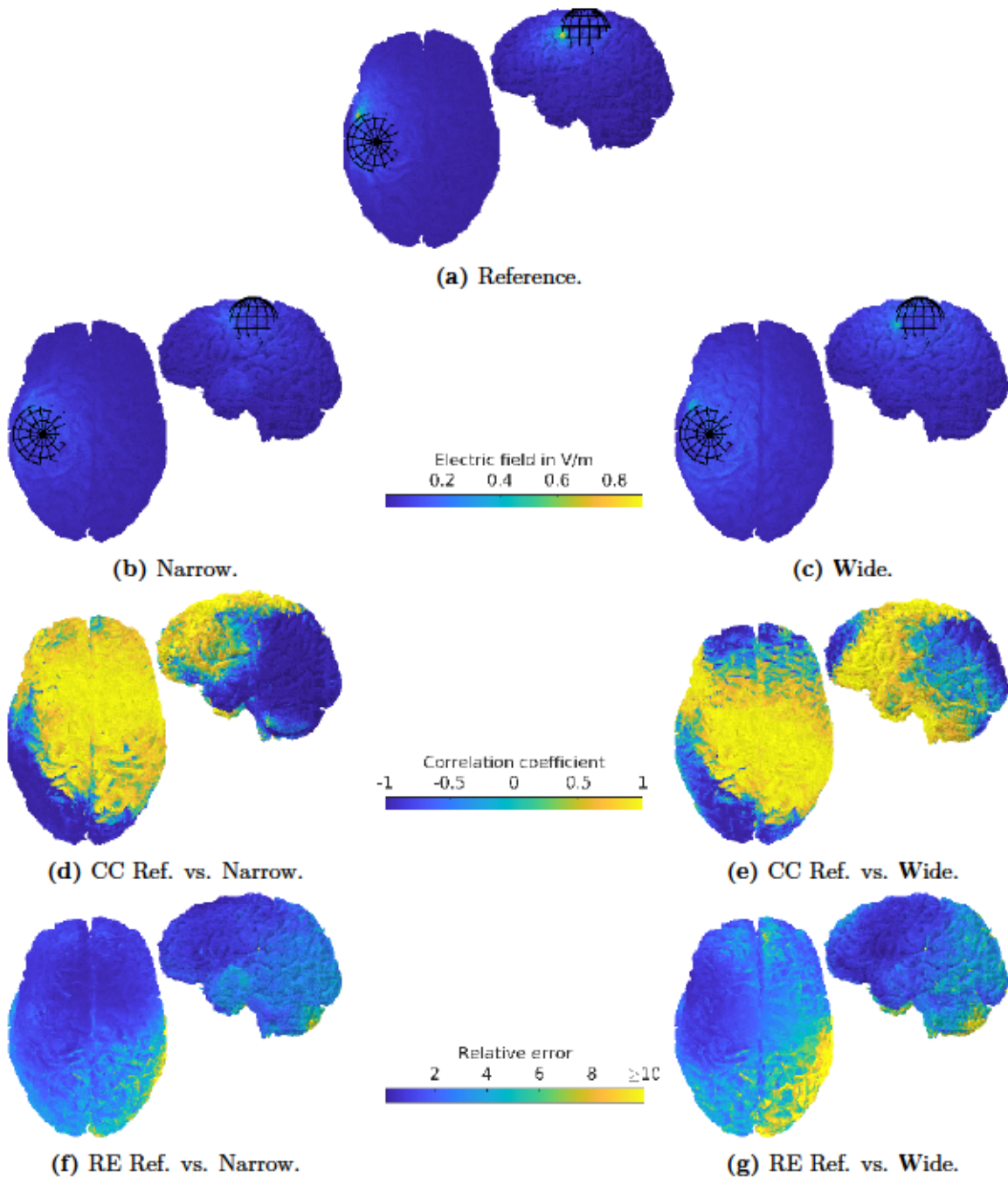


Figure 2.12: Qualitative comparison of electric field distributions for the target in left precentral gyrus with direction of the mean surface normal of the gray matter surface in the parcel (see Figure 2.10). Electric field distributions on gray matter surface from *max intensity* as reference (a) and SPHARecip *narrow* (b) and *wide* (c) configurations with a 25 mm mesh sphere surrounding the target position. Correlation coefficient calculated from the reference vs. *narrow* (d) and *wide* (e) as test configurations. Relative error calculated from the reference vs. *narrow* (f) and *wide* (g) as test configurations. Views from top (cf. Figure 2.7) and from left.

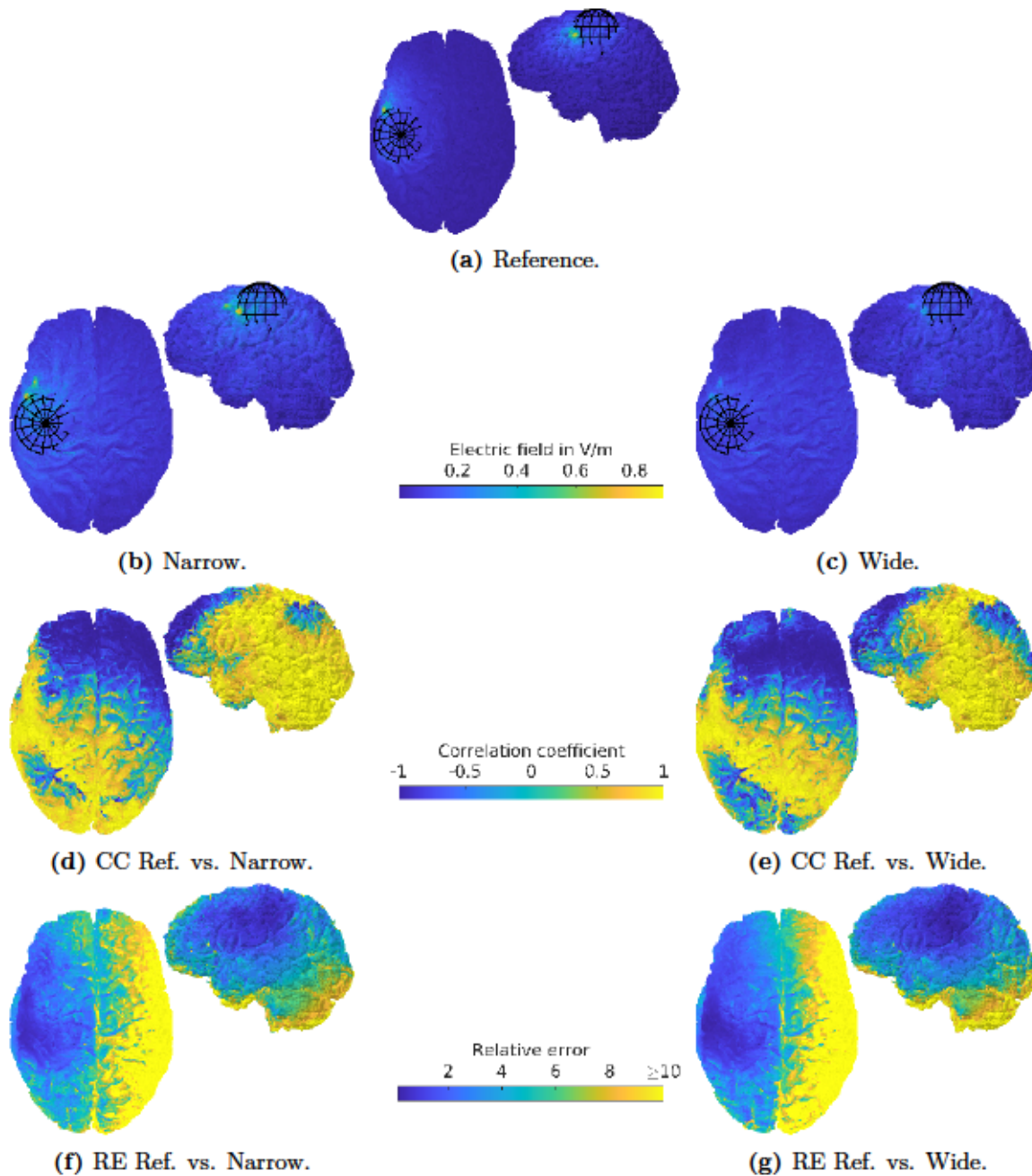


Figure 2.13: Qualitative comparison of electric field distributions for the target in left precentral gyrus with orientation in anterior direction (see Figure 2.11). Electric field distributions on gray matter surface from *max intensity* as reference (a) and SPHARecip *narrow* (b) and *wide* (c) configurations with a 25 mm mesh sphere surrounding the target position. Correlation coefficient calculated from the reference vs. *narrow* (d) and *wide* (e) as test configurations. Relative error calculated from the reference vs. *narrow* (f) and *wide* (g) as test configurations. Views from top (cf. Figure 2.7) and from left.

Table 2.7: Figures of merit for the target in the left precentral gyrus with direction of the mean surface normal of the gray matter surface in the parcel.

Figure of Merit	<i>ref</i>	<i>narrow</i>	<i>wide</i>
\hat{E} in V/m	0.90	0.30	0.50
E_{target} in V/m	0.09	0.08	0.11
<i>COS</i>	0.54	0.91	0.97
<i>FWHM</i> in %	0.01	0.28	0.04

Table 2.8: Hot spot quantities for the target in the left precentral gyrus with direction of the mean surface normal of the gray matter surface in the parcel.

Figure of Merit	<i>ref</i>	<i>narrow</i>		<i>wide</i>
# hot spots	1	2		1
$D_{cent-tar}$ in mm	26.51	21.90	21.38	26.05
E_{mean} in V/m	0.89	0.28	0.27	0.50
<i>COS</i>	0.84	0.36	0.39	0.94
E_{frac} in %	3.52	2.08	2.08	1.02

For the target in anterior direction, the *reference* configuration also incorporated the electrodes F3 as anode and C3 as cathode. Table 2.9 summarizes the quantitative comparison of the three stimulation configurations. Again, the test configurations provided more specific stimulation to the target as they better met the targeted orientation and the E_{target} values reached higher values compared to the reference configuration. Especially the *narrow* configuration reached a E_{target} with 0.2 V/m more than twice the E_{target} of the reference configuration.

Table 2.9: Figures of merit for the target in the left precentral gyrus with orientation in anterior direction.

Figure of Merit	<i>ref</i>	<i>narrow</i>	<i>wide</i>
\hat{E} in V/m	0.90	0.80	0.35
E_{target} in V/m	0.09	0.20	0.13
<i>COS</i>	0.80	0.94	0.95
<i>FWHM</i> in %	0.01	0.04	0.14

The hot spots, distant to the target, again appeared less pronounced for the test configurations compared to the reference configuration. Table 2.10 summarizes the quantities derived for the hot spots with amplitudes higher than 90 % of \hat{E} for each of the three stimulation configurations. Here especially the *wide* configuration demonstrated only a

week hot spot compared to the *ref* configuration with approximately one third in mean amplitude.

Table 2.10: Hot spot quantities for the target in the left precentral gyrus with orientation in anterior direction.

Figure of Merit	<i>ref</i>	<i>narrow</i>	<i>wide</i>
# hot spots	1	1	1
$D_{cent-tar}$ in mm	26.51	26.45	25.37
E_{mean} in V/m	0.89	0.76	0.31
COS	-0.05	0.21	0.57
E_{frac} in %	3.52	0.95	0.51

The distribution and statistical measures of the figures of merit introduced in section 2.2.2 across the three stimulation configurations provided a global outcome comparison. Figures 2.14 to 2.24 present the distributions of figures of merit for the *max intensity* as reference (*ref*) configuration and the test *narrow* and *wide* configurations. Mean values, their confidence intervals, the interquartile range and the data distribution are depicted. Pairwise statistically significant differences between stimulation configuration outcomes are indicated as well.

The electric field intensity at the target position varied statistically significant across the three stimulation configurations as indicated in Figure 2.14. The *wide* configurations provided the highest mean intensity with 0.104 V/m, followed by the *narrow* configuration with 0.095 V/m (91.4 %) and the *ref* configuration with 0.046 V/m (43.7 %). The confidence intervals of the mean electric field from the *wide* and *narrow* configurations did not overlap as the lower bound of the confidence interval for the *wide* configurations was 0.101 V/m and the upper bound of the confidence interval for the *narrow* configurations was 0.099 V/m.

A topographic representation of the electric field intensity at the target position is depicted in Figure 2.15. Even though the *wide* configurations provided the highest intensities, on average, Figure 2.15b clearly indicates high electric field intensities above 0.2 V/m at targets in frontal, central, and superior temporal regions with anterior-posterior or medial-lateral orientation for *narrow* configurations.

Figure 2.16 presents the directionality measure, at which again the *wide* configurations provided the highest mean value with 0.804 for the COS of the angle between the target dipole and the electric field vector at the target position. The COS for the *ref* configurations demonstrated the most narrow distribution with only positive values and a mean of 0.725. The lowest mean value of 0.566 was provided by the *narrow* configuration. The three distributions mutually differed significantly from each other.

From the topographic representation of the directionality measure in Figure 2.17, it is con-

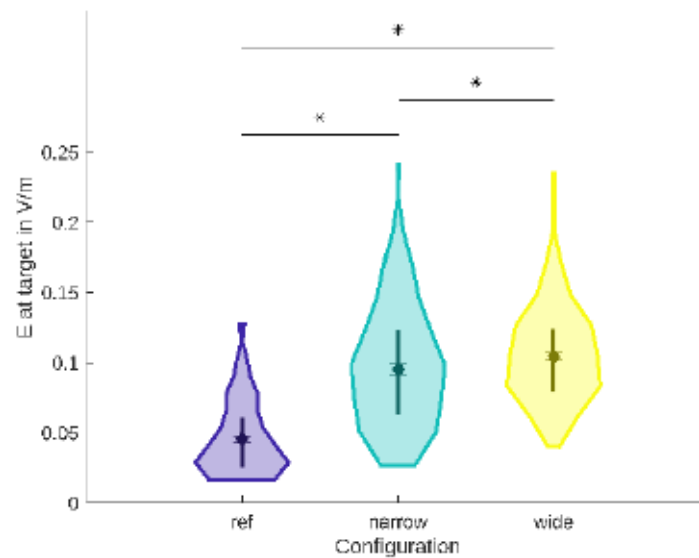


Figure 2.14: Distributions of electric field intensity at target position. Statistical characteristics are depicted by the mean value (diamond), confidence intervals of the mean (horizontal lines), the interquartile range (vertical lines), and the distribution of the data (colored areas). Significant differences are indicated by *.

ceivable, that a single negative extreme value of -0.5 for the COS in the planum polare of the superior temporal gyrus with medial-lateral orientation caused the tail of the distribution for the *wide* configurations (cf. Figure 2.17c). In contrast, the directionality measure was negative for 55 targets for *narrow* configurations. The most extreme values occurred on the right hemisphere in the parahippocampal gyrus with inferior-superior orientation and the inferior frontal sulcus in surface normal direction with values of -0.37 and -0.27 (not depicted in Figure 2.17), a value of -0.27 also occurred in the area of the subcentral gyrus and sulcus for a target orientation parallel to the surface normal of this area on the left hemisphere (cf. Figure 2.17b).

For the electric field $FWHM$ gray matter volume fraction, the *ref* configuration demonstrated the most narrow distribution with the smallest mean value of 0.435% as presented in Figure 2.18. In comparison, the *narrow* and *wide* configurations provided rather broad distributions with mean values of 0.775% and 1.113% . Again the confidence intervals of the mean values from the three stimulation configurations did not overlap.

Figure 2.19 presents topographic maps of the electric field $FWHM$ gray matter volume fraction. The tail of the $FWHM$ distribution above 5% for the *wide* configurations was caused by three extreme values. Figure 2.19c indicates one of these extreme values of 5.2% in the inferior temporal sulcus for the target in anterior direction. The other two extreme values of 6.7% and 5.7% occurred on the right hemisphere in the lingual gyrus and the

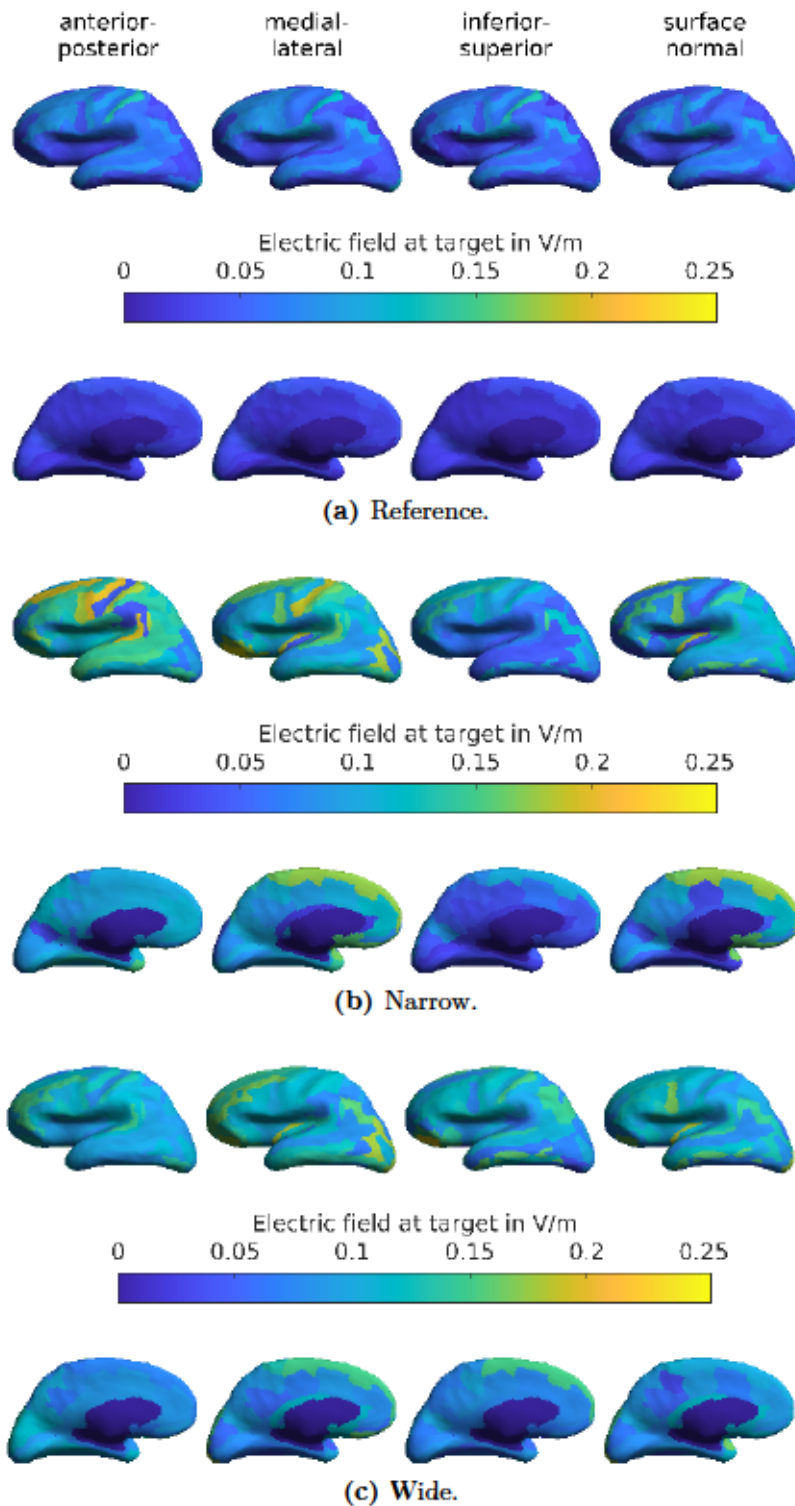


Figure 2.15: Electric field intensity at target positions for the Destrieux atlas parcels on the inflated surface of the left hemisphere. Top rows: view of the exterior side. Bottom rows: view of the interior side.

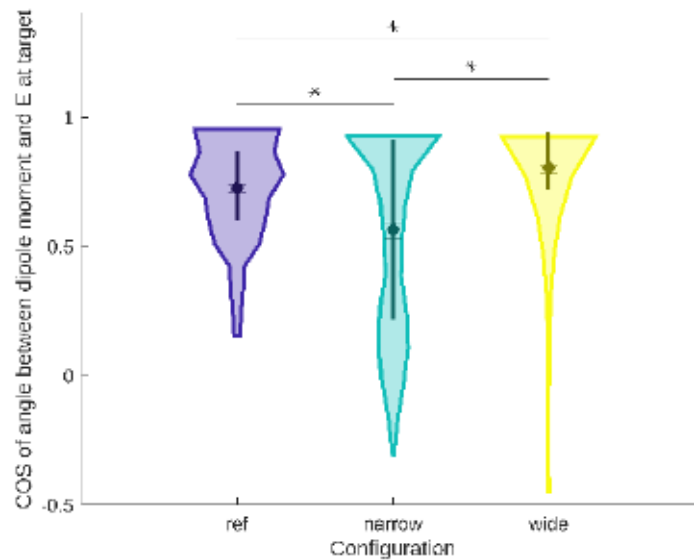


Figure 2.16: *COS* distributions of the angle between the target dipole and the electric field vector at target position. Statistical characteristics are depicted as introduced in Figure 2.14.

posterior-ventral part of the cingulate gyrus, both for targets with inferior-superior orientation.

Exact two electrodes were active by definition, in the stimulation montages of the *ref* configurations. Therefore these configurations did not generate a distribution of activated electrodes as indicated by a single diamond in Figure 2.20. For the test configurations the number of active electrodes was not predefined. However, for the *narrow* and *wide* configurations also the number of two active electrodes was the lower bound. On average 3.2 electrodes (16.8 % of available electrodes) were activated in the *narrow* configurations. By design, the *wide* configurations should distribute the stimulation current on many electrode which resulted in an average of 10.4 activated electrodes (54.7 % of available electrodes).

Figure 2.21 presents the distributions of the number of hot spots. Overall, the *wide* configurations provided the most hot spots with a total number of 1576. On average, *wide* configurations generated 2.7 hot spots, the confidence interval of this mean value was [2.5; 2.9]. According to the Wilcoxon rank sum test, this distribution varied significantly from the distributions generated from *narrow* and *ref* configurations with on average 2.3 and 2.0 hot spots. Even though their confidence intervals of [2.1; 2.5] and [1.9; 2.1] also did not overlap, the statistical test indicated no significance difference. The total numbers of hot spots were 1362 and 1162 for *narrow* and *ref* configurations.

The number of hot spots is topographically mapped on the inflated surface of the left hemisphere in Figure 2.22. The tails of the distributions for *narrow* and *wide* configurations

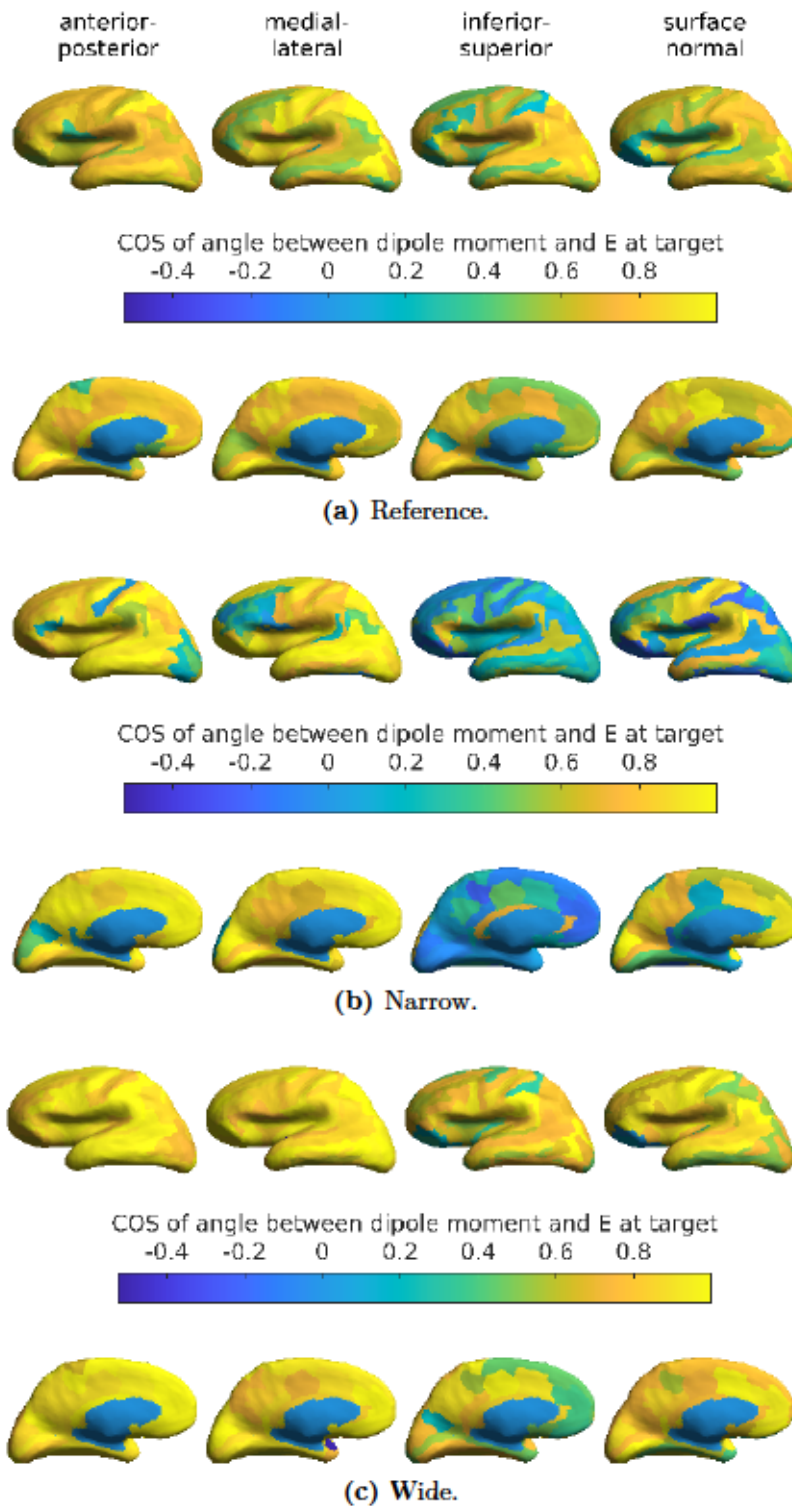


Figure 2.17: *COS* distribution of the angle between the target dipole and the electric field vector at target positions for the Destrieux atlas parcels on the inflated surface of the left hemisphere. Top rows: view of the exterior side. Bottom rows: view of the interior side.

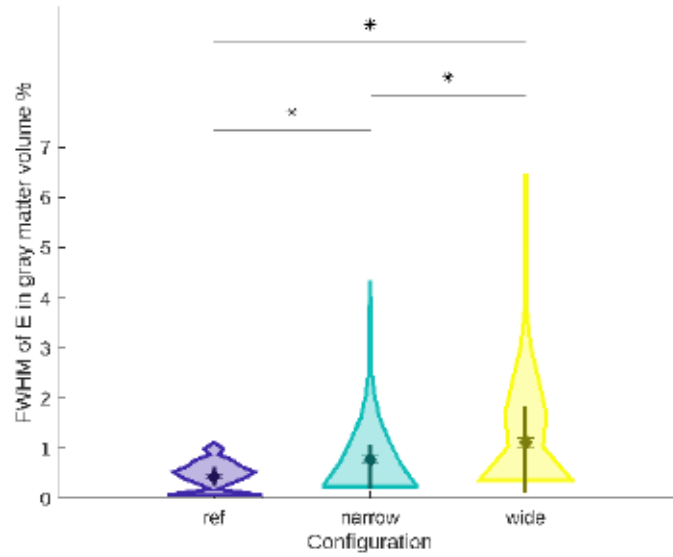


Figure 2.18: Distributions of fractions of gray matter volume in % containing electric field intensities $> 50\%$ of \hat{E} in gray matter. Statistical characteristics are depicted as introduced in Figure 2.14.

were caused by 7 and 5 configurations generating more than 10 hot spots. The *narrow* configuration targeting the area of the medial occipito-temporal and lingual sulci of the right hemisphere (not depicted in Figure 2.22) in lateral direction provided the highest number of hot spots of 16. The maximal number of hot spots of 15 in the *wide* configurations occurred in the area of the inferior temporal sulcus of the left hemisphere (depicted in Figure 2.22c) for the target with anterior-posterior orientation.

Hot spots generated from *narrow* configurations located closest to the target with a mean distance of 43.0 mm. The mean distances for the *wide* and *ref* configurations were 43.8 mm and 45.2 mm. According to the Wilcoxon rank sum test, the distributions did not differ significantly, which was supported by their overlapping confidence intervals of $[41.9; 44.0] \cdot \text{mm}$, $[42.7; 44.9] \cdot \text{mm}$, and $[44.0; 46.6] \cdot \text{mm}$ for *wide*, *narrow* and *ref* configurations as visible in Figure 2.23.

The mean electric field intensities in the hot spots were 0.31 V/m, 0.29 V/m, and 0.26 V/m for the *narrow*, *wide*, and *ref* configurations. In Figure 2.24, the *ref* configurations demonstrated a distinct bi-modal distribution with mean hot spot intensities of 0.840 V/m for 136 hot spots and 0.184 V/m for 1026 hot spots. The Wilcoxon rank sum test indicated significant differences between all distributions, which was supported by the mutually distinct confidence intervals for the mean electric field intensity in the hot spots with ranges of $[0.306; 0.318] \cdot \text{V/m}$, $[0.281; 0.292] \cdot \text{V/m}$, and $[0.249; 0.273] \cdot \text{V/m}$ for the *narrow*, *wide*, and *ref* configurations.

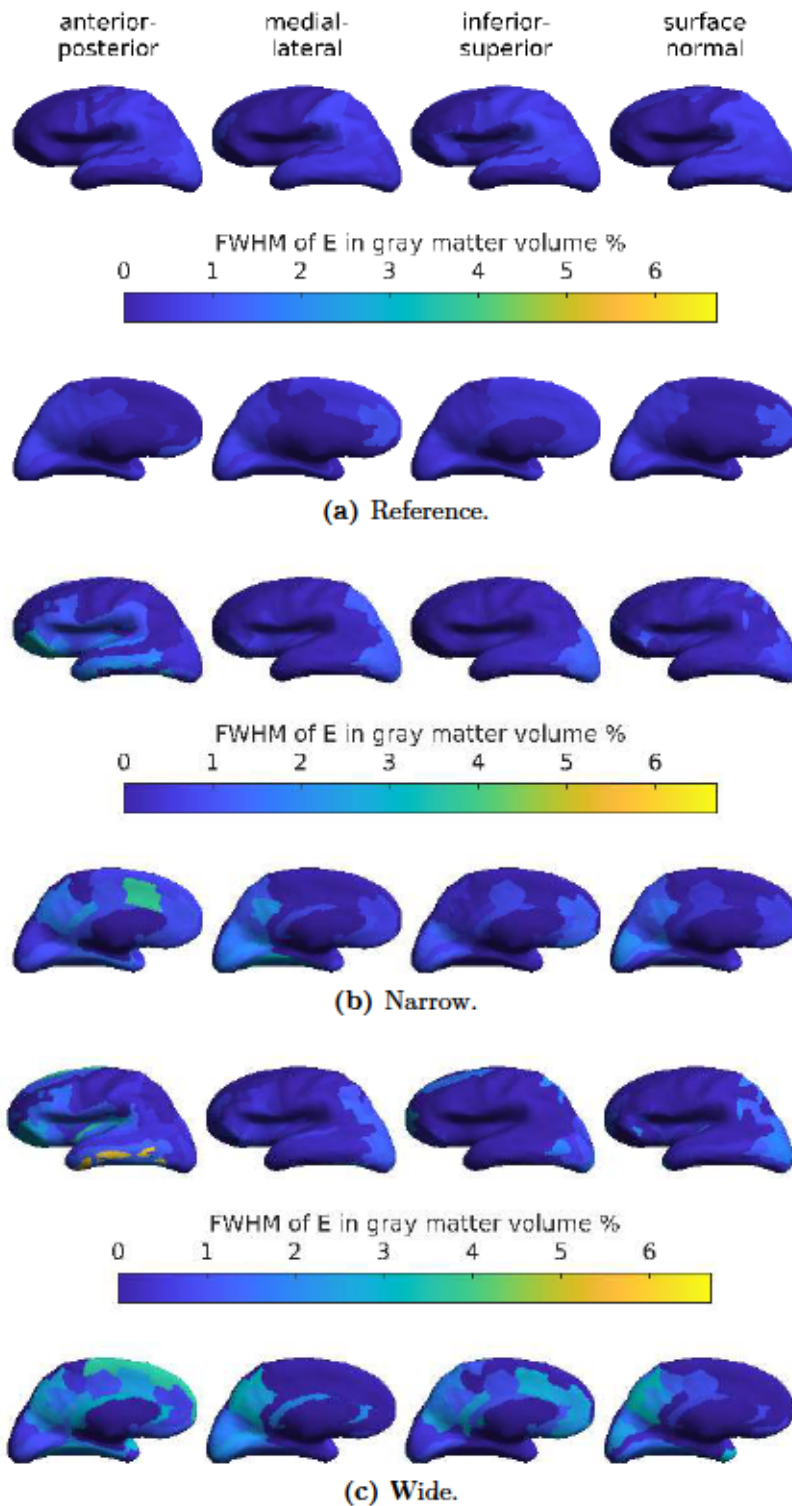


Figure 2.19: Fractions of gray matter volume in % containing electric field intensities $> 50\%$ of \hat{E} in gray matter for the Destrieux atlas parcels on the inflated surface of the left hemisphere. Top rows: view of the exterior side. Bottom rows: view of the interior side.

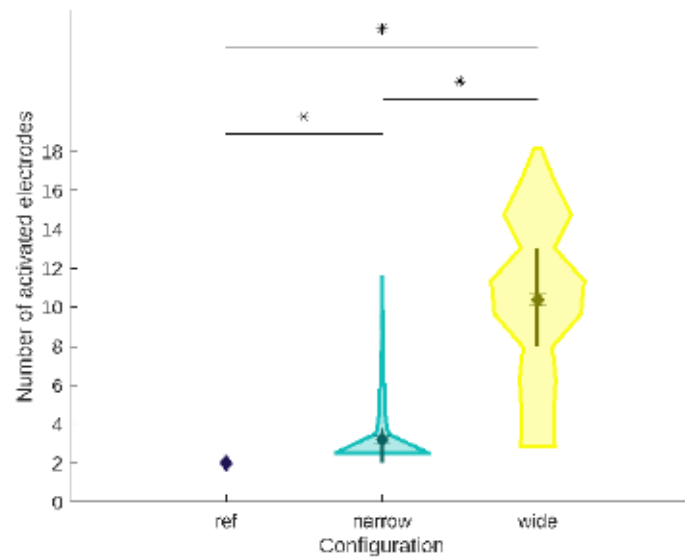


Figure 2.20: Number of activated electrodes in the stimulation configurations. Statistical characteristics are depicted as introduced in Figure 2.14.

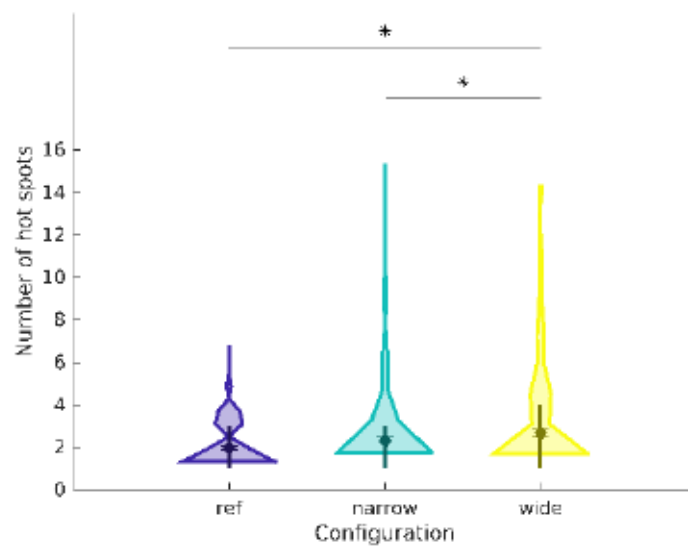


Figure 2.21: Number of hot spots occurring in gray matter. The total numbers are 1162, 1362, and 1576 for *ref*, *narrow*, and *wide* configurations, respectively. Statistical characteristics are depicted as introduced in Figure 2.14.

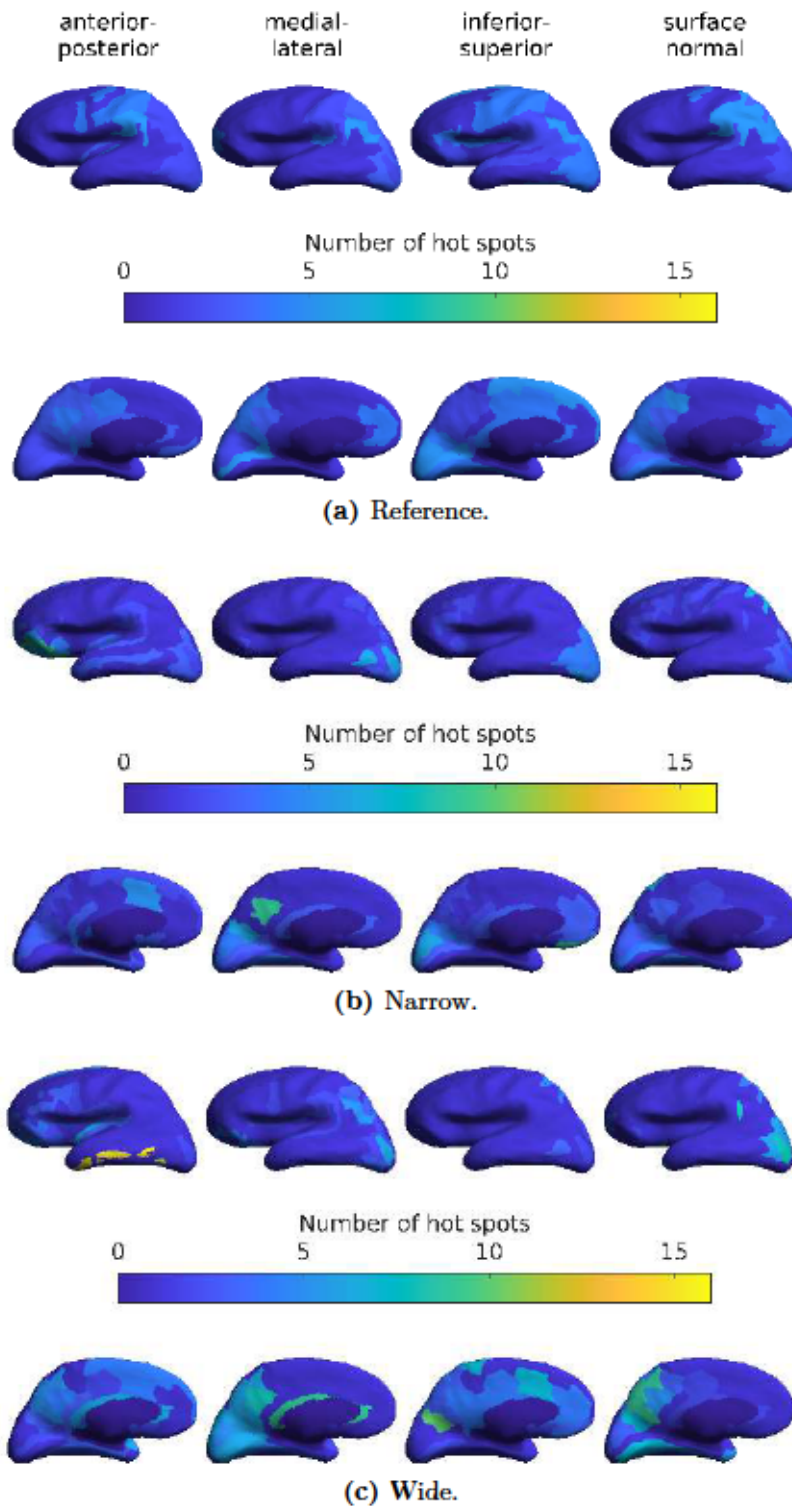


Figure 2.22: Number of hot spots occurring in simulated target stimulations to the Destrieux atlas parcels on the inflated surface of the left hemisphere. Top rows: view of the exterior side. Bottom rows: view of the interior side.

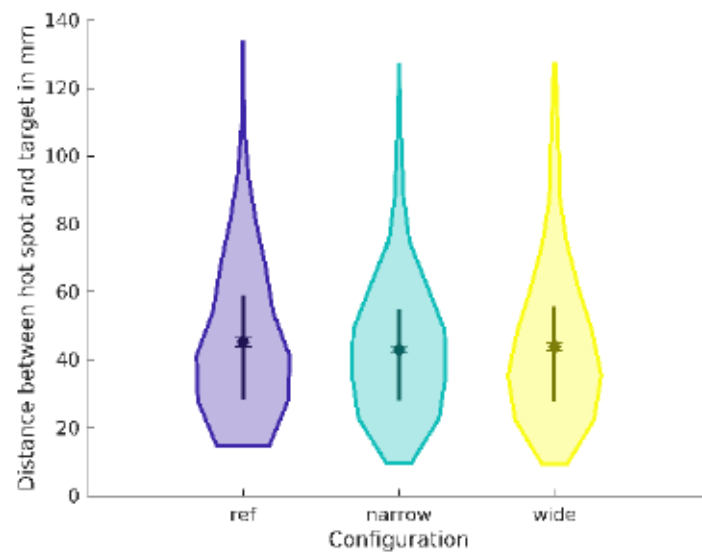


Figure 2.23: Distributions of distances between hot spots with electric field intensities $> 90\%$ of \hat{E} in gray matter and the target positions. N is 1162, 1362, and 1576 for *ref*, *narrow*, and *wide* configurations. Statistical characteristics are depicted as introduced in Figure 2.14.

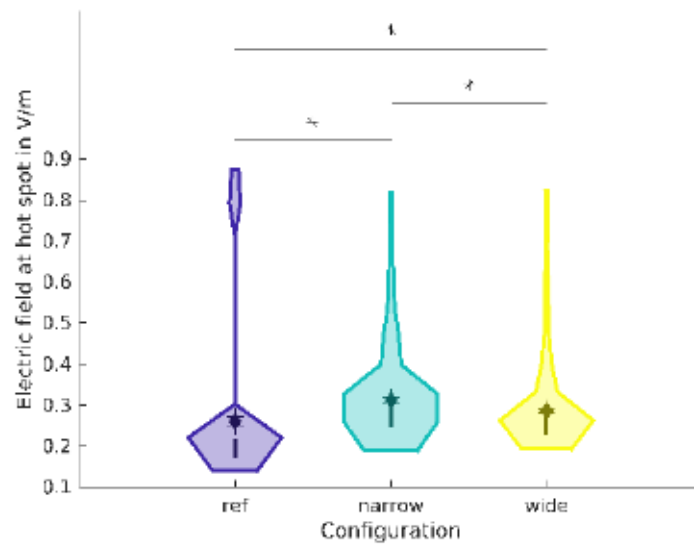


Figure 2.24: Distributions of the mean electric field intensity in hot spots occurring in gray matter. N is 1162, 1362, and 1576 for *ref*, *narrow*, and *wide* configurations. Statistical characteristics are depicted as introduced in Figure 2.14.

2.2.4 Discussion

The proposed approach, SPHARecip, utilized Helmholtz reciprocity to distribute stimulation currents across a predefined layout of electrodes, with an area of 16 cm² each, integrated in a textile stimulation cap. Scalar electric potential distributions on the stimulation electrodes, which originated from forward simulations of single target dipoles, were transferred into stimulation current distributions. Two stimulation configurations, namely *narrow* and *wide*, accounted for the main intensity features and the main topography of the electric potential distribution, respectively. A reference configuration based on a *max intensity* optimization served as comparison for the two SPHARecip configurations.

The electric field evaluation in the target positions demonstrated the high ability of the SPHARecip configurations to specifically target the stimulation in the applied setting. With respect to the stimulation intensity in the target, both SPHARecip configurations significantly outperformed the reference configuration reaching on average only 44 % of the mean intensity of 0.1 V/m provided by the *wide* configurations. Also considering directionality, the *wide* configurations provided on average the highest measures, whereat a single extremely deviating electric field directions from the target in lateral direction in the planum polare of the superior temporal gyrus (cf. Figure 2.17) broadened the *COS* distribution in Figure 2.16. In contrast the *ref* configurations provided the most narrow distribution for this measure with a mean value of 90 % compared to the averaged *COS* of the *wide* configurations. Further, the *ref* configurations generated the most focal electric field distribution in gray matter (cf. Figure 2.18), which was due to the consequent incorporation of exact two stimulation electrodes (cf. Figure 2.20). However, this concentration of electric field intensity was not necessarily directly linked to the target, for 136 among the 592 evaluated targets the *ref* configurations generated rather high electric field intensities in remote gray matter, which is reflected in the two examples presented in Figures 2.12 and 2.13 as well as in the bi-modal distribution in Figure 2.24. However, overall *ref* configurations generated the smallest amount of hot spots (cf. Figure 2.21).

Electric field intensities in the order of 0.1 V/m in the target have been shown in other modeling studies (Miranda et al., 2013; Saturnino et al., 2015) and also with other electrode configurations (Martin et al., 2017; Huang et al., 2018). Further, electric field intensities in this range were also reported from measurements with intracranial electrodes in epilepsy patients (Opitz et al., 2016). With respect to the orientation of the electric field, the SPHARecip configurations based on Helmholtz reciprocity demonstrated electrode adaptations (number and positions of electrodes involved) to address the specific target orientation (cf. samples introduced in Figures 2.12 and 2.13). Similarly, a previously introduced approach based on Helmholtz reciprocity indicated different numbers of stimulation electrodes to address targets with different orientations (Fernández-Corazza et al., 2016). In contrast, the *max intensity* optimization (Dmochowski et al., 2011) resulted in the same stimula-

tion layout for different target orientations in the precentral gyrus as presented in section 2.2.3. Intensity maximization and least square methods focus more on focality (Fernández-Corazza et al., 2020), thus the approach based on Helmholtz reciprocity resulted in more broad electric field distributions on average.

A possible application for the SPHARecip approach lies in the stimulation of patient specific areas based on measured electroencephalographic data. For example, if a primary sensory area is to be stimulated, the evoked potential distribution might serve as a basis for the computation of the current distribution at the stimulation electrodes. The algorithm implementing Helmholtz reciprocity introduced in section 2.2.2 was specifically designed for a textile stimulation cap with a predefined electrode montage, which incorporated 19 electrodes with 4 cm x 4 cm side length. Further, the presented approach could be used to design individualized caps comprising electrode configurations indicated by measurements or source simulations. For example a patient specific textile cap can be produced employing the individual head geometry and the individual electrode configuration, as indicated by the solution from the here introduced targeting approach.

The proposed multi-channel stimulation cap was based on 19 electrodes positioned according to an adaptation from the international 10–20 system (Jasper, 1958; Klem et al., 1999). Applying this convention, the coverage of the scalp surface was limited. This led to configurations where the electrodes failed to capture essential portions of the electric potential distributions from the forward solution (cf. Figure 2.10). In such cases one pole of the potential distribution was not captured and predominantly monopolar distributions occurred at the electrodes (Dmochowski et al., 2017). For retrieving the stimulation current distribution, the Helmholtz reciprocity procedure was adapted as indicated in section 2.2.2. All targets with inferior-superior orientation generated predominantly monopolar distributions of the electric potential at the electrodes. Only few of these targets, such as in the lingual gyrus and the parahippocampal gyrus, led to extreme values in the distributions of the figures of merit, e.g. the focality and directionality measures. However, targets generating predominantly dipolar electric potential distributions, e.g. in the inferior temporal sulcus with anterior-posterior orientation and in the planum polare of the superior temporal gyrus with medial-lateral orientation, also contributed to extreme values in the distributions of the focality and directionality measures.

The finite elements model of the volume conductor used for the computations incorporated the main five tissue compartments of the head, namely white and gray matter, CSF, skull and scalp. A higher number of compartments would account for more details of the volume conductor and also include anisotropic structures (Haueisen et al. 2002; Güllmar et al. 2010; Opitz et al. 2015). A shortcoming in the utilized model lies in the skull modeling, since it was approximated with only one bulk skull compartment. Considering the layered structure of the skull with hard and soft bone will lead to slightly different current density distributions in the brain (Wagner et al. 2014; Opitz et al. 2015).

The total stimulation current was 1 mA for each stimulation configuration to keep results across all stimulation configurations comparable. This current amplitude is widely used and thus, our results can be readily used for guidance or comparison in experimental studies. Different current amplitudes at the electrodes while keeping the intensity ratios across electrodes constant will yield scaled current distributions in the brain.

The proposed method represents a simple approach for the estimation of currents at stimulation electrodes in a textile cap based on Helmholtz reciprocity. The results provide evidence for the feasibility of the method to address different target positions and orientations in the brain. This method can be applied to measured potential distributions and expanded to derive patient-specific electrode montages.

3 Application systems for transcranial electric stimulation

3.1 Textile stimulation cap

3.1.1 Introduction

Electric stimulation of biological tissue necessarily involves at least two electrodes, a current source and a current sink. Initial applications of weak currents in the range of 1–2 mA to the human head facilitated exactly one anode above the motor cortex and one cathode at a contralateral prefrontal position (Nitsche and Paulus, 2000), whereat the geometry was identical for both electrodes. In further studies, different electrode geometries such as concentric (Martin et al., 2017) and distributed (Datta et al., 2009a) configurations have been applied. Such electrode and stimulation configurations as described in section 2.2 involve multiple electrodes that are not trivial to position and fixate.

In the conventional systems, rectangular rubber electrodes of several square centimeters in area are placed in saline soaked sponges and hold in place by rubber bands or spread with conductive gel to contact the skin. These two complicated procedures demand professionally trained personnel, which hampers more extensive applications in non-medical environment. Moreover the manual and unstable electrode placement limits reproduction in multi-session or multi-participant studies. Further, the rectangular shape limits the electrode’s ability to follow the curved skin surface leading to partial displacement due to bending and protruding.

To overcome those limitations, a compliant solution for secure and reproducible electrode positioning with sufficient ease of use in various application scenarios was desired. Electroencephalography systems with recording electrodes integrated in textile caps served as model for such a solution. Such caps ensure standardized and secure electrode positioning to various heads and provide flexibility in adaptation to specific requirements.

Here a novel flexible and compliant cap system with integrated textile stimulation electrodes is proposed.

Parts of these developments have been previously presented in abstract form (Fiedler et al., 2015a) and in a journal publications (Wunder et al., 2018; Hunold et al., 2020c).

3.1.2 Material and Methods

The basic material of the cap was a highly flexible thread of cotton and elastane. The thread was industrially processed in flat knitting to manufacture fabric caps allowing for customized cap adaptation (research collaboration partner warmX GmbH, Apolda, Germany). A second knitting magazine, holding conductive silver-coated poly-amide threads, implemented reproducible tES electrodes with respect to their size and position in the caps.

Pockets of the flexible fabric on top of the electrodes held sponges, sockets and studs of snap fasteners. The later contacted the conductive thread, which fed into the pocket's outer side, to provide an electric contact for medical grade press stud cables. The sponges, accessible for a syringe via the snap socket, provided an electrolyte reservoir when soaked with saline solution, to realize the electron-ion interface for the electric contact from the textile electrode to the skin.

In order to ensure stability with respect to the effective electrode configurations, a barrier needed to prevent diffusion of saline solution throughout the flexible textile. Therefore, medical grade low viscosity silicone (Silpuran 2400, Wacker Chemie AG, Munich, Germany) was coated into the flexible fabric surrounding the electrode with the electrolyte reservoir pocket.

The flat knitted fabric was mechanically characterized by means of uni-axial tensile tests with a tensile-compression testing machine (Z005, ZwickRoell GmbH & Co. KG, Ulm, Germany). In accordance with the norm DIN EN ISO 13934-1, the tensile tests with a pre-load of 0.5 N were carried out with corrugated Vulkollan (Covestro AG, Leverkusen, Germany) specimen grips, holding samples of 50 mm \times 200 mm taken along and orthogonal to the knitting direction. Tensile tests were force limited to 20 N, which was estimated to be the maximally applied force when placing the cap on participants head. Force-elongation curves were recorded up to the maximal force and in return to the starting position for each three samples taken along and orthogonal to the knitting direction.

The electrical contact of the textile stimulation electrode and the integrity of the silicone frame as diffusion barrier were examined by means of impedance measurements in one participant. After an initial settling time of 10 min, 96 impedance samples were recorded using an impedance analyzer (Agilent / HP 4192A LF Impedance Analyzer, HP Inc., Palo Alto, USA) with a 2,000 k Ω cutoff. For impedance measurements, a sinusoidal signal with a frequency of 10 Hz was applied in a two-point setup. A sintered silver/silver-chloride (Ag/AgCl) ring electrode, as conventionally applied in EEG measurements, was attached via Ten-20 conductive EEG paste (Weaver and Company, Aurora, USA) to the skin of the forehead, which established the reference terminal. The terminals for electrical contact testings incorporated five positions in the stimulation cap: the contact terminal of the stimulation electrode at Oz and four positions in the textile, surrounding the silicone frame,

roughly at the positions POz, PO5, PO6 and Iz, according to the 10–10 system (Jasper, 1958; Klem et al., 1999). A series of five measurements sequentially revisited the five test terminal in the stimulation cap and lasted for 30 min, which reflected a typical application time of tES.

Performance and integrity of the textile cap with integrated stimulation electrodes and silicone diffusion barrier were tested considering the cap’s life cycle including laundering. In one participant, impedance testings have been repeated with a stimulation cap after 50 and 100 machine laundings using Spee liquid (Henkel AG & Co. KGaA, Düsseldorf, Germany) in the delicate setting (W1, Miele & Cie. KG, Gütersloh, Germany).

The usability of the flexible cap with integrated textile stimulation electrodes (*System C*) was evaluated in comparison to the conventional application of rubber electrodes placed in saline soaked sponges fixated by rubber bands (*System R*).

The study incorporated twenty participants (age: 24.0 a \pm 1.6 a; 7 female), who gave written informed consent and two operators (age 23 a, one female) without considerable prior experience in tES studies. Participants came for three sessions with randomized time slots in the morning, in the afternoon and in the evening with at least one day break between sessions. In each session, participants received the stimulation cap and the conventional system in randomized order. Each of the two operators performed 30 sessions with 10 participants. Figure 3.1 depicts the two application systems on a head model.

Participants received sham stimulation (sinus, 50 μ A peak to peak, 85 Hz) from two channels of a DC-STIMULATOR MC (neuroConn GmbH, Ilmenau, Germany) for 30 min (Padberg et al., 2017). The stimulator recorded the applied current and the adjusted voltage with a sampling rate of 8 ksps. A finite impulse response band-pass filter between 80 Hz and 90 Hz was applied to these recorded sinusoidal signals for pre-processing. The filter was designed using a Hamming window. The impedance was calculated, after an initial settling time of 10 min, using the effective current and voltage values. These effective values were calculated in sliding signal windows of 10 sinus cycles with 50 % overlap. Finally, the mean impedance was calculated for each channel. The two stimulation channels contacted 4 cm \times 4 cm electrodes positioned at Fp1 and F3 for one channel and Fp2 and F4 for the other channel (Jasper, 1958; Klem et al., 1999). After the first stimulation, the application system was changed and the participant received a second sham stimulation. The time to administer the electrodes was recorded for each application system. Electrode positions were recorded based on their four corners immediately after application and at the end of the stimulation (after 30 min), with a Polaris Spectra system (Northern Digital Inc., Waterloo, Canada). Euclidean distances between position recordings within a session indicated electrode position stability (sD). The initial digitizations from the second and third session were aligned to the initial digitizations from the first session using an iterative closest point search (Per Bergström, Matlab, The Mathworks Inc., Natick, USA)

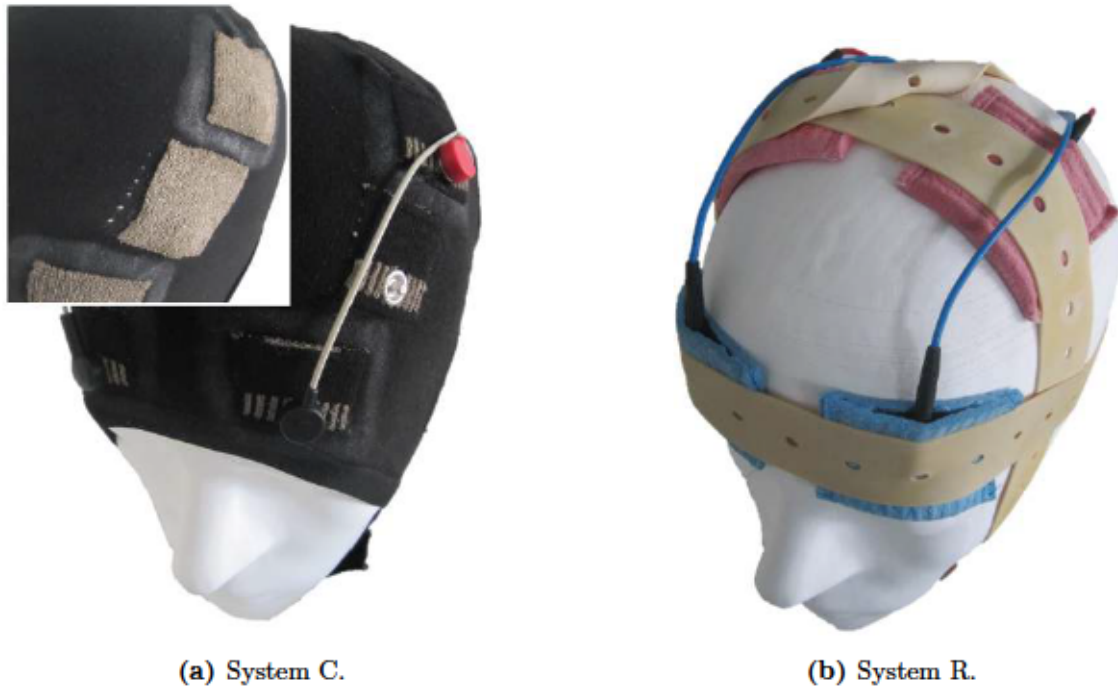


Figure 3.1: Electrode configurations of the flexible cap with integrated textile stimulation electrodes (a) and the conventional application of rubber electrodes placed in saline soaked sponges fixated by rubber bands (a) on a head model. The inset in (a) depicts the inside of the cap with the textile stimulation electrodes exposed.

and assessed with respect to the Euclidean inter-recording distance per electrode corner for reproducibility evaluation (rD).

At the beginning and throughout the stimulation sessions (after 10 min, 20 min, and 30 min), participants reported their status by filling a questionnaire (Appendix).

The functionality of the flexible cap with integrated textile stimulation electrodes was tested in a tDCS stimulation of the visual system. Stimulation effects were objectively evaluated in visual evoked potentials (VEPs) recorded with dry EEG electrodes (Fiedler et al., 2015b) integrated in the a bifunctional cap for simultaneous EEG and tES (Wunder et al., 2018).

Ten participants (age: $24.8 \text{ a} \pm 2.5 \text{ a}$; 2 female) volunteered to receive visual stimuli and being electrically stimulated by tDCS. The visual checkerboard reversal stimuli were generated with eevolve (version 2.2, Advanced Neuro Technology B.V., Enschede, The Netherlands) and presented on a LCD display (MYRICA V30-1, Fujitsu Siemens Computers GmbH, Augsburg, Germany) with 300 repetitions, according to the ISCEV recommendations (50 cm distance from eyes to screen, display size $65 \text{ cm} \times 39 \text{ cm}$, field of view of

66.0 degrees \times 42.6 degrees, checks of 3.7 cm \times 2.8 cm, pattern duration 455 ms (repetition frequency 1.1 Hz), Michelson contrast of pattern 98 %, mean luminance 173.5 cd/m²) published by Odom et al. (2010).

Visually evoked potentials were recorded with dry EEG electrodes on seven channels (POz, PO1, PO2, PO5, PO6, PO9, PO10) according to the international 10–10 system (Jasper, 1958; Klem et al., 1999). Conventional sintered Ag/AgCl ring electrodes positioned at Fz and AFz served as reference and ground electrodes, which contacted the skin with Ten-20 conductive EEG paste (Weaver and Company, Aurora, USA). A NEUROPRAX MR system (neuroConn GmbH, Ilmenau, Germany) with a DC-coupled EEG amplifier recorded the EEG with a sampling rate of 4000 sps on a dynamic range of \pm 184 mV with a 24 bit resolution.

The tDCS was applied using a DC-STIMULATOR PLUS (neuroConn GmbH, Ilmenau, Germany) with textile stimulation electrodes at Oz as cathode and Cz as anode (Jasper, 1958; Klem et al., 1999), measuring 4.5 cm \times 3.5 cm and 4.5 cm \times 4.0 cm at a head with 58 cm circumference. Saline-soaked sponges placed in a textile pocket on the outside of the electrodes ensured low electrode–skin impedance, recommended to be less than 5 k Ω to prevent saturation of the EEG amplifier during tDCS, which was achieved in 5 out of 10 participants. The tDCS stimulation was applied for 10 min with 1 mA intensity and additional fade-in/-out intervals of 5 s with linear intensity change from/to 0 mA.

For the experiment, reference and ground electrodes, and the bifunctional cap were positioned on participants' head and participants settled in a headrest in front of the display. Six VEP recordings were performed: one at baseline before tDCS (VEP1), two during tDCS at 1 min (VEP2) and 5 min (VEP3) in the stimulation and three after tDCS at 1 min (VEP4), 15 min (VEP5) and 30 min (VEP6) post stimulation. After VEP1, the saline-soaked sponge pads for tDCS were inserted into the designated pockets of the cap, and the stimulation was initiated. The sponge pads were removed before conducting the VEP recordings VEP4–VEP6. All sessions were performed by the same operator (S.W.) (Wunder et al., 2018).

VEP data processing was performed in Matlab by referencing all active channels to Fz and applying an offset-correction. A comb filter at 50 Hz and harmonics (Butterworth, order: 80) and a bandpass filter from 1 Hz to 100 Hz (Butterworth, order: 10) were applied, according to the ISCEV recommendations (Odom et al., 2010). Manual artifact rejection resulted in 225 evaluable trials for each VEP recording and each participant. The trials were baseline corrected using the mean of each trial before the stimulus (-100 ms – 0 ms). The grand average of the VEPs was calculated per channel and session for all participants. Amplitudes (peak maximum) of the N75 and P100 components were calculated and statistically evaluated. The stimulation effect on the N75 component was previously described by Antal et al. (2004a), which replication served as reference to demonstrate the functionality of the bifunctional cap and the P100 component presented further prominent changes

based on a initial visual inspection.

The distributions of data samples from various measures were evaluated using descriptive statistics. The differences between sample distributions, were pairwise tested using the Wilcoxon rank sum test (equivalent to Mann-Whitney U-test) on a significance level of 5 %. Further, the 95 % confidence intervals of the samples' mean values were calculated based on 100,000 bootstrap samples. Bland-Altman-Plots directly compared two conditions based on the difference of the analyzed outcome measures (Bland and Altman, 1986). The median of the difference deviating from zero represented a bias towards one of the conditions and 95 % of the differences were expected to deviate less than the reproducibility coefficient (RPC) given by

$$RPC = 1.45 \cdot IQR(d), \quad (3.1)$$

with the interquartile range IQR of the difference d from the median.

3.1.3 Results

The cap, which resulted from the above outlined production, optimally suited heads with a circumference of ≥ 58 cm. It was equipped with a Velcro strip underneath the chin to ensure stability on the head and sufficient contact pressure.

The flexible textile cap material (knitted threads of cotton, elastane and polyamide) showed an elongation (mean \pm std) of $234.78 \% \pm 1.40 \%$ along and $320.81 \% \pm 1.44 \%$ orthogonal to the knitting direction at an applied force of 20 N with a hysteresis as shown in Figure 3.2. The coated silicone provided a elongation at break of 600 %, which ensured sufficient mechanical security margin.

A new cap with a stimulation electrode at Oz without the silicone frame served as reference (*ref*) in impedance measurements for evaluating the basic performance of the textile stimulation electrodes and the silicone frame as diffusion barrier. The electrode of this *ref* cap provided a mean impedance of $44.3 \text{ k}\Omega \pm 2.5 \text{ k}\Omega$ (mean \pm std) with a confidence interval for the mean value of $[44.0; 44.5] \cdot \text{k}\Omega$, as shown in Figure 3.3.

Impedance measurements at positions in the textile surrounding the electrode (approximately POz, PO5, PO6, Iz) comprised two aspects. First, the 384 samples from position POz were consistently above the cutoff impedance at 2,000 k Ω . Second, the remaining 1152 samples from the other positions in electrode vicinity had a mean impedance of $59.4 \text{ k}\Omega \pm 22.5 \text{ k}\Omega$ (confidence intervals $[58.1; 60.8] \cdot \text{k}\Omega$) as presented in Figure 3.4.

Introducing the silicone frame as diffusion barrier surrounding the stimulation electrode changed the impedance values measured at the four positions in the electrode vicinity to

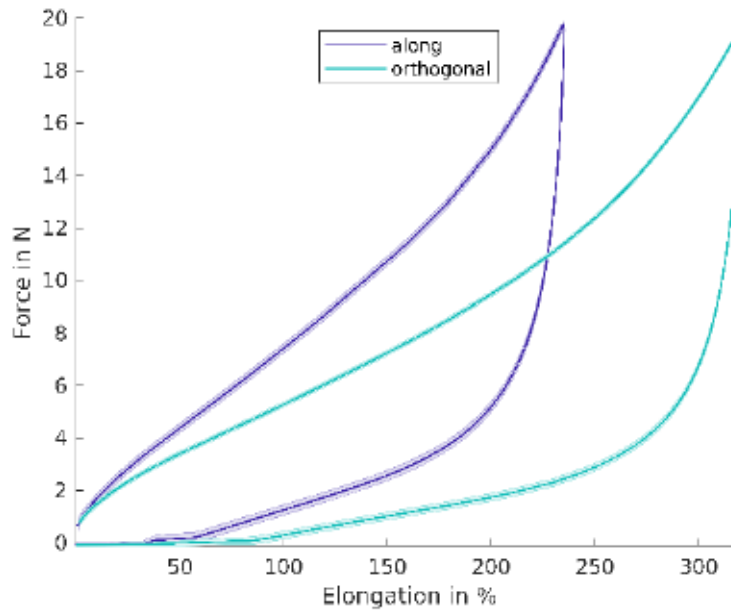


Figure 3.2: Averaged force-elongation curves of both tested directions with respect to the knitting direction. Shaded areas indicate standard deviations across the three tested samples per direction. Colors code test directions along and orthogonal to the knitting direction.

$466.1 \text{ k}\Omega \pm 434.0 \text{ k}\Omega$ averaged from 89 samples (confidence intervals $[381.1; 560.5] \cdot \text{k}\Omega$), the remaining 1447 impedance values were above the cutoff impedance. The stimulation electrode showed a mean impedance of $40.2 \text{ k}\Omega \pm 3.1 \text{ k}\Omega$ with a confidence interval for the mean value of $[40.0; 40.5] \cdot \text{k}\Omega$.

After 50 machine launderings, the impedance measured at positions in the electrode vicinity was $517.0 \text{ k}\Omega \pm 340.3 \text{ k}\Omega$ averaged from 340 out of 1536 samples (confidence intervals $[482.1; 554.5] \cdot \text{k}\Omega$), the remaining impedance samples were above the cutoff. At this stage, the stimulation electrode provided a mean impedance of $38.5 \text{ k}\Omega \pm 5.6 \text{ k}\Omega$ (confidence interval $[38.0; 39.0] \cdot \text{k}\Omega$).

The total of 100 machine launderings resulted in a number of evaluable impedance samples of 280, which provided a mean impedance of $383.2 \text{ k}\Omega \pm 309.6 \text{ k}\Omega$ (confidence intervals $[349.4; 422.2] \cdot \text{k}\Omega$). The impedance of the stimulation electrode averaged to $26.7 \text{ k}\Omega \pm 11.7 \text{ k}\Omega$ (confidence interval $[25.7; 27.8] \cdot \text{k}\Omega$).

The impedance distributions measured from the stimulation electrode at the different stages during the cap's life cycle (new cap w/o silicone frame; cap with silicone frame, after 50 and 100 machine launderings) indicated mutually significant differences by non-overlapping confidence intervals of the mean impedance values (cf. Figure 3.3). Considering the impedance value distributions measured at positions in the electrode vicinity, the sta-

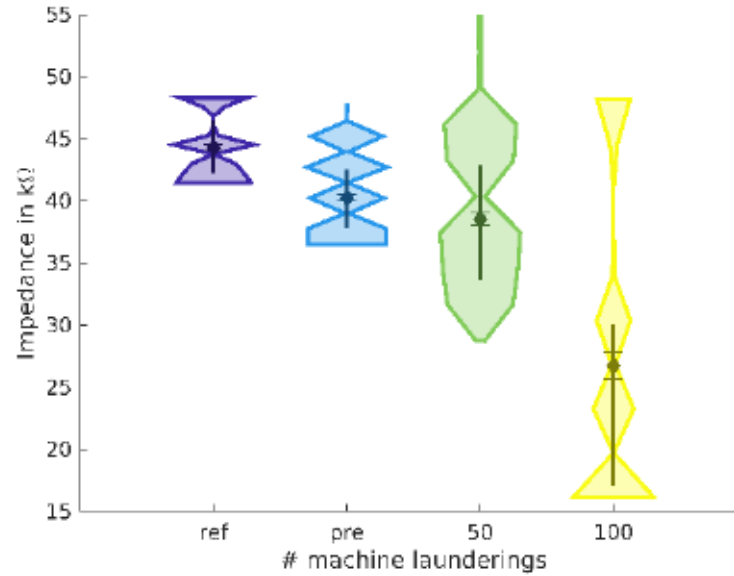


Figure 3.3: Distributions of impedance values measured at the textile stimulation electrode (at position Oz). Labels indicate a new cap without diffusion barrier (*ref*), this cap with a silicone frame surrounding the electrode as diffusion barrier (*pre*), this cap after 50 and 100 machine launderings. Statistical characteristics are depicted by the mean (diamond), confidence intervals of the mean (horizontal lines), the interquartile range (vertical lines) and the distribution of the data of $n = 384$ samples (colored areas).

tistical test also indicated mutually significant differences between impedance distributions, except for the comparison of the distributions measured *pre* and after 100 machine launderings, where no significant difference was indicated. However, the confidence interval of the mean value from the *pre* distribution incorporated the confidence boundaries from both the impedance distributions measured after 50 and 100 machine launderings. The confidence intervals from the distributions measured after 50 and 100 machine launderings did not mutually overlap.

In addition to the technical reliability, the usability of the newly developed cap was evaluated in a realistic application scenario. A flexible cap, which incorporated four textile electrodes (*System C*), was evaluated in direct comparison to the conventional application of four rubber electrodes in saline soaked sponges fixated by rubber bands (*System R*).

The participants rated their perceptions of itching, sweating and pressure feeling at different positions throughout the stimulation periods of 30 min as summarized in Figure 3.5. The load on the participants increased over time independent of the application system, such that the number of responses deviating from 'no' increased consistently over

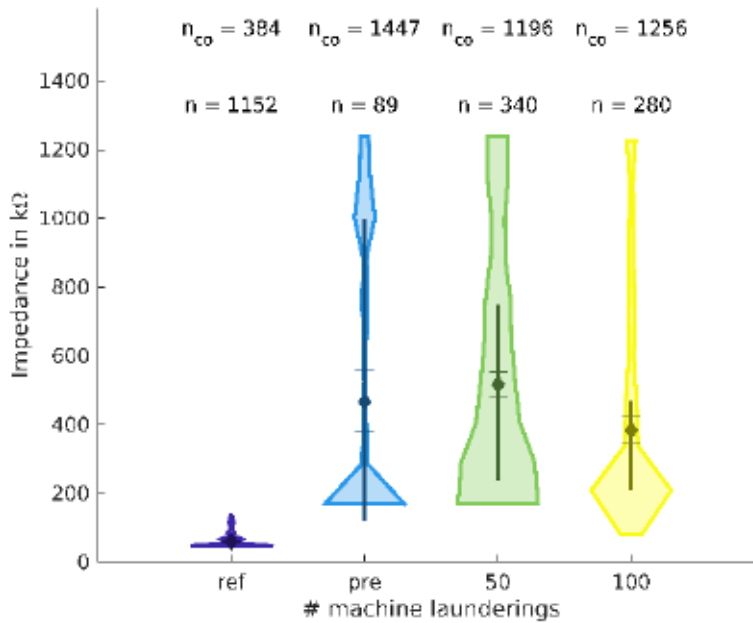


Figure 3.4: Distributions of impedance values measured in the textile surrounding the silicone frame (approximately positions POz, PO5, PO6, Iz). The n above the distributions indicate the number of samples contributing to the analysis, the n_{co} indicate the number of samples above the cutoff impedance at 2,000 k Ω ; in total 1536 samples were measured at each position. Further labels are in accordance with Figure 3.3.

time. With respect to itching and sweating, the differences of the application systems were marginally as only 5.6 % ($n = 10$) and 1.1 % ($n = 2$) of the responses indicated 'modest' or 'strong' sensations, when *System R* was applied. In contrast, participants indicated pressure sensation more than twice as often for *System R* than for *System C*. A fraction of 17.9 % ($n = 129$ out of 720) of the responses indicated 'modest' or 'strong' pressure sensations at various positions. The responses per location revealed a predominance of the chin strap in *System C*, which caused 73.3 % ($n = 63$ out of 86) of the pressure sensations. For *System R*, the most vulnerable positions were the straps and temples, which caused 34.1 % ($n = 71$ out of 208) and 26.0 % ($n = 54$ out of 208) of the pressure sensations.

Accordingly to the detailed assessment, the majority of 54 responses evaluated *System C* as 'very comfortable' or 'comfortable' and only 18 responses indicated these ratings for *System R*. On the contrary 24 responses indicated *System R* to be 'uncomfortable' or 'very uncomfortable' as depicted in Figure 3.6.

The operators rated their effort in application and the material flexibility of the two stimulation systems as depicted in Figure 3.7. The application of *System C* was described

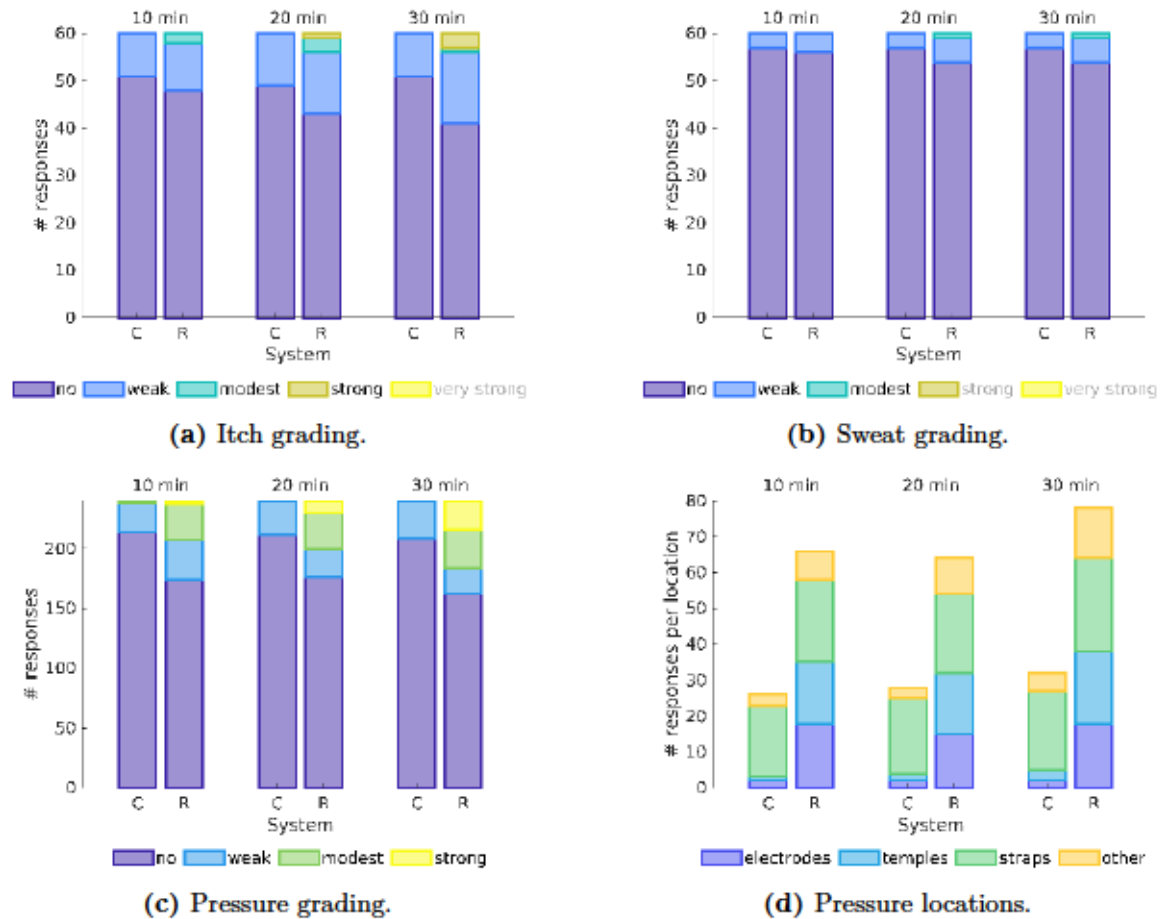


Figure 3.5: Histograms of participant’s responses on the evaluation of itching (a), sweating (b) and pressure (c, d) sensations. Sample sizes per column are $n = 60$ in (a, b), $n = 240$ (60 times four locations) in (c) and $n = 240 - \#('no')$ from (c) columns in (d). The tES application systems are labeled with *C* for the flexible cap with textile electrodes and *R* for the rubber electrodes in saline soaked sponges fixated by rubber bands. Gray labels indicate not applicable categories.

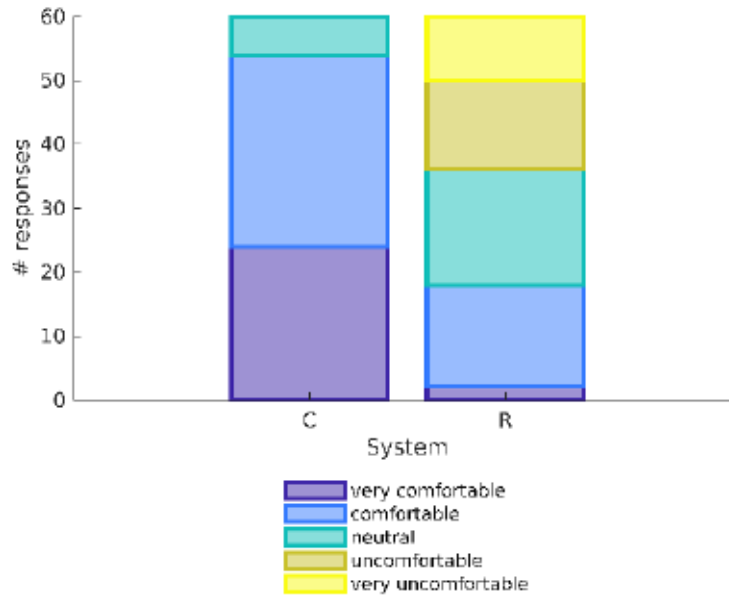


Figure 3.6: Histograms of participant’s responses on the overall comfort evaluation at the end of each session for *System C* and *System R*. The number of samples is $n = 60$ responses from 20 participants with each three sessions.

as 'very easy' or 'easy' in 86.7 % ($n = 52$ out of 60) of the responses, accompanied by a rating of the material as 'very flexible' or 'flexible' in 98.3 % ($n = 59$ out of 60) of the applications. In two (3.3 %) out of the total 60 applications of *System C* operators found it 'difficult' to fit the cap to participant’s head. In contrast the material of *System R* was evaluated as 'flexible' in only 43.3 % ($n = 26$ out of 60) of the applications. The adjustment of *System R* to participant’s head was described as 'difficult' in 13.3 % ($n = 8$) and 'very difficult' in 8.3 % ($n = 5$) out of the 60 applications.

Quantitatively, the applications of *System C* and *System R* were compared based on channel impedance values and electrode positions.

The impedance values of *System C* averaged to $10.0 \text{ k}\Omega \pm 4.4 \text{ k}\Omega$ (mean \pm std), with a confidence interval of the mean value of $[8.8; 11.4] \cdot \text{k}\Omega$. In contrast *System R* demonstrated considerably lower impedance values with a mean and standard deviation of $5.3 \text{ k}\Omega \pm 3.1 \text{ k}\Omega$ and a confidence interval of the mean of $[4.8; 5.9] \cdot \text{k}\Omega$. Figure 3.8a depicts the distributions of $n = 120$ impedance samples from two stimulation channels measured at 20 volunteers in three sessions, each. Further, the Bland-Altman-Plot in Figure 3.8b comparing the two application systems showed a median difference of 3.1 $\text{k}\Omega$ indicating a bias towards *System R*. The *RPC* (cf. equation 3.1) of 8.4 $\text{k}\Omega$ span a range around the median incorporating only 89.2 % of the samples.

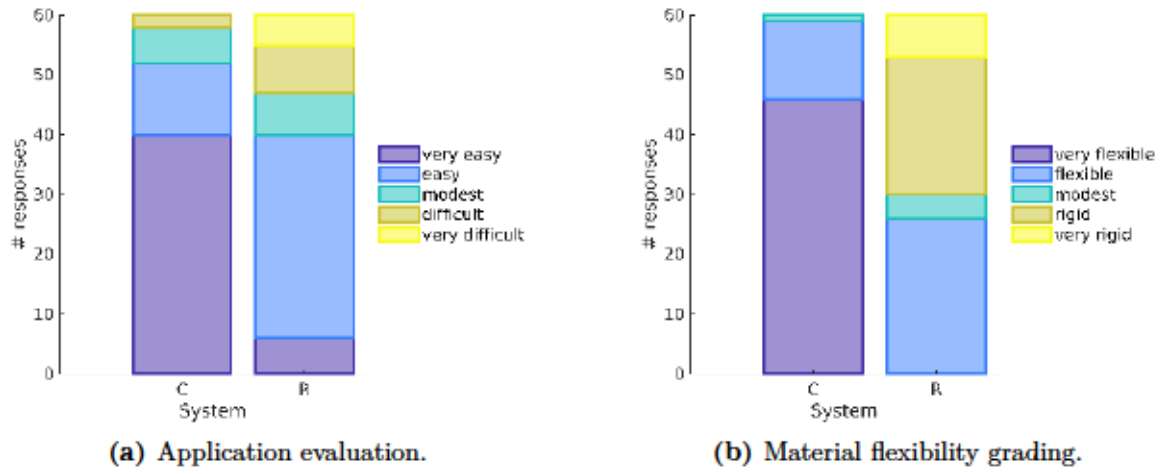


Figure 3.7: Histograms of operators' responses on the evaluation of ease of application (a) and material flexibility (b). The number of samples is $n = 60$ responses from 2 operators performing 30 sessions each.

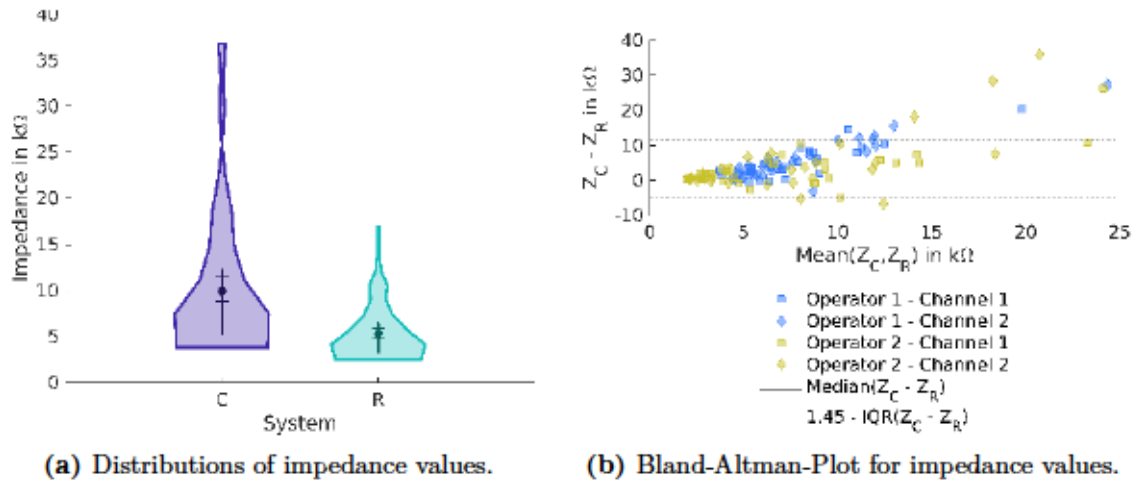


Figure 3.8: Impedance values derived from *System C* and *System R*. (a) Distributions as introduced in Figure 3.4. (b) Band-Altman-Plot with markers indicating samples derived from applications of the two operators (colors) and the two stimulation channels (type). Solid and dashed lines indicate levels of the median difference and the reproduction interval calculated as 1.45 times the interquartile range (IQR). Subscripts C and R refer to the application systems *System C* and *System R*. Sample sizes are $n = 120$ impedance values from two stimulation channels measured at 20 participants in three sessions each.

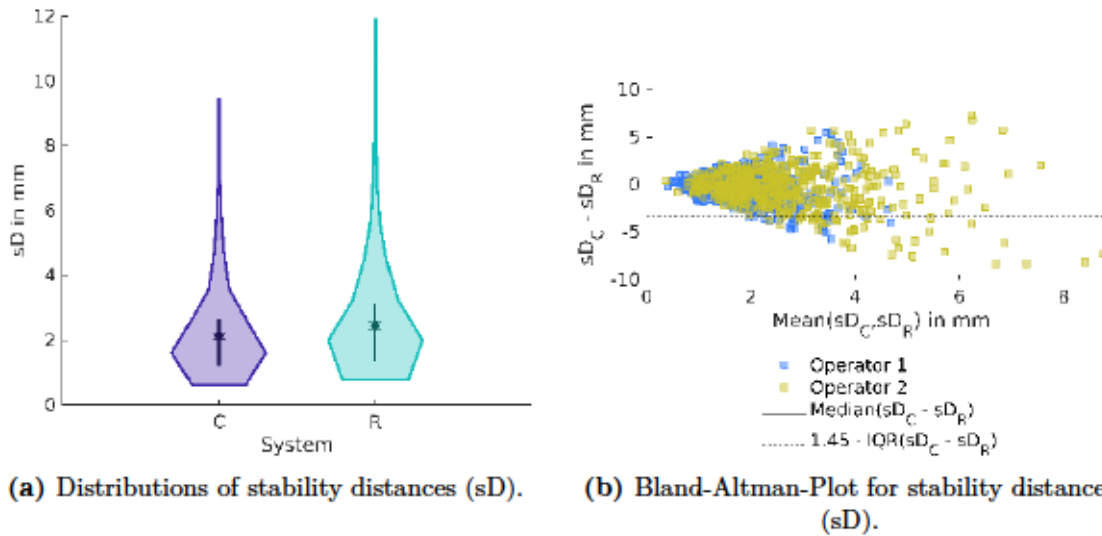


Figure 3.9: Stability distances (sD) calculated as Euclidean distance between electrode corner digitizations directly after application and at the end of the stimulation (after 30 min). Labels and color-codes correspond to Figure 3.8. Sample size is $n = 960$ Euclidean distances from four corners of four stimulation electrodes measured at 20 participants in three sessions.

The electrode positions were monitored at the four corners of each electrode directly after application and at the end of the stimulation after 30 min, providing a measure of electrode position stability throughout a stimulation. These stability distances (sD) between the electrode corner digitizations for *System C* averaged to $2.1 \text{ mm} \pm 1.4 \text{ mm}$ (mean \pm std), with a confidence interval of the mean value of $[2.0; 2.2] \cdot \text{mm}$. Similarly, *System R* demonstrated comparable values with a mean and standard deviation of $2.4 \text{ mm} \pm 1.6 \text{ mm}$ and a confidence interval of the mean of $[2.3; 2.6] \cdot \text{mm}$. Figure 3.9a depicts the distributions of $n = 960$ sD samples from four corners of four electrodes measured on 20 volunteers in three sessions. Further, the Bland-Altman-Plot in Figure 3.9b shows a median difference of -0.2 mm indicating no meaningful difference. The *RPC* (cf. equation 3.1) of 3.2 mm span a range around the median incorporating only 90.2 % of the samples.

The distances between initial electrode corner digitizations aligned from the three application sessions per system provided a measure of electrode position reproducibility (rD). The distances of reproduced electrode positions for *System C* averaged to $3.0 \text{ mm} \pm 1.5 \text{ mm}$ (mean \pm std), with a confidence interval of the mean value of $[2.9; 3.1] \cdot \text{mm}$. In contrast *System R* demonstrated considerably higher distances between reproduced applications with a mean and standard deviation of $9.8 \text{ mm} \pm 4.7 \text{ mm}$ and a confidence interval of the mean of $[9.5; 10.2] \cdot \text{mm}$. Figure 3.10a depicts the distributions of $n = 640$ rD samples from four corners of four electrodes measured on 20 volunteers in two repeated applications (session 1 – session 2, session 1 – session 3). Further, the Bland-Altman-Plot in Figure 3.10b

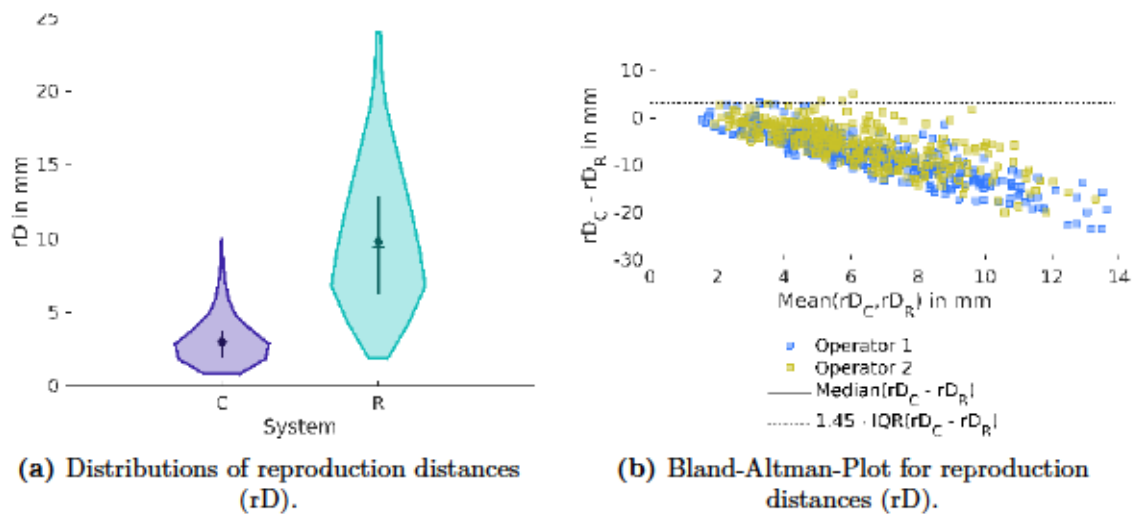


Figure 3.10: Reproduction distances (rD) calculated as Euclidean distance between the initial electrode corner digitizations of each application aligned across sessions. Labels and color-codes correspond to Figure 3.8. Sample size is $n = 640$ Euclidean distances from four corners of four stimulation electrodes measured at 20 participants for two placement repetitions (session 1 – session 2, session 1 – session 3).

shows a median difference of -6.2 mm indicating a bias towards *System C*. The *RPC* (cf. equation 3.1) of 9.4 mm span a range around the median incorporating 94.8% of the samples.

The new flexible cap showed reliable technical performance, improved usability and application reproducibility. The actual functionality of the new cap was tested in a combined tDCS–EEG study aiming to replicate an amplitude decreasing after effect of cathodal tDCS on the N75 component in VEP. The grand average traces of all participants presented in Figure 3.11 indicate that cathodal tDCS over the visual cortex modulated the amplitude of the early VEP components, namely N75 and P100. This effect verifying a reliable tES and EEG functionality of the novel cap. The N75 amplitude was reduced after tDCS (cf. Figure 3.11a), which is in line with previously reported tDCS effects on VEPs (Antal et al., 2004a). The performance of the bifunctional cap in simultaneous tES–EEG experiments was investigated in the VEP sessions during tDCS. Here the P100 amplitude was decreased (cf. Figure 3.11b). The Bland-Altman-Plot in Figure 3.12a comparing the N75 amplitudes in channels PO1, PO2 and POz from VEP1 and VEP4 showed a median difference of $-0.5 \mu V$. This negative difference demonstrates the decrease of the N75 amplitude in VEP4; equal or higher amplitudes in VEP4 compared to VEP1 would result a difference of zero or with a positive value. In VEP1 the median of the N75 amplitude was $-3.0 \mu V$, thus the difference

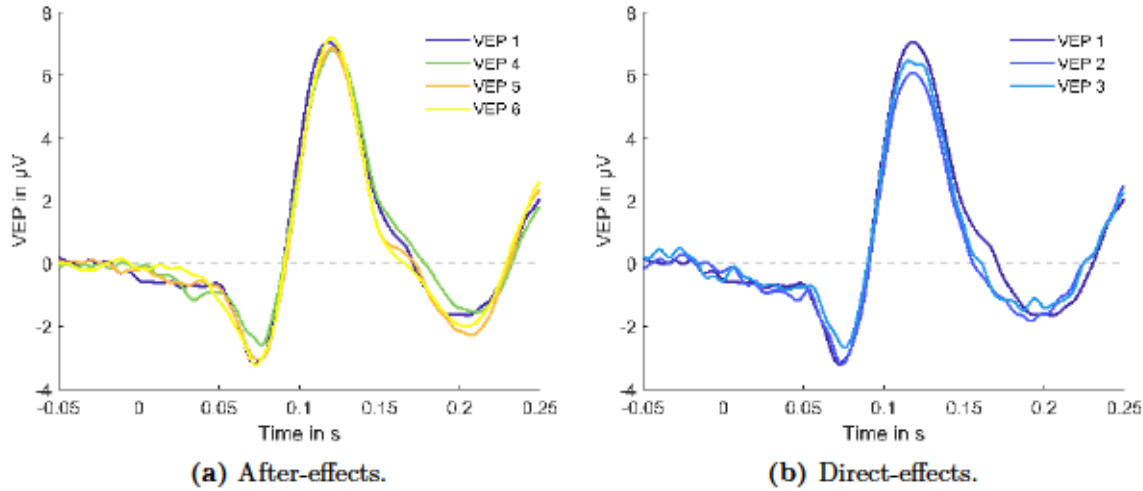


Figure 3.11: Grand average traces across all participants of the VEPs in channel PO2 before vs. after (a) and before vs. during (b) tDCS. Adapted from Wunder et al. (2018).

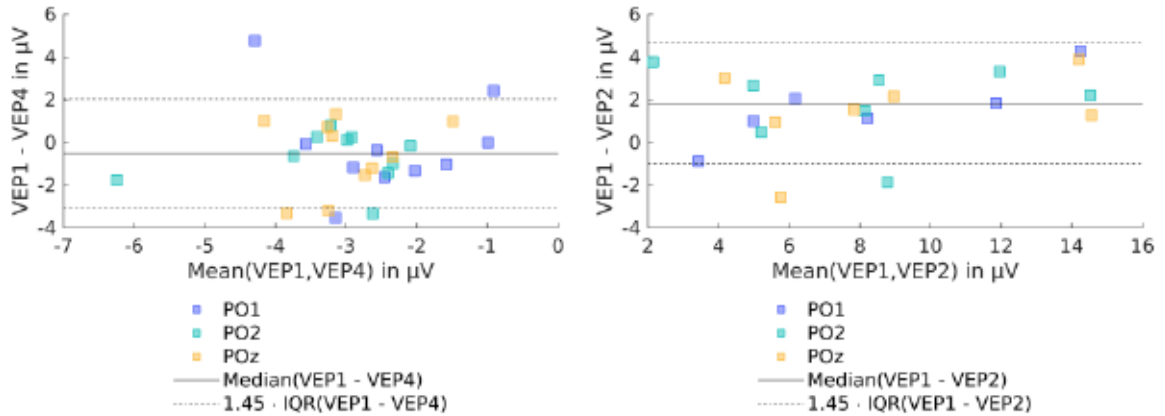
of $-0.5 \mu\text{V}$ was equivalent to a decrease in amplitude of 16.7 %.

Investigating possible acute effects of the cathodal tDCS stimulation on the VEP, the P100 component in VEP2 demonstrated most prominent changes. A Bland-Altman-Plot compares the P100 amplitudes from VEP1 and VEP2 in Figure 3.12b and shows a median difference of $1.8 \mu\text{V}$. This positive difference demonstrates a decrease of the P100 amplitude in VEP2; equal or higher amplitudes in VEP2 compared to VEP1 would result a difference of zero or with a negative value. In VEP1 the median of the P100 amplitude was $6.5 \mu\text{V}$, thus the difference of $1.8 \mu\text{V}$ was equivalent to a decrease in amplitude of 27.7 %. Further details on the study outcome were presented in the publication by Wunder et al. (2018).

3.1.4 Discussion

The newly introduced application system for tES consists of a flexible cap with integrated electrodes. The multi-compartment electrodes comprised a contact area of silver-coated threads, a pocket behind the fabric holding saline-soaked sponges and a diffusion barrier of silicone surrounding the electrode.

A simultaneous application with dry EEG electrodes (Fiedler et al., 2015b) verified the cap's functionality by replicating a previously described after-effect of cathodal tDCS on VEPs (Antal et al., 2004a). The flexible cap with integrated textile stimulation electrodes and



(a) Comparison of N75 amplitudes from VEP1 and VEP4. (b) Comparison of P100 amplitudes from VEP1 and VEP2.

Figure 3.12: Bland-Altman-Plots for after (a) and acute (b) stimulation effects. Colored markers indicate samples derived from EEG channels PO1, PO2 and POz. Solid and dashed lines indicate levels of the median difference and the reproduction interval calculated as 1.45 times the interquartile range (IQR).

dry EEG electrodes further enabled to observe novel acute stimulation effects on the EEG during the course of tES, and therefore introduced a new tool applicable in neuroscience and electrophysiology (Wunder et al., 2018).

Fastening conventional electrode systems by rubber bands limits the number of electrodes in use as well as the positions that can be addressed (Klein et al., 2013). The flexible cap allows the integration of multiple electrodes as indicated in Figure 3.1. Thus, multi-channel tES applications are possible by using the flexible cap with multiple integrated electrodes. Multi-channel tES applications are essential for addressing target areas (Dmochowski et al., 2011) or administering currents from multiple sources (Grossman et al., 2017). The production of the textile cap allows full personalization, which also supports stimulation of individual targets.

In applications of the conventional system, it is challenging to achieve stable and reproducible electrode configurations (DaSilva et al., 2011). Evaluations of electrode positions revealed an increase in electrode configuration stability and reproducibility, when facilitating the flexible cap. In particular, the electrode location and orientation is critical for precise tES, as shown in a simulation study (Opitz et al., 2015). Positioning the textile stimulation electrodes integrated in a flexible cap essentially lowered the position uncertainty from approximately 10 mm (achieved on average with the conventional system) down to 3 mm on average, for the flexible cap.

The flexibility of the fabric allowed an optimal fit to individual head shapes with an elongation of about 320 %. This, together with the diffusion barrier of silicone ensured the

desired effective electrode area. With textile stimulation electrodes, the entire predefined electrode area contributed to the stimulation without partial displacements due to bending or protruding or incomplete contact through the hair layer, as experienced in many conventional tES applications (Fertonani et al., 2015).

Further, the textile electrodes were easily loaded with the saline-soaked sponges in the pockets of the cap and were conveniently contacted by snap fastener cables via directly accessible snap fastener studs at the pockets' outside.

These aspects improved the usability for study participants and potentially patients, and allow the use of the cap without trained medical personnel. Further improvements of user experience in terms of itching, sweating and pressure sensations as well as the overall comfort were drawn from a direct comparison of the new flexible cap to the conventional system, which incorporated rubber electrodes in saline soaked sponges fixated by rubber bands. The rating of itching and sweating sensations indicated a marginal load on the participants in applications of both systems. The most relevant difference between the systems were in comfort and pressure grading. A fraction of 14 % of the responses revealed 'modest' or 'strong' pressure sensations in applications of the conventional *System R*, only one out of 240 responses indicated a 'modest' pressure sensation when the cap (*System C*) was applied. The participants reported that the locations for the pressure sensation were mostly associated with the rubber straps in *System R*. Due to the specifics of the applied montage, one rubber strap crossed the forehead and the temples, which have the lowest pressure threshold on the head (Cuadrado et al., 2010). In *System C*, the discomfort was mainly caused by the chinstrap that tightens the cap on the persons' heads. The summarizing comfort rating favored the cap. According to the participants' responses, *System C* was overall more comfortable for tES application. Further, the ratings for *System C* were stable which can help to keep the focus on potential experiments and reduce variations in the test conditions (Antal et al., 2017a).

Similarly, the operators appreciated the cap material's flexibility, which allowed an electrode placement easier than with the conventional system. Thus *System C* introduced advantages, which can help to reduce training time and to ease the use of tES for different operators. In the present study, the time for fitting the electrodes onto participant's head showed a difference of mean values of approximately 3 min in favor of *System C*, which translates to a decrease of the temporal effort almost by a factor of two. This also decreased the time burden for participants and it is important in clinical environment.

The flexible cap with integrated textile stimulation electrodes required no skin preparation or extra electrolyte gel, reducing the risk of skin irritations and hair loss. This advanced the new cap applications system over other caps (van Schouwenburg et al., 2017) using gel-based Ag/AgCl electrode configurations for tES.

Further the textile stimulation electrodes could be designed according to individual needs, which would eliminate restrictions on areas and shapes of electrodes to predefined elec-

trodes. This also reduces the risk of exceeding the current density limit (Iyer et al., 2005) for too small electrode areas.

Considering the application safety, the electrodes provided sufficiently low impedance values for the electrode–skin interface, on average in the range from 26 k Ω to 44 k Ω . These impedance values were below the safety threshold of 50 k Ω implemented in commercially available tES stimulators (neuroConn). The textile electrodes, in combination with the saline soaked sponges, required a settling time of approximately 10 min, which was comparable to other electrodes used to measure bio-electric potentials (Tallgren et al., 2005). Impedance tests outside of the electrode area provided results above the considered cutoff impedance at 2,000 k Ω in 85 % of the measurements. Remaining impedance samples averaged in the range from 380 k Ω to 520 k Ω . This minimal conductivity encountered outside of the electrodes in the flexible textile was unlikely to increase the effective electrode area, since the hair layer still prevents direct skin contact. Impacting loads on the cap during its life cycle including up to 100 machine launderings revealed no destructive impact on the impedance performance.

The stimulation signal in the comparison study of the new flexible cap and the conventional system was used to evaluate the electric contact, only. No treatment or intervention was intended. Therefore, a sinusoidal sham stimulation signal with a frequency of 80 Hz was applied, since a stimulation with this signal remained without an effect (Antal and Paulus, 2013). However, the influence of sham stimulation desires further investigation (Fonteneau et al., 2019). In direct comparison of the new flexible cap to the conventional system, the impedance values for the flexible cap of about 10 k Ω were approximately twice as high as for the conventional system with about 5 k Ω . However, even the value of 10 k Ω is fully acceptable for a typical electric stimulation (with up to 2 mA), which translate to a voltage of 20 V, that is within the safety limit (Bikson et al., 2016). Impedance measurements during active stimulation with the textile stimulation electrodes were below 10 k Ω , as shown by Wunder et al. (2018).

The quantitative comparisons of impedance values and distance measures revealed no essential differences between the operators, as their influence was incorporated as co-factor in the Bland-Altman-Plots.

One shortcoming of the caps presented in the studies above was its cut pattern optimized for a head circumference of 58 cm, which was adjustable to larger circumferences due to its flexibility, but limited the fit to smaller heads. This issue is addressed in developments exceeding this thesis. First a cap size system considering head height and circumference for more than 80 % of the adult German population is under development. Second a pipeline for individual cap production based on three dimensional scans of the head is being evolved.

Fitting the cap on too large heads would not be limited by the cap material's flexibility but would result in electrode shape distortions as the knitted fabric stretches unequally along and orthogonal with respect to the knitting direction. This issue is being addressed by improving the electrodes' integrity in the process of cap adaptations to head sizes.

The higher electrode-skin impedance values reported for the flexible cap compared to the conventional system could potentially lead to more current sensations in real stimulation and thus limit the cap's applications in sham controlled studies. Further it might limit the compatibility with bio-signal amplifiers in general and so hamper the combination with EEG. However, the textile stimulation electrodes have been successfully applied in a simultaneous tDCS-EEG experiment and thus have shown compatibility with modern EEG amplifiers. Still, the textile stimulation electrodes require an electrolyte reservoir, which is an obstacle in application and restricts long-term use. Ultimately, stimulation electrodes are desired, which directly contact the skin without the need of external liquid or gel-based electrolyte. Such stimulation electrodes would increase the ease of use and broaden the application scenarios of tES, comparably to dry measurement electrodes for EEG (Fiedler et al., 2015b).

The distance measures derived from electrode digitizations incorporated uncertainties from both, the applied digitization system (in the order of 1 mm) and from the operators. This aspect might limit especially the reliability of the stability distance as the measured values were in the same range as the measurement uncertainty.

The here introduced flexible cap with integrated textile stimulation electrodes marked a milestone in tES application. This application system improved stimulation precision with more reproducible electrode positioning and a better controlled effective electrode area. The flexible cap with integrated textile stimulation electrodes overcomes some of the fundamental limitations of the conventional tES application systems.

3.2 Dry stimulation electrodes

3.2.1 Introduction

The flexible cap with integrated textile stimulation electrodes overcame some of the fundamental limitations of conventional tES application systems. However some technological and usability limitations remained.

Considering the knitting procedure, the cap shape excluded electrode locations in the central area of the tapering, which formed a star shaped material reduction. Further, the material flexibility supporting the fit to individual head shapes on the one hand, limited the electrode shape stability on the other hand.

The saline solution deposited in the sponges provided the electrolytes for contacting the skin by penetrating the hair layer. This relied on diffusion of saline solution through the hair layer inevitably expanding the effective electrode area, ultimately affecting the stimulation intensity and location. Long-term applications in the range of some hours were limited by the drying of the electrolyte solution in the reservoir.

Other approaches for the realization of electrodes for tES involved conductive gels (Woods et al., 2016) or adhesive layers (Paneri et al., 2016) to contact electrodes to the skin. For montages with higher spatial resolution, cups holding silver or Ag/AgCl electrodes filled with various electrolyte gels have been evaluated (Minhas et al., 2010). The facilitation of electrolyte gels limited the spatial and temporal contact stability. The electrode gels tend to leak and spread, which alters the effective electrode geometry, and to dehydrate, which limits electrode–skin interface stability.

For tES applications to hair-less positions, such as the forehead or neck, electrodes based on polymer based hydrogels have been proposed (Khadka et al., 2018). The flat polymer layer covering the electrode prevented penetration of the hair layer, which consequently limited application positions to hair-less locations.

Here materials for additive manufacturing of dry multi-pin electrodes for tES application are characterized and resulting electrode prototypes are tested regarding functionality in a tES application.

3.2.2 Material and Methods

Following the design of dry electrodes for electroencephalography, the concept of multiple pins on a common base plate (Fiedler et al., 2015b) was adapted for stimulation electrodes. In tES, the requirements for spatial resolution and low current density pose a conflict. An electrode diameter of 20 mm was considered appropriate in simulations (Saturnino et al., 2015) and would enable current densities below the safety margin of around 1 mA/cm² (Bikson et al., 2016).

Pins on stimulation electrodes required a defined surface to provide a current density in a controlled manner. At the same time pins needed to pass the hair and contact the skin. The newly designed pins had a flat top with a diameter of 2 mm describing an area of 3.14 mm^2 . The pin base with a diameter of 3 mm generated a conical shape on a height of 7 mm. Pins were distributed in the center of the base and on two concentric rings with radii of 4 mm and 8 mm. In total 22 pins with a mutual distance of approximately 5 mm generated an effective contact area of 69 mm^2 (approximately 0.7 cm^2). For this contact area, a current strength of 0.7 mA represented the safety limit.

The 2 mm thick base plate was extended in a truncated cone shape. The truncated cone had a height of 4 mm, a top diameter of 10 mm and contained a recess for a snap fastener. Figure 3.13 depicts the computer aided design (CAD) model of the stimulation electrode generated in SolidWorks (Dassault Systèmes SolidWorks Corporation, Waltham, USA).

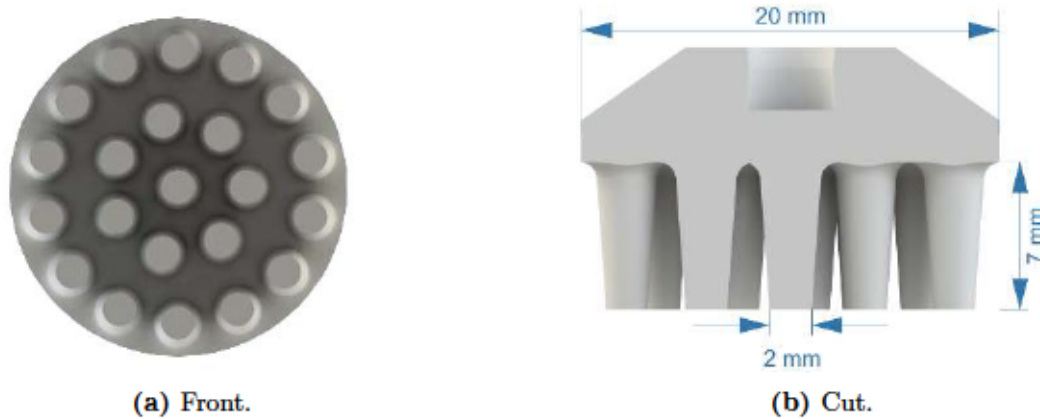


Figure 3.13: Computer aided design model of the stimulation electrode in front (a) and centrally cut side (b) view.

Additive manufacturing implemented the electrode design on a fused deposition modeling (FDM) printer (N2 Plus, Raise 3D Technologies Inc., Irvine, USA) according to the print commands, which were generated by the slicer software Simplify3D (Simplify3D Inc., Cincinnati, USA).

Two carbon doped polylactic acid (PLA) filaments, the Electrically Conductive Composite PLA (*eccPLA*) Proto-pasta (Protoplant, Vancouver, Canada) and the Functionalize F-Electric (*fePLA*) (Functionalize, Seattle, USA), were used for electrode realization. The printed electrodes were characterized with respect to their impedance values and open circuit potentials (OCP).

Printed electrodes were characterized in contact with 0.9 % sodium chloride (NaCl) solution. Impedance spectra were measured from 0.01 Hz to 1 MHz in a two-point setup on

a Reference 600 potentiostat (Gamry Instruments, Warminster, USA). Impedance spectra were repeatedly measured five times on three pairs of electrodes.

Measurements of the open circuit potential provided the voltage difference between a printed electrode under test and a Ag/AgCl ring electrode as reference. For three samples of each material, OCP recordings were conducted twice over 1 h, representing twice the typical application times of tES up to 30 min.

The functionality of the printed dry stimulation electrodes was tested in a tACS stimulation of the visual system. Stimulation effects were objectively evaluated by means of changes in signal power at the individual α -frequency (IAF) recorded with dry EEG electrodes (Fiedler et al., 2015b). Both electrode types were integrated in an advanced bifunctional cap for simultaneous EEG and tES with dry electrodes only.

Six participants (age: $27.2 \text{ a} \pm 3.0 \text{ a}$; 2 female) volunteered to conduct a vigilance test and being electrically stimulated by tACS. In a first stage, IAFs were determined in spontaneous EEG from three interleaved sequences with open and closed eyes for 30 s duration per sequence. The second stage consisted of a 3 min pre-stimulus, a 10 min tACS and a 3 min post-stimulus interval during which spontaneous EEG was recorded. During the entire second stage, participants had to focus on a red cross which rotated for 200 ms in intervals between 35 s and 45 s. The participants had to respond to a rotating cross with a finger tap on a capacitive sensor as vigilance test. The fixation cross rotation stimuli were generated with eevolve (version 2.2, Advanced Neuro Technology B.V., Enschede, The Netherlands) and presented on a LCD display (MYRICA V30-1, Fujitsu Siemens Computers GmbH, Augsburg, Germany). This vigilance test was designed according to Zaehle et al. (2010).

Spontaneous EEG was recorded with dry EEG electrodes on six channels (Pz, POz, PO3, PO4, O1, O2) according to the international 10–10 system (Jasper, 1958; Klem et al., 1999). Conventional sintered Ag/AgCl cup electrodes positioned at the left and right mastoids served as reference and ground electrodes, which contacted the skin with Ten-20 conductive EEG paste (Weaver and Company, Aurora, USA). A NEUROPRAX MR system (neuroConn GmbH, Ilmenau, Germany) with a DC-coupled EEG amplifier recorded the EEG with a sampling rate of 4000 sps on a dynamic range of $\pm 184 \text{ mV}$ with a 24 bit resolution.

The tACS with a sinusoidal current of 0.7 mA root mean square (mArms) at IAF was applied using the DC-STIMULATOR MC (neuroConn GmbH, Ilmenau, Germany). The terminals of one current source were connected to additively manufactured dry stimulation electrodes at Oz and Cz (Jasper, 1958; Klem et al., 1999).

For the experiment, reference and ground electrodes and the advanced bifunctional cap were positioned on participants' heads and they settled in a headrest in front of the display. The room was darkened such that the stimulation display as well as the monitors of the stimulation and recording computers were the only light sources.

EEG data processing was performed in Matlab by referencing all active channels to the channel recorded with the electrode at the left mastoid. A comb filter at 50 Hz and harmonics (Butterworth, order: 80) and a bandpass filter from 5 Hz to 15 Hz (Butterworth, order: 10) were applied.

IAFs were determined in power spectra calculated via Fast Fourier Transform (FFT) from 10 s of the eyes-open and eyes-closed intervals recorded in the first stage. Power spectra were averaged per channel across the three repetitions of the eyes-open and eyes-closed conditions. The frequency with the maximal power in one of the recorded channels was considered as IAF.

EEG data from the pre- and post-stimulus intervals were segmented in trials of 1 s duration. Trials containing triggers from rotating crosses or finger taps were excluded. The first 150 remaining trials were offset corrected and their amplitude spectra were calculated by means of FFT. The resulting 150 spectra were averaged for pre- and post-stimulus intervals per participant. Spectral components in the range of $\text{IAF} \pm 1 \text{ Hz}$ were used for quantitative evaluation of stimulation effects.

The DC-STIMULATOR MC recorded the applied current and the adjusted voltage (sampling rate: 8 ksp/s). The current and voltage time traces were processed with the filters introduced above. The impedance was calculated using the effective current and voltage values, eliminating an initial settling time of 5 min. These effective values were obtained from sliding signal windows of 10 sinus cycles. Finally, the mean impedance was calculated.

The distributions of IAF amplitudes from pre- and post-stimulus intervals were evaluated using descriptive statistics.

3.2.3 Results

The applied additive manufacturing procedure, which utilized conductive filaments in the FDM technology resulted in reproducible electrodes as depicted in Figure 3.14.

The tested materials *eccPLA* and *fePLA* were characterized with respect to their impedance and their electrode potential.

The impedance spectra from 0.01 Hz to 1 MHz demonstrated pronounced capacitive properties for frequencies below 100 Hz as shown in Figure 3.15. The impedance values below 50 k Ω at distinct frequencies are summarized in Table 3.1. Considering only samples 2 and 3 from *fePLA* would result in an average impedance value of 16.1 k $\Omega \pm 3.0 \text{ k}\Omega$ at 10 Hz.

Voltage difference between a printed electrode under test and a Ag/AgCl ring electrode as reference measured by means of open circuit potentials are summarized in Figure 3.16.

The average OCP were $-15 \text{ mV} \pm 15 \text{ mV}$ and $-27 \text{ mV} \pm 23 \text{ mV}$ for *eccPLA* and *fePLA*.

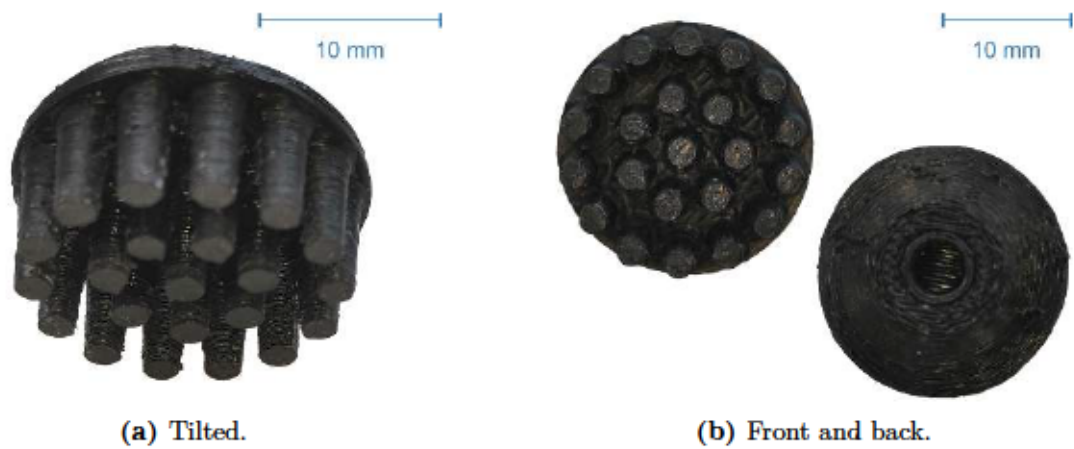


Figure 3.14: Dry stimulation electrode printed of *eccPLA* in FDM additive manufacturing technology.

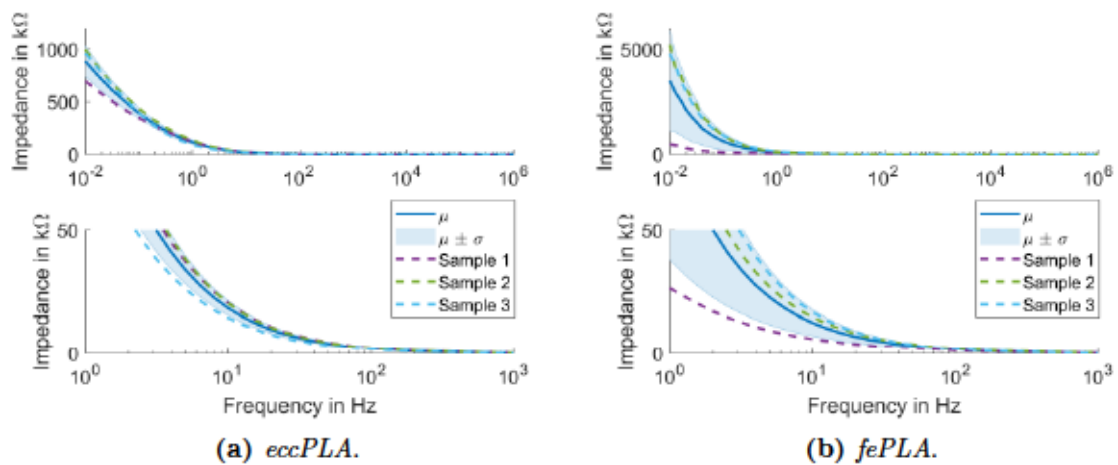


Figure 3.15: Averaged impedance data each from three pairs of printed electrode in contact with 0.9 % NaCl solution. Color-coded dashed lines represent averaged data across five impedance spectra from 0.01 Hz to 1 MHz for each sample pair. Solid lines and shaded areas represent the overall mean (μ) and the range of its standard deviation (σ) around the mean ($\mu \pm \sigma$). Lower panels focus on the frequency range from 1 Hz to 1 kHz and up to an impedance of 50 k Ω .

Table 3.1: Impedance values in $k\Omega$ (overall mean and std) for the tested dry stimulation electrodes at distinct frequencies.

Material		10 Hz	100 Hz	1000 Hz
<i>eccPLA</i>	mean	18.8	2.2	0.3
	std	3.0	0.3	0.03
<i>fePLA</i>	mean	12.8	1.8	0.3
	std	5.4	0.4	0.05

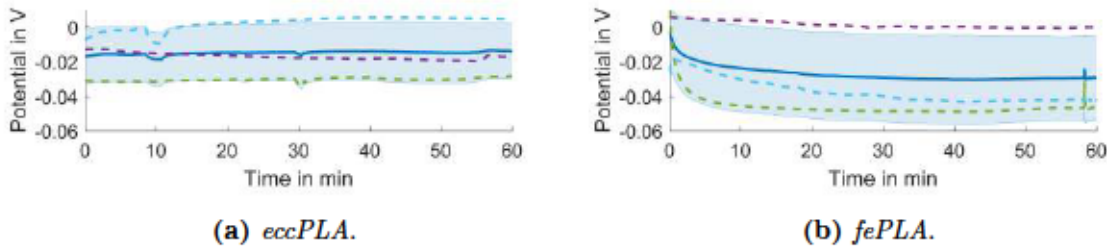


Figure 3.16: Averaged open circuit potential data each from three samples of printed electrodes with a Ag/AgCl ring electrode as reference in 0.9 % NaCl solution. Color-coded dashed lines represent averaged data over two measurements for each sample. Solid lines and shaded areas represent the overall mean (μ) and the range of the standard deviation (σ) around the mean ($\mu \pm \sigma$). The legend of colored lines and areas is equivalent as in Figure 3.15.

The advanced bifunctional cap is depicted in Figure 3.17. The six participants reported no uncomfortable fit experience of the cap with the incorporated electrodes. In the beginning (approximately during the first 60 s) of the stimulation, four out of six participants reported an unpleasant tingling at the stimulation electrodes. TACS was performed successfully in all volunteers, and no skin sensations were reported. The impedance values of the advanced bifunction cap averaged to $29.5 k\Omega \pm 5.5 k\Omega$ (mean \pm std) during the last five minutes of the tACS with 0.7 mArms across the six volunteers.

The IAFs of the six volunteers ranged from 8.3 Hz to 11 Hz ($10.0 \text{ Hz} \pm 0.7 \text{ Hz}$). All participants performed the vigilance test throughout the session lasting for 16 min in total. Figure 3.18 shows EEG data and amplitude spectra from the pre- and post-stimulus intervals from a single representative volunteer with a IAF of 10.9 Hz .

Comparing the amplitudes in the considered frequency range from 5 Hz to 15 Hz, Figures 3.18 and 3.19a reveal a discrepancy in signal amplitudes between pre- and post-stimulus intervals. The separation between the averaged spectra with their margins representing the standard error of the mean was most pronounced between 7 Hz and 11 Hz in Figure 3.19a with increased amplitudes in the post-stimulus interval.



Figure 3.17: The advanced bifunctional cap (black textile) with dry stimulation electrodes printed of *eccPLA* (black multi-pin electrodes at Cz and Oz) and dry EEG electrodes (grey multi-pin electrodes at Pz, POz, PO3, PO4, O1 and O2). The cap is turned inside out on this photo.

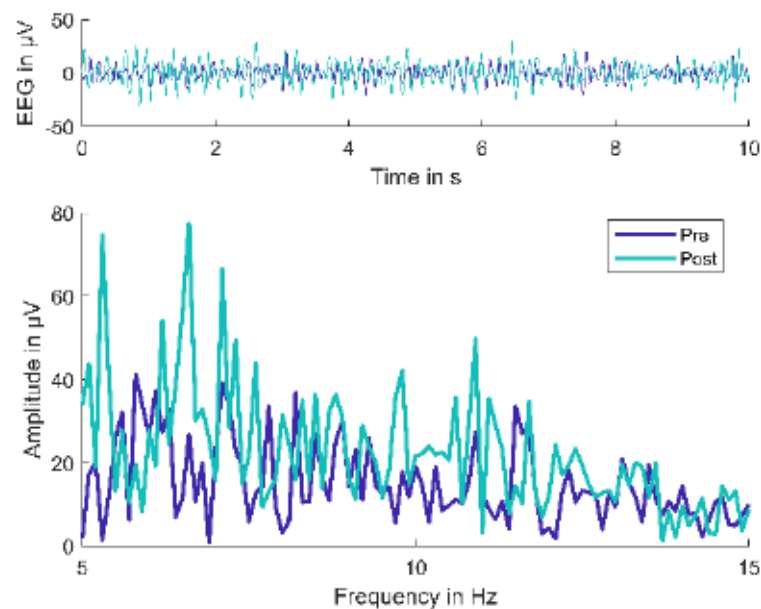


Figure 3.18: EEG traces (top) and amplitude spectra (bottom) from an individual subject with an IAF of 10.9 Hz. Colors code pre- and post-stimulus intervals.

In the range of $IAF \pm 1$ Hz, the EEG amplitude in the post-stimulus interval was on average $158.3 \% \pm 61.4.0 \%$ (mean \pm std) of the EEG amplitude in the pre-stimulus interval (cf. Figure 3.19b).

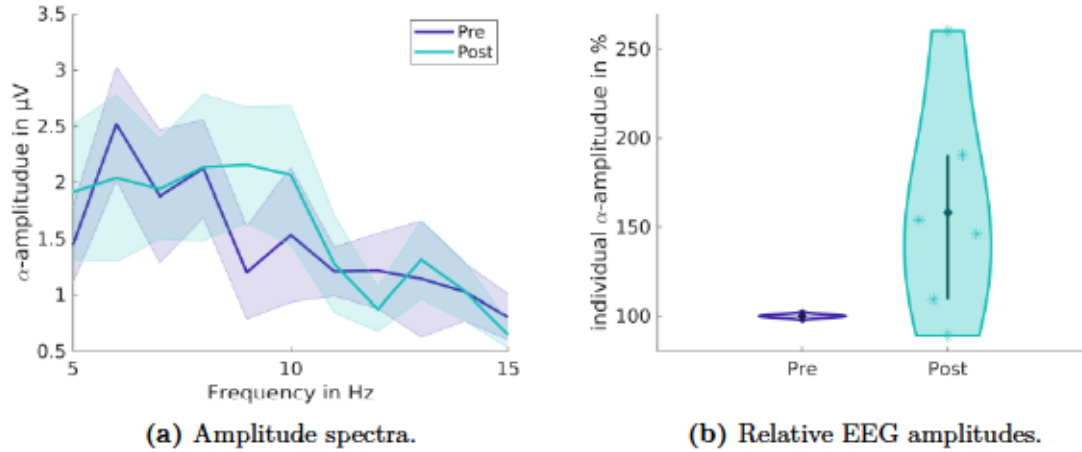


Figure 3.19: EEG amplitudes from the color-coded pre- and post-stimulation intervals. (a) Amplitude spectra grand average (solid line) and range of the standard error of the mean around the grand average (colored area) across all volunteers and channels. (b) Distributions of EEG amplitudes in the range of individual α -frequency ($IAF \pm 1$ Hz) in % relative to the EEG amplitude in the pre-stimulus interval (shaded areas) with mean values (diamonds) and interquartile ranges (vertical lines). Asterisks indicate amplitude ratios from individual participants.

3.2.4 Discussion

The novel stimulation electrodes were additively manufactured by FDM on a 3D printer, which used carbon doped PLA filament. These dry stimulation electrodes were integrated in a flexible cap also holding dry EEG recording electrodes.

The cap, which comprised only dry electrodes for stimulation and recording, demonstrated an essential advancement of the cap with fully textile stimulation electrode relying on an electrolyte solution for the electrode–skin contact as introduced in chapter 3.1.

The functionality of the combined application of dry EEG electrodes (Fiedler et al., 2015b) and dry stimulation electrodes in a fully dry cap was verified by replicating a previously described tACS induced enhancement of α -activity (Zaehle et al., 2010). In the present proof-of-principle study, the participants ($n = 6$) received a 10 min 0.7 mArms tACS at IAF , administered with dry stimulation electrodes at Cz and Oz. The result showed an increased EEG α -activity in the post-stimulation interval compared to the baseline value from the pre-stimulus interval.

The relatively high electrode–skin interface impedance around 30 k Ω , introduced by the dry stimulation electrodes, disadvantageously influenced the derivations of the electric potential difference by the EEG electrodes. Consequently, EEG data during the 10 min tACS stimulation were strongly affected by the tACS artifact, and thus were not analyzed so far. However, severity and cause of tACS artifact are under debate (Noury et al., 2016; Neuling et al., 2017; Noury and Siegel, 2018) and removal techniques (Schlegelmilch et al., 2013; Kohli and Casson, 2019) are available for EEG data extraction.

The utilized conductive PLA filaments *eccPLA* and *fePLA* proved to be suitable for multi-pin electrode printing in FDM technology. The characterization of electrodes printed from these filaments provided impedance and electrode properties in acceptable ranges for tACS applications.

Electrodes from both conductive PLA filaments demonstrated capacitive properties when in contact with physiological NaCl (0.9 %) solution. In the frequency range above 100 Hz, the impedance values were well below 10 k Ω , indicating very good electrode–skin contact. Current wave forms in this frequency range were administered in experiments with transcranial random noise stimulation (tRNS) (Qi et al., 2019), amplitude-modulated high-frequency (Negahbani et al., 2018), and temporal interference (Grossman et al., 2017) transcranial electric stimulation. Impedance values below 50 k Ω , marking a safety limit implemented in state of the art constant current stimulation devices, were ensured for stimulation frequencies higher than 5 Hz. Thus dry stimulation electrodes from both materials could be applied in experiments interfering with physiological oscillations, e.g. of the visual (Schutter and Hortensius, 2010; Kasten et al., 2016) and the motor system (Guerra et al., 2016; Gundlach et al., 2017). In the frequency range below 5 Hz, the charge carrier interface between electron and ion conduction implemented capacitive barriers with impedance values well above 50 k Ω . This capacitive property of the electrodes in contact with electrolytes marked their application unsuitable for use with slowly oscillating or even direct currents (Bikson et al., 2016; Antal et al., 2017a).

The open circuit potentials measured between the printed electrodes and a sintered Ag/AgCl electrode ranged between 10 mV and -50 mV. These values indicated that the open circuit potentials did not dominate the electric potential differences in tES applications, which are typically in the order of 1 V and above (Bikson et al., 2016).

Despite the generally similar properties of the electrodes printed from *eccPLA* and *fePLA*, there were some differences in the material characteristics. Electrodes printed from *eccPLA* demonstrated smaller and more stable open circuit potentials, especially during the first 30 min, whereat this interval represents the typical tES application time. Even though the *eccPLA* revealed slightly higher averaged impedance values below 100 Hz, the values from the tested sample were more consistent.

Consequently, electrodes printed from *eccPLA* were used in the cap, which combined dry stimulation and recording electrodes for functionality verification in a tACS experiment.

Considering the frequency range covered by the dry stimulation electrodes, the selected scenario that addresses the individual α -frequency uses a point of operation at the lower bound of the working range.

The high impedance values for frequencies below 5 Hz provided by the two tested PLA materials excluded their applications in direct current stimulation scenarios. This implemented a major limitation as tDCS represented the most frequently used tES type.

However, a usability study evaluating the comfort and application effort could demonstrate the advantages of the dry stimulation cap. Further, such an investigation could show the reproducibility with respect to impedance and electrode positioning, especially in combination with simultaneously applied EEG electrodes.

The dry stimulation electrodes themselves desire further characterization with more samples (especially for new materials) in four-point impedance measurement setups and long term OCP measurements over several hours. Further the materials' durability needs to be evaluated throughout the electrodes' life cycle incorporating several cleaning procedures using sanitizers.

However, the design, material selection, and manufacturing process give rise to many degrees of freedom for further adaptations of dry stimulation electrodes for tES application. The presented investigations have addressed these aspects on a first stage, and further developments need to be supported by application studies.

The here introduced dry stimulation electrode produced by additive manufacturing based on carbon doped filament has great potential to increase flexibility in tES applications. Caps incorporating such dry stimulation electrodes ensure controlled effective electrode areas, improved reproducibility in electrode positioning and are easy to use. Thus self-application in home environment and long term applications become feasible for tES.

4 Verification of transcranial electric stimulation concepts

4.1 Temporal interference TES

4.1.1 Introduction

Targeting the impressed electric field to specific functional neuronal units was desired in tES applications as described in chapter 2. Towards this issue, previous sections of this thesis addressed the electrodes as sites of current imprinting and the distribution of different current intensities. Considering time variant stimulation signals as used in tACS, the signal frequency provided a further degree of freedom for targeting.

One concept to focus waveforms lies in the superimposition of two waves with different frequencies which result in an interference with amplitude changes in the regime of the difference frequency. The approach of interference is widely used in many physical fields (e.g. mechanics and optics), including medical applications. The superposition of sent and reflected mechanical pressure waves with different frequencies is facilitated in the Doppler ultrasonography (Doppler, 1842; Franceschi, 1979). In optical coherence tomography, low-coherent infrared light beams are reflected from a mirror and the tissue sample. An interference occurs when the travel distance difference is less than a coherence length and therefore focuses on a specific spot. A specimen, e.g. the retina, is scanned with optical coherence tomography by adapting the mirror configuration (Drexler et al., 2001). Applications of interfering electric currents in medical applications were introduced in physiotherapeutic pain treatments (Nemec, 1959) whereat specific muscles are targeted (Beatti et al., 2011).

In neuroscience, the concept of interfering current waves, named temporal interference tES (TI-tES), was introduced to focally stimulate targets located deep in the brain (Grossman et al., 2017). The idea facilitated the temporal inertia of neurons (with membrane time constants in ms range) to follow fast charge carrier fluctuations (with frequencies > 1 kHz). Thus two current sources generated sinusoidal signals in the kHz-range whereat the frequencies of the two sources deviated with a low frequency, e.g. a difference frequency below 100 Hz. The stimulation signals were administered to the subject via two pairs of electrodes, such that sinusoidal signals superimposed in the head and the interference max-

imized in the target. Non-target areas should receive the superimposed sinusoidal signal in the kHz-range without pronounced interference.

The system components utilized for the generation of TI-tES need to provide output stability across a wide range of experimental configurations with respect to both, the load impedance, and the signal frequency. The load on the current sources might change over the course of the experiments due to bio-electrochemical compensation processes or frequency dependent resistance (i.e. impedance) changes. Further, the temporal dynamics of the stimulation sources are required to ensure constant output across the full frequency range up to a few kHz.

A high degree of linearity in all signal defining and current generating components is required to prevent intermodulation distortion (IMD).

Further, the two current sources need to be isolated to prevent cross-talk between the stimulation channels.

Here a setup for TI-tES is introduced and concepts on characteristics and adaptation mechanisms are verified in TI-tES scenarios applied in a homogeneous volume conductor.

Parts of this chapter have been previously presented in abstract form Hunold et al. (2018b, 2020a).

4.1.2 Material and Methods

The concept of TI-tES was tested in a controlled environment, providing a realistic conductivity setup but eliminating geometric disturbances. An aquarium with dimensions of 120 cm \times 80 cm \times 70 cm (length \times width \times height) and 12 mm wall thickness spanned a Cartesian coordinate system in $x \times y \times z$ directions and supplied the geometric frame for TI-tES tests. The aquarium was filled up to a height of 60 cm. This filling with 552 l saline solution of 0.17 wt% established a homogeneous volume conductor with 0.33 S/m (at 25 °C) ionic conductivity, which mimicked the electric configuration of soft tissue in the head (Geddes and Baker, 1967).

Squared rubber electrodes with 5 cm side length were fixated by vacuum seal tape to the inner aquarium side walls at a center height of $z = 30$ cm as depicted in Figure 4.1. Two pairs of electrodes located symmetrically at the y - z side walls with a mutual electrode distance of 20 cm, the electrodes located at $y = 29$ cm (78/2-10; E1 and E3) and $y = 49$ cm (78/2+10; E2 and E4). The two pairs of electrodes fixated at the x - z side walls located asymmetrically to span a trapeze. The side length of this trapeze in x -direction were 102.6 cm with the electrodes in distance of 7.5 cm to the side walls (E5 and E6) and 17.6 cm with the electrodes in distance of 50 cm to the side walls (E7 and E8).

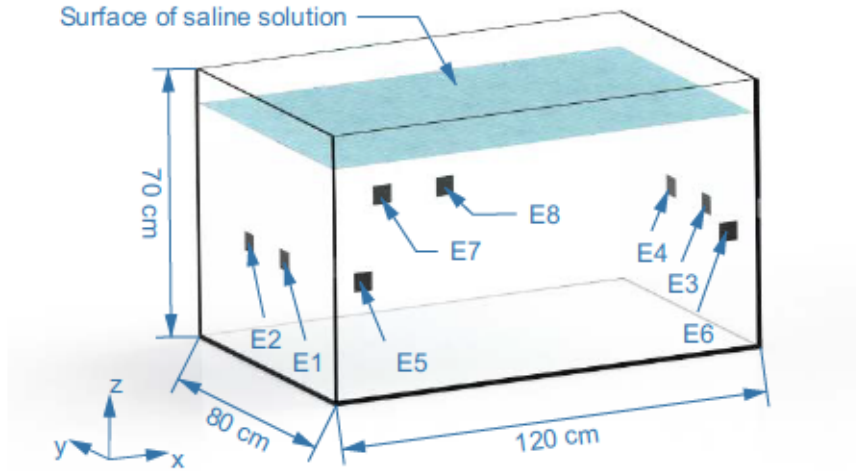


Figure 4.1: Model of the aquarium with outer dimensions of $x = 120 \text{ cm} \times y = 80 \text{ cm} \times z = 70 \text{ cm}$, filled with saline solution to $z = 60 \text{ cm}$ (indicated by the blue surface) to represent a homogeneous volume conductor. Electrodes with 5 cm side length are depicted as black squares, whereat E1 and E2 are positioned symmetric to E3 and E4, E5 and E6 span a trapeze with E7 and E8).

Two pairs of these electrodes were connected to the two sources in each stimulation setup. Table 4.1 provides an overview of the realized montages.

Table 4.1: TI-tES montages with each two electrodes connected to the two sources generating indicated current intensities in mApp.

Montage	Source 1		Source 2	
	Electrodes	mApp	Electrodes	mApp
Opposite (Opp)	E1–E2	2	E3–E4	2
Parallel (Par)	E1–E3	2	E2–E4	2
Parallel asymmetric (ParA)	E1–E3	1	E2–E4	2
Parallel crossed (ParX)	E1–E4	2	E2–E3	2
Trapeze (Trap)	E5–E7	2	E6–E8	2
Trapeze asymmetric (TrapA)	E5–E7	2	E6–E8	1
Trapeze crossed (TrapX)	E5–E8	2	E6–E7	2

A multi-channel constant current stimulator (DC-STIMULATOR MC, neuroConn GmbH, Ilmenau, Germany) provided two isolated current sources. The stimulation signals consisted of sinusoidal waves with a peak-to-peak amplitude of 2 mA (mApp). According to the manufacturer, the current sources incorporated a 3 dB cut-off frequency of 700 Hz. Targeting an interference with an envelope beating at 10 Hz, the frequencies of 643 Hz

and 653 Hz were selected as stimulation frequencies. The numbers 643 and 653 represent the two highest prime numbers with a difference of ten below 700. Prime numbers were preferred for stimulation frequencies to minimize artifact disturbances.

To steer the interference, asymmetric stimulation configurations have been designed such that one source generated a sinusoidal wave with an amplitude reduced to 1 mApp.

A 3D measurement array holding 57 Ag/AgCl pellet electrodes with a diameter of 1.5 mm (cf. Figure 4.2a) was used to measure potential differences in the volume conductor. The 55 measurement electrodes located in three levels, whereat the bottom and central levels held 23 electrodes and the top level comprised of 9 electrodes (cf. Figure 4.2b). The electrodes were held by rods, which supported two or three electrodes starting at a height of 87 mm with a mutual distance of 20 mm between levels in z-direction. The rods located on a grid base with distances of 10 mm between columns and rows in x- and y-direction. The array incorporated two more electrodes at a height of 37 mm in the central row in a distance of 16 mm to the lateral rods in row 3. These two electrodes were designed as reference electrodes but not used in the present study. In the present study a single Ag/AgCl disc electrode with a diameter of 4 mm fixed in the center of the aquarium floor was used as reference electrode.

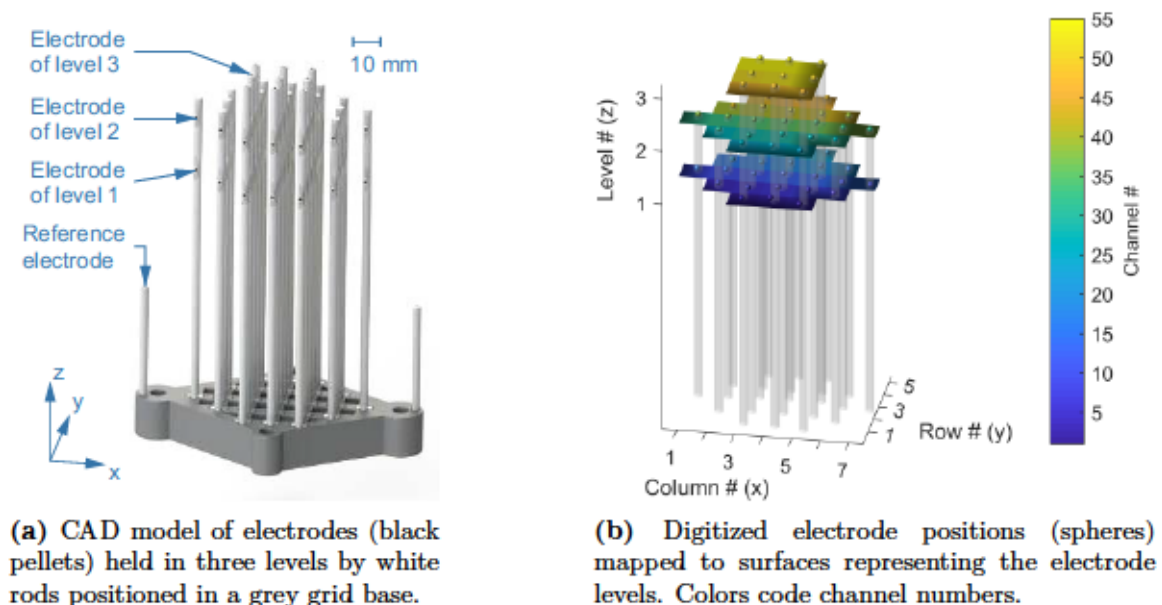


Figure 4.2: Representations of the 3D measurement array as CAD model (a) and as visualization based on the electrode digitization (b).

The hollow rods and the grid base were manufactured from polyactid acid (PLA) filament (Verbatim, Eschborn, Germany) on a fused deposition modeling (FDM) printer (N2 Plus Raise 3D Technologies Inc., Irvine, USA). The 1.5 mm Ag/AgCl pellet electrodes (MedCat GmbH, Munich, Germany) were positioned in predefined holes in the rods and soldered

to 0.0035 mm^2 flexible cable ending in 37-pole SUB-D terminals positioned in an adapter box. Two 37-pole SUB-D cables connected the adapter box to a multifunction I/O device (NI USB-6255, National Instruments Germany GmbH, Munich, Germany) with 80 analog input channels. The referential setup incorporated the measurement electrodes, connected to analog inputs, and the fixed reference electrode in the center of the aquarium floor, connected to the analog sense channel on the NI USB-6255. Data were recorded with a sampling rate of 10 ksp/s and quantified with $3 \mu\text{V}$ steps between -100 mV and 100 mV (16 bit). Data were stored to ASCII text files in the software Signal Express (National Instruments Germany GmbH, Munich, Germany) on a PC connected via USB to the NI USB-6255.

The 3D measurement array was used to sequentially capture the electric potential distributions throughout a central volume slice of the aquarium. With the measurement electrodes of the top level at the central height of the stimulation electrodes ($z = 30 \text{ cm}$), the array was moved in x - and y -direction. Starting in the center of the aquarium at $x = 59 \text{ cm}$ and $y = 39 \text{ cm}$ indicated by the central black array in Figure 4.3, the array was moved to overall 21 positions with a spacing of 15 cm and 20 cm in x - and y -direction, represented by translucent arrays in Figure 4.3.

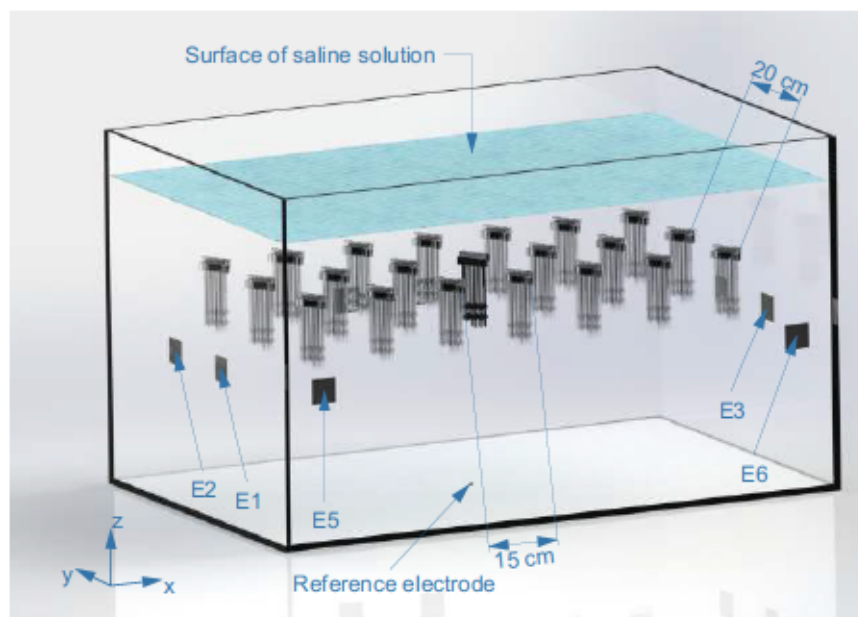


Figure 4.3: Model of the experimental setup with the 3D measurement array (cf. Figure 4.2) turned upside down in the central initial array position (black) and the sequentially captured positions represented by translucent arrays. All stimulation montages (cf. Table 4.1) were measured at each array position. The stimulation electrodes are indicated by E1–E8.

Measurements incorporated ten seconds noise recording followed by active stimulation with 5 s fade-in, 30 s constant current amplitude and 5 s fade out. Signal processing, analysis and visualization was performed in Matlab (The Mathworks Inc., Natick, USA). Recorded data were offset corrected by subtracting the mean of 5 s noise data per channel. The central 20 s data interval during the constant amplitude stimulation was bidirectionally filtered by a band-pass finite impulse response filter between 640 Hz and 656 Hz. Eleven segments (1 s duration) of the filtered data were phase-synchronized and averaged. The envelope, also called the instantaneous amplitude, of the averaged signal was calculated as the magnitude of its analytic signal. The analytic signal was found using the Hilbert transform (Lawrence Marple, 1999). A spectral analysis was performed for both, the averaged signal and the envelope. A segment of 200 ms duration of envelopes and averaged signals were used for further analysis.

The resulting envelope trace was used to define essential features on the interference: the maximum $\hat{\varphi}$ and the minimum $\check{\varphi}$ as extreme values of the envelope and the amplitude $\tilde{\varphi}$ of the envelope as difference between these extreme values. The envelope parameters are indicated in Figure 4.4.

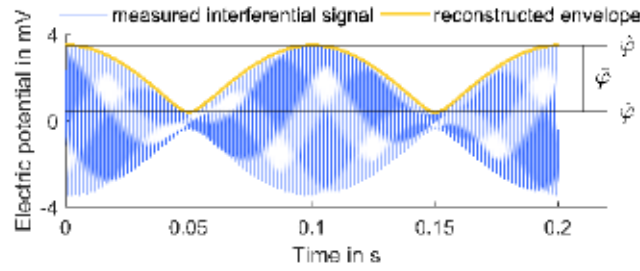


Figure 4.4: Time traces of a recorded interferential electric potential (blue) and the calculated envelope (yellow) with labeled envelope parameters.

Signal features at corrupted channels were reconstructed by interpolation from their four next neighboring channels. In case of low signal-to-noise ratio (SNR), i.e. in recordings with average $\hat{\varphi}$ below 1 mV, an amplitude calculation was not carried out for the entire array at the position under question for the present stimulation montage.

Topographies of the envelope features extracted from the 55 recording channels at the 21 array positions were compared based on a modified relative distance measure (RDM^*) (Meijs et al., 1989)

$$RDM^* = \sqrt{\sum_{i=1}^n \left(\frac{\varphi_{i,r}}{\sqrt{\sum_{j=1}^n \varphi_{j,r}^2}} - \frac{\varphi_{i,t}}{\sqrt{\sum_{j=1}^n \varphi_{j,t}^2}} \right)^2}, \quad (4.1)$$

with i and j being channel indices, and r and t indicating reference and test configurations.

The RDM^* ranges from 0 to 2, which indicated identical and inverted topographies. Amplitude differences between a original montage as reference and its asymmetric or crossed modifications (c.f. Table 4.1) as test montages were assessed by a relative magnitude difference (MAG_{rel}) value (Güllmar et al., 2006)

$$MAG_{rel} = \left| 1 - \frac{\sqrt{\sum_{i=1}^n \varphi_{i,t}^2}}{\sqrt{\sum_{i=1}^n \varphi_{i,r}^2}} \right|, \quad (4.2)$$

with the channel index i , and reference and test configurations indicated by r and t .

4.1.3 Results

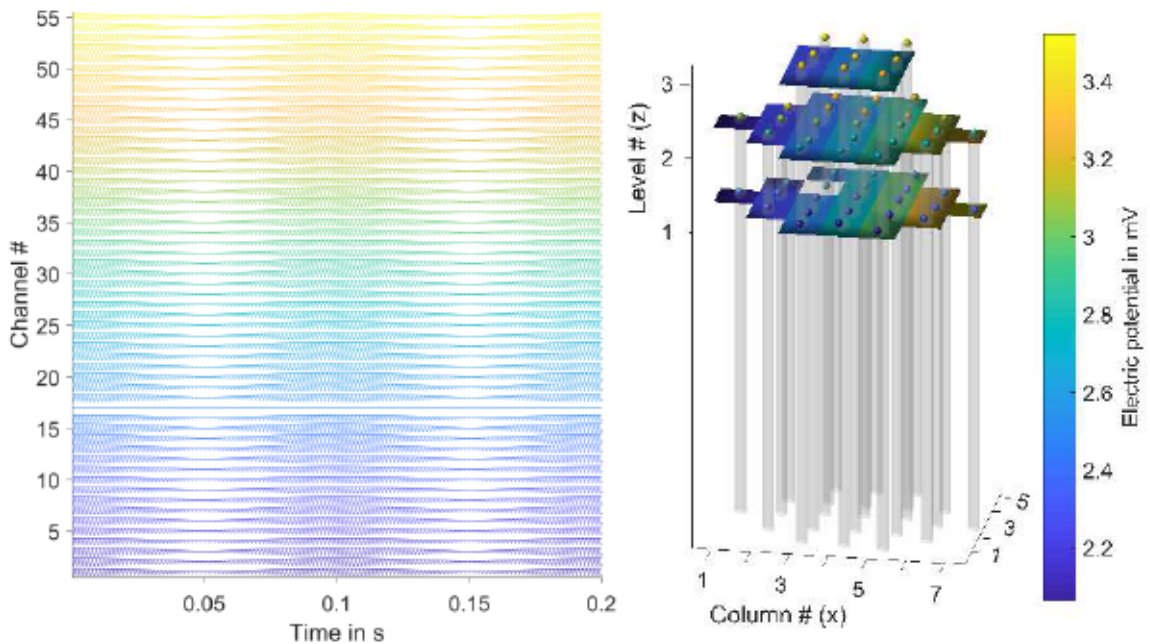
The recordings from the TI-tES experiments contained high-frequency sinusoidal time traces as depicted in Figure 4.5a. The recorded signals comprised an interference of the two stimulation signals with frequencies of 643 Hz and 653 Hz as shown in Figure 4.5c. The envelope calculated from the interference signals, as depicted by the low-frequency sinusoidal time traces in Figure 4.5a, revealed the amplitude variation with a frequency of 10 Hz (cf. Figure 4.5d). This frequency matched with the difference frequency between the two stimulation signals.

The extreme values and the amplitude (as difference between maximum and minimum) of the envelope provided topographies of the interference. Figures 4.6 and 4.7 depict interference features extracted at the 23 electrodes in the central level out of the 55 recording electrodes in the 21 array positions. Maximal values of $\hat{\varphi}$ consistently occurred in the vicinity of the stimulation electrodes: E1, E2, E3, E4 for Opp and Par montages; E5, E6, E7, E8 for Trap montages.

Recorded potential values were particularly high, when the electric fields from the two sources were parallel (left and right line in Figure 4.6c) or electrodes effectively recorded only one source (left and right front corners in Figure 4.6e). In contrast, electric fields with deviating directions superimposed not optimally, whereby smaller values were measured at e.g. the three central array positions ($x = [44 \ 59 \ 74]$ cm) in the back ($y = 59$ cm) of Figure 4.6e in vicinity to E7 and E8 (where components of Sources 1 and 2 contributed with perpendicular orientation).

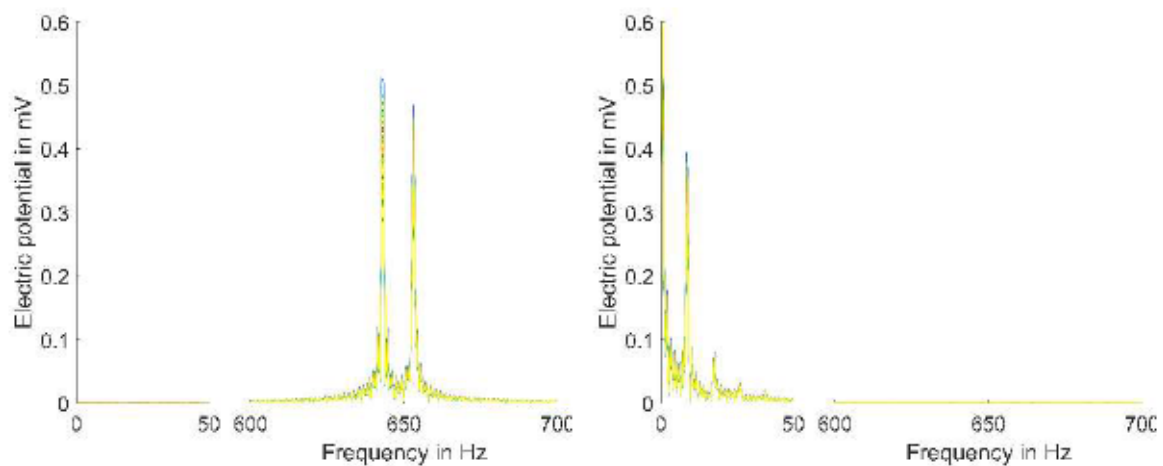
The envelope amplitude $\tilde{\varphi}$ normalized by the envelope maximum $\hat{\varphi}$ indicated the level of the interference. Thus, a ratio of 1 indicated the absence of a minimal envelope baseline ($\tilde{\varphi} = 0$). Ratios below 1 revealed the presence of a baseline ($\tilde{\varphi} > 0$), e.g. from $\tilde{\varphi}/\hat{\varphi} = 0.6$ it appears that there is a baseline of 40 % with respect to $\hat{\varphi}$ ($\tilde{\varphi}/\hat{\varphi} = 0.4$).

This means, the interference evoked by the Opp montage fully developed only in the central x -line of the aquarium. Notably, the envelope amplitude $\tilde{\varphi}$ accounted for only 20 % of $max(\hat{\varphi})$ at these positions, which are rather distant to the stimulation electrodes. In



(a) Interference and envelope traces for each channel, color-coded according to Figure 4.2b.

(b) Array electrodes (cf. Figure 4.2b) and electric potential values from time 0.1 s in (a) mapped to the surface representations.



(c) Amplitude spectra of interference traces.

(d) Amplitude spectra of envelope traces.

Figure 4.5: Measured electric potential traces from TI-tES experiments. Traces of interference and envelope signals in time domain (a) with values at 0.1 s mapped to electrode surface representation (b), and in frequency domain (c, d). Spectra are focused on the ranges below 50 Hz and from 600 Hz to 700 Hz. The spectra for all channels are plotted one above the other and are therefore dominated by the color of the last channel plotted. If not otherwise stated, colors code channel numbers as introduced in Figure 4.2b (note electric potential distribution in b). A flat trace indicates a corrupted channel (# 17).

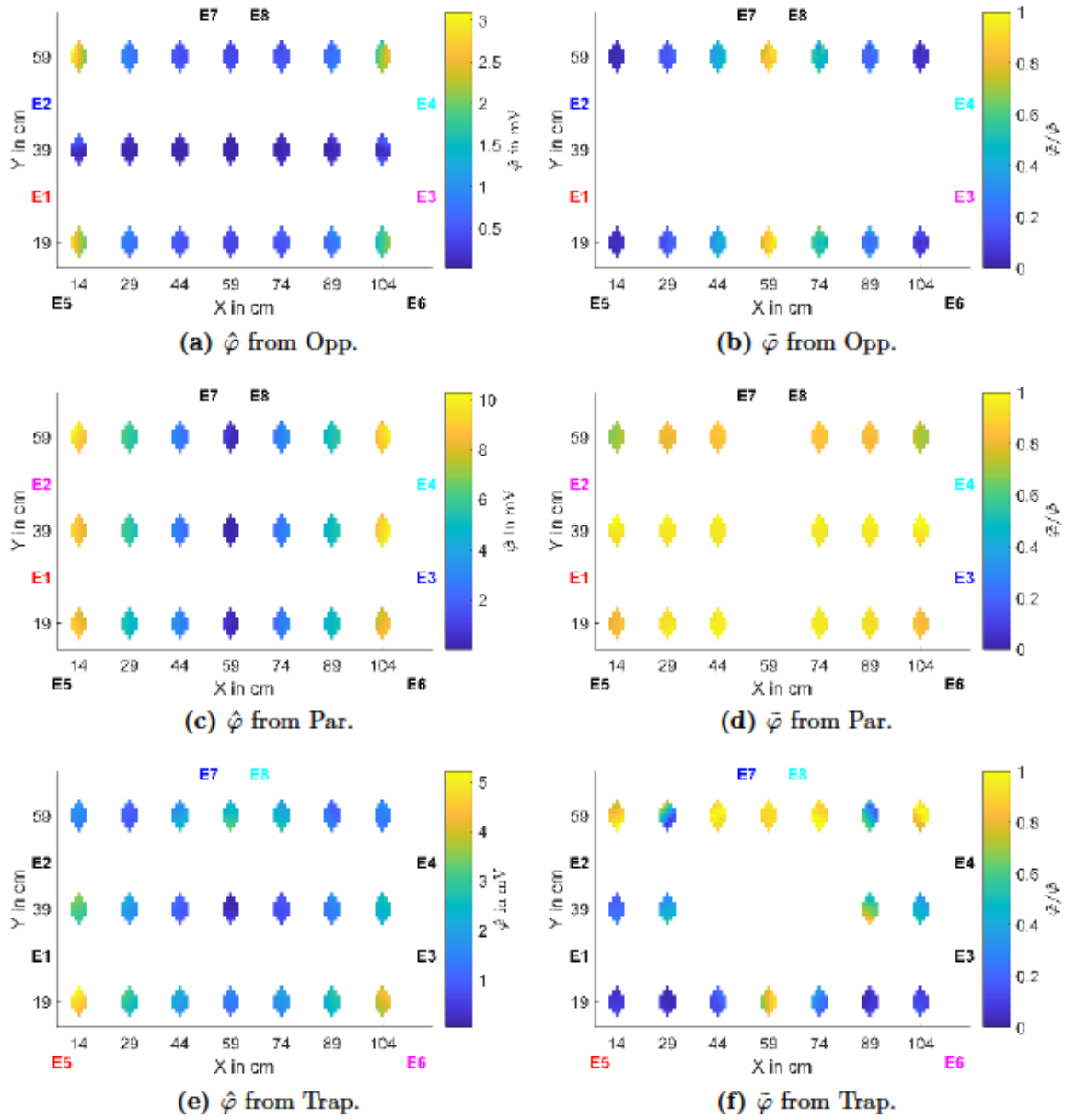


Figure 4.6: Envelope parameters $\hat{\varphi}$ (left) and $\tilde{\varphi}$ normalized to the $\hat{\varphi}$ in each channel (right) from stimulation montages Opp (a,b), Par (c,d), and Trap (e,f) (cf. Table 4.1). View from top on parameter distributions mapped on the surfaces of the 23 electrodes in the central level 2 (cf. Figure 4.2b) for all positions of the array in the aquarium (cf. Figure 4.3) as indicated by aquarium x- and y-coordinates. Missing array positions in $\tilde{\varphi}$ distributions indicate recordings with $\hat{\varphi}$ below 1 mV, and thus low SNR, for which amplitude calculation was not performed. Labeled stimulation montages are indicated by colored stimulation electrode labels (E1–E8), which represent current Source 1 (red–blue) and Source 2 (magenta–cyan) according to the montages introduced in Table 4.1.

contrast, for the Par montage, the envelope oscillated with the full amplitude in extended areas left and right to the central x-line. For the Trap montage, the envelope amplitude maximized focally in the three array positions in front of E7 and E8 (cf. Figure 4.6f) with maximal envelope values $\hat{\varphi}$ of approximately 50 % of $\max(\hat{\varphi})$ (cf. Figure 4.6e). Further, the corners distant to the stimulation electrodes demonstrated fully developed envelope amplitudes, as the electric fields were uniformly bend at the boundary of the aquarium and no source predominated in these areas.

The RDM^* between array level topographies for the envelope parameters depicted in Figure 4.6 were 0.06 ± 0.11 and 0.07 ± 0.11 (mean \pm std) for $\hat{\varphi}$ and $\bar{\varphi}/\hat{\varphi}$ across array positions and stimulation montages. Maximal RDM^* were found for the Opp montage with values of 0.71 and 0.48 for $\hat{\varphi}$ and $\bar{\varphi}/\hat{\varphi}$.

Modifications of the stimulation montages with respect to asymmetric source intensities and source configuration with crossing current paths (ParX, TrapX) resulted in changes in the $\bar{\varphi}/\hat{\varphi}$ distributions depicted in Figure 4.7. The envelope amplitude $\bar{\varphi}$ maximized at positions with similar intensity contributions from Sources 1 and 2.

Figure 4.7a-c presents $\bar{\varphi}/\hat{\varphi}$ distributions from the Par montage and its modifications. Impressing an intensity of only 1 mA on Source 1 (E1–E3) the maximal envelope amplitude $\bar{\varphi}$ appeared in the front corners, shifted along the y-direction towards the stimulation electrodes of Source 1 (E1–E3). Comparing the $\bar{\varphi}/\hat{\varphi}$ distributions from the original and the asymmetric Par montage for the 21 array positions, the MAG_{rel} and RDM^* were 0.29 ± 0.11 and 0.05 ± 0.07 (cf. purple distributions in Figure 4.8a). Changing the source configuration to the ParX montage resulted in a concentration of the maximal envelope amplitude $\bar{\varphi}$ in the central y-line. The MAG_{rel} and RDM^* were 0.09 ± 0.14 and 0.07 ± 0.14 with respect to the original Par montage as depicted by the green distributions in Figure 4.8a.

Figure 4.7d-f presents $\bar{\varphi}/\hat{\varphi}$ distributions from the Trap montage and its modifications. Impressing an intensity of only 1 mA on Source 2 (E6–E8) the maximal envelope amplitude $\bar{\varphi}$ appeared in the central y-line shifted along the x-direction towards the stimulation electrodes of Source 2 (E6–E8). Comparing the $\bar{\varphi}/\hat{\varphi}$ distributions from the original and the asymmetric Trap montage for the 21 array positions, the MAG_{rel} and RDM^* were 0.43 ± 0.19 and 0.11 ± 0.09 (cf. purple distributions in Figure 4.8b). Changing the source configuration to the TrapX montage resulted in a concentration of the maximal envelope amplitude $\bar{\varphi}$ in the central x-y-intersection. The MAG_{rel} and RDM^* with respect to the original Trap montage were 0.83 ± 1.24 and 0.30 ± 0.23 as depicted by the green distributions in Figure 4.8b. The positive outliers in MAG_{rel} occurred at array positions in the front most y-line with minimal envelope amplitudes in the original Trap montage.

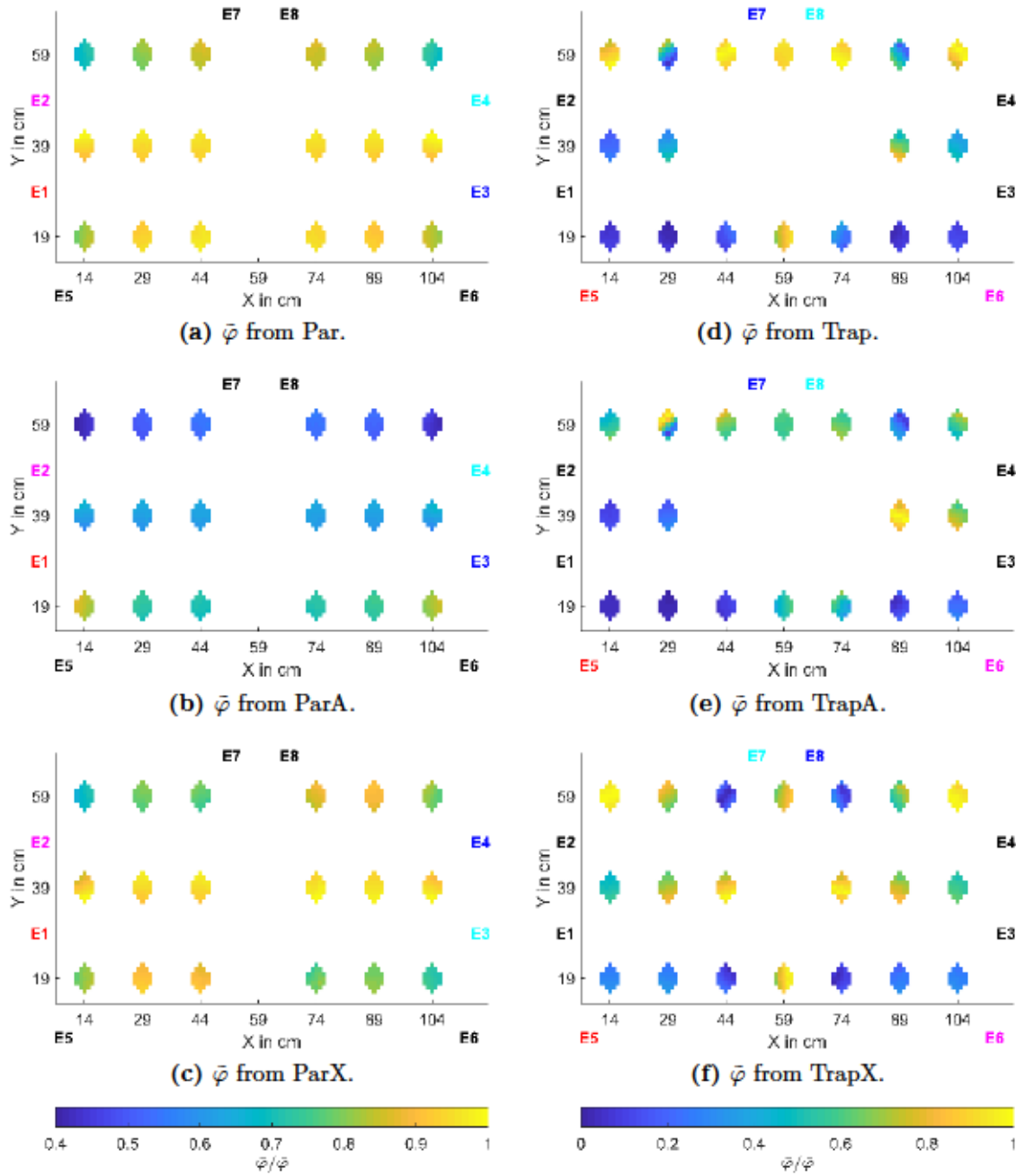


Figure 4.7: Envelope amplitude $\tilde{\varphi}$ normalized to the $\hat{\varphi}$ in each channel from stimulation montages Par (a-c) and Trap (d-f) (cf. Table 4.1). View from top on amplitude distributions mapped on the surfaces of the 23 electrodes in the central level 2 (cf. Figure 4.2b) for all positions of the array in the aquarium (cf. Figure 4.3) as indicated by aquarium x- and y-coordinates. Parallel (left) and Trapeze (right) stimulation montages include asymmetric source strength (b,e) and 'crossing' current pathways (c,f), indicated by colored stimulation electrode labels (E1–E8), which represent current Source 1 (red–blue) and Source 2 (magenta–cyan). Note the different amplitude color scales.

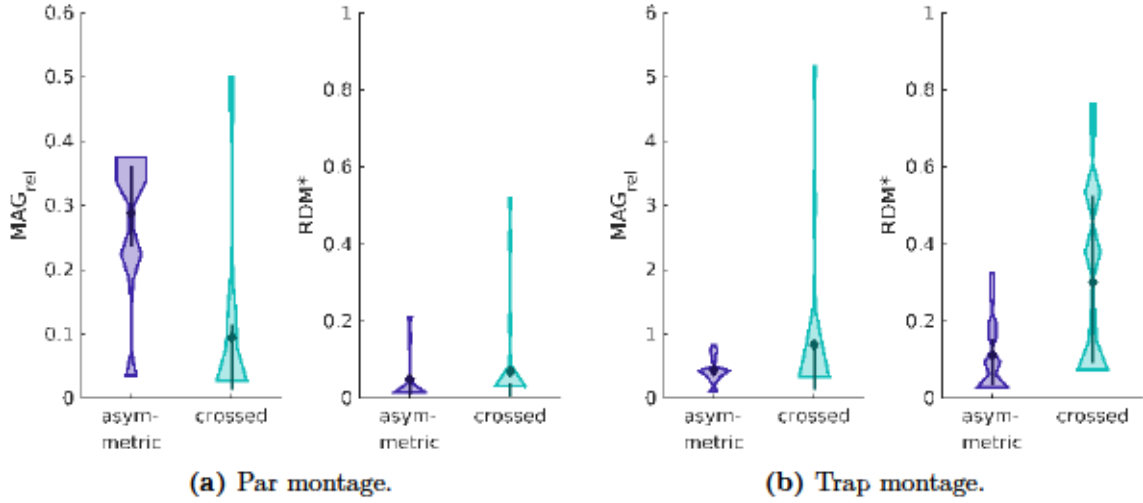


Figure 4.8: Distributions (shaded areas) of MAG_{rel} and RDM^* values determined for the 21 array positions comparing original and asymmetric (purple) or crossed (green) Par (a) and Trap (b) montages, with mean values (diamonds) and interquartile ranges (vertical lines). Note the different scales for MAG_{rel} .

Overall MAG_{rel} and RDM^* values, as summarized in Table 4.2, resulted when considering the 21 array positions as one entity for each stimulation configuration. With respect to magnitude changes, the asymmetric Par configuration provided the most pronounced difference, with a MAG_{rel} of 0.28. The quantification for topography changes generated a maximal value of RDM^* with 0.52 for the TrapX montage.

Table 4.2: Overall MAG_{rel} and RDM^* values for $\hat{\varphi}/\hat{\phi}$ comparisons of original (reference) and asymmetric or crossed (test) montages.

Test montage	MAG_{rel}		RDM^*	
	Par	Trap	Par	Trap
asymmetric	0.28	0.15	0.17	0.38
crossed	0.07	0.02	0.20	0.52

4.1.4 Discussion

The TI-tES scenarios realized in a homogeneous volume conductor by means of an aquarium filled with saline solution demonstrated the generation of interferences in an artificial setup. The utilized multi-channel stimulator demonstrated the ability to generate waveforms without considerable IMDs, as the measured interference contained mainly the initial stimulation frequencies. In contrast, the envelope calculated to the interference exhibited a strong contribution of the difference frequency, as expected.

The maximum $\hat{\varphi}$ and the amplitude $\tilde{\varphi}$ of the envelope represented essential morphological features of the interference. Topographies of the envelopes' maximum and amplitude demonstrated distributions as expected from previous investigations (Treffene, 1983) and simulations (Grossman et al., 2017; Hunold et al., 2018b). The envelope maximum $\hat{\varphi}$ occurred in the vicinity to the stimulation electrodes in action. In contrast the envelope amplitude $\tilde{\varphi}$ provided more distinct topographies to the stimulation montages. The envelope amplitude $\tilde{\varphi}$ maximized in areas with equal contributions from both stimulation sources (Treffene, 1983). This led to rather distinct spots with maximal envelope amplitude for montages Opp and Trap and a nearly homogeneously pronounced envelope amplitude distribution for the Par montage.

Modifications in the source strength and in the stimulation montages resulted in topography changes as presented in Figure 4.7.

For asymmetric source strength, the position with the maximal envelope amplitude was shifted towards the stimulation electrodes adjacent to the weaker source. Especially, for the Par montage the asymmetric source strength disturbed the homogeneity in the source contributions and thus strongly affected the envelope amplitude characteristic. In the Trap montage, this modification led to a focus of the maximal envelope amplitude to a single measurement position in the present setup.

Wiring the stimulation electrodes to the current sources such that the current paths crossed (ParX, TrapX), led to focusing of the maximal envelope amplitude to positions which point-symmetrically localized to the current path intersection.

Stimulation of neuronal tissue with alternating currents in the range from 1 kHz to 100 kHz (also called middle-frequency) demonstrated a temporal summation effect in neurons, the so called 'Gildemeister Effekt' (Gildemeister, 1944). The subsequent positive and negative half-waves asymmetrically de- and re-polarized the neuronal cell membrane, eventually leading to the release of an action potential (Bromm and Lullies, 1966). However, continuous stimulation with such frequencies resulted in conduction blocks (Wedensky, 1903). To prevent the formation of conduction blocks, burst and amplitude modulated middle-frequency stimulations have been used in various applications as summarized by Ward (2009). In particular, the stimulation with two interfering alternating currents with frequencies in the range from 1 kHz to 100 kHz, which deviated by a difference frequency in the range from 1 Hz to 100 Hz was introduced as 'interferential therapy' to treat musculoskeletal conditions, e.g. controlling pain (Nemec, 1959). In clinical applications, both superimposing as well as modulated alternating currents with frequencies around 4 kHz recruited nerve fibers in extremities (Ozcan et al., 2004). However, this did not necessarily imply the existence of a demodulation mechanisms at the neuronal level (Grossman et al., 2017). Modeling studies suggest mechanisms of action for TI-tES on the neuronal level based on an interplay of tonic activity modulation and conduction blocks (Mirzakhilili

et al., 2020), and oscillation modulation in a canonical network model (Esmailpour et al., 2021).

The orientation of the interference in the target likely plays an essential role in the stimulation of neuronal tissue. Conventionally, the direction perpendicular to the local cortical surface is thought to be the most effective stimulation orientation. In the present study a consistent reference electrode at the bottom of the aquarium provided a fix point in the potential difference measurements. Therefore, global topographies of interference features were provided here. Local orientations of the effective interference stimulation were not considered.

The temporal properties demonstrated in this study realistically reproduced the generation of the interference and the derived envelope features. However, the initial stimulation frequencies of 643 Hz and 653 Hz might induce direct stimulation effects in neuronal tissue also generating intrinsic activity with 600 Hz (Haueisen et al., 2001). Thus these frequencies below 1 kHz are considered unsuitable for application in stimulation of neuronal tissue. Two independent constant current sources were used as stimulation generators, which ensured the desired current intensity at the stimulation electrodes. Although the same type of stimulation electrodes were wired and placed in the same way, identical conditions could not be guaranteed. In case of different electrode or electrode–electrolyte impedance, the voltage regulation in the current sources resulted in varying potential differences between the stimulation electrodes of the two stimulation channels. Such a discrepancy between stimulation channels led to asymmetries in the topographies of the signal features.

The technical equipment enabled the performance of TI-tES as suggested by Grossman et al. (2017). Applying asymmetric source strength and adapted current paths resulted in expected modification of the generated stimulation pattern as observable in a homogeneous volume conductor.

4.2 TES applied to a head phantom

4.2.1 Introduction

Stimulation schemes for tES require methodologies for verification when facilitating new electrode montages (cf. chapter 2), more complex waveforms (e.g. amplitude modulation or temporal interference), and new application systems (cf. chapter 3). Technical feasibility of stimulation concepts and electrode materials were tested in homogeneous electrolyte volume conductors (cf. sections 3.2 and 4.1). These metrological inspections allowed the inclusion of certain aspects of real-world environmental influences and provided information on the technical feasibility of the concepts under test.

However, new tES schemes require exact knowledge about the spread of the electromagnetic field inside the head, and the interactions between new application systems and the head. These aspects require knowledge about the volume conductor, i.e. the conductivity profile within the human head. Computer models of the volume conductor derived from human MRI data and parameterized with conductivity values from literature incorporate essential uncertainties regarding the conductivity configuration (McCann et al., 2019). Within a physical head phantom, a large part of the uncertainties regarding the conductivity geometry can be overcome. The geometry of a phantom is predefined by its design and manufacturing processes, and the conductivity properties of the phantom materials can be measured in advance.

Considering the human head as a volume conductor, the skull provides the major conductivity barrier. Consequently, three conductivity compartments are of particular interest: scalp (soft tissue outside of the skull), skull, and intracranial volume (Stenroos et al., 2014). The soft tissue compartments with higher conductivity encase the skull compartment with low conductivity. A widely used conductivity value for intracranial volume is 0.33 S/m (Geddes and Baker, 1967). According to literature, the ratios for the skull-to-soft tissue conductivity ranges from 1:120 (Homma et al., 1995) to 1:5 (Wendel et al., 2008).

Previous approaches established head phantoms based on doped saline solutions for the verification of tES simulations (Jung et al., 2013; Kim et al., 2015). These phantoms incorporated saline solutions with different electrolyte concentrations to obtain different conductivity values. Interfacing multiple compartments based on different saline solutions introduces concentration gradients leading to diffusion processes. The time-dependent electrolyte diffusion limits the stability of the relevant conductivity configurations in such phantoms.

Here a multi-compartmental and realistically shaped physical head phantom is presented, which is implemented by synthetic materials with inherently different conductivity values. The phantom is used for verification of different tES schemes administered by application systems introduced in chapter 3.

Parts of this chapter have been previously presented in abstract form (Hauelsen and Hunold, 2017) and in journal publications (Hunold et al., 2018c, 2020b).

4.2.2 Material and Methods

The phantom design was based on the geometry of a human head. A computer tomography (CT) data set of a 51 years old male obtained on a Lightspeed VCT (GE Healthcare, Chicago, USA) with 0.625 mm slice thickness and an isotropic inplane resolution of 0.492 mm served as data base (Hunold et al., 2019). The CT images were segmented in Seg3D (<http://www.sci.utah.edu/cibc-software/seg3d.html>), using Otsu thresholds to reconstruct compartments of the inner skull volume, the skull and the scalp, as shown in Figure 4.9.

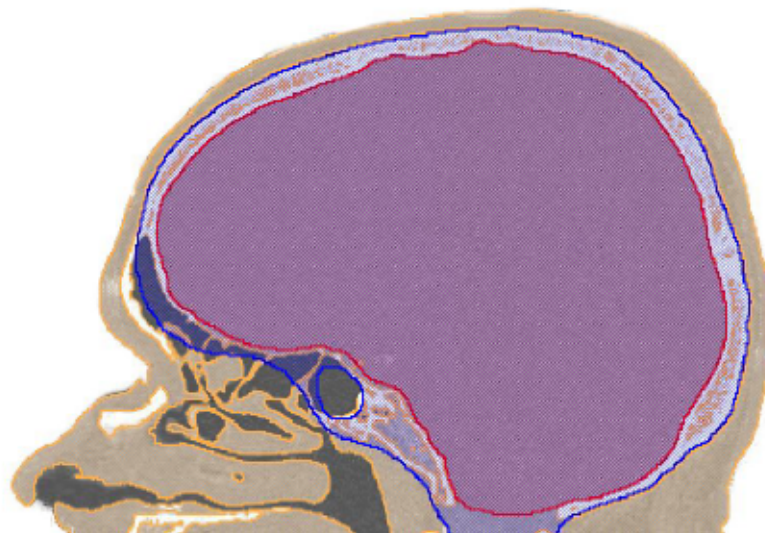


Figure 4.9: Segmented CT image with labeled intracranial (red), skull (blue) and scalp (orange) compartments.

Representations of the outer surfaces of these compartments were imported to a computer aided design (CAD) software (SolidWorks, Dassault Systèmes SolidWorks Corporation, Waltham, USA).

A solid body of the skull compartment was created based on the surface representations of the inner and outer skull. An oval cylinder with inner axis length of 80 mm in anterior-posterior and 110 mm in lateral direction, and a thickness of 10 mm extended the skull base as an artificial neck.

The outer contour of the scalp compartment ended on a circle with a diameter of 200 mm. A common ground plate was constructed to hold the oval neck and the round end of the

scalp compartment on its top. The ground plate also accommodated an oval base plate inserted from the bottom. This base plate held modular parts for interior structures, such as the 3D measurement array introduced in section 4.1.2. The oval shape of the neck and the base plate ensured anti-twisting and form-fit, the frictional connections were designed as adhesive (neck – ground plate) and screw (base plate – ground plate) connections. Both, ground and base plates, had funnel-shaped surfaces and contained holes for filling and venting, which were closed with plugs. Figure 4.10 depicts the phantom design with two cavities: the scalp compartment and the intracranial volume.

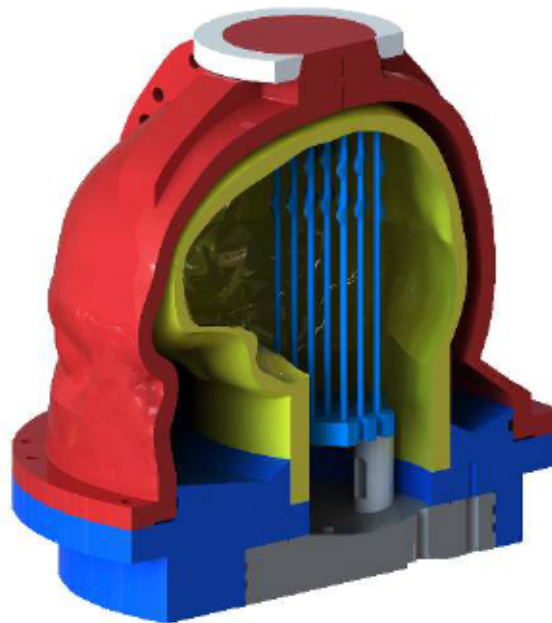


Figure 4.10: Phantom CAD model with ground plate (dark blue), skull compartment (yellow), casting mold for the scalp layer (red), base plate (gray) and measurement array (cyan).

Casting molds for the skull and scalp compartments were constructed based on the outer skull, the inner skull and the outer skin boundaries.

The inner skull mold was derived from the inner skull boundary and the neck extension. Therefore, the inner skull boundary was thickened 8 mm towards the inside. At the neck, the inner skull mold incorporated an orthogonal bracing (15 mm x 15 mm) along the oval main axis, which exceeded the mold for 20 mm. The exterior skull mold held the bracing of the inner skull mold and represented the outer skull boundary with three parts: lower anterior and posterior parts separated along the main axis of the oval neck, and one superior part covering the calvaria. The mold parts were extended with a brim, which incorporated through holes for screws realizing frictional connection. Figure 4.12a depicts the CAD model of the skull molds.

The scalp mold was a 5-mm thick representation of the outer skin boundary separated in an anterior and a posterior part and extended with a brim at the lower end, and at the separation section. The brim incorporated through holes for screws and dowel pins, which realized separate form and frictional connection between the two mold parts as well as between the mold parts and the ground plate. The scalp design was based on the above described skull as interior bounding structure.

The casting molds were additively manufactured with different 3D printing techniques and materials. The scalp mold was created of a liquide photopolymer (R5, envsiontec GmbH, Gladbeck, Germany) cured in ultraviolet light in a digital light processing (DLP) printer (P4K, envsiontec GmbH, Gladbeck, Germany) at the Physikalisch Technische Bundesanstalt (PTB) Berlin administered by Dirk Gutkelch. The skull molds were printed on a FDM printer (N2 Plus, Raise 3D Technologies Inc., Irvine, USA). The outer skull mold consists of Acrylnitril-Butadien-Styrol (ABS) (Verbatim GmbH, Eschborn, Germany), whereat the surface was smoothed by acetone vapor deposition. The inner skull mold was printed of Filaflex with a Shore hardness of 82A (Recreus Industries S.L., Elda, Spain).

Castable and electrolyte conducting materials were selected and characterized, for realization of the three phantom compartments.

An electrolyte solution of NaCl (Sodium chloride ≥ 99 %, Carl Roth GmbH & Co. KG, Karlsruhe, Germany) in de-ionized water provided the charge carriers in the head phantom. The conductivity of the NaCl solution was tested with a conductivity meter ProfiLine Cond 3310 (Xylem Analytics Germany Sales GmbH & Co. KG, Weilheim, Germany).

For the scalp layer, 2 wt% agarose (Agarose Broad Range, Carl Roth GmbH + Co. KG, Karlsruhe, Germany) was applied as a solidifying agent in the 0.17 % NaCl solution. The agarose was added to the heated electrolyte solution (65 °C) under constant steering. The milky dispersion was heated to about 80 °C until a clear solution emerged. The agarose electrolyte solution was kept in liquid state, at around 65 °C, until poured in the casting mold. After cooling to room temperature, the agarose electrolyte solution formed a mechanically stable hydrogel.

To mold a realistically shaped and mechanically durable skull compartment, gypsum powder (Stewaform, Glorex GmbH, Rheinfeldern, Germany) was selected to prepare a casting compound. In gypsum, the solid crystal embodies a structural conductivity barrier. The Stewaform powder was mixed with 0.17 % NaCl solution in the ratio of 2:1 to form a casting compound. The casting compound was poured in negative molds of the desired form, and let dry at 40 °C for 2 h. To protect the gypsum structures from dissolving when coming in contact with the aqueous NaCl solutions, the gypsum was infiltrated for one minute in a two-component epoxy resin XTC-3D (Smooth-On Inc., Macungie, PA, USA) with a ratio of 2:1 (epoxy resin:hardener). The infiltrated gypsum was dried again at 40 °C for 10 min.

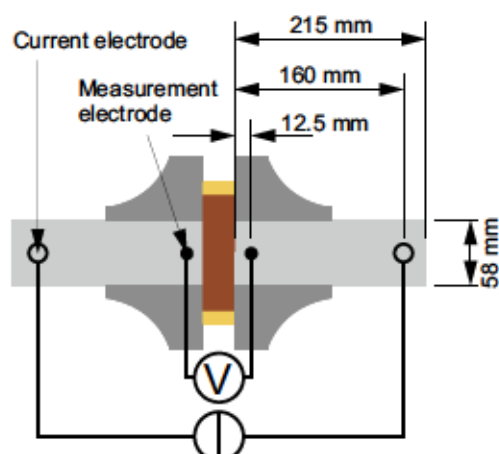


Figure 4.11: Scheme of the impedance measurement setup. The measurement cell with a material sample (brown) in plastic tubes filled with NaCl solution (light gray) incorporates the paired measurement electrodes (black dots) and the outer electrode pair (black circles) for current application, both being connected to the Gamry Reference 600 Plus impedance analyzer. A sealing ring (yellow) and POM flanges (dark gray) complete the setup. Adapted from Hunold et al. (2018c, 2020b).

Electrical properties of material samples were tested by means of four-electrode impedance measurements (Schwan and Ferris, 1968) at room temperature. An impedance analyzer (Reference 600 Plus, Gamry Instruments, Warminster, PA, USA) measured the impedance of the measurement cell comprising of the material sample clamped between two NaCl solution compartments with a concentration of 0.17 % NaCl in de-ionized water as depicted in Figure 4.11.

The NaCl solution compartments held an outer pair of silver/silver-chloride lens electrodes (diameter 4 mm) with a distance of 160 mm to the sample for impressing an electric current, and an inner pair of silver/silver-chloride pellet electrodes (1.5 mm diameter, 3 mm length) for measuring the resulting potential difference. A more detailed description of the setup can be found in (Hunold et al., 2018c, 2020b).

The impedance was tested for three samples of 0.17 % NaCl solution (NC1, NC2, NC3), agar hydrogel with 2 wt% agarose (AH1, AH2, AH3), and one sample of gypsum (GNC1). The gypsum sample was tested three times in this procedure after it has been drying at ambient air for at least 20 h. Each series of measurements were carried out over the frequencies of 0.1 Hz to 100 kHz and for 10 min at 1 Hz. There was a 30-min pause between each series of measurements.

Further, three samples of agar hydrogel with 2 wt% agarose (AH4, AH5, AH6) and three samples of gypsum (GNC2, GNC3, GNC4) were tested on an extended frequency range of 0.01 Hz to 100 kHz and for an extended duration of 60 min at 10 Hz. The agar hydrogel

samples (AH4, AH5, AH6) where tested three times with a 6-h pause between each series of measurements.

Simultaneous to measuring the impedances, the temperature in the cell was measured with an electrically insulated stainless steel probe connected to a Traceable[®] Excursion-Trac (VWR International bvba, Leuven, Belgium).

The experimental measurements were carried out at ambient temperatures. To compare to existing literature values, the measured values were adjusted for the temperature difference. First, the impedance of the cell containing only NaCl solution, Z_{NaCl} , was measured to use as the reference. The impedance can then be adjusted using

$$Z_{25} = \frac{Z_{meas} - Z_{25}}{1 + \alpha \cdot (\vartheta_{meas} - 25)}, \quad (4.3)$$

where Z_{25} is the impedance adjusted to 25 °C, Z_{meas} is the measured impedance, ϑ_{meas} in °C is the temperature at the time of measurement, and α is the linear factor (also called cell constant). The cell constant was determined through measurements of a cell containing 0.17 % NaCl solution only. The material conductivity is computed from the temperature-compensated net impedance Z_{25} using

$$\kappa = \frac{d}{Z_{25} \cdot A}, \quad (4.4)$$

where d is the material sample thickness and A is the surface area.

The characterized materials were utilized to manufacture the head phantom compartments in a multistage procedure.

First the skull of gypsum (Stewaform dispersed in 0.17 % NaCl solution) was cast in the negative skull molds described above. The exterior molds were opened after 3 h to let the gypsum dry at ambient air. One day after casting, the exterior and interior molds were removed. The hollow body of the skull was infiltrated with epoxy resin XTC-3D (Smooth-On Inc., Macungie, PA, USA) in a ratio of 2:1 (epoxy resin:hardener). The infiltrated gypsum was dried again at 40 °C for 10 min.

The finished skull was glued into the oval recess on the upper side of the ground plate. Figure 4.12 depicts stages of the skull manufacturing.

Second, the scalp was cast onto the skull compartment in the ground plate. Therefore, the scalp molds were fixated on the ground plate, which established the cavity for the scalp compartment (Figure 4.13a). The phantom was turned upside down (Figure 4.13b), for the casting process with the hot agar (2 wt% agarose in 0.17 % NaCl solution). The agar jellified while it cooled at ambient air for at least 12 h.

Third, the intracranial volume was filled with 0.17 % NaCl solution.

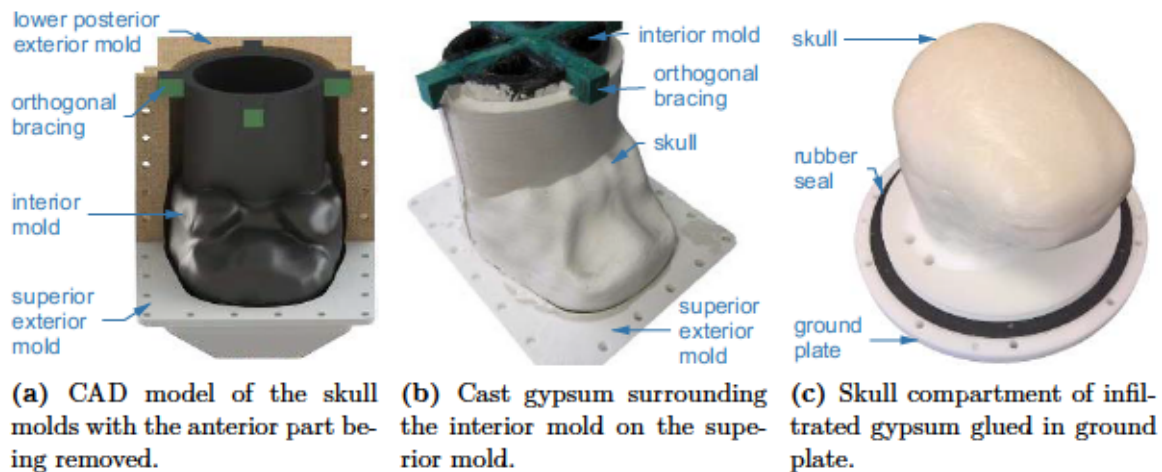


Figure 4.12: Stages of skull manufacturing procedure. (a) Skull molds: black interior mold with orthogonal bracing (green), posterior part (beige), and superior part (white) of the exterior molds, the anterior mold was removed to look inside. (b) Gypsum skull with interior mold inside and superior part of the exterior mold underneath. (c) Extracted and infiltrated skull in view from diagonally above. The black ring is a rubber seal.

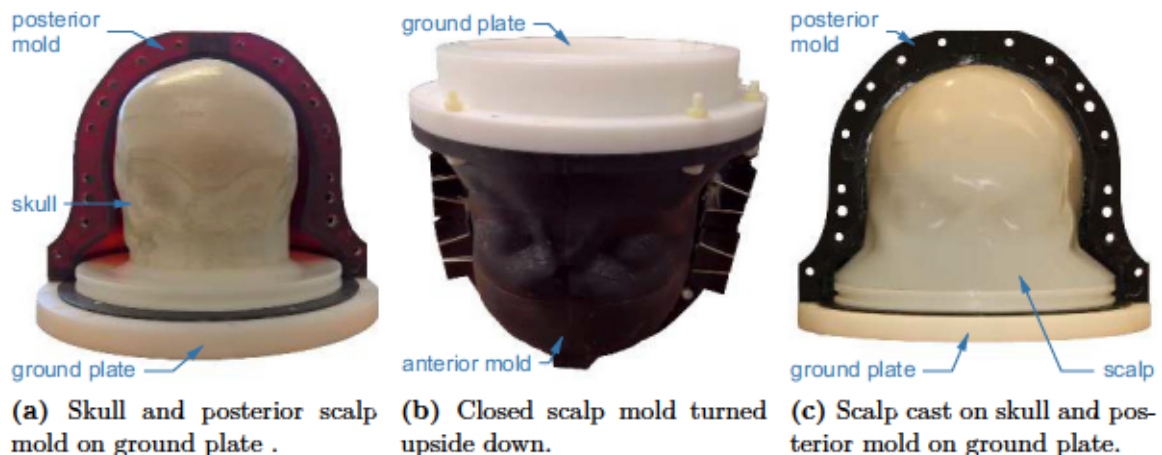


Figure 4.13: Stages of scalp manufacturing procedure. (a) Skull glued in ground plate and posterior mold (red) without the anterior mold showing the cavity for the casting process. (b) Closed scalp molds turned upside down for casting. (c) Anterior mold removed showing cast scalp. The black ring is a rubber seal.

Fourth, the measurement array, which was attached to the base plate, was inserted in the intracranial volume and the base plate sealed the phantom.

Finally, the phantom was turned upright and the scalp molds were removed (Figure 4.13c). The resulting phantom was ready for use in experimental procedures (Figure 4.14).



Figure 4.14: Finished phantom in upright position on ground plate with scalp (semi-transparent) on skull (white). The black ring is a sealing used in scalp casting.

Rubber electrodes of $4\text{ cm} \times 4\text{ cm}$, textile stimulation electrodes of $4\text{ cm} \times 4\text{ cm}$ integrated in a textile cap (cf. section 3.1), and circular multi-pin dry electrodes with a diameter of 2 cm (cf. section 3.2) were subsequently placed at positions F3, F4, P3, and P4, according to the international 10–20 system (Jasper, 1958; Klem et al., 1999). Electrodes F3/P3 and F4/P4 were connected to anode/cathode sockets of Source 1 and Source 2 of a DC-STIMULATOR MC (neuroConn GmbH, Ilmenau, Germany). Figure 4.15 depicts the stimulation and measurement setup.

The two isolated current sources provided sinusoidal waves with an amplitude (peak-to-peak) of 2 mApp , 4 mApp , or 8 mApp at frequencies of 1 Hz , 10 Hz , or 100 Hz for tACS stimulation. An amplitude modulated signal

$$u_{AM}(t) = \hat{a}_c \cdot \sin(2 \cdot \pi \cdot f_c \cdot t) \cdot (1 + \hat{a}_m \cdot \sin(2 \cdot \pi \cdot f_m \cdot t)), \quad (4.5)$$

with the carrier amplitude \hat{a}_c of 1 mApp , the carrier frequency f_c of 653 Hz , the modulator amplitude \hat{a}_m of 1 mApp , and the modulator frequency f_m of 10 Hz , was predefined as binary file signal and loaded onto the stimulator. For amplitude modulated tES (AM-tES), this signal was provided by Source 1 and Source 2. For TI-tES with a difference frequency of 10 Hz , Source 1 and Source 2 provided sinusoidal waves with an amplitude of 2 mApp and frequencies of $f_1 = 643\text{ Hz}$ and $f_2 = 653\text{ Hz}$, respectively.

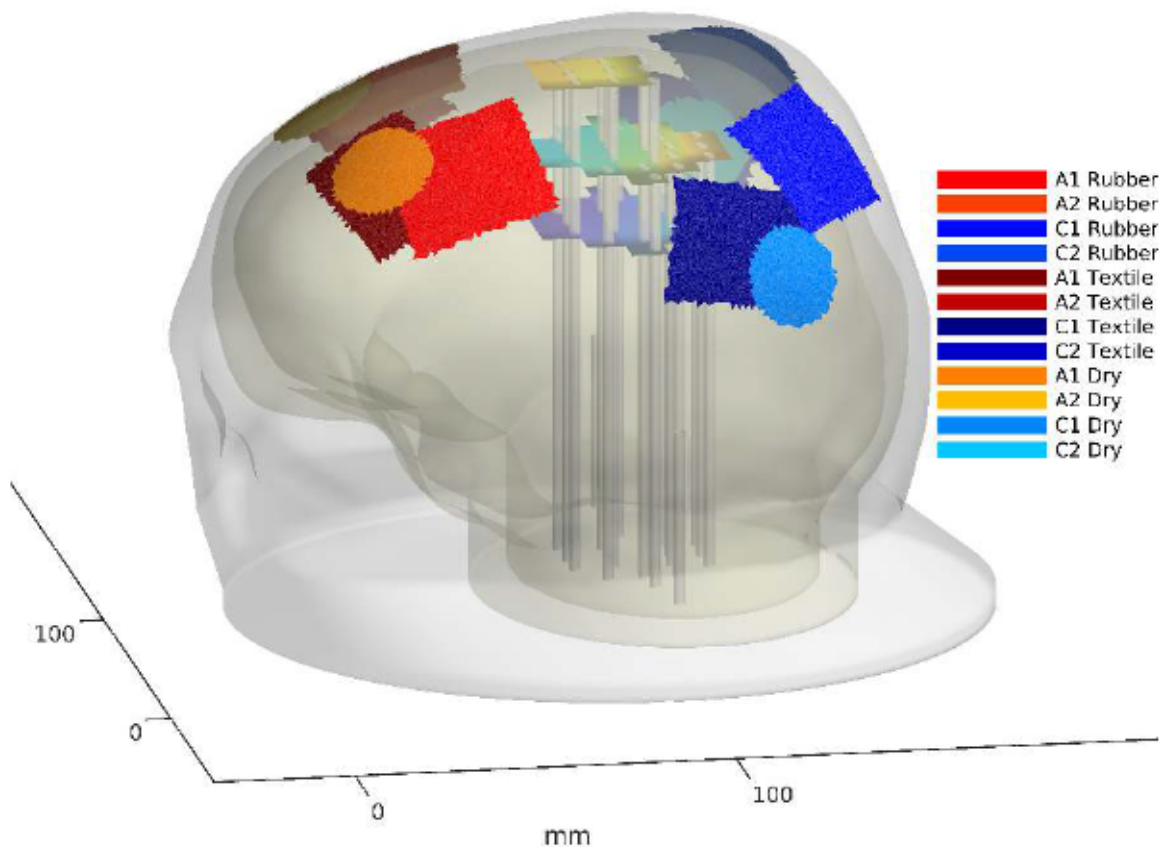


Figure 4.15: Model of the head phantom represented by the transparent surfaces of the three compartments with the 3D measurement array (cf. Figure 4.2b) inside and color coded tES electrodes of labeled materials mapped on the triangulated scalp surface. Scalp surface triangulation lead to ragged electrode edges. Labels A and C refer to electrodes connected to the anode and cathode sockets and numbers 1 and 2 decode current Sources 1 and 2.

Measurements incorporated active stimulation with 5 s fade-in, 60 s constant current, and 5 s fade out, followed by at least ten seconds noise recording. Signal processing, analysis and visualization was performed in Matlab (The Mathworks Inc., Natick, USA). Recorded data were offset corrected by subtraction of the mean of 10 s noise data per channel. The data from the central twenty-seconds during the constant stimulation were bidirectionally filtered by finite impulse response filters. The filters had characteristics of a low-pass up to 3 Hz for 1 Hz stimulation, a band-pass between 7 Hz and 13 Hz for 10 Hz stimulation, a band-pass between 97 Hz and 103 Hz for 100 Hz stimulation, and a band-pass between 640 Hz and 666 Hz for stimulation with 643 Hz, 653 Hz or the amplitude modulated signal. Five segments of the filtered data were averaged with a duration of 3 s each. Data segments were channel-wise averaged and transferred to frequency domain by discrete Fourier transform.

In case of AM- or TI-tES, an envelope was reconstructed to the averaged signal. The envelope was calculated as the magnitude of the analytic signal, based on the Hilbert transform (Lawrence Marple, 1999). A spectral analysis was performed for the averaged signal and the envelope. Segments with a 200-ms duration of envelopes and averaged signals were used for further analysis. Phase differences between channels were derived from the complex spectra of the envelopes with respect to the reference channel providing the highest absolute signal value.

The maximum $\hat{\varphi}$ and the amplitude $\tilde{\varphi}$ of the envelope were used to describe signal features, as introduced in Figure 4.5a of section 4.1.2.

Amplitude differences and topographies of the envelope features extracted from AM- and TI-tES were compared based on the MAG_{rel} (equation 4.2) and the RDM^* (equation 4.1).

4.2.3 Results

The 0.17 % NaCl solution provided conductivities of $0.299 \text{ S/m} \pm 0.005 \text{ S/m}$ (mean $\mu \pm$ standard deviation σ) on the ProfiLine Cond 3310 (0.5 % uncertainty) at temperatures of $20.04 \text{ }^\circ\text{C} \pm 0.70 \text{ }^\circ\text{C}$. With temperature compensation to $25 \text{ }^\circ\text{C}$ at the ProfiLine Cond 3310, conductivities of $0.333 \text{ S/m} \pm 0.001 \text{ S/m}$ were measured in 0.17 % NaCl solutions, in line with previously published data (Lide, 2012). Considering an inner electrode distance of 25 mm and a tube diameter of 58 mm in the experimental setup (cf. Figure 4.11), the reference impedance of the 0.17 % NaCl solution was calculated from the conductivity to be $31.69 \text{ } \Omega$ at $20 \text{ }^\circ\text{C}$ and $28.45 \text{ } \Omega$ at $25 \text{ }^\circ\text{C}$ (Z_{25ref}). The measured impedance of the reference 0.17 % NaCl solutions in the four-electrode setup was $31.41 \text{ } \Omega \pm 0.14 \text{ } \Omega$ (Z_{meas}) which resulted in a conductivity value of $0.301 \text{ S/m} \pm 0.002 \text{ S/m}$ (cf. equation 4.4). During these measurements, the temperature in the 0.17 % NaCl solutions was $21.04 \text{ }^\circ\text{C} \pm 0.18 \text{ }^\circ\text{C}$ (ϑ_{meas}). The cell constant α for the four-electrode setup was determined to -0.026 . The cell constant was calculated from equation 4.3 using Z_{25ref} , Z_{meas} and ϑ_{meas} from the impedance measurements with only 0.17 % NaCl solution in the cell.

After applying equation 4.3 to adjust for the differences in the temperature at the time of measurement, the impedance of 0.17 % NaCl solution was equivalent of $28.39 \text{ } \Omega \pm 0.19 \text{ } \Omega$ at $25 \text{ }^\circ\text{C}$, which is a conductivity of $0.332 \pm 0.003 \text{ S/m}$. These values were found to be consistent for frequencies of 0.1 Hz to 100 kHz (Figure 4.16 top) and at 1 Hz over 10 min (Figure 4.16 bottom).

The 2 wt% agar hydrogel in 0.17 % NaCl solution ($n = 6$) has a conductivity of $0.277 \text{ S/m} \pm 0.008 \text{ S/m}$ at a temperature of $20.82 \text{ }^\circ\text{C} \pm 0.18 \text{ }^\circ\text{C}$, equivalent of $0.308 \text{ S/m} \pm 0.008 \text{ S/m}$ at $25 \text{ }^\circ\text{C}$ (adjusted using equation 4.3). These values were found to be consistent for frequencies of 0.1 Hz to 100 kHz (Figure 4.17a top) and at 1 Hz over 10 min (Figure 4.17a bottom) as well as for the extended frequency range of 0.01 Hz to 100 kHz (Figure 4.17b top) and for the extended duration of 60 min at 10 Hz (Figure 4.17b bottom).

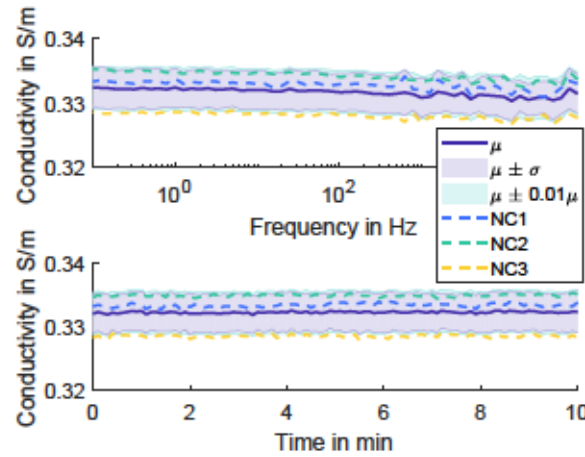


Figure 4.16: The average conductivity data ($n = 3$) at 25 °C of 0.17 % NaCl solution for 0.1 Hz to 100 kHz (top) and at 1 Hz for 10 min (bottom). The dashed lines show the average for each sample taken over three series of measurements with 30 min in between. The shaded regions show $\mu \pm \sigma$ (purple) and $\mu \pm 0.01\mu$ (green) for comparison.

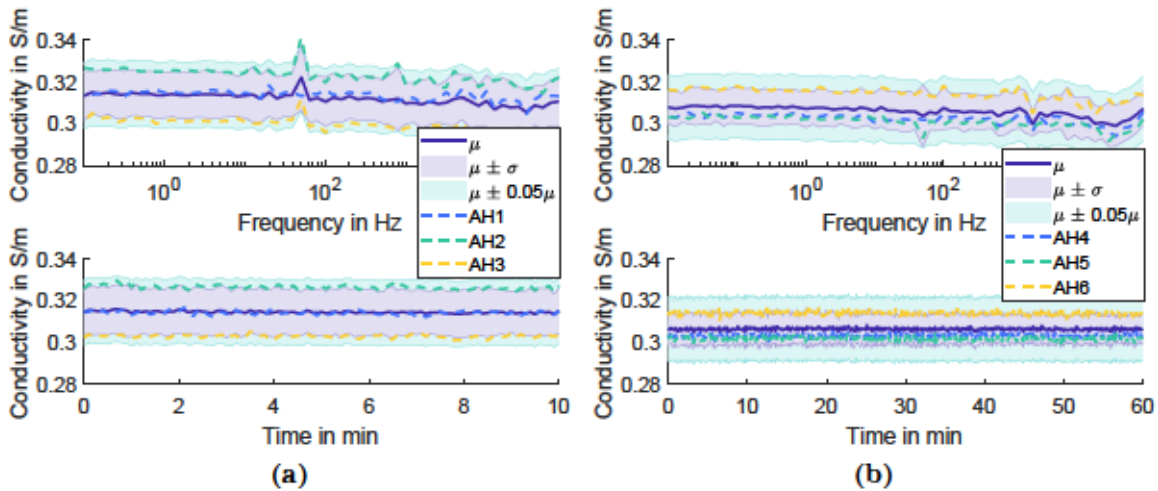


Figure 4.17: The average conductivity of 2 wt% agar samples in 0.17 % NaCl solution adjusted to 25 °C. (a) The conductivity of three samples (colored dashed lines for AH1, AH2, AH3) each averaged over three series of measurements with frequencies of 0.1 Hz to 100 kHz (top) and 1 Hz for 10 min (bottom), with 30 min in between series of measurements. (b) The conductivity of three samples (colored dashed lines for AH4, AH5, AH6) each averaged over three series of measurements with frequencies of 0.01 Hz to 100 kHz (top) and 10 Hz for 60 min (bottom), with 6 h in between series of measurements. The shaded regions show $\mu \pm \sigma$ (purple) and $\mu \pm 0.05\mu$ (green) for comparison.

Even though measurements were conducted in a grounded Faraday cage, the spike at 50 Hz in the spectra (cf. Figure 4.17 top) was likely due to power-line interference.

Three series of measurements were made on one sample of Stewaform gypsum with letting the sample rest in ambient air for 20 h between series of measurement (cf. Figure 4.18a). This gypsum sample has a conductivity of $0.037 \text{ S/m} \pm 0.001 \text{ S/m}$ at $18.85 \text{ }^\circ\text{C} \pm 0.19 \text{ }^\circ\text{C}$, which is equivalent of $0.043 \text{ S/m} \pm 0.002 \text{ S/m}$ at $25 \text{ }^\circ\text{C}$ (adjusted using equation 4.3). Three samples of gypsum were tested for an extended frequency range of 0.01 Hz to 100 kHz (cf. Figure 4.18b top) and duration of 60 min at 10 Hz (cf. Figure 4.18b bottom). The conductivity was found to stay consistent in this extended range, with $0.037 \text{ S/m} \pm 0.002 \text{ S/m}$ at $19.75 \text{ }^\circ\text{C} \pm 0.26 \text{ }^\circ\text{C}$, equivalent of $0.042 \text{ S/m} \pm 0.003 \text{ S/m}$ at $25 \text{ }^\circ\text{C}$ (adjusted using equation 4.3).

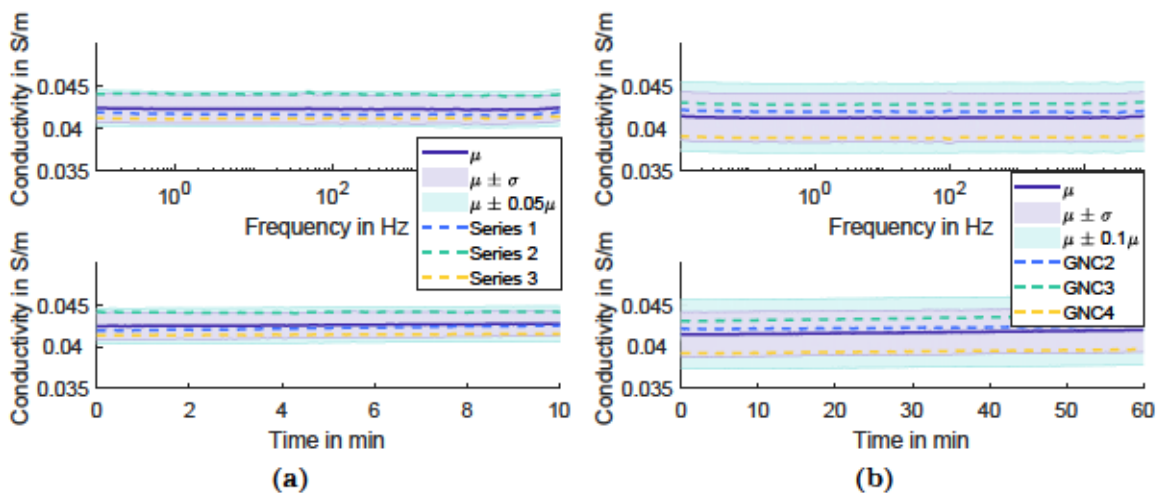


Figure 4.18: The average conductivity of the gypsum samples in 0.17 % NaCl solution adjusted to 25 °C. (a) The conductivity of one sample (GNC1) averaged over three series of measurements (colored dashed lines) with frequencies of 0.1 Hz to 100 kHz (top) and 1 Hz for 10 min (bottom), with 20 h in between series of measurements. (b) The average conductivity of three samples (colored dashed lines for GNC2, GNC3, GNC4) from series of measurements with frequencies of 0.01 Hz to 100 kHz (top) and 10 Hz for 60 min (bottom). The shaded regions show $\mu \pm \sigma$ (purple) and (a) $\mu \pm 0.05\mu$, (b) $\mu \pm 0.1\mu$ (green) for comparison.

The recordings of the electric potential from tACS with 1 Hz, 10 Hz, and 100 Hz administered with rubber, textile, and dry electrodes contained sinusoidal time traces as depicted in Figure 4.19. The two active sources with a current intensity of 2 mA were connected to the electrode pairs at F3/P3 and F4/P4.

Since the stimulation electrode size was different and their positions varied as depicted in Figure 4.15, channel amplitudes across application systems were in the same range but varied in direct channel comparison. Time traces in Figure 4.19 which depict three

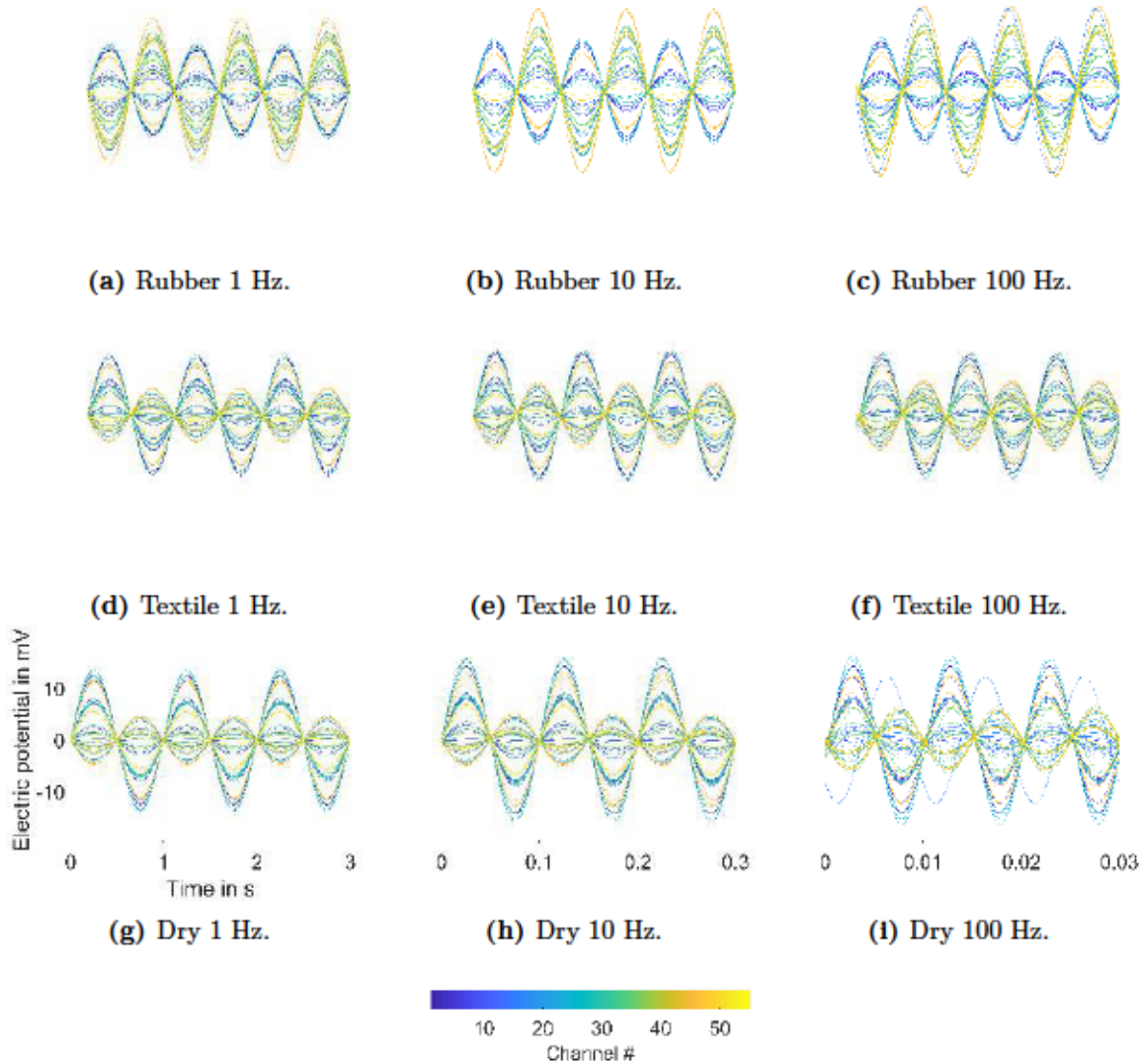


Figure 4.19: Sinusoidal time traces of electric potentials recorded from the 3D measurement array inside the phantom for stimulations with 1 Hz, 10 Hz, and 100 Hz administered with rubber, textile, and dry stimulation electrode pairs approximately positioned at F3/P3 and F4/P4 as depicted in Figure 4.15. Colors code channel numbers as introduces in Figure 4.2b. Channel 1 is located on the right side of the frontal row on the inferior level 1. Channels 9 and 15 are the right and left lateral electrodes in the central row of level 1. Channel 23 is at the left position in the posterior row on the inferior level 1. The central level 2 starts with channel 24 at the right frontal position. Channels 32 and 38 are the right and left lateral electrodes in the central row of level 2. Channel 46 is at the left position in the posterior row on the central level 2. The superior level 3 starts with channel 47 at the right frontal position. Channel 50 is at the right position of the intermediate row of level 3. Channel 55 is at the left position in the posterior row of level 3.

sinusoidal periods on different time scales reflecting the dominant frequencies. Especially for 100 Hz stimulations, up to five channels (cf. Figure 4.19i) revealed considerable phase shifts.

Figure 4.20 shows the distributions of the maximal amplitudes per channel for a more direct comparison of different stimulation frequencies and current intensities. Consistently, stimulations with 1 Hz generated the lowest amplitudes for all stimulation setups. The increase of the mean value of the distributions in Figure 4.20a was 8.3 % (1 Hz – 10 Hz) and 2.9 % (10 Hz – 100 Hz) for stimulations with rubber electrodes, and 11.5 % (1 Hz – 10 Hz) and 6.3 % (10 Hz – 100 Hz) for stimulations with dry electrodes. These indicated trends for increasing amplitudes with increasing stimulation frequencies. Stimulations with textile electrodes resulted in the absolute lowest amplitudes. For these stimulation electrodes, the distributions in Figure 4.20a showed no consistent trend of amplitude changes with stimulation frequencies as the mean values changed with 9.6 % (1 Hz – 10 Hz) and -2 % (10 Hz – 100 Hz).

The measured electric potential amplitudes reflected changes of the applied stimulation intensity as depicted in Figure 4.20b. A doubling of the stimulation intensity gave rise to an increase in the averaged amplitudes by a factor of 2.0 for all stimulation setups.

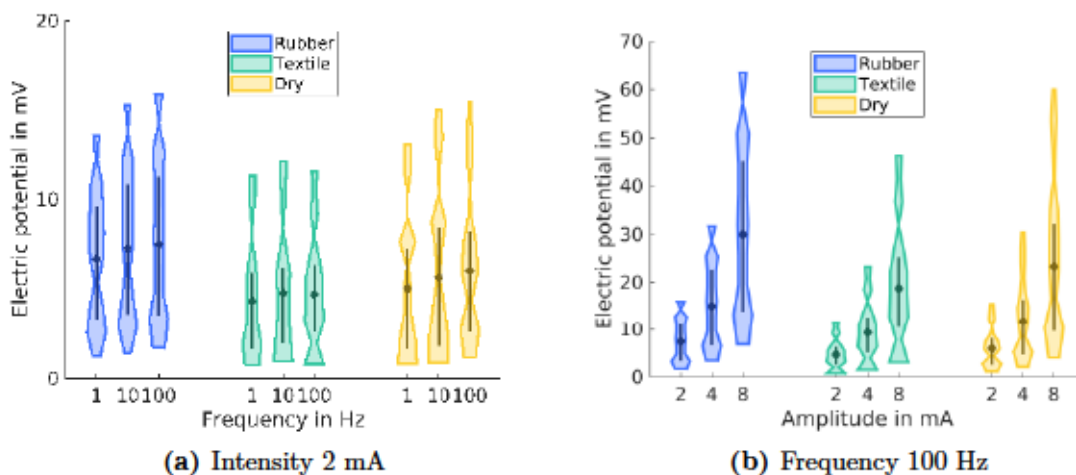


Figure 4.20: Frequency and amplitude characterization for stimulation frequencies 1 Hz, 10 Hz, and 100 Hz (a) and stimulation intensities 2 mA, 4 mA, and 8 mA (b). Distributions (shaded areas) of maximal amplitudes per channel for the application systems of (color-coded) rubber, textile and dry stimulation electrodes, with mean values (diamonds) and interquartile ranges (vertical lines).

More complex stimulation patterns were elaborated by means of amplitude modulated (AM) and temporal interference (TI) tES configurations. Figure 4.21 demonstrates the time traces and their spectral components of both, the measured electric potentials and their

envelopes for each channel. Figure 4.22 depicts the distinct stimulation and measurement configuration used in AM- and TI-tES experiments.

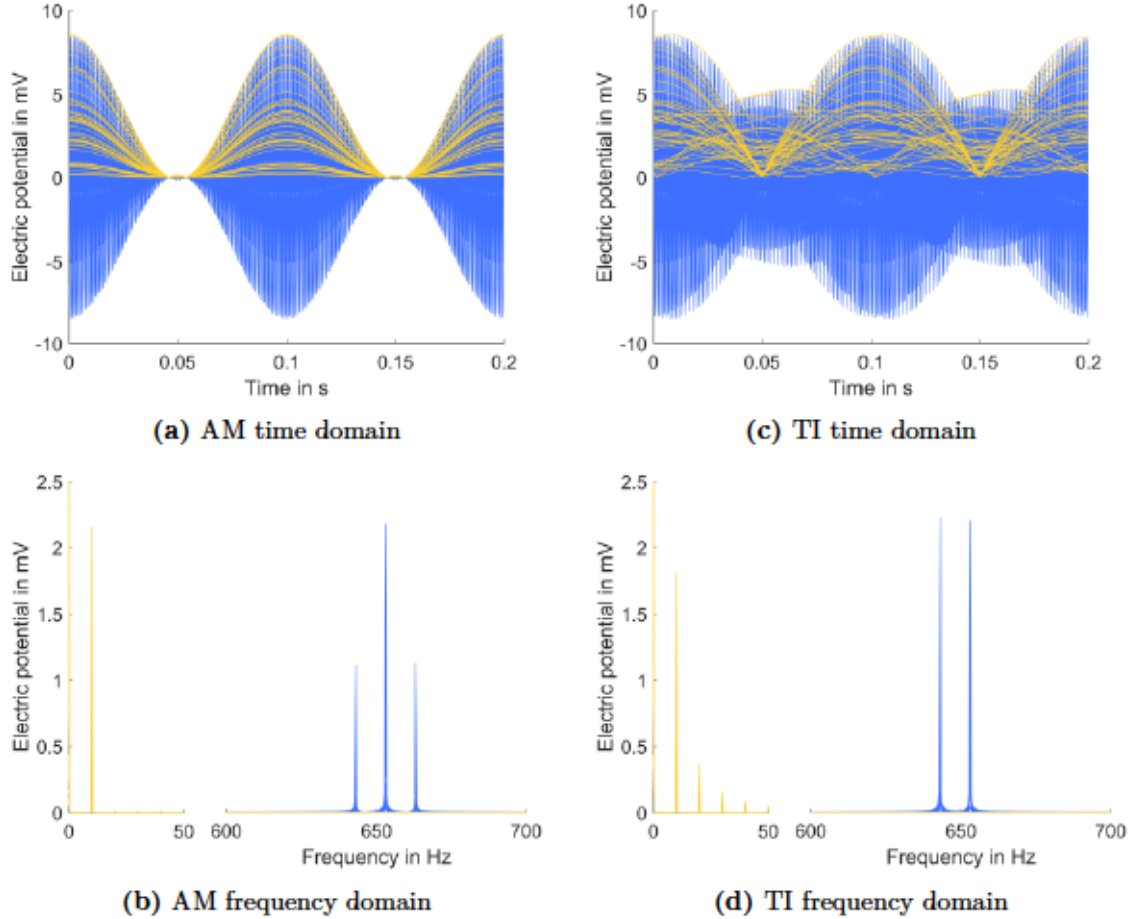


Figure 4.21: Electric potential traces (blue) and their signal envelopes (yellow) in time (top) and frequency domain (bottom) measured at the 55 electrodes inside the phantom during amplitude modulated (AM) (a,b) and temporal interference (TI) (c,d) tES applied with textile stimulation electrodes.

For AM-tES, electric potential waveforms appeared temporally aligned and reflected an electric potential distribution in different wave amplitudes (cf. Figure 4.21a). The recorded waveforms contained the carrier frequency of 653 Hz, and the side bands at 643 Hz and 663 Hz induced by the modulator frequency of 10 Hz. The signal envelopes revealed a single spectral component at the modulator frequency of 10 Hz (cf. Figure 4.21b). In contrast, the signal envelopes reconstructed to the TI-tES waveforms incorporated spectral components at the difference frequency of 10 Hz and its harmonics (cf. Figure 4.21d). The recorded potential waveforms from TI-tES contained the spectral components of the initial stimulation signals at 643 Hz and 653 Hz with an amplitude difference of 0.9 %. For

TI-tES, envelope waveforms revealed phase shifts larger than 10 degrees in 20 channels (up to 84.8 degrees, cf. Figure 4.21c).

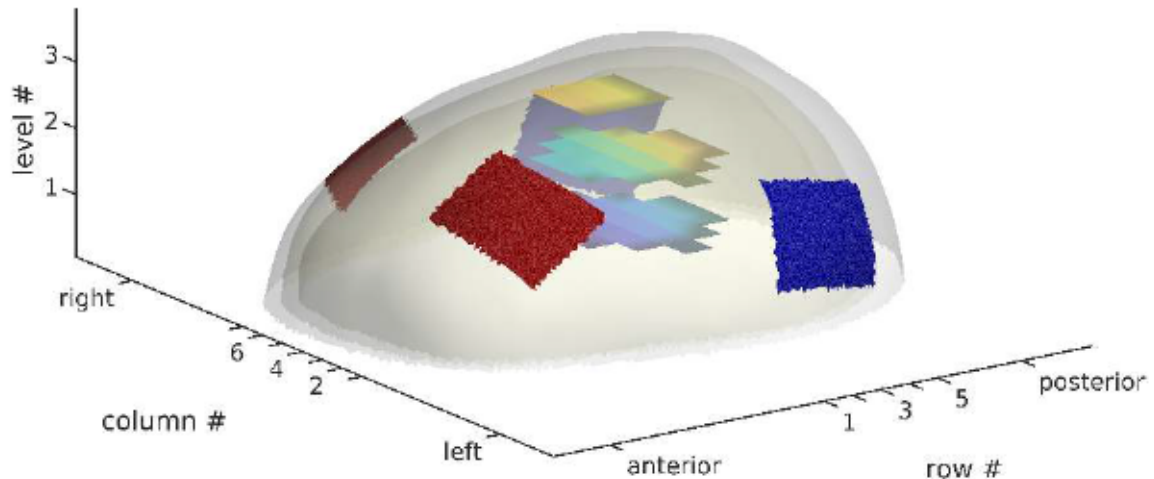


Figure 4.22: Model of the head phantom represented by the transparent surfaces of the three compartments with color coded surfaces representation of the 3D measurement array (cf. Figure 4.2b) and the textile tES electrodes as introduced in Figure 4.15 used to generate the results presented in Figures 4.21 and 4.23.

The spatial distributions of phase shifts between envelope waveforms of different recording channels are visualized in Figures 4.23a and 4.23d. Consistently, the AM envelope waveforms showed no phase differences. The spatial distribution of the phase differences between TI envelopes revealed phase differences in electrode rows 3 and 4, whereat off central electrodes in row 3 indicated a polarity reversal with phase differences up to 180 degrees.

Highest envelope maximum values $\hat{\varphi}$ were found in the anterior electrode row with smallest distances to the frontal stimulation electrodes (F3 and F4) and the electrode closest to the stimulation electrode at P4 (row 4, column 6, level 1), for both AM and TI stimulation (cf. Figures 4.23b and 4.23e). For AM stimulation, the most electrodes (columns 2 – 7) in the central row contained $\hat{\varphi}$ below 10 % of $\max(\hat{\varphi})$ indicating a zero-line with respect to the reference electrodes located in the same row. For TI stimulation, the minimum in $\hat{\varphi}$ with values below 10 % of $\max(\hat{\varphi})$ was limited to the very central electrodes (row 3, column 4) in levels 1 and 2.

Figures 4.23c and 4.23f demonstrate the spatial distribution of the envelope amplitude $\tilde{\varphi}$ with respect to the channels' $\hat{\varphi}$.

Within the AM stimulation, the $\tilde{\varphi}$ was inherently defined by the stimulation waveform and therefore expected to equal $\hat{\varphi}$ in every recording position. The maximal deviation between $\tilde{\varphi}$ and $\hat{\varphi}$ was 5.5 % in Figure 4.23c.

In TI stimulation, the ratio of $\tilde{\varphi}/\hat{\varphi}$ was maximal in positions with equal amplitude contri-

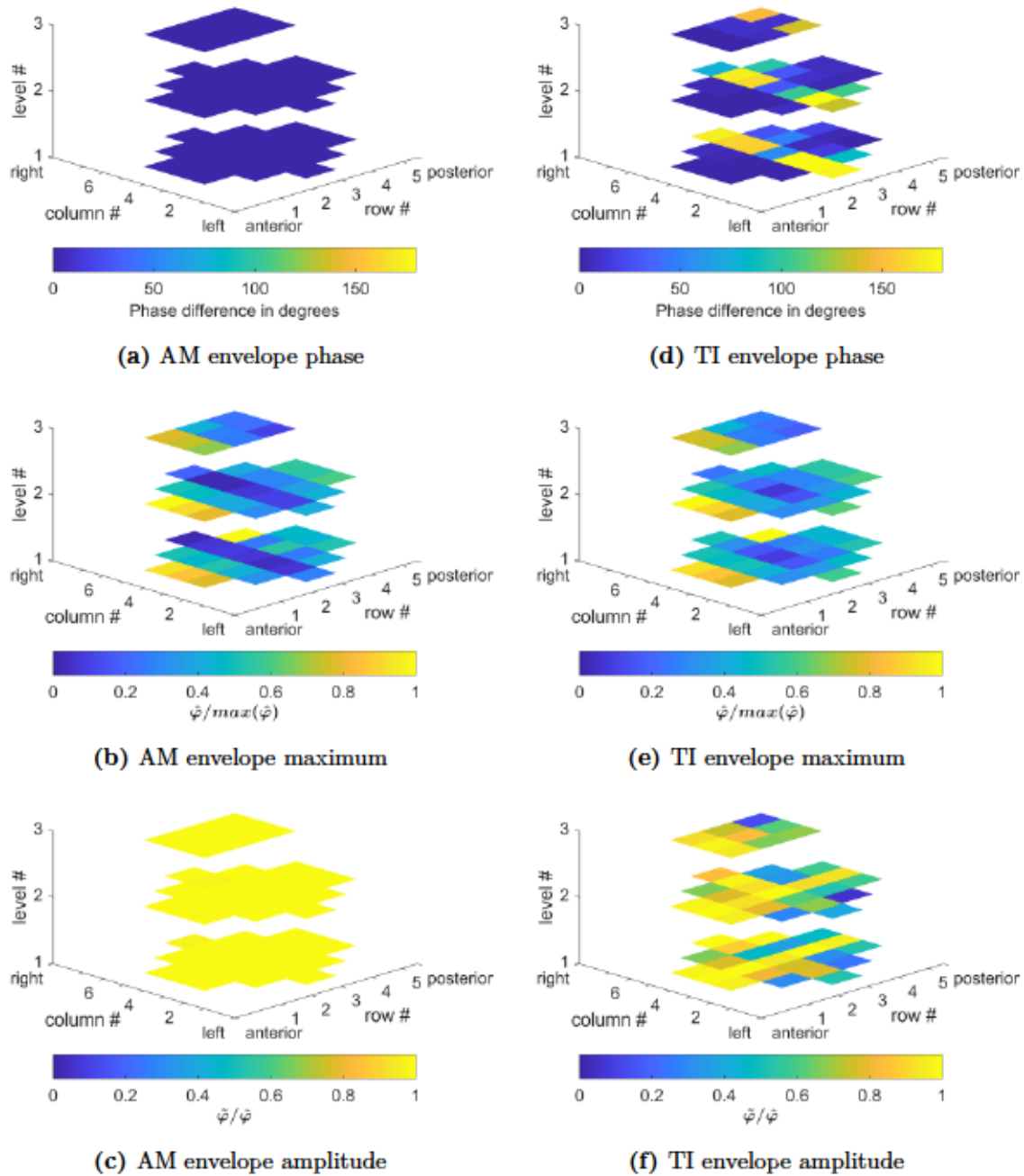


Figure 4.23: Spatial distribution of envelope parameters for amplitude modulated (AM) and temporal interference (TI) tES. Sub-figures color-code the phase difference between recording channels (a,d), the envelope maximum $\hat{\varphi}$ normalized to the total maximum $max(\hat{\varphi})$ (b,e) and the envelope amplitude $\tilde{\varphi}$ normalized to $\hat{\varphi}$ in each channel (c,f). Axis indicate electrode rows in anterior-posterior (x) direction, columns in lateral (y) direction and levels in longitudinal (z) direction.

butions from the two sources. Consequently, the ratio $\bar{\varphi}/\hat{\varphi}$ maximized in the central column (levels 1 and 2). Further, frontal recording electrodes in row 1 and right lateral electrodes ([row, column, level]: [3,7,1], [4,6,1], [3,(5,6),2]) indicated $\bar{\varphi}/\hat{\varphi}$ ratios above 90 %.

Differences between the topographies in Figures 4.23b and 4.23e, and Figures 4.23c and 4.23f were quantified by means of MAG_{rel} and RDM^* as summarized in Table 4.3. The MAG_{rel} anticipated the small differences in the relative maximum values $\hat{\varphi}/max(\hat{\varphi})$ between AM- and TI-tES. In the $\bar{\varphi}/\hat{\varphi}$ comparison, the MAG_{rel} reflected the smaller amount of electrodes with high $\bar{\varphi}/\hat{\varphi}$ in TI-tES. The topography differences from both the $\hat{\varphi}/max(\hat{\varphi})$ ratio and the $\bar{\varphi}/\hat{\varphi}$ ratio were reflected in the RDM^* values.

Table 4.3: MAG_{rel} and RDM^* values for $\hat{\varphi}/max(\hat{\varphi})$ and $\bar{\varphi}/\hat{\varphi}$ comparisons of AM- and TI-tES.

Parameter	MAG_{rel}	RDM^*
$\hat{\varphi}/max(\hat{\varphi})$	0.04	0.24
$\bar{\varphi}/\hat{\varphi}$	0.24	0.35

4.2.4 Discussion

A three-compartmental head phantom was established, which realistically resembled the geometry of a human head derived from a CT data set. The materials, agar hydrogel, gypsum, and sodium chloride, implemented realistic electrolyte conductivity levels for modeling intracranial volume, scalp, and skull compartments. The resulting physical head phantom was applied in experiments to investigate new electrodes and current waveforms for tES.

The 0.17 % NaCl solution demonstrated a conductivity of 0.33 S/m at 25 °C which corresponds to the value that is widely used to model the conductivity of intracranial volume (Geddes and Baker, 1967). Consequently, this saline solution established the fundamental electrolyte concentration that prevailed throughout all compartments. In the closed phantom design, this saline solution was used to model the intracranial volume.

Doping the NaCl solution with agarose as a solidifying agent enabled the formation of a mechanically durable scalp layer. The conductivity value of the agar hydrogel decreased by 5.5 % for 2 wt% agarose compared to the pure NaCl solution. The variations in conductivity over time and frequency after multiple repetitions were well within $\mu \pm 0.05\mu$. The average measured conductivity of 0.31 S/m at 25 °C is equivalent to 0.4 S/m at 37 °C when linearly extrapolated, which was acceptable according to Burger and Milaan (1943), reporting a conductivity of 0.435 S/m at 37 °C. Further, the average measured conductivity was within the range of 0.137 S/m to 2.1 S/m summarized by McCann et al. (2019).

The Stewaform gypsum samples provided stable results within a margin of $\pm 5\%$ of μ across multiple measurement series, which was reproducible between multiple samples within a margin of $\pm 10\%$ of μ . The measured average conductivity value of 0.0425 S/m at 25 °C is equivalent to 0.063 S/m at 37 °C when linearly extrapolated, which was in good accordance with skull conductivity range from 0.03 S/m to 0.08 S/m measured at 37 °C as reported by Hoekema et al. (2003). This gypsum as skull model and other phantom materials established a skull-to-soft tissue conductivity ratios of 1:8, in close relation to the ratio of 1:12 reported by Oostendorp et al. (2000).

The physical head phantom build from the characterized materials realized the widely used approximation of the head as volume conductor comprising intracranial volume, skull, and scalp (Stenroos et al., 2014). The electrolyte conductivity in all materials was based on a 0.17 % NaCl solution. Consequently, the three-compartmental head phantom incorporating these materials possessed a practically stationary ion concentration. Thus, the limitation of transient conductivity configurations due to diffusion processes across compartments with varying ion concentration (Sadleir et al., 2009) could be overcome. All materials used to manufacture the samples were commercially available. Using these products and standardized production procedures ensured the reproducibility of the phantom manufacturing. However, all samples have been manually produced and sample properties, i.e. the area A and the thickness d , used in equation 4.4 had tolerances influencing the calculated conductivity values. Further, the geometry parameters of the measurement cell, reflected in the cell constant, affected the results of the temperature compensation according to equation 4.3. Impedance measurements were conducted at room temperature in a non-air-conditioned environment, and measured values were afterwards converted to the reference temperature of 25 °C (ISO/TC 147, 1985) for comparability.

The conductivities resulting from measurements with the four-electrode setup demonstrated high reproducibility with a coefficient of variation (CV) of 0.8 % and reliability with a difference of 0.2 % when compared to values obtained with the ProfiLine Cond 3310.

The tested materials demonstrated consistent results when measured across several days. Consequently, the head phantom assembled with these materials had the potential of being stable throughout multi-day experiments, when the drying of the agar layer is suppressed.

The aqueous NaCl solution allowed the insertion of interior structures for signal measurements (i.e. the 3D measurement array) without interfering with the inherent structure of this compartment. Further, the NaCl concentration can be adapted to change the conductivity configuration of the entire phantom. Adapting the agarose concentration up to 4 wt% allows the modification of the agar hydrogel mechanical durability without changing the conductivity to values outside of the acceptable range. With an agar concentration of 4 wt%, applications such as EEG experiments using dry multi-pin electrodes become feasible (Fiedler et al., 2018). The Stewaform gypsum material demonstrated a considerable conductivity barrier which can be adapted by changing the NaCl concentration in the cast-

ing compound. This could be used to cover a wide range of skull conductivity values, which can be found in literature (Homma et al., 1995; Wendel et al., 2008). However, lowering the conductivity of the skull compartment could increase capacitive effects and changing the NaCl concentration with respect to the other compartments comes with the cost of potential chemical instability due to diffusion.

The characterized materials, NaCl solution, agar hydrogel and gypsum demonstrated applicability in modeling intracranial volume, scalp and skull of the physical head phantom. Agar hydrogel and gypsum are well-known moldable materials that are available at low cost and inherently mechanically stable and permeable for ions. The Stewaform gypsum provided a stable conductivity barrier that implements physiologically plausible skull conductivity values in contact with NaCl solution. The casting procedure, introduced in section 4.2.2, identified gypsum as suitable for producing a hollow skull compartment, that can be coated with agar hydrogel realistically mimicking the scalp layer. Both materials can have varying thicknesses in the range of 1 mm to 10 mm, which supported realistically shaped phantom implementations.

The phantom realized by the characterized materials as described in section 4.2.2, equipped with the 3D measurement array inside, demonstrated consistent electric potential distributions in the intracranial volume when tACS was applied by different stimulation electrodes (cf. Figure 4.19). The amplitude changes in the order of 10 % (cf. Figure 4.20) for stimulation frequencies of 1 Hz, 10 Hz, and 100 Hz can be related to the stimulation electrodes, since the phantom material indicated no frequency dependent conductivity values in this range. As expected, the strongest influence of stimulation frequencies on recorded amplitudes was given for the dry stimulation electrodes, which was most likely caused due to capacitive coupling effects. When rubber electrodes attached to the agar scalp via saline soaked sponge pockets impressed the current, the recorded amplitudes showed a slight increase for increasing stimulation frequency. Possibly, the electron–electrolyte interface at the stimulation site influenced the current flow, although it was buffered by the electrolyte solution in the sponges. Current stimulation applied via textile stimulation electrodes showed least influence of stimulation frequencies on recorded amplitudes, whereat the silver threads were embedded in the electrolyte solution spreading from the sponges onto the agar scalp. Capacitive effects on recorded electric potential amplitudes have also been reported from invasive measurement in monkeys and humans (Opitz et al., 2016).

When doubling the stimulation amplitude, the recorded amplitudes also increased by a factor of two, independently of the stimulation electrodes, which supported the amplitude linearity of the entire system.

The system of textile stimulation electrodes, the physical head phantom, and the measurement array was used to evaluate AM- and TI-tES. The recorded waveforms demonstrated the expected spectral components of the carrier frequency with the respective side

bands for AM stimulation and the two distinct stimulation frequencies separated by the difference frequency in TI stimulation as presented in Figure 4.21. Consequently, the 10 Hz component was prominent in the envelopes for both AM- and TI-tES. However, the recordings of TI-tES revealed additional spectral components at the harmonics of the difference frequency. Further, the spectral components of the two stimulation signals were not equally reflected in the recorded signals and the envelopes to the recorded waveforms from TI-tES revealed phase shifts different from phase reversals (180 degrees shifts), most prominently observable in Figure 4.21c. The spatial distribution of these phase shifts demonstrated that the phase shift appeared in vicinity to positions with phase reversals (cf. Figure 4.23d). This indicated spatial transitions of the interference envelopes. The spatial distribution of the envelope amplitude $\tilde{\varphi}$ for TI-tES indicated a concentration in the center of the stimulation setting (central column 4 in levels 1 and 2, most central with respect to the stimulation electrodes). Further, anterior electrodes, closest to the frontal stimulation electrodes and lateral right electrodes close to the right parietal stimulation electrode indicated high $\tilde{\varphi}$ values for TI-tES. These distinct hotspots in the $\tilde{\varphi}$ distributions for TI-tES were in contrast to the homogeneous $\tilde{\varphi}$ distribution across the entire measurement array for AM-tES (cf. Figures 4.23f vs. 4.23c). Also the envelope maximal values $\hat{\varphi}$ detected for TI-tES showed a more focal minimum in the centers of levels 1 and 2, whereat the entire central row indicated a zero-line for AM-tES (cf. Figures 4.23e vs. 4.23b). The intensity hot spots in envelope parameter distributions for TI-tES appeared in favor of the aim to target distinct regions through the application interference stimulation (Grossman et al., 2017).

Here the phantom served for evaluating new tES stimulation electrodes and schemes. Due to the phantom stability for several hours, multiple electrode configurations were applied under otherwise identical conditions. This gave rise to the identification of differences in the capacitive properties across the tested electrode materials, i.e. conductive rubber, silver coated textile and carbon doped PLA. The textile stimulation electrodes indicated the least capacitive properties, marking them as best applicable in tES. Further, the measurements of potential distributions inside the phantom originating from different stimulation schemes, i.e. AM- and TI-tES, allowed the evaluation of the resulting stimulation pattern. The results presented here, indicated clear differences between AM- and TI-tES in the spectral components of electric potentials measured inside the phantom. Since the stimulation signals inherited different frequency components, this was an expected outcome. Also the dominant 10 Hz component in envelopes constructed to the measured electric potential signals, was anticipated. The spatial distributions of the envelope amplitude $\tilde{\varphi}$ as one of the essential stimulation parameters in TI-tES referring to Grossman et al. (2017), demonstrated some degree of focalization as predicted in modeling studies (Rampersad et al., 2019; Lee et al., 2020) but also showed scattered hot spots as indicated in peripheral stimulation studies (Ozcan et al., 2004; Beatti et al., 2011).

When evaluating the outcome from the tES experiments, the stimulation and measurement setup needs to be considered. The 3D measurement array provided only a limited coverage of the intracranial volume with a spatial resolution of 10 mm in x-y-direction and 20 mm in z-direction.

The rods holding the measurement electrodes were printed of PLA and thus disturbed the distribution of the electric potential inside the phantom volume, which potentially influenced especially the interference of the two currents applied in TI-tES. A further influence on the envelopes' amplitude and phase distributions in TI-tES could originate from asymmetries in the positioning of the stimulation electrodes and their electrode-skin interface impedance. This is also supported by the deviation between the spectral amplitude components of the two sources and the asymmetry in the amplitude distribution in AM-tES, provided by the same electrodes.

Also the geometry of the phantom incorporated potential asymmetries originating from uncertainties in the multistage manufacturing process employing several negative molds for the subsequent casting processes. During the measurement campaign, the phantom was covered with cling film to prevent the drying of the scalp compartment of agar hydrogel. However, a certain drying of the agar hydrogel could not be completely excluded.

5 Significance and prospect

Many tES applications consider simplified models of inward-flowing current underneath the anode enhancing cortical excitability and outward-flowing current underneath the cathode reducing cortical excitability. Such assumptions originate from observations in animal models with smooth cortical surfaces (Bindman et al., 1964; Purpura and McMurtry, 1965), which need to be reconsidered in the light of the cortical folding in humans (Datta et al., 2009a; Saturnino et al., 2015).

Ultimately, this implies the need of current flow modeling, which apply individual volume conductor models and account for current orientation and cortical folding in the target area (Karabanov et al., 2019). The targeting approach based on Helmholtz reciprocity described in section 2.2 incorporates target dipoles defined with perpendicular orientation to the local cortical surface. The resulting stimulation schemes inherently adhere to the consideration of current orientation based on the local brain curvature, when individual volume conductor models are applied.

However, direct translation of modeling results to potential effects in the targeted neuronal system is challenging in humans. One possibility to infer from current flow modeling results to neuro-physiological effects lies in the use of evoked phosphenes as surrogate marker for current flow (Sabel et al., 2020b). Thus, the retina was selected as target structure in this thesis. The calculated current density distributions in the retina showed hot spots that were compared to phosphenes reported by participants, stimulated with the respective montages (Sabel et al., 2020a). The differences in current density distributions resulting from the various simulated montages contribute to the importance of electrode placement in tES applications (Opitz et al., 2018) and can be used to predict stimulation responses (Albizu et al., 2020).

Volume conductor models applied in such modeling studies are limited to the resolution provided by the medical imaging data (mostly MRI), they are derived from. Thus further sophistication is desired in future studies with eye models based on MRI data with sub-millimeter resolution. Such data is also beneficial for correct representation of cranial structures such as the CSF, spongy and compact bone (Mikkonen et al., 2020; Puonti et al., 2020).

Verification of current flow modeling was performed in surgical patients (Opitz et al., 2016; Huang et al., 2017) and human cadaver (Vöröslakos et al., 2018) with intrinsic limitations regarding disruptions of the head anatomy by the surgical intervention and uncertain

conductivity configurations. Further, physical phantoms were introduced, which partially mimicked tES configurations (Jung et al., 2013; Kim et al., 2015). In the present thesis, a reproducible head phantom with realistic volume conductivity and geometry was introduced for tES verification as described in section 4.2.

This phantom can also serve for characterization and testing of new tES application systems as introduced in chapter 3. Such integrated and easy-to-use systems are desired for therapeutic tES interventions, repeatedly applied over month or years (Sandran et al., 2019) and allow target specific, individual dose adaptation (Evans et al., 2020).

The flexible stimulation cap with integrated textile stimulation electrodes was developed and evaluated during the course of this thesis. It provides the basis for adaptations to multiple use-cases in tES with different electrode layouts. A process for size adjustments to different head sizes is initiated and potentially leads to a cap size system transferable also to other modalities, e.g. EEG, electrical impedance tomography (EIT) and near-infrared spectroscopy (NIRS).

The physical head phantom, developed during the course of this thesis, was applied in methodological evaluations of current density imaging (CDI) with ultra-low-field magnetic resonance imaging (ULF-MRI) (Hömmen et al., 2020) and in evaluations of EIT applied to different conductivity configurations. Further, experiments for verification of source and connectivity reconstructions from EEG and MEG measurements were performed with electrical dipoles inserted in the physical head phantom.

Prospectively, the physical head phantom will be applied in evaluation of further methodologies such as neural current imaging (NCI) and in multi-modal scenarios such as combined stimulation and recording scenarios, e.g. tES-EEG and tES-MEG. Adaptations of the physical head phantom for applications in other frequency ranges, as needed e.g. in high-field MRI, are in the planning phase.

Bibliography

- Albizu, A., Fang, R., Indahlastari, A., O'Shea, A., Stolte, S. E., See, K. B., Boutzoukas, E. M., Kraft, J. N., Nissim, N. R., and Woods, A. J. (2020). Machine learning and individual variability in electric field characteristics predict tDCS treatment response. *Brain Stimul.*, 13(6):1753–1764. (Cited on page 119.)
- Antal, A., Alekseichuk, I., Bikson, M., Brockmüller, J., Brunoni, A. R., Chen, R., Cohen, L. G., Douthwaite, G., Ellrich, J., Flöel, A., Fregni, F., George, M. S., Hamilton, R., Haueisen, J., Herrmann, C. S., Hummel, F. C., Lefaucheur, J. P., Liebetanz, D., Loo, C. K., McCaig, C. D., Miniussi, C., Miranda, P. C., Moliadze, V., Nitsche, M. A., Nowak, R., Padberg, F., Pascual-Leone, A., Poppendieck, W., Priori, A., Rossi, S., Rossini, P. M., Rothwell, J., Rueger, M. A., Ruffini, G., Schellhorn, K., Siebner, H. R., Ugawa, Y., Wexler, A., Ziemann, U., Hallett, M., and Paulus, W. (2017a). Low intensity transcranial electric stimulation: Safety, ethical, legal regulatory and application guidelines. *Clin. Neurophysiol.*, 128(9):1774–1809. (Cited on pages 3, 8, 24, 26, 69, and 80.)
- Antal, A., Kincses, T. Z., Nitsche, M. A., Bartfai, O., and Paulus, W. (2004a). Excitability Changes Induced in the Human Primary Visual Cortex by Transcranial Direct Current Stimulation: Direct Electrophysiological Evidence. *Investig. Ophthalmol. Vis. Sci.*, 45(2):702–707. (Cited on pages 57, 66, and 67.)
- Antal, A., Kincses, T. Z., Nitsche, M. A., and Paulus, W. (2003). Modulation of moving phosphene thresholds by transcranial direct current stimulation of V1 in human. *Neuropsychologia*, 41(13):1802–1807. (Cited on page 7.)
- Antal, A., Nitsche, M. A., Kincses, T. Z., Kruse, W., Hoffmann, K.-P., and Paulus, W. (2004b). Facilitation of visuo-motor learning by transcranial direct current stimulation of the motor and extrastriate visual areas in humans. *Eur.J.Neurosci.*, 19(10):2888–2892. (Cited on page 3.)
- Antal, A. and Paulus, W. (2013). Transcranial alternating current stimulation (tACS). *Front. Hum. Neurosci.*, 7. (Cited on page 70.)
- Antal, A., Paulus, W., and Rohde, V. (2017b). New Results on Brain Stimulation in Chronic Pain. *Neurol. Int. Open*, 01(04):E312–E315. (Cited on page 3.)

- Baillet, S., Rira, J. J., Main, G., Magin, J. F., Aubert, J., and Ganero, L. (2001). Evaluation of inverse methods and head models for EEG source localization using a human skull phantom. *Phys. Med. Biol.*, 46(1):77–96. (Cited on page 5.)
- Baker, J. M., Rorden, C., and Fridriksson, J. (2010). Using transcranial direct-current stimulation to treat stroke patients with aphasia. *Stroke*, 41(6):1229–1236. (Cited on page 3.)
- Baumann, S. B., Wozny, D. R., Kelly, S. K., and Meno, F. M. (1997). The electrical conductivity of human cerebrospinal fluid at body temperature. *IEEE Trans Biomed Eng*, 44(3):220–223. (Cited on page 9.)
- Beatti, A., Rayner, A., Chipchase, L., and Souvlis, T. (2011). Penetration and spread of interferential current in cutaneous, subcutaneous and muscle tissues. *Physiotherapy*, 97(4):319–326. (Cited on pages 83 and 117.)
- Berger, H. (1929). Über das Elektrenkephalogramm des Menschen. *Arch. Psychiatr. Nervenkr.*, 87(1):527–570. (Cited on page 1.)
- Berti, G. (2004). Image-based unstructured 3D mesh generation for medical applications. In *Eur. Congr. Comput. Methods Appl. Sci. Eng.*, pages 1–20. (Cited on page 8.)
- Bikson, M., Bulow, P., Stiller, J. W., Datta, A., Battaglia, F., Karnup, S. V., and Postolache, T. T. (2008). Transcranial direct current stimulation for major depression: A general system for quantifying transcranial electrotherapy dosage. *Curr. Treat. Options Neurol.*, 10(5):377–385. (Cited on page 4.)
- Bikson, M., Datta, A., Rahman, A., and Scaturro, J. (2010). Electrode montages for tDCS and weak transcranial electrical stimulation: Role of 'return' electrode's position and size. *Clin. Neurophysiol.*, 121(12):1976–1978. (Cited on page 3.)
- Bikson, M., Grossman, P., Thomas, C., Zannou, A. L., Jiang, J., Adnan, T., Mourdoukoutas, A. P., Kronberg, G., Truong, D., Boggio, P., Brunoni, A. R., Charvet, L., Fregni, F., Fritsch, B., Gillick, B., Hamilton, R. H., Hampstead, B. M., Jankord, R., Kirton, A., Knotkova, H., Liebetanz, D., Liu, A., Loo, C., Nitsche, M. A., Reis, J., Richardson, J. D., Rotenberg, A., Turkeltaub, P. E., and Woods, A. J. (2016). Safety of Transcranial Direct Current Stimulation: Evidence Based Update 2016. *Brain Stimul.*, 9(5):641–661. (Cited on pages 4, 8, 70, 72, and 80.)
- Bindman, L. J., Lippold, O. C., and Redfearn, J. W. (1964). The Action of Brief Polarizing Currents on the Cerebral Cortex of the Rat (1) During Current Flow and (2) in the Production of Long-Lasting After-Effects. *J. Physiol.*, 172:369–382. (Cited on page 119.)

- Bland, M. J. and Altman, D. G. (1986). Statistical Methods for Assessing Agreement Between Two Methods of Clinical Measurement. *Lancet*, 327(8476):307–310. (Cited on page 58.)
- Bliss, T. V. and Lømo, T. (1973). Long-lasting potentiation of synaptic transmission in the dentate area of the anaesthetized rabbit following stimulation of the perforant path. *J. Physiol.*, 232(2):331–356. (Cited on page 1.)
- Bortoletto, M., Rodella, C., Salvador, R., Miranda, P. C., and Miniussi, C. (2016). Reduced Current Spread by Concentric Electrodes in Transcranial Electrical Stimulation (tES). *Brain Stimul.*, 9(4):525–528. (Cited on page 5.)
- Brindley, G. S. (1955). The site of electrical excitation of the human eye. *J. Physiol.*, 127(1):189–200. (Cited on page 1.)
- Bromm, B. and Lullies, H. (1966). Über den Mechanismus der Reizwirkung mittelfrequenter Wechselströme auf die Nervenmembran. *Pflügers Arch. Gesamte Physiol. Menschen Tiere*, 289(4):215–226. (Cited on page 95.)
- Buchner, H., Knoll, G., Fuchs, M., Rienäcker, A., Beckmann, R., Wagner, M., Silny, J., and Pesch, J. (1997). Inverse localization of electric dipole current sources in finite element models of the human head. *Electroencephalogr. Clin. Neurophysiol.*, 102(4):267–278. (Cited on page 4.)
- Burger, H. C. and Milaan, van, J. B. (1943). Measurements of the specific Resistance of the human Body to direct Current. *Acta Med. Scand.*, 114(6):584–607. (Cited on pages 9 and 114.)
- Cancelli, A., Cottone, C., Tecchio, F., Truong, D. Q., Dmochowski, J., and Bikson, M. (2016). A simple method for EEG guided transcranial electrical stimulation without models. *J. Neural Eng.*, 13(3):036022. (Cited on page 27.)
- Cerletti, U. (1954). Electroshock therapy. *J. Clin. Exp. Psychopathol.*, 15(3):191–217. (Cited on page 1.)
- Chaieb, L., Antal, A., and Paulus, W. (2015). Transcranial random noise stimulation-induced plasticity is NMDA-receptor independent but sodium-channel blocker and benzodiazepines sensitive. *Front. Neurosci.*, 9. (Cited on page 2.)
- Creutzfeldt, O. D., Fromm, G. H., and Kapp, H. (1962). Influence of transcortical d-c currents on cortical neuronal activity. *Exp. Neurol.*, 5(6):436–452. (Cited on page 1.)
- Cuadrado, M. L., Valle, B., Fernández-De-Las-peñas, C., Madeleine, P., Barriga, F. J., Arias, J. A., Arendt-Nielsen, L., and Pareja, J. A. (2010). Pressure pain sensitivity

- of the scalp in patients with nummular headache: A cartographic study. *Cephalalgia*, 30(2):200–206. (Cited on page 69.)
- Dannhauer, M., Brooks, D., Tucker, D., and MacLeod, R. (2012). A pipeline for the simulation of transcranial direct current stimulation for realistic human head models using SCIRun/BioMesh3D. *Proc. Annu. Int. Conf. IEEE Eng. Med. Biol. Soc. EMBS*, c:5486–5489. (Cited on page 4.)
- DaSilva, A. F., Volz, M. S., Bikson, M., and Fregni, F. (2011). Electrode positioning and montage in transcranial direct current stimulation. *J. Vis. Exp.*, (51):e2744. (Cited on page 68.)
- Datta, A., Baker, J. M., Bikson, M., and Fridriksson, J. (2011). Individualized model predicts brain current flow during transcranial direct-current stimulation treatment in responsive stroke patient. *Brain Stimul.*, 4(3):169–174. (Cited on page 28.)
- Datta, A., Bansal, V., Diaz, J., Patel, J., Reato, D., and Bikson, M. (2009a). Gyri-precise head model of transcranial direct current stimulation: Improved spatial focality using a ring electrode versus conventional rectangular pad. *Brain Stimul.*, 2(4):201–207. (Cited on pages 3, 4, 5, 6, 24, 53, and 119.)
- Datta, A., Bikson, M., and Fregni, F. (2010). Transcranial direct current stimulation in patients with skull defects and skull plates: High-resolution computational FEM study of factors altering cortical current flow. *Neuroimage*, 52(4):1268–1278. (Cited on page 4.)
- Datta, A., Elwassif, M., and Bikson, M. (2009b). Bio-heat transfer model of transcranial DC stimulation: Comparison of conventional pad versus ring electrode. In *Proc. 31st Annu. Int. Conf. IEEE Eng. Med. Biol. Soc. Eng. Futur. Biomed. EMBC 2009*, pages 670–673. (Cited on page 4.)
- Datta, A., Truong, D., Minhas, P., Parra, L. C., and Bikson, M. (2012). Inter-individual variation during transcranial direct current stimulation and normalization of dose using MRI-derived computational models. *Front. Psychiatry*, 3. (Cited on page 3.)
- Destrieux, C., Fischl, B., Dale, A., and Halgren, E. (2010). Automatic parcellation of human cortical gyri and sulci using standard anatomical nomenclature. *Neuroimage*, 53(1):1–15. (Cited on page 27.)
- Dmochowski, J. P., Datta, A., Bikson, M., Su, Y., and Parra, L. C. (2011). Optimized multi-electrode stimulation increases focality and intensity at target. *J. Neural Eng.*, 8(4). (Cited on pages 4, 26, 32, 49, and 68.)

- Dmochowski, J. P., Koessler, L., Norcia, A. M., Bikson, M., and Parra, L. C. (2017). Optimal use of EEG recordings to target active brain areas with transcranial electrical stimulation. *Neuroimage*, 157:69–80. (Cited on pages 27 and 50.)
- Doppler, J. (1842). Über das farbige Licht der Dopplersterne und einiger anderer Gestirne des Himmels. *Abhandlungen der Königlichen Böhmischen Gesellschaft der Wissenschaften*, 2:465–482. (Cited on page 83.)
- Drexler, W., Morgner, U., Ghanta, R. K., Kärtner, F. X., Schuman, J. S., and Fujimoto, J. G. (2001). Ultrahigh-resolution ophthalmic optical coherence tomography. *Nat. Med.*, 7(4):502–506. (Cited on page 83.)
- Duchenne (de Boulogne), G. (1855). *De l'électrisation localisée et de son application à la physiologie, à la pathologie et à la thérapeutique*. Baillière, Paris. (Cited on page 1.)
- Edwards, D., Cortes, M., Datta, A., Minhas, P., Wassermann, E. M., and Bikson, M. (2013). Physiological and modeling evidence for focal transcranial electrical brain stimulation in humans: A basis for high-definition tDCS. *Neuroimage*, 74:266–275. (Cited on page 5.)
- Esmailpour, Z., Kronberg, G., Reato, D., Parra, L. C., and Bikson, M. (2021). Temporal interference stimulation targets deep brain regions by modulating neural oscillations. *Brain Stimul.*, 14(1):55–65. (Cited on page 96.)
- Evans, C., Bachmann, C., Lee, J. S., Gregoriou, E., Ward, N., and Bestmann, S. (2020). Dose-controlled tDCS reduces electric field intensity variability at a cortical target site. *Brain Stimul.*, 13(1):125–136. (Cited on pages 4 and 120.)
- Fang, Q. and Boas, D. A. (2009). Tetrahedral mesh generation from volumetric binary and grayscale images. In *Proc. - 2009 IEEE Int. Symp. Biomed. Imaging From Nano to Macro, ISBI 2009*, pages 1142–1145. (Cited on page 8.)
- Faugeras, O., Clément, F., Deriche, R., Keriven, R., Papadopoulos, T., Roberts, J., Viéville, T., Devernay, F., Gomes, J., Hermosillo, G., Kornprobst, P., and Lingrand, D. (1999). The Inverse EEG and MEG Problems : The Adjoint State Approach I: The Continuous Case. *Sophia*, page 28. (Cited on page 1.)
- Fedorov, A., Jobke, S., Bersnev, V., Chibisova, A., Chibisova, Y., Gall, C., and Sabel, B. A. (2011). Restoration of vision after optic nerve lesions with noninvasive transorbital alternating current stimulation: A clinical observational study. *Brain Stimul.*, 4(4):189–201. (Cited on page 7.)

- Fernández-Corazza, M., Turovets, S., Luu, P., Anderson, E., and Tucker, D. (2016). Transcranial electrical neuromodulation based on the reciprocity principle. *Front. Psychiatry*, 7. (Cited on pages 27 and 49.)
- Fernández-Corazza, M., Turovets, S., and Muravchik, C. H. (2020). Unification of optimal targeting methods in transcranial electrical stimulation. *Neuroimage*, 209. (Cited on page 50.)
- Fertonani, A., Ferrari, C., and Miniussi, C. (2015). What do you feel if I apply transcranial electric stimulation? Safety, sensations and secondary induced effects. *Clin. Neurophysiol.*, 126(11):2181–2188. (Cited on page 69.)
- Fiedler, P., Hunold, A., Müller, C., Rosner, G., Schellhorn, K., and Haueisen, J. (2015a). Novel flexible cap with integrated textile electrodes for rapid transcranial electrical stimulation. *Brain Stimul.*, 8(2):405–406. (Cited on pages 27, 53, XVII, and XIX.)
- Fiedler, P., Muhle, R., Griebel, S., Pedrosa, P., Fonseca, C., Vaz, F., Zanow, F., and Haueisen, J. (2018). Contact Pressure and Flexibility of Multipin Dry EEG Electrodes. *IEEE Trans. Neural Syst. Rehabil. Eng.*, 26(4):750–757. (Cited on page 115.)
- Fiedler, P., Pedrosa, P., Griebel, S., Fonseca, C., Vaz, F., Supriyanto, E., Zanow, F., and Haueisen, J. (2015b). Novel Multipin Electrode Cap System for Dry Electroencephalography. *Brain Topogr.*, 28(5):647–656. (Cited on pages 56, 67, 71, 72, 74, and 79.)
- Fischl, B. (2012). FreeSurfer. *Neuroimage*, 62(2):774–781. (Cited on pages 8 and 27.)
- Fonteneau, C., Mondino, M., Arns, M., Baeken, C., Bikson, M., Brunoni, A. R., Burke, M. J., Neuvonen, T., Padberg, F., Pascual-Leone, A., Poulet, E., Ruffini, G., Santarnecchi, E., Sauvaget, A., Schellhorn, K., Suaud-Chagny, M. F., Palm, U., and Brunelin, J. (2019). Sham tDCS: A hidden source of variability? Reflections for further blinded, controlled trials. *Brain Stimul.*, 12(3):668–673. (Cited on page 70.)
- Franceschi, C. (1979). *L'Investigation Vasculaire Par Ultrasonographie Doppler*. Masson, Paris, 2 edition. (Cited on page 83.)
- Fregni, F., Boggio, P. S., Mansur, C. G., Wagner, T., Ferreira, M. J., Lima, M. C., Rigonatti, S. P., Marcolin, M. A., Freedman, S. D., Nitsche, M. A., and Pascual-Leone, A. (2005a). Transcranial direct current stimulation of the unaffected hemisphere in stroke patients. *Neuroreport*, 16(14):1551–1555. (Cited on page 3.)
- Fregni, F., Boggio, P. S., Nitsche, M., Bermanpohl, F., Antal, A., Feredoes, E., Marcolin, M. A., Rigonatti, S. P., Silva, M. T., Paulus, W., and Pascual-Leone, A. (2005b). Anodal transcranial direct current stimulation of prefrontal cortex enhances working memory. *Exp. Brain Res.*, 166(1):23–30. (Cited on page 3.)

- Fregni, F., Thome-Souza, S., Nitsche, M. A., Freedman, S. D., Valente, K. D., and Pascual-Leone, A. (2006). A controlled clinical trial of cathodal DC polarization in patients with refractory epilepsy. *Epilepsia*, 47(2):335–342. (Cited on page 3.)
- Freitag, S., Hunold, A., Klemm, M., Klee, S., Link, D., Nagel, E., and Haueisen, J. (2019). Pulsed Electrical Stimulation of the Human Eye Enhances Retinal Vessel Reaction to Flickering Light. *Front. Hum. Neurosci.*, 13. (Cited on pages 2, 7, 11, and 22.)
- Gabriel, C. (1996). Compilation of the Dielectric Properties of Body Tissues at RF and Microwave Frequencies. Technical Report June, KING'S COLL LONDON (UNITED KINGDOM) DEPT OF PHYSICS. (Cited on page 9.)
- Gabriel, S., Lau, R. W., and Gabriel, C. (1996). The dielectric properties of biological tissues: III. Parametric models for the dielectric spectrum of tissues. *Phys. Med. Biol.*, 41(11):2271–2293. (Cited on page 9.)
- Gall, C., Fedorov, A. B., Ernst, L., Borrmann, A., and Sabel, B. A. (2010). Repetitive transorbital alternating current stimulation in optic neuropathy. *NeuroRehabilitation*, 27(4):335–341. (Cited on page 7.)
- Gall, C., Schmidt, S., Schittkowski, M. P., Antal, A., Ambrus, G. G., Paulus, W., Dannhauer, M., Michalik, R., Mante, A., Bola, M., Lux, A., Kropf, S., Brandt, S. A., and Sabel, B. A. (2016). Alternating current stimulation for vision restoration after optic nerve damage: A randomized clinical trial. *PLoS One*, 11(6):1–19. (Cited on pages 7 and 24.)
- Gall, C., Sgorzaly, S., Schmidt, S., Brandt, S., Fedorov, A., and Sabel, B. A. (2011). Noninvasive transorbital alternating current stimulation improves subjective visual functioning and vision-related quality of life in optic neuropathy. *Brain Stimul.*, 4(4):175–188. (Cited on page 7.)
- Galvani, L. (1791). De viribus electricitatis in motu muscularis commentarius. *Bononiensi Sci. Artium Inst. atque Acad. Comment.* (Cited on page 1.)
- Geddes, L. A. and Baker, L. E. (1967). The specific resistance of biological material—A compendium of data for the biomedical engineer and physiologist. *Med. Biol. Eng.*, 5(3):271–293. (Cited on pages 84, 97, and 114.)
- Gildemeister, M. (1944). Untersuchungen über die Wirkung der Mittelfrequenzströme auf den Menschen. *Pflugers Arch. Gesamte Physiol. Menschen Tiere*, 247(4-5):366–404. (Cited on page 95.)

- Graichen, U., Eichardt, R., Fiedler, P., Strohmeier, D., Zanow, F., and Haueisen, J. (2015). SPHARA - A generalized spatial fourier analysis for multi-sensor systems with non-uniformly arranged sensors: Application to EEG. *PLoS One*, 10(4). (Cited on page 29.)
- Grossman, N., Bono, D., Dedic, N., Kodandaramaiah, S. B., Rudenko, A., Suk, H. J., Cassara, A. M., Neufeld, E., Kuster, N., Tsai, L. H., Pascual-Leone, A., and Boyden, E. S. (2017). Noninvasive Deep Brain Stimulation via Temporally Interfering Electric Fields. *Cell*, 169(6):1029–1041.e16. (Cited on pages 68, 80, 83, 95, 96, and 117.)
- Guerra, A., Pogosyan, A., Nowak, M., Tan, H., Ferreri, F., Di Lazzaro, V., and Brown, P. (2016). Phase Dependency of the Human Primary Motor Cortex and Cholinergic Inhibition Cancellation during Beta tACS. *Cereb. Cortex*, 26(10):3977–3990. (Cited on page 80.)
- Guler, S., Dannhauer, M., Erem, B., Macleod, R., Tucker, D., Turovets, S., Luu, P., Erdogmus, D., and Brooks, D. H. (2016). Optimization of focality and direction in dense electrode array transcranial direct current stimulation (tDCS). *J. Neural Eng.*, 13(3). (Cited on page 4.)
- Güllmar, D., Haueisen, J., Eiselt, M., Gießler, F., Flemming, L., Anwander, A., Knösche, T. R., Wolters, C. H., Dämpelmann, M., Tuch, D. S., and Reichenbach, J. R. (2006). Influence of anisotropic conductivity on EEG source reconstruction: Investigations in a rabbit model. *IEEE Trans. Biomed. Eng.*, 53(9):1841–1850. (Cited on page 89.)
- Güllmar, D., Haueisen, J., and Reichenbach, J. R. (2010). Influence of anisotropic electrical conductivity in white matter tissue on the EEG/MEG forward and inverse solution. A high-resolution whole head simulation study. *Neuroimage*, 51(1):145–163. (Cited on pages 4 and 24.)
- Gundlach, C., Müller, M. M., Nierhaus, T., Villringer, A., and Sehm, B. (2017). Modulation of somatosensory alpha rhythm by transcranial alternating current stimulation at Mu-frequency. *Front. Hum. Neurosci.*, 11. (Cited on page 80.)
- Harms, E. (1955). HISTORICAL NOTE. *Am. J. Psychiatry*, 111(12):933–934. (Cited on page 1.)
- Haueisen, J. and Hunold, A. (2017). Concept of a physical head phantom MEG-MRI and NCI/CDI. In *Brain twitter Conf. #brainTC Neurosci. Mak. an impact*. (Cited on page 98.)
- Haueisen, J., Ramon, C., Czapski, P., and Eiselt, M. (1995). On the Influence of Volume Currents and Extended Sources on Neuromagnetic Fields: A Simulation Study. *Ann. Biomed. Eng.*, 23(6):728–739. (Cited on page 24.)

- Haueisen, J., Schack, B., Meier, T., Curio, G., and Okada, Y. (2001). Multiplicity in the high-frequency signals during the short-latency somatosensory evoked cortical activity in humans. *Clin. Neurophysiol.*, 112(7):1316–1325. (Cited on page 96.)
- Hebb, D. (1949). *The Organization of Behavior*. Wiley, New York. (Cited on page 1.)
- Helmholtz, H. (1853). Ueber einige Gesetze der Vertheilung elektrischer Ströme in körperlichen Leitern mit Anwendung auf die thierisch-elektrischen Versuche. *Ann. Phys.*, 165(6):211–233. (Cited on page 27.)
- Hoekema, R., Wieneke, G. H., Leijten, F. S., Van Veelen, C. W., Van Rijen, P. C., Huiskamp, G. J., Ansems, J., and Van Huffelen, A. C. (2003). Measurement of the conductivity of skull, temporarily removed during epilepsy surgery. *Brain Topogr.*, 16(1):29–38. (Cited on page 115.)
- Homma, S., Musha, T., Nakajima, Y., Okamoto, Y., Blom, S., Flink, R., and Hagbarth, K. E. (1995). Conductivity ratios of the scalp-skull-brain head model in estimating equivalent dipole sources in human brain. *Neurosci. Res.*, 22(1):51–55. (Cited on pages 97 and 116.)
- Hömmen, P., Mäkinen, A. J., Hunold, A., Machts, R., Haueisen, J., Zevenhoven, K. C., Ilmoniemi, R. J., and Körber, R. (2020). Evaluating the Performance of Ultra-Low-Field MRI for in-vivo 3D Current Density Imaging of the Human Head. *Front. Phys.*, 8. (Cited on page 120.)
- Huang, Y., Datta, A., Bikson, M., and Parra, L. C. (2018). ROAST: An Open-Source, Fully-Automated, Realistic Volumetric-Approach-Based Simulator for TES. In *Proc. Annu. Int. Conf. IEEE Eng. Med. Biol. Soc. EMBS*. (Cited on page 49.)
- Huang, Y., Datta, A., Bikson, M., and Parra, L. C. (2019). Realistic volumetric-approach to simulate transcranial electric stimulation - ROAST - a fully automated open-source pipeline. *J. Neural Eng.*, 16(5). (Cited on page 4.)
- Huang, Y., Liu, A. A., Lafon, B., Friedman, D., Dayan, M., Wang, X., Bikson, M., Doyle, W. K., Devinsky, O., and Parra, L. C. (2017). Measurements and models of electric fields in the in vivo human brain during transcranial electric stimulation. *Elife*, 6:e18834. (Cited on pages 6 and 119.)
- Hunold, A., Berkes, S., Schellhorn, K., Antal, A., and Haueisen, J. (2020a). Feasibility of new stimulator setup for temporal interference TES and its application in a homogeneous volume conductor. In *Int. Conf. Non-Invasive Brain Stimul.* (Cited on page 84.)

- Hunold, A., Freitag, S., Schellhorn, K., and Haueisen, J. (2015). Simulation of the current density distribution for transcranial electric current stimulation around the eye. *Brain Stimul.*, 8(2):406. (Cited on pages 8 and 24.)
- Hunold, A., Funke, M. E., Eichardt, R., Stenroos, M., and Haueisen, J. (2016). EEG and MEG: Sensitivity to epileptic spike activity as function of source orientation and depth. *Physiol. Meas.*, 37(7):1146–1162. (Cited on page 4.)
- Hunold, A., Güllmar, D., and Haueisen, J. (2019). CT Dataset of a Human Head. (Cited on page 98.)
- Hunold, A., Haueisen, J., Ahtam, B., Doshi, C., Harini, C., Camposano, S., Warfield, S. K., Grant, P. E., Okada, Y., and Papadelis, C. (2014). Localization of the epileptogenic foci in tuberous sclerosis complex: A pediatric case report. *Front. Hum. Neurosci.*, 8. (Cited on page 4.)
- Hunold, A., Kresinsky, A., Sabel, B. A., and Haueisen, J. (2018a). Simulation of the current density in the retina for transorbital electric current stimulation. In *Work. Biosignalverarbeitung 'Innovative Verarbeitung bioelektrischer und Biomagn. Signale' der Fachausschüsse Biosignale und Magn. Methoden der Medizin der DGBMT im VDE*. (Cited on pages 8 and 24.)
- Hunold, A., Machts, R., and Haueisen, J. (2020b). Head phantoms for bioelectromagnetic applications: a material study. *Biomed. Eng. Online*, 19(1):87. (Cited on pages 98 and 101.)
- Hunold, A., Ortega, D., Schellhorn, K., and Haueisen, J. (2020c). Novel flexible cap for application of transcranial electrical stimulation: A usability study. *Biomed. Eng. Online*, 19(1). (Cited on pages 53, XVII, and XIX.)
- Hunold, A., Schellhorn, K., and Haueisen, J. (2018b). Simulating the superposition of transcranial electric stimulations targeting the visual cortex. In *Int. Conf. Biomagn.* (Cited on pages 84 and 95.)
- Hunold, A., Strohmeier, D., Fiedler, P., and Haueisen, J. (2018c). Head phantoms for electroencephalography and transcranial electric stimulation: A skull material study. *Biomed. Tech.*, 63(6):647–655. (Cited on pages 98 and 101.)
- Indahlastari, A., Kasinadhuni, A. K., Saar, C., Castellano, K., Mousa, B., Chauhan, M., Mareci, T. H., and Sadleir, R. J. (2018). Methods to compare predicted and observed phosphene experience in TACS subjects. *Neural Plast.*, 2018:8525706. (Cited on pages 8, 23, and 24.)

- ISO/TC 147, S. (1985). *ISO 7888:1985(R2017) Water quality - Determination of electrical conductivity*. International Organization for Standardization. (Cited on page 115.)
- Iyer, M. B., Mattu, U., Grafman, J., Lomarev, M., Sato, S., and Wassermann, E. M. (2005). Safety and cognitive effect of frontal DC brain polarization in healthy individuals. *Neurology*, 64(5):872–875. (Cited on page 70.)
- Jasper, H. H. (1958). The ten twenty electrode system of the international federation. *Electroencephalogr. Clin. Neurophysiol.* (Cited on pages 9, 28, 50, 55, 57, 74, and 104.)
- Jefferys, J. G. R., Deans, J., Bikson, M., and Fox, J. (2003). Effects of weak electric fields on the activity of neurons and neuronal networks. *Radiat. Prot. Dosimetry*, 106(4):321–323. (Cited on page 26.)
- Jung, Y.-J., Kim, J.-H., Kim, D., and Im, C.-H. (2013). An image-guided transcranial direct current stimulation system: a pilot phantom study. *Physiol. Meas.*, 34(8):937–950. (Cited on pages 5, 97, and 120.)
- Karabanov, A., Thielscher, A., and Siebner, H. R. (2016). Transcranial brain stimulation: Closing the loop between brain and stimulation. *Curr. Opin. Neurol.*, 29(4):397–404. (Cited on page 3.)
- Karabanov, A. N., Saturnino, G. B., Thielscher, A., and Siebner, H. R. (2019). Can transcranial electrical stimulation localize brain function? *Front. Psychol.*, 10. (Cited on page 119.)
- Kasten, F. H., Dowsett, J., and Herrmann, C. S. (2016). Sustained aftereffect of α -tACS lasts up to 70 min after stimulation. *Front. Hum. Neurosci.*, 10. (Cited on page 80.)
- Kessler, S. K., Minhas, P., Woods, A. J., Rosen, A., Gorman, C., and Bikson, M. (2013). Dosage Considerations for Transcranial Direct Current Stimulation in Children: A Computational Modeling Study. *PLoS One*, 8(9). (Cited on page 4.)
- Khadka, N., Borges, H., Zannou, A. L., Jang, J., Kim, B., Lee, K., and Bikson, M. (2018). Dry tDCS: Tolerability of a novel multilayer hydrogel composite non-adhesive electrode for transcranial direct current stimulation. *Brain Stimul.*, 11(5):1044–1053. (Cited on pages 5 and 72.)
- Kim, D., Jeong, J., Jeong, S., Kim, S., Jun, S. C., and Chung, E. (2015). Validation of computational studies for electrical brain stimulation with phantom head experiments. *Brain Stimul.*, 8(8):914–925. (Cited on pages 5, 97, and 120.)
- Klein, E., Mann, A., Huber, S., Bloechle, J., Willmes, K., Karim, A. A., Nuerk, H. C., and Moeller, K. (2013). Bilateral Bi-Cephalic Tdcs with Two Active Electrodes of the Same

- Polarity Modulates Bilateral Cognitive Processes Differentially. *PLoS One*, 8(8):1–11. (Cited on pages 26 and 68.)
- Klem, G. H., Lüders, H. O., Jasper, H. H., and Elger, C. (1999). The ten-twenty electrode system of the International Federation. *Electroencephalogr. Clin. Neurophysiol.* (Cited on pages 9, 28, 50, 55, 57, 74, and 104.)
- Kohli, S. and Casson, A. J. (2019). Removal of gross artifacts of transcranial alternating current stimulation in simultaneous EEG monitoring. *Sensors (Switzerland)*, 19(1). (Cited on page 80.)
- Krause, M. R., Vieira, P. G., Csorba, B. A., Pilly, P. K., and Pack, C. C. (2019). Transcranial alternating current stimulation entrains single-neuron activity in the primate brain. *Proc. Natl. Acad. Sci. U. S. A.*, 116(12):5747–5755. (Cited on page 2.)
- Laakso, I. and Hirata, A. (2013). Computational analysis shows why transcranial alternating current stimulation induces retinal phosphenes. *J. Neural Eng.*, 10(4):046009. (Cited on pages 4, 7, 23, and 24.)
- Lawrence Marple, S. (1999). Computing the discrete-time analytic signal via fft. *IEEE Trans. Signal Process.*, 47(9):2600–2603. (Cited on pages 88 and 106.)
- Le Roy, J.-B. (1755). Histoire de l’Académie royale des sciences ... avec les mémoires de mathématique & de physique... tirez des registres de cette Académie. *Académie des Sci.*, pages 9–11. (Cited on page 1.)
- Leahy, R. M., Mosher, J. C., Spencer, M. E., Huang, M. X., and Lewine, J. D. (1998). A study of dipole localization accuracy for MEG and EEG using a human skull phantom. *Electroencephalogr. Clin. Neurophysiol.*, 107(2):159–173. (Cited on page 5.)
- Lee, C., Jung, Y. J., Lee, S. J., and Im, C. H. (2017). COMETS2: An advanced MATLAB toolbox for the numerical analysis of electric fields generated by transcranial direct current stimulation. *J. Neurosci. Methods*, 277:56–62. (Cited on page 4.)
- Lee, S., Lee, C., Park, J., and Im, C.-H. (2020). Individually customized transcranial temporal interference stimulation for focused modulation of deep brain structures: a simulation study with different head models. *Sci. Rep.*, 10(1):11730. (Cited on page 117.)
- Lew, S., Wolters, C. H., Dierkes, T., Röer, C., and MacLeod, R. S. (2009). Accuracy and run-time comparison for different potential approaches and iterative solvers in finite element method based EEG source analysis. *Appl. Numer. Math.*, 59(8):1970–1988. (Cited on page 28.)

- Li, L. M., Uehara, K., and Hanakawa, T. (2015). The contribution of interindividual factors to variability of response in transcranial direct current stimulation studies. *Front. Cell. Neurosci.*, 9. (Cited on page 3.)
- Lide, D. R. (2012). CRC Handbook of Chemistry and Physics, 93rd Edition. In Haynes, W., Lide, D. R., and Bruno, T., editors, *Handb. Chem. Phys.*, pages 5–73. CRC Press. (Cited on page 106.)
- Liehr, M. and Haueisen, J. (2008). Influence of anisotropic compartments on magnetic field and electric potential distributions generated by artificial current dipoles inside a torso phantom. *Phys. Med. Biol.*, 53(1):245–254. (Cited on page 5.)
- Lindenblatt, G. and Silny, J. (2001). A model of the electrical volume conductor in the region of the eye in the ELF range. *Phys Med Biol*, 46(11):3051–3059. (Cited on page 9.)
- Liu, A., Vöröslakos, M., Kronberg, G., Henin, S., Krause, M. R., Huang, Y., Opitz, A., Mehta, A., Pack, C. C., Krekelberg, B., Berényi, A., Parra, L. C., Melloni, L., Devinsky, O., and Buzsáki, G. (2018). Immediate neurophysiological effects of transcranial electrical stimulation. (Cited on page 6.)
- Mansour, A. G., Ahdab, R., Khazen, G., El-Khoury, C., Sabbouh, T. M., Salem, M., Yamak, W., Chalah, M. A., Ayache, S. S., and Riachi, N. (2020). Transcranial Direct Current Stimulation of the Occipital Cortex in Medication Overuse Headache: A Pilot Randomized Controlled Cross-Over Study. *J. Clin. Med.*, 9(4):1075. (Cited on page 4.)
- Martin, A. K., Huang, J., Hunold, A., and Meinzer, M. (2017). Sex Mediates the Effects of High-Definition Transcranial Direct Current Stimulation on "Mind-Reading". *Neuroscience*, 366:84–94. (Cited on pages 4, 5, 49, and 53.)
- McCann, H., Pisano, G., and Beltrachini, L. (2019). Variation in Reported Human Head Tissue Electrical Conductivity Values. *Brain Topogr.*, 32(5):825–858. (Cited on pages 97 and 114.)
- Meijs, J. W., Weier, O. W., Peters, M. J., and Van Oosterom, A. (1989). On the Numerical Accuracy of the Boundary Element Method. *IEEE Trans. Biomed. Eng.*, 36(10):1038–1049. (Cited on page 88.)
- Merrill, D. R., Bikson, M., and Jefferys, J. G. (2005). Electrical stimulation of excitable tissue: Design of efficacious and safe protocols. (Cited on page 5.)
- Mikkonen, M., Laakso, I., Tanaka, S., and Hirata, A. (2020). Cost of focality in TDCS: Interindividual variability in electric fields. *Brain Stimul.*, 13(1):117–124. (Cited on page 119.)

- Minhas, P., Bansal, V., Patel, J., Ho, J. S., Diaz, J., Datta, A., and Bikson, M. (2010). Electrodes for high-definition transcutaneous DC stimulation for applications in drug delivery and electrotherapy, including tDCS. *J. Neurosci. Methods*, 190(2):188–197. (Cited on pages 5, 26, and 72.)
- Miranda, P. C., Lomarev, M., and Hallett, M. (2006). Modeling the current distribution during transcranial direct current stimulation. *Clin. Neurophysiol.*, 117(7):1623–1629. (Cited on page 4.)
- Miranda, P. C., Mekonnen, A., Salvador, R., and Ruffini, G. (2013). The electric field in the cortex during transcranial current stimulation. *Neuroimage*, 70:48–58. (Cited on pages 6 and 49.)
- Mirzakhaili, E., Barra, B., Capogrosso, M., and Lempka, S. F. (2020). Biophysics of Temporal Interference Stimulation. *Cell Syst.*, 0(0). (Cited on page 95.)
- Moliadze, V., Antal, A., and Paulus, W. (2010). Electrode-distance dependent after-effects of transcranial direct and random noise stimulation with extracephalic reference electrodes. *Clin. Neurophysiol.*, 121(12):2165–2171. (Cited on page 4.)
- Moliadze, V., Lyzhko, E., Schmanke, T., Andreas, S., Freitag, C. M., and Siniatchkin, M. (2018). 1 mA cathodal tDCS shows excitatory effects in children and adolescents: Insights from TMS evoked N100 potential. *Brain Res. Bull.*, 140:43–51. (Cited on page 3.)
- Moreno-Duarte, I., Gebodh, N., Schestatsky, P., Guleyupoglu, B., Reato, D., Bikson, M., and Fregni, F. (2014). Transcranial Electrical Stimulation: Transcranial Direct Current Stimulation (tDCS), Transcranial Alternating Current Stimulation (tACS), Transcranial Pulsed Current Stimulation (tPCS), and Transcranial Random Noise Stimulation (tRNS). In *Stimul. Brain Cogn. Enhanc. Using Non-Invasive Brain Stimul.*, pages 35–59. Elsevier Science & Technology. (Cited on page 2.)
- Myers, C. E., Klein, B. E., Meuer, S. M., Swift, M. K., Chandler, C. S., Huang, Y., Gangaputra, S., Pak, J. W., Danis, R. P., and Klein, R. (2015). Retinal thickness measured by spectral-domain optical coherence tomography in eyes without retinal abnormalities: The Beaver Dam Eye Study. *Am. J. Ophthalmol.*, 159(3):445–456.e1. (Cited on page 24.)
- Negahbani, E., Kasten, F. H., Herrmann, C. S., and Fröhlich, F. (2018). Targeting alpha-band oscillations in a cortical model with amplitude-modulated high-frequency transcranial electric stimulation. *Neuroimage*, 173:3–12. (Cited on page 80.)
- Nemec, H. (1959). Interferential therapy: a new approach in physical medicine. *Br J Physiother*, 12:9–12. (Cited on pages 83 and 95.)

- Neuling, T., Ruhnau, P., Weisz, N., Herrmann, C. S., and Demarchi, G. (2017). Faith and oscillations recovered: On analyzing EEG/MEG signals during tACS. *Neuroimage*, 147:960–963. (Cited on page 80.)
- Nikolin, S., Loo, C. K., Bai, S., Dokos, S., and Martin, D. M. (2015). Focalised stimulation using high definition transcranial direct current stimulation (HD-tDCS) to investigate declarative verbal learning and memory functioning. *Neuroimage*, 117:11–19. (Cited on page 5.)
- Nitsche, M. A. and Paulus, W. (2000). Excitability changes induced in the human motor cortex by weak transcranial direct current stimulation. *J. Physiol.*, 527(3):633–639. (Cited on pages 1, 3, 4, 26, and 53.)
- Noury, N., Hipp, J. F., and Siegel, M. (2016). Physiological processes non-linearly affect electrophysiological recordings during transcranial electric stimulation. *Neuroimage*, 140:99–109. (Cited on page 80.)
- Noury, N. and Siegel, M. (2018). Analyzing EEG and MEG signals recorded during tES, a reply. *Neuroimage*, 167:53–61. (Cited on page 80.)
- Odom, J. V., Bach, M., Brigell, M., Holder, G. E., McCulloch, D. L., Tormene, A. P., and Vaegan (2010). ISCEV standard for clinical visual evoked potentials (2009 update). *Doc. Ophthalmol.*, 120(1):111–119. (Cited on page 57.)
- Oostendorp, T. F., Delbeke, J., and Stegeman, D. F. (2000). The conductivity of the human skull: Results of in vivo and in vitro measurements. *IEEE Trans. Biomed. Eng.*, 47(11):1487–1492. (Cited on page 115.)
- Opitz, A., Falchier, A., Yan, C. G., Yeagle, E. M., Linn, G. S., Megevand, P., Thielscher, A., Deborah, R. A., Milham, M. P., Mehta, A. D., and Schroeder, C. E. (2016). Spatiotemporal structure of intracranial electric fields induced by transcranial electric stimulation in humans and nonhuman primates. *Sci. Rep.* (Cited on pages 6, 49, 116, and 119.)
- Opitz, A., Paulus, W., Will, S., Antunes, A., and Thielscher, A. (2015). Determinants of the electric field during transcranial direct current stimulation. *Neuroimage*, 109:140–150. (Cited on page 68.)
- Opitz, A., Yeagle, E., Thielscher, A., Schroeder, C., Mehta, A. D., and Milham, M. P. (2018). On the importance of precise electrode placement for targeted transcranial electric stimulation. *Neuroimage*, 181:560–567. (Cited on page 119.)
- Ozcan, J., Ward, A. R., and Robertson, V. J. (2004). A comparison of true and premodulated interferential currents. *Arch. Phys. Med. Rehabil.*, 85(3):409–415. (Cited on pages 95 and 117.)

- Padberg, F., Kumpf, U., Mansmann, U., Palm, U., Plewnia, C., Langguth, B., Zwanzger, P., Fallgatter, A., Nolden, J., Burger, M., Keeser, D., Rupprecht, R., Falkai, P., Hasan, A., Egert, S., and Bajbouj, M. (2017). Prefrontal transcranial direct current stimulation (tDCS) as treatment for major depression: study design and methodology of a multicenter triple blind randomized placebo controlled trial (DepressionDC). *Eur. Arch. Psychiatry Clin. Neurosci.*, 267(8):751–766. (Cited on pages 3, 26, and 55.)
- Palm, U., Schiller, C., Fintescu, Z., Obermeier, M., Keeser, D., Reisinger, E., Pogarell, O., Nitsche, M. A., Möller, H. J., and Padberg, F. (2012). Transcranial direct current stimulation in treatment resistant depression: A randomized double-blind, placebo-controlled study. *Brain Stimul.*, 5(3):242–251. (Cited on page 3.)
- Paneri, B., Adair, D., Thomas, C., Khadka, N., Patel, V., Tyler, W. J., Parra, L., and Bikson, M. (2016). Tolerability of Repeated Application of Transcranial Electrical Stimulation with Limited Outputs to Healthy Subjects. *Brain Stimul.*, 9(5):740–754. (Cited on page 72.)
- Parazzini, M., Fiocchi, S., Rossi, E., Paglialonga, A., and Ravazzani, P. (2011). Transcranial direct current stimulation: Estimation of the electric field and of the current density in an anatomical human head model. *IEEE Trans. Biomed. Eng.*, 58(6):1773–1780. (Cited on page 24.)
- Park, J. H., Hong, S. B., Kim, D. W., Suh, M., and Im, C. H. (2011). A novel array-type transcranial direct current stimulation (tDCS) system for accurate focusing on targeted brain areas. *IEEE Trans. Magn.*, 47(5):882–885. (Cited on page 26.)
- Paulus, W. (2010). On the difficulties of separating retinal from cortical origins of phosphenes when using transcranial alternating current stimulation (tACS). *Clin. Neurophysiol.*, 121(7):987–991. (Cited on page 7.)
- Pedrosa, P., Fiedler, P., Pestana, V., Vasconcelos, B., Gaspar, H., Amaral, M. H., Freitas, D., Haueisen, J., Nóbrega, J. M., and Fonseca, C. (2018). In-service characterization of a polymer wick-based quasi-dry electrode for rapid pasteless electroencephalography. *Biomed. Tech.*, 63(4):349–359. (Cited on page 5.)
- Perdue, K. L. and Diamond, S. G. (2014). T1 magnetic resonance imaging head segmentation for diffuse optical tomography and electroencephalography. *J. Biomed. Opt.*, 19(2):026011. (Cited on page 8.)
- Peterchev, A. V., Wagner, T. A., Miranda, P. C., Nitsche, M. A., Paulus, W., Lisanby, S. H., Pascual-Leone, A., and Bikson, M. (2012). Fundamentals of transcranial electric and magnetic stimulation dose: Definition, selection, and reporting practices. *Brain Stimul.*, 5(4):435–453. (Cited on pages 4 and 26.)

- Pinto, C. B., Teixeira Costa, B., Duarte, D., and Fregni, F. (2018). Transcranial Direct Current Stimulation as a Therapeutic Tool for Chronic Pain. (Cited on page 3.)
- Plonsey, R. and Heppner, D. B. (1967). Considerations of quasi-stationarity in electrophysiological systems. *Bull. Math. Biophys.*, 29(4):657–664. (Cited on page 4.)
- Puonti, O., Van Leemput, K., Saturnino, G. B., Siebner, H. R., Madsen, K. H., and Thielscher, A. (2020). Accurate and robust whole-head segmentation from magnetic resonance images for individualized head modeling. *Neuroimage*, 219:117044. (Cited on pages 4 and 119.)
- Purpura, D. P. and McMurtry, J. G. (1965). Intracellular Activities and Evoked Potential Changes During of motor cortex. *Neurophysiol*, 28(1):166–185. (Cited on page 119.)
- Qi, F., Nitsche, M. A., and Zschorlich, V. R. (2019). Interaction between transcranial random noise stimulation and observation-execution matching activity promotes motor cortex excitability. *Front. Neurosci.*, 13. (Cited on page 80.)
- Radman, T., Su, Y., Je, H. A., Parra, L. C., and Bikson, M. (2007). Spike timing amplifies the effect of electric fields on neurons: Implications for endogenous field effects. *J. Neurosci.*, 27(11):3030–3036. (Cited on page 6.)
- Ramon, C., Schimpf, P., Haueisen, J., Holmes, M., and Ishimaru, A. (2004). Role of soft bone, CSF and gray matter in EEG simulations. *Brain Topogr.*, 16(4):245–248. (Cited on page 9.)
- Rampersad, S., Roig-Solvas, B., Yarossi, M., Kulkarni, P. P., Santarnecchi, E., Dorval, A. D., and Brooks, D. H. (2019). Prospects for transcranial temporal interference stimulation in humans: A computational study. *Neuroimage*, 202. (Cited on page 117.)
- Rampersad, S. M., Janssen, A. M., Lucka, F., Aydin, U., Lanfer, B., Lew, S., Wolters, C. H., Stegeman, D. F., and Oostendorp, T. F. (2014). Simulating transcranial direct current stimulation with a detailed anisotropic human head model. *IEEE Trans. Neural Syst. Rehabil. Eng.*, 22(3):441–452. (Cited on page 4.)
- Reed, T. and Cohen Kadosh, R. (2018). Transcranial electrical stimulation (tES) mechanisms and its effects on cortical excitability and connectivity. (Cited on page 2.)
- Rolando, L. (1809). Saggio Sopra la Vera Struttura Del Cervello Dell’uomo e Degli Animali Sopra le Funzioni del Sistema Nervoso. (*Sassari, Stamperia di S. S. R. M. Privil.* (Cited on page 1.)
- Rubner, Y., Tomasi, C., and Guibas, L. J. (2000). Earth mover’s distance as a metric for image retrieval. *Int. J. Comput. Vis.*, 40(2):99–121. (Cited on page 12.)

- Sabel, B. A., Henrich-Noack, P., Fedorov, A., and Gall, C. (2011). Vision restoration after brain and retina damage: The 'residual vision activation theory'. *Prog. Brain Res.*, 192:199–262. (Cited on page 7.)
- Sabel, B. A., Kresinsky, A., Cardenas-Morales, L., Haueisen, J., Hunold, A., Dannhauer, M., and Antal, A. (2020a). Validating current density modeling of eye and brain current stimulation with phosphene thresholds. *under Revis.* (Cited on pages 7, 11, 22, 119, XVII, and XIX.)
- Sabel, B. A., Thut, G., Haueisen, J., Henrich-Noack, P., Herrmann, C. S., Hunold, A., Kammer, T., Matteo, B., Sergeeva, E. G., Waleszczyk, W., and Antal, A. (2020b). Vision modulation, plasticity and restoration using non-invasive brain stimulation – An IFCN-sponsored review. (Cited on pages 8 and 119.)
- Sadleir, R. J., Neralwala, F., Te, T., and Tucker, A. (2009). A controllably anisotropic conductivity or diffusion phantom constructed from isotropic layers. *Ann. Biomed. Eng.*, 37(12):2522–2531. (Cited on page 115.)
- Sadleir, R. J., Vannorsdall, T. D., Schretlen, D. J., and Gordon, B. (2012). Target optimization in transcranial direct current stimulation. (Cited on page 26.)
- San-Juan, D., Morales-Quezada, L., Orozco Garduño, A. J., Alonso-Vanegas, M., González-Aragón, M. F., López, D. A. E., Vázquez Gregorio, R., Anshel, D. J., and Fregni, F. (2015). Transcranial direct current stimulation in epilepsy. *Brain Stimul.*, 8(3):455–464. (Cited on page 3.)
- Sandran, N., Hillier, S., and Hordacre, B. (2019). Strategies to implement and monitor in-home transcranial electrical stimulation in neurological and psychiatric patient populations: A systematic review. (Cited on page 120.)
- Sarvas, J. (1987). Basic mathematical and electromagnetic concepts of the biomagnetic inverse problem. *Phys. Med. Biol.*, 32(1):11–22. (Cited on page 4.)
- Saturnino, G. B., Antunes, A., and Thielscher, A. (2015). On the importance of electrode parameters for shaping electric field patterns generated by tDCS. *Neuroimage*, 120:25–35. (Cited on pages 9, 49, 72, and 119.)
- Schimpf, P. H., Ramon, C., and Haueisen, J. (2002). Dipole models for the EEG and MEG. *IEEE Trans. Biomed. Eng.*, 49(5):409–418. (Cited on page 27.)
- Schlegelmilch, F., Schellhorn, K., and Stein, P. (2013). P 215. A method for online correction of artifacts in EEG signals during transcranial electrical stimulation. *Clin. Neurophysiol.*, 124(10):e166–e168. (Cited on page 80.)

- Schutter, D. J. and Hortensius, R. (2010). Retinal origin of phosphenes to transcranial alternating current stimulation. *Clin. Neurophysiol.*, 121(7):1080–1084. (Cited on page 80.)
- Schwan, H. P. and Ferris, C. D. (1968). Four-electrode null techniques for impedance measurement with high resolution. *Rev. Sci. Instrum.*, 39(4):481–485. (Cited on page 101.)
- Seibt, O., Brunoni, A. R., Huang, Y., and Bikson, M. (2015). The pursuit of DLPFC: Non-neuronavigated methods to target the left dorsolateral pre-frontal cortex with symmetric bicephalic transcranial direct current stimulation (tDCS). *Brain Stimul.*, 8(3):590–602. (Cited on pages 4 and 5.)
- Sonntag, H., Vorwerk, J., Wolters, C. H., Grasedyck, L., Haueisen, J., and Maess, B. (2013). Leakage Effect in Hexagonal FEM Meshes of the EEG Forward Problem. *Clin. EEG Neurosci.*, 44(4):E60. (Cited on page 24.)
- Sprugnoli, G., Monti, L., Lippa, L., Neri, F., Mencarelli, L., Ruffini, G., Salvador, R., Oliveri, G., Batani, B., Momi, D., Cerase, A., Pascual-Leone, A., Rossi, A., Rossi, S., and Santarnecchi, E. (2019). Reduction of intratumoral brain perfusion by noninvasive transcranial electrical stimulation. *Sci. Adv.*, 5(8). (Cited on page 5.)
- Stenroos, M., Hunold, A., and Haueisen, J. (2014). Comparison of three-shell and simplified volume conductor models in magnetoencephalography. *Neuroimage*, 94:337–348. (Cited on pages 32, 97, and 115.)
- Stenroos, M., Mäntynen, V., and Nenonen, J. (2007). A Matlab library for solving quasi-static volume conduction problems using the boundary element method. *Comput. Methods Programs Biomed.*, 88(3):256–263. (Cited on page 4.)
- Tallgren, P., Vanhatalo, S., Kaila, K., and Voipio, J. (2005). Evaluation of commercially available electrodes and gels for recording of slow EEG potentials. *Clin. Neurophysiol.*, 116(4):799–806. (Cited on page 70.)
- Tang, C., You, F., Cheng, G., Gao, D., Fu, F., Yang, G., and Dong, X. (2008). Correlation between structure and resistivity variations of the live human skull. *IEEE Trans. Biomed. Eng.*, 55(9):2286–2292. (Cited on page 9.)
- Tavakoli, A. V. and Yun, K. (2017). Transcranial alternating current stimulation (tACS) mechanisms and protocols. (Cited on page 2.)
- Tenner, U., Haueisen, J., Nowak, H., Leder, U., and Brauer, H. (1999). Source localization in an inhomogeneous physical thorax phantom. *Phys. Med. Biol.*, 44(8):1969–1981. (Cited on page 5.)

- Thielscher, A., Antunes, A., and Saturnino, G. B. (2015). Field modeling for transcranial magnetic stimulation: A useful tool to understand the physiological effects of TMS? In *Proc. Annu. Int. Conf. IEEE Eng. Med. Biol. Soc. EMBS*, volume 2015-Novem, pages 222–225. (Cited on page 4.)
- Treffene, R. J. (1983). Interferential Fields in a Fluid Medium. *Aust. J. Physiother.*, 29(6):209–216. (Cited on page 95.)
- van Schouwenburg, M. R., Zanto, T. P., and Gazzaley, A. (2017). Spatial attention and the effects of frontoparietal alpha band stimulation. *Front. Hum. Neurosci.*, 10. (Cited on page 69.)
- Vöröslakos, M., Takeuchi, Y., Brinyiczki, K., Zombori, T., Oliva, A., Fernández-Ruiz, A., Kozák, G., Kincses, Z. T., Iványi, B., Buzsáki, G., and Berényi, A. (2018). Direct effects of transcranial electric stimulation on brain circuits in rats and humans. *Nat. Commun.*, 9(1). (Cited on pages 5, 6, and 119.)
- Vorwerk, J., Cho, J. H., Rampp, S., Hamer, H., Knösche, T. R., and Wolters, C. H. (2014). A guideline for head volume conductor modeling in EEG and MEG. *Neuroimage*, 100:590–607. (Cited on page 4.)
- Vossen, A., Gross, J., and Thut, G. (2015). Alpha power increase after transcranial alternating current stimulation at alpha frequency (a-tACS) reflects plastic changes rather than entrainment. *Brain Stimul.*, 8(3):499–508. (Cited on page 2.)
- Wagner, S., Burger, M., and Wolters, C. H. (2016). An optimization approach for well-targeted transcranial direct current stimulation. *SIAM J. Appl. Math.*, 76(6):2154–2174. (Cited on pages 4 and 26.)
- Wagner, S., Rampersad, S. M., Aydin, Ü., Vorwerk, J., Oostendorp, T. F., Neuling, T., Herrmann, C. S., Stegeman, D. F., and Wolters, C. H. (2014). Investigation of tDCS volume conduction effects in a highly realistic head model. *J. Neural Eng.*, 11(1):14pp. (Cited on pages 4 and 9.)
- Ward, A. R. (2009). Electrical Stimulation Using Kilohertz-Frequency Alternating Current. *Phys. Ther.*, 89(2):181–190. (Cited on page 95.)
- Wedensky, N. E. (1903). Die Erregung, Hemmung und Narkose. *Pflüger, Arch. für die Gesamte Physiol. des Menschen und der Thiere*, 100(1-4):1–144. (Cited on page 95.)
- Wendel, K., Narra, N. G., Hannula, M., Kauppinen, P., and Malmivuo, J. (2008). The influence of CSF on EEG sensitivity distributions of multilayered head models. *IEEE Trans. Biomed. Eng.*, 55(4):1454–1456. (Cited on pages 97 and 116.)

- Wetterling, F., Liehr, M., Schimpf, P., Liu, H., and Haueisen, J. (2009). The localization of focal heart activity via body surface potential measurements: Tests in a heterogeneous torso phantom. *Phys. Med. Biol.*, 54(18):5395–5409. (Cited on page 5.)
- Windhoff, M., Opitz, A., and Thielscher, A. (2013). Electric field calculations in brain stimulation based on finite elements: An optimized processing pipeline for the generation and usage of accurate individual head models. *Hum. Brain Mapp.*, 34(4):923–935. (Cited on page 4.)
- Woods, A. J., Antal, A., Bikson, M., Boggio, P. S., Brunoni, A. R., Celnik, P., Cohen, L. G., Fregni, F., Herrmann, C. S., Kappenman, E. S., Knotkova, H., Liebetanz, D., Miniussi, C., Miranda, P. C., Paulus, W., Priori, A., Reato, D., Stagg, C., Wenderoth, N., and Nitsche, M. A. (2016). A technical guide to tDCS, and related non-invasive brain stimulation tools. (Cited on pages 3 and 72.)
- Wunder, S., Hunold, A., Fiedler, P., Schlegelmilch, F., Schellhorn, K., and Haueisen, J. (2018). Novel bifunctional cap for simultaneous electroencephalography and transcranial electrical stimulation. *Sci. Rep.*, 8(1). (Cited on pages 27, 53, 56, 57, 67, 68, 70, XVII, and XIX.)
- Zaehle, T., Rach, S., and Herrmann, C. S. (2010). Transcranial Alternating Current Stimulation Enhances Individual Alpha Activity in Human EEG. *PLoS One*, 5(11). (Cited on pages 74 and 79.)

Appendix

Questionnaire Usability evaluation of TES application systems

To be filled by the operator.

ID

Date

Session

Time

Trial

System

C

R

Please answer the following questions about the usability of the two application systems. Your answers will help to evaluate the stability, repeatability and manageability of the two systems.

Application of electrodes

How did you find the application of the electrodes?

very comfortable

comfortable

neutral

uncomfortable

very uncomfortable

How do you evaluate the duration of the electrode application?

very fast

fast

neutral

slow

very slow

Did you feel any pressure during application? If yes, where and how did you felt it.

	light	intermediate	strong
at the electrodes	<input type="checkbox"/>	<input type="checkbox"/>	<input type="checkbox"/>
at the temples	<input type="checkbox"/>	<input type="checkbox"/>	<input type="checkbox"/>
at the strap	<input type="checkbox"/>	<input type="checkbox"/>	<input type="checkbox"/>
others ...	<input type="checkbox"/>	<input type="checkbox"/>	<input type="checkbox"/>
non	<input type="checkbox"/>		

During the stimulation

10 min in stimulation

Do you sweat at your head?

<input type="checkbox"/>	<input type="checkbox"/>	<input type="checkbox"/>	<input type="checkbox"/>	<input type="checkbox"/>
no	slight	moderate	strong	very strong

Do you feel itching at your head?

<input type="checkbox"/>	<input type="checkbox"/>	<input type="checkbox"/>	<input type="checkbox"/>	<input type="checkbox"/>
no	slight	moderate	strong	very strong

Do you feel any pressure? If yes, where and how do you feel it.

	light	intermediate	strong
at the electrodes	<input type="checkbox"/>	<input type="checkbox"/>	<input type="checkbox"/>
at the temples	<input type="checkbox"/>	<input type="checkbox"/>	<input type="checkbox"/>
at the strap	<input type="checkbox"/>	<input type="checkbox"/>	<input type="checkbox"/>
others ...	<input type="checkbox"/>	<input type="checkbox"/>	<input type="checkbox"/>
non	<input type="checkbox"/>		

20 min in stimulation

Do you sweat at your head?

<input type="checkbox"/>	<input type="checkbox"/>	<input type="checkbox"/>	<input type="checkbox"/>	<input type="checkbox"/>
no	slight	moderate	strong	very strong

Do you feel itching at your head?

<input type="checkbox"/>	<input type="checkbox"/>	<input type="checkbox"/>	<input type="checkbox"/>	<input type="checkbox"/>
no	slight	moderate	strong	very strong

Do you feel any pressure? If yes, where and how do you feel it.

	light	intermediate	strong
at the electrodes	<input type="checkbox"/>	<input type="checkbox"/>	<input type="checkbox"/>
at the temples	<input type="checkbox"/>	<input type="checkbox"/>	<input type="checkbox"/>
at the strap	<input type="checkbox"/>	<input type="checkbox"/>	<input type="checkbox"/>
others ...	<input type="checkbox"/>	<input type="checkbox"/>	<input type="checkbox"/>
non	<input type="checkbox"/>		

After the stimulation

Do you sweat at your head?

<input type="checkbox"/>	<input type="checkbox"/>	<input type="checkbox"/>	<input type="checkbox"/>	<input type="checkbox"/>
no	slight	moderate	strong	very strong

Do you feel itching at your head?

<input type="checkbox"/>	<input type="checkbox"/>	<input type="checkbox"/>	<input type="checkbox"/>	<input type="checkbox"/>
no	slight	moderate	strong	very strong

Do you feel any pressure? If yes, where and how do you feel it.

	light	intermediate	strong
at the electrodes	<input type="checkbox"/>	<input type="checkbox"/>	<input type="checkbox"/>
at the temples	<input type="checkbox"/>	<input type="checkbox"/>	<input type="checkbox"/>
at the strap	<input type="checkbox"/>	<input type="checkbox"/>	<input type="checkbox"/>
others ...	<input type="checkbox"/>	<input type="checkbox"/>	<input type="checkbox"/>
non	<input type="checkbox"/>		

How do you evaluate the overall comfort of the application system?

<input type="checkbox"/>	<input type="checkbox"/>	<input type="checkbox"/>	<input type="checkbox"/>	<input type="checkbox"/>
very comfortable	comfortable	neutral	uncomfortable	very uncomfortable

Professional experience

- Since 01/2013** **Technische Universität Ilmenau**
Department of Computer Science and Automation,
Institute of Biomedical Engineering and Informatics
Teaching: Supervision of > 40 students (up to 5 in parallel)
 Seminars within the framework of courses
 Organisation of the 7th International Summer School in
 Biomedical Engineering
Research projects:
Since 06/2018 multiTES: Leading employee, essential contribution to application
 Granted by Thüringer Aufbaubank
01/2016 – 12/2018 Breakben: Leading employee, contribution to application
 Granted by European Commission within FET-Open
 program
01/2013 – 12/2015 EyeTSS: Project employee, contribution to application
 Granted by German ministry for education and research
- Since 05/2020** **neuroCare Group GmbH**
Consulting the production of a small series and certification
- 04/2018 – 05/2018** **University of Queensland**
Center of Clinical Reserach
Guest researcher with Prof. Marcus Meinzer
Project: Simulation and application of transkraniel electrical stim-
 ulation
- 04/2016 – 09/2017** **neuroCare Group GmbH**
Trainer and consultant
- 12/2015** **Aalto University**
Department of Neuroscience and Biomedical Engineering
Guest researcher with Dr. Matti Stenroos
Project: Volume conductor modeling for EEG and MEG
- 04/2012 – 10/2012** **Boston Children's Hospital / Harvard Medical School**
Department of Neurology
Master student with Prof. Christos Papadelis und Prof. Yoshio Okada
Project: EEG and MEG studies of pediatric epilepsy patients

-
- 12/2015** **University of Porto**
Faculdade de Engenharia
Student intern with Prof. Carlos Fonseca
Project: Ag/AgCl coating of polyurethane
- 09/2010 – 03/2011** **University of Utah**
Magnetic Source Imaging
Bachelor student with Prof. Michael Funke
Project: Simulation of epileptic activity in EEG and MEG signals
- 09/2009** **HELIOS Klinikum, Erfurt**
Intern at radiology
- 09/2008** **Siemens AG**
Apprenticeship workshop
Basic internship in engineering
- 06/2007 – 08/2007** **Assistant**
Automotive industry, electric installation

Awards

- 03/2018** **Young Investigator Award**, third place at Workshop Biosignals 2018 in Biomedical Engineering
- 10/2007 – 12/2012** **Stipend**, German National Academic Foundation
- 10/2012** **Annual Award** by LIONS Club Arnstadt/Ilmenau for excellent course achievement and social engagement
- 01/2012** **Foreign Exchange Scholarship** (6 months), German National Academic Foundation
- 06/2010** **Foreign Exchange Scholarship** (7 months), German National Academic Foundation

Training courses

03/2016 Project management: Scrum Foundation, Master, Product Owner

04/2012 Software course: Brainstorm 3.0, MIT, Cambridge, MA, USA

04/2012 MEG Symposium, McGovern Institute, MIT, Cambridge, MA, USA

09/2011 Summer School, German National Academic Foundation

Topic: Neurocomputational models of maladaptive behaviour and psychiatric disease

09/2011 Summer School, German National Academic Foundation

Topic: Molecular diagnostics to therapy / Magnetic resonance imaging

Skills

IT	MATLAB, Basics in Python, C++, C#, Pascal IDEs: Qt Creator, MS Visual Studio, Eclipse Linux environment, bash scripting Comsol
CAD	SolidWorks, PSpice
Prototyping	Fused Deposition Modeling, Polyjet Printing, UV-LCD-Sterolithography, Selective Laser Sintering, vacuum casting, Structured Light 3D Scanner
Project Management	Scrum Product Owner, Master, Foundation (certified by TÜV Süd), JIRA
Office	MS Office (Word, PowerPoint, Excel, Visio, Outlook, Project), Latex, Corel

Voluntary engagements

Peer reviews Journal of Neural Engineering, Human Brain Mapping, NeuroImage Clinical, Journal of NeuroEngineering and Rehabilitation, IEEE Access and Journal of Sensors

2013 – 2014 **Mentor**, Student group in Biomedical Engineering

2013 – 2014 **Student Member**, Program commission Biomedical Engineering, Technische Universität Ilmenau

2008 – 2010 **Student Member**, Study council, Technische Universität Ilmenau

1996 – 2014 **German Catholic Scout Organization (DPSG)**

2006 – 2009 Youth leader – organisation of national and international meetings

List of publications

Peer reviewed journal papers

1. **Hunold, A.**, Machts, R.; Haueisen, J. (2020) Head phantoms for bioelectromagnetic applications: a material study. *Biomedical Engineering Online*. 19(1):87.
2. **Hunold, A.**, Ortega, D.; Schellhorn, K.; Haueisen, J. (2020) Novel flexible cap for application of transcranial electric stimulation: a usability study. *Biomedical Engineering Online*. 19(1):50.
3. Blum, M.-C.; **Hunold, A.**; Solf, B.; Klee, S. (2020) The Effects of an Ocular Direct Electrical Stimulation on Pattern-Reversal Electroretinogram. *Frontiers in Neuroscience*. 14:588.
4. Hömmen, P.; Mäkinen, A.J.; **Hunold, A.**; Machts, R.; Haueisen, J.; Zevenhoven, K.C.J.; Ilmoniemi, R.J.; Körber, R. (2020) Evaluating the Performance of Ultra-Low-Field MRI for In-vivo 3D Current Density Imaging of the Human Head. *Frontiers in Physics, section Medical Physics and Imaging*. 8:105.
5. Sabel, B.A.; Thut, G.; Haueisen, J.; Henrich-Noack, P.; Herrmann, C.S.; **Hunold, A.**; Kammer, T.; Matteo, B.; Sergeeva, E.G.; Waleszczyk, W.; Antal, A. (2020) Vision modulation, plasticity and restoration using non-invasive brain stimulation – An IFCN-sponsored review. *Clinical Neurophysiology*. 131(4):887-911.
6. Freitag, S.; **Hunold, A.**; Klemm, M.; Klee, S.; Link, D.; Nagel, E.; Haueisen, J. (2019) Pulsed Electrical Stimulation of the Human Eye Enhances Retinal Vessel Reaction to Flickering Light. *Frontiers in Human Neuroscience*. 13:371.
7. Machts, R.; **Hunold, A.**; Drebenstedt, C.; Rock, M.; Leu, C.; Haueisen, J. (2019) Measurement and analysis of partial lightning currents in a head phantom. *PLoS one*. 14(9):e0223133.
8. Eichardt, R.; Strohmeier, D.; **Hunold, A.**; Machts, R.; Haueisen, J.; Oelsner, G.; Schmidt, C.B.; Volkmar Schultze, V.; Stolz, R.; Graichen, U. (2019) Sensitivity studies and optimization of arrangements of optically pumped magnetometers in simulated magnetoencephalography. *COMPEL-The international journal for computation and mathematics in electrical and electronic engineering*. 38(3):953-964.

9. Gbadeyan, O.; Steinhäuser, M.; **Hunold, A.**; Martin, A.K.; Haueisen, J.; Meinzer, M. (2019), Modulation of adaptive cognitive control by prefrontal high definition transcranial direct current stimulation in older adults. *The Journals of Gerontology: Series B*. 74(7):1174-1183.
10. Martin, A.K.; Huang, J.; **Hunold, A.**; Meinzer, M. (2018), Dissociable Roles Within the Social Brain for Self-Other Processing: A HD-tDCS Study. *Cerebral Cortex*. 29(8):3642-3654.
11. **Hunold, A.**; Strohmeier, D.; Fiedler, P.; Haueisen, J. (2018), Head phantoms for electroencephalography and transcranial electric stimulation: a skull material study. *Biomedical Engineering/Biomedizinische Technik*. 63(6):683-689
12. Wunder, S.; **Hunold, A.**; Fiedler, P.; Schlegelmilch, F.; Schellhorn, K.; Haueisen J. (2018), Novel bifunctional cap for simultaneous electroencephalography and transcranial electrical stimulation. *Scientific Reports*. 8:7259.
13. Martin, A.K.; Huang, J.; **Hunold, A.**; Meinzer, M. (2017), Sex Mediates the Effects of High-Definition Transcranial Direct Current Stimulation on 'Mind-Reading'. *Neuroscience*. 366:84-94.
14. **Hunold, A.**; Funke, M.E.; Eichardt, R.; Stenroos, M.; Haueisen, J. (2016), EEG and MEG: sensitivity to epileptic spike activity as function of source orientation and depth. *Physiological Measurement*. 37(7):1146-1162.
15. Kunze, T.; **Hunold, A.**; Haueisen, J.; Jirsa, V.; Spiegler, A. (2016), Transcranial Direct Current Stimulation Changes Resting State Functional Connectivity: A Large-Scale Brain Network Modeling Study, *NeuroImage*, 140:174-187.
16. **Hunold, A.**; Haueisen, J.; Ahtam, B.; Doshi, C.; Harini, C.; Camposano, S.; Warfield, S. K.; Grant, P. E.; Okada, Y.; Papadelis, C. (2014): Localization of the epileptogenic foci in tuberous sclerosis complex: a pediatric case report, *Frontiers in Human Neuroscience*, 8:175.
17. Stenroos, M.; **Hunold, A.**; Haueisen, J. (2014): Comparison of three-shell and simplified volume conductor models in magnetoencephalography, *NeuroImage*, 94:337-348.

Oral presentations

1. **Hunold, A.**; Haueisen, J. (2019): Temperature changes during transcranial direct current stimulation. 4th International Conference on Basic and Clinical Multimodal Imaging; September 14, Chengdu, China

-
2. **Hunold, A.**; Graichen, U.; Schellhorn, K.; Haueisen, J. (2018): Simulated current density and technical parameters of TES applied with a flexible cap. 52th DGBMT Annual Conference; October 27, Aachen, Germany
 3. **Hunold, A.** (2018): Transcranial Electric Stimulation - Modeling, Application and Verification, Seminar at Center of Advanced Imaging (CAI) at the University of Queensland, Brisbane, Australia
 4. **Hunold, A.**; Kresinsky, A.; Sabel, B. A.; Haueisen, J. (2018): Simulation of the current density in the retina for transorbital electric current stimulation. Workshop 'Innovative Verarbeitung bioelektrischer und biomagnetischer Signale'; March 22nd, Erfurt, Germany
 5. **Hunold, A.**; Graichen, U.; Schellhorn, K.; Haueisen, J. (2018): Flexible stimulation cap for TES applications: technical parameters and current density simulations. 62th Annual conference of the German Society on Clinical Neurophysiology; March 3, Berlin, Germany
 6. **Hunold, A.**; Schellhorn, K.; Haueisen, J. (2016): Dipole forward simulation guides transcranial electric stimulation of the hand knob area. URSI International Symposium on Electromagnetic Theory (EMTS); August 18, Aalto University, Espoo, Finland
 7. **Hunold, A.**; Schellhorn, K.; Haueisen, J. (2016): Transcranial electric stimulation of the hand knob area guided by a dipole forward simulation. Workshop 'Innovative Verarbeitung bioelektrischer und biomagnetischer Signale'; April 7-8, TU Berlin, Germany
 8. **Hunold, A.**; Schellhorn, K.; Haueisen, J. (2015): Simulation of multichannel transcranial electric stimulation. 6th International Summer School in Biomedical Engineering - New Instrumentation for brain measurements and stimulation; August 17 - 29, Lutherstadt Wittenberg, Germany
 9. **Hunold, A.**; Fiedler, P.; Lau, S.; Güllmar, D.; Haueisen, J. (2014): Skull-equivalent material for an EEG physical head phantom. 48th DGBMT Annual Conference; October 8-10, Hannover, Germany
 10. **Hunold, A.**; Funke, M.; Eichardt, R.; Haueisen, J. (2014): Complementary Sensitivity of EEG and MEG to Tangential and Radial Epileptic Spike Activity: Influence of Source Depth. 4th Conference on Information Technologies in Biomedicine; June 2nd - 4th, Kamien Slaski, Poland
 11. **Hunold, A.**; Funke, M.; Eichardt, R.; Haueisen, J. (2014): Complementary Sensitivity of EEG and MEG to Tangential and Radial Epileptic Spike Activity: Influence

- of Source Depth. Workshop 'Innovative Verarbeitung bioelektrischer und biomagnetischer Signale'; April 10-11, PTB Berlin, Germany
12. **Hunold, A.**; Funke, M.; Eichardt, R.; Haueisen, J. (2013): Simultaneous measurement of EEG and MEG. 6th International Summer School in Biomedical Engineering - Multimodal integration of brain measurements in research and clinical practice; September 23 - October 6, Havana, Cuba
 13. **Hunold, A.** (2011): Sensitivity of EEG and MEG to epileptic-form activity depending on source orientation and depth, Seminar at Scientific Computing and Imaging Institute (SCI) at the University of Utah, Salt Lake City, USA
 14. **Hunold, A.** (2011): Introduction to MEG and sensitivity simulations, Seminar at Department of Biomedical Engineering at the University of Utah, Salt Lake City, USA

Peer reviewed conference papers

1. Machts, R.; **Hunold, A.**; Drebenstedt, C.; Rock, M.; Leu, C.; Haueisen, J. (2020): Effects of rain on human head during direct lightning strike. In 34th International Conference on Lightning Protection (ICLP)
2. Machts, R.; **Hunold, A.**; Rock, M.; Leu, C.; Haueisen, J. (2019): Simulation of Lightning Current Distributions in a realistic Human Head Model. International Conference on Software, Telecommunications and Computer Networks (SoftCOM). Split, Croatia. 1-6
3. Machts, R.; **Hunold, A.**; Drebenstedt, C.; Rock, M.; Leu, C.; Haueisen, J. (2019). Experimental Application of Lightning Currents to a Human Head Phantom. In: Németh B. (eds) Proceedings of the 21st International Symposium on High Voltage Engineering. ISH 2019. Lecture Notes in Electrical Engineering. 599:763-772.
4. Blum, M. C.; **Hunold, A.**; Link, D.; Freitag, S.; Klee, S. (2019). Amplitude changes in the electrophysiological response of retinal cells during simultaneous current stimulation. *Investigative Ophthalmology & Visual Science*. 60(9):2504.
5. Fiedler, P.; Strohmeier, D.; **Hunold, A.**; Griebel, S.; Mühle, R.; Schreiber, M.; Fonseca, C.; Vaz, F.; Haueisen, J. (2016). Modular multipin electrodes for comfortable dry EEG. In 38th Annual International Conference of the IEEE Engineering in Medicine and Biology Society (EMBC). Orlando, FL, USA. 5705-5708.
6. Machts, R.; **Hunold, A.**; Leu, C.; Haueisen, J.; Rock, M. (2016). Development of a head-phantom and measurement setup for lightning effects. In 38th Annual

International Conference of the IEEE Engineering in Medicine and Biology Society (EMBC). Orlando, FL, USA. 3590-3593.

7. Freitag, S.; **Hunold, A.**; Klemm, M.; Klee, S.; Rieger, S.; Link, D.; Haueisen, J. (2016). Anodal direct current stimulation at the eye evokes temporary variations in retinal vessel response to flicker. *Investigative Ophthalmology & Visual Science*. 57(12):4620.
8. Kunze, T.; **Hunold, A.**; Haueisen, J.; Jirsa, V.; Spiegler, A. (2015). Investigating the effect of electrical brain stimulation using a connectome-based brain network model. *BMC neuroscience*. 16(1):1-2.
9. **Hunold, A.**; Weise, K.; Di Rienzo, L.; Codecasa, L.; Haueisen, J. (2015): Sensitivity of Transcranial Electric Stimulation to Tissue Conductivities Using Non-intrusive Polynomial Chaos Expansion. In 20th International Conference on the Computation of Electromagnetic Fields (COMPUMAG). Montreal, Canada.
10. **Hunold, A.**; Freitag, S.; Schellhorn, K.; Haueisen, J. (2015). Simulation of the current density distribution for transcranial electric current stimulation around the eye. *Brain Stimulation*. 8(2). 406.
11. Fiedler, P.; **Hunold, A.**; Müller, C.; Rosner, G.; Schellhorn, K.; Haueisen, J. (2015). Novel flexible cap with integrated textile electrodes for rapid transcranial electrical stimulation. *Brain Stimulation*. 8(2). 405-406.
12. **Hunold, A.**; Haueisen, J.; Ahtam, B.; Doshi, C.; Harini, C.; Camposano, S.; Warfield, S. K.; Grant, P. E.; Okada, Y.; Papadelis, C. (2013): LP31: EEG and MEG source localization of the epileptogenic foci in tuberous sclerosis complex: a pediatric case report. *Clinical Neurophysiology*. 125(Supplement 1):S174-S175.
13. **Hunold, A.**; Funke, M.; Eichardt, R.; Haueisen, J. (2013): Sensitivity Analysis to Epileptic Sources in Electro- and Magnetoencephalography. In 21st International Conference on Software, Telecommunications and Computer Networks-(SoftCOM 2013). Primosten, Split, Croatia. 1-3.

Conference abstracts

1. **Hunold, A.**; Berkes, S.; Schellhorn, K.; Antal, A.; Haueisen J. (2020): Feasibility of new stimulator setup for temporal interference TES and its application in a homogeneous volume conductor. 7th International Conference on Non-invasive Brain Stimulatio, November 10
2. Machts, R.; **Hunold, A.**; Haueisen, J. (2019): The effect of dipole housing and feeding wires in physical phantoms for EEG. 53th Annual scientific conference of

- the German Society for Biomedical Engineering, September 25, Frankfurt am Main, Germany
3. Hömmen, P.; Mäkinen, A.; Storm, J.H.; Höfner, N.; **Hunold, A.**; Machts, R.; Haueisen, J.; Körber, R. (2019): An optimized ultra-low field MRI setup for zero-field encoded current density imaging of the human head. 53th Annual scientific conference of the German Society for Biomedical Engineering, September 25, Frankfurt am Main, Germany
 4. Hömmen, P.; Mäkinen, A.; **Hunold, A.**; Machts, R.; Haueisen, J.; Körber, R. (2019) Evaluating the Performance of Ultra-Low Field MRI in In-vivo 3D Current Density Imaging of the Human Head. Workshop "Today's Noise Tomorrow's Signal", February 2, Berlin, Germany
 5. Haueisen J.; **Hunold, A.** (2019): Bifunctional cap for simultaneous EEG and tES. 13th International Conference on Complex Medical Engineering (CME), September 24, Dortmund, Germany
 6. **Hunold, A.**; Blum, M.-C.; Haueisen J. (2019): Evaluation of pH changes and skin redness in direct current stimulation to the forearm. 13th International Conference on Complex Medical Engineering (CME), September 23, Dortmund, Germany
 7. **Hunold, A.**; Haueisen, J. (2019): Specific Absorption Rate and Temperature change during transcranial direct current stimulation. 4th International Conference on Basic and Clinical Multimodal Imaging, September 14, Chengdu, China
 8. **Hunold, A.**; Haueisen, J. (2019): Simultaneous electroencephalography and transcranial electric stimulation using innovative electrode materials integrated in a flexible cap. Brain Twitter Conference 2019 #braintc, March 12
 9. **Hunold, A.**; Graichen, U.; Schellhorn, K.; Haueisen, J. (2018): Flexible Stimulationshaube für TES Anwendungen: Technische Parameter und Stromdichtesimulationen. Annual meeting of the German Society for Clinical Neurophysiology (DGKN), March 16, Berlin, Germany
 10. **Hunold, A.**; Kesinsky, A.; Sabel, B.A.; Haueisen, J. (2018): Simulation of the current density in the retina for transorbital electric current stimulation. Workshop "Innovative Verarbeitung bioelektrischer und biomagnetischer Signale", March 22, Erfurt, Germany
 11. **Hunold, A.**; Graichen, U.; Schellhorn, K.; Haueisen, J. (2018): Simulated current density and technical parameters of TES applied with a flexible cap. 52th Annual scientific conference of the German Society for Biomedical Engineering, September 27, Aachen

-
12. **Hunold, A.**; Schellhorn, K.; Haueisen, J. (2018): Simulating the superposition of transcranial electric stimulations targeting the visual cortex. 21th International Conference on Biomagnetism, August 28, 2018, Philadelphia, USA
 13. **Hunold, A.**; Schellhorn, K.; Haueisen, J. (2018): Simulating the superposition of transcranial electric stimulations targeting the visual cortex. 21th International Conference on Biomagnetism, August 28, 2018, Philadelphia, USA
 14. Hömmen, P.; Storm, J.H.; Höfner, N.; **Hunold, A.**; Machts, R.; Haueisen, J.; Körber, R. (2018): Current Density Imaging in the Head using Ultra-Low Field Magnetic Resonance An Advanced Phantom Study. 21th International Conference on Biomagnetism, August 28, 2018, Philadelphia, USA
 15. Eichardt, R.; Strohmeier, D.; **Hunold, A.**; Haueisen, J.; Oelsner, G.; Schmidt, C.B.; Schultze, V.; Graichen, U. (2018): Sensitivity evaluations of new optically-pumped magnetometers in simulated magnetoencephalography. 21th International Conference on Biomagnetism, August 28, 2018, Philadelphia, USA
 16. Dinh, C.; Samuelsson, J.G.; **Hunold, A.**; Khan, S.; Hämäläinen M.S. (2018): Deep Learning for MEG/EEG Distributed Source Estimation - CMNE. 21th International Conference on Biomagnetism, August 28, 2018, Philadelphia, USA
 17. Graichen, U.; Eichardt, R.; **Hunold, A.**; Haueisen, J. (2018): Estimating the spatial frequency response of realistic head models. World Congress on Medical Physics and Biomedical Engineering, June 3-8, Prague, Czech Republic
 18. Lau, S.; Fiedler, P.; **Hunold, A.**; Haase, E.; Grölllich, D.; Pietsch, K.; Höhn, K.; Schmauder, M.; Rödel, H.; Haueisen, J. (2017): Perception thresholds of cutaneous electric stimulation around the upper arm. 51th Annual scientific conference of the German Society for Biomedical Engineering, September 12, Dresden, Germany
 19. Machts, R.; **Hunold, A.**; Haueisen, J. (2017): Realization and Testing of a 3D Electrode Array for measuring Electric Potential Differences in a Volume Conductor. 51th Annual scientific conference of the German Society for Biomedical Engineering, September 12, Dresden, Germany
 20. Machts, R.; **Hunold, A.**; Haueisen, J.; Rock, M.; Leu, C. (2017): Analyse von Blitzstromverteilungen in einem Kopfphantom mittels Messungen und Simulationen. Präsentation auf der 12. VDE/ABB-Blitzschutztagung, Oktober 12, Aschaffenburg, Germany
 21. Kresinsky, A.; Cárdenas-Morales, L.; Haueisen, J.; **Hunold, A.**; Dannhauer, M.; Antal, A. and Sabel, B.A. (2017): How current density models of eye and brain relate to phosphene thresholds following alternating current stimulation. 4th International Symposium 'Low Vision and the Brain', November 25, Berlin, Germany

22. **Hunold, A.**; Haueisen, J. (2017): Simulated current density magnitudes and orientations for transcranial direct current stimulation montages used in depression studies. 3rd International Conference on Basic and Clinical Multimodal Imaging, September 1, Bern, Switzerland
23. Haueisen, J.; Hunold, A. (2017): Concept of a physical head phantom MEG-MRI and NCI/CDI. Brain Twitter Conference 2017 #braintc - Neuroscience making an impact, April 20
24. **Hunold, A.**; Schellhorn, K.; Haueisen, J. (2016): Transcranial electric stimulation of the hand knob area guided by a dipole forward simulation. 'Innovative Verarbeitung bioelektrischer und biomagnetischer Signale', April 8, Berlin, Germany
25. Fiedler, P.; Strohmeier, D.; **Hunold, A.**; Griebel, S.; Schreiber, M.; Haueisen, J. (2016): Novel electrode technologies for neurosciences. 'Innovative Verarbeitung bioelektrischer und biomagnetischer Signale', April 8, Berlin, Germany
26. Freitag, S.; **Hunold, A.**; Klemm, M.; Haueisen, J. (2016): Variation der retinalen Gefäßreaktion während elektrischer Stimulation am Auge. Workshop 'Innovative Verarbeitung bioelektrischer und biomagnetischer Signale', April 8, Berlin, Germany
27. **Hunold, A.**; Lau, S.; Okada, Y.; Papadelis, C.; Haueisen, J. (2016): Calcified cortical tubers influence single dipole source localization. 20th International Conference on Biomagnetism, October 4, 2016, Seoul, Republic of Korea
28. Horn, C.; **Hunold, A.**; Haueisen, J.; Funke, M.E. (2016): Comparison of dipole localization to interictal spikes in individual and standardized BEM upon three different age group. 20th International Conference on Biomagnetism, October 4, 2016, Seoul, Republic of Korea
29. Eichardt, R.; Haueisen, J.; **Hunold, A.**; Graichen, U. (2016). Scheduling of Machines with Storage and Limited Availability using a Random Search Heuristic. 14th International Workshop on Optimization and Inverse Problems in Electromagnetism, September 14, 2016, Rome, Italy
30. **Hunold, A.**; Schellhorn, K.; Haueisen, J. (2016): Transcranial electric stimulation guided by dipole forward simulation. 6th International Conference on Transcranial Brain Stimulation, September 8, Göttingen, Germany
31. Kunze, T.; **Hunold, A.**; Haueisen, J.; Jirsa, V.; Spiegler, A. (2015): Transcranial Direct Current Stimulation Establishes Additional Functional Links in a Computational Brain Network Model. 49th Annual scientific conference of the German Society for Biomedical Engineering, September 16, Lübeck, Germany
32. Freitag, S.; **Hunold, A.**; Klemm, M.; Enders, G.; Nagel, E.; Haueisen, J. (2015): Effects of pulsed anodal transcranial electrical stimulation at the eye. 49th Annual

-
- scientific conference of the German Society for Biomedical Engineering, September 18, Lübeck, Germany
33. **Hunold, A.**; Haueisen, J.; Siniatchkin, M.; Moliadze, V. (2015): Cortical current density magnitudes during transcranial direct current stimulation correlate with skull thickness in children and adults. 2nd International Conference on Basic and Clinical Multimodal Imaging, September 2, Utrecht, The Netherlands
 34. Titova, O.; Freitag, S.; **Hunold, A.**; Klemm, M.; Haueisen, J. (2015): Effects of anodal transcranial direct current stimulation at the eye on the electroretinogram. 2nd International Scientific Symposium 'Sense. Enable. SPITSE.', June 24, St. Petersburg, Russia
 35. **Hunold, A.**; Freitag, S.; Schellhorn, K.; Haueisen, J. (2015): Simulation of the current density distribution for transcranial electric current stimulation around the eye. 21st Annual meeting of the Organization for Human Brain Mapping, June 15, Honolulu, USA
 36. **Hunold, A.**; Haueisen, J.; Ahtam, B.; Doshi, C.; Grant, P. E.; Okada, Y.; Papadelis, C. (2013): Time shift between the interictal spikes in simultaneous EEG and MEG recordings reflects different epileptogenic generators. 19th International Conference on Biomagnetism, August 27, Halifax, Canada
 37. Eichardt, R.; Graichen, U.; **Hunold, A.**; Haueisen, J. (2014): Multi-level conflict-free scheduling for electroplating plants. 13th International Workshop on Optimization and Inverse Problems in Electromagnetism, September 12, Delft, The Netherlands
 38. **Hunold, A.**; Haueisen, J.; Ahtam, B.; Doshi, C.; Harini, C.; Grant, P. E.; Okada, Y.; Papadelis, C. (2013): Simultaneous EEG and MEG Source Localization in Pediatric Tuberous Sclerosis Complex related Epilepsy. International Conference on Basic and Clinical Multimodal Imaging, September 7, Geneva, Switzerland
 39. **Hunold, A.**; Funke, M.; Eichardt, R.; Haueisen, J. (2013): Sensitivity of EEG and MEG to Orientation Selective Source Strength Variations. International Conference on Basic and Clinical Multimodal Imaging, September 7, Geneva, Switzerland

Declaration of authorship

I affirm that I have produced the present work without the unauthorized assistance of third parties and without the use of any other means than those indicated. Data and concepts taken directly or indirectly from other sources are marked with the source.

The persons listed below have helped me with the selection and evaluation of the following material in the manner described in each case, without payment:

1. Prof. Dr. Bernd Sabel: Prof. Sabel provided the motivation for the electrode design and positioning of the test configurations in section 2.1, which are also reflected in a jointly submitted manuscript (Sabel et al., 2020a).
2. Dr. Uwe Graichen: Dr. Graichen provided the SPHARA operators for the SPHARecip approach in section 2.2.
3. Anna Kongo: Ms. Kongo conducted a part of the usability study in section 3.1 as part of her Master thesis under my co-supervision, which is acknowledged in the resulting publication (Hunold et al., 2020c).
4. Michael Werthmann: Mr. Werthmann conducted a part of the usability study in section 3.1 as part of his Bachelor thesis under my co-supervision, which is acknowledged in the resulting publication (Hunold et al., 2020c).
5. Daniela Ortega: Ms. Ortega helped with the data consolidation of the usability studies for section 3.1, this collaboration resulted in a joint publication (Hunold et al., 2020c).
6. Dr. Patrique Fiedler (PhD thesis at BMTI): Preparatory work for the textile stimulation electrodes used in section 3.1 was carried out in collaboration with Dr. Fiedler, which resulted in a joint abstract (Fiedler et al., 2015a).
7. Sophia Wunder: Ms. Wunder worked on the bifunctional cap and performed the study on tDCS stimulation affecting the VEP for section 3.1 as part of her Master thesis under my co-supervision, this collaboration resulted in a joint publication (Wunder et al., 2018).

8. Paul Zwinscher: Mr. Zwinscher performed impedance and open circuit potential measurements of electrodes additively manufactured from carbon doped filaments used in section 3.2 as part of his Master thesis under my co-supervision.
9. Yongna Fu: Ms. Fu assembled the advanced bifunctional cap and performed the study of tACS stimulation of the visual system for section 3.2 as part of her Bachelor thesis under my co-supervision.
10. Dr. René Machts (PhD thesis at BMTI): Designs, constructions and parts of casting molds of electrodes and phantom components used in sections 3.2, 4.1 and 4.2 were developed in cooperation with Dr. Machts (Master thesis under my co-supervision).
11. Dirk Gutkelch (Physikalisch Technische Bundesanstalt): Designs and constructions of phantom components used in section 4.2 were developed in cooperation with Mr. Gutkelch.
12. Theresa Stephan: Ms. Stephan assembled the 3D measurement array and performed the TES measurements in the aquarium and the phantom for sections 4.1 and 4.2 as part of her Bachelor thesis, a scientific assistant job and her Master thesis under my co-supervision.

I conceptualized the study paradigms and measurement setups, I performed pilot measurements, supervised measurement and study series and conducted the data analysis.

No other persons were involved in the content-related and material preparation of the present dissertation. In particular, I did not make use of the services of mediation or counseling services (promotion consultants or other persons). No one has received any direct or indirect monetary benefits from me for work related to the content of the submitted dissertation.

The work has not yet been submitted to an examination board in the same or a similar form either in Germany or abroad.

It has been pointed out to me that the inaccuracy of the above declaration will be assessed as an attempt at deception and will result in the termination of the doctoral procedure in accordance with § 7 paragraph 10 of the doctoral regulations.

Ilmenau, November 26, 2020



Alexander Hunold

Erklärung

Ich versichere, dass ich die vorliegende Arbeit ohne unzulässige Hilfe Dritter und ohne Benutzung anderer als der angegebenen Hilfsmittel angefertigt habe. Die aus anderen Quellen direkt oder indirekt übernommenen Daten und Konzepte sind unter Angabe der Quelle gekennzeichnet.

Bei der Auswahl und Auswertung folgenden Materials haben mir die nachstehend aufgeführten Personen in der jeweils beschriebenen Weise unentgeltlich geholfen:

1. Prof. Dr. Bernd Sabel: Prof. Sabel lieferte die Motivation für das Elektrodendesign und die Positionierung der Testkonfigurationen in Abschnitt 2.1, die sich auch in einem gemeinsam eingereichten Manuskript widerspiegeln (Sabel et al., 2020a).
2. Dr. Uwe Graichen: Dr. Graichen erstellte die SPHARA-Operatoren für den SPHARecip-Ansatz im Abschnitt 2.2.
3. Anna Kongo: Frau Kongo führte einen Teil der Usability-Studie in Abschnitt 3.1 im Rahmen ihrer Masterarbeit unter meiner Ko-Betreuung durch, was in der daraus resultierenden Veröffentlichung (Hunold et al., 2020c) anerkannt wurde.
4. Michael Werthmann: Herr Werthmann führte einen Teil der Usability-Studie in Abschnitt 3.1 im Rahmen seiner Bachelorarbeit unter meiner Ko-Betreuung durch, was in der daraus resultierenden Veröffentlichung (Hunold et al., 2020c) anerkannt wurde.
5. Daniela Ortega: Frau Ortega half bei der Datenkonsolidierung der Usability-Studien für den Abschnitt 3.1, diese Zusammenarbeit führte zu einer gemeinsamen Publikation (Hunold et al., 2020c).
6. Dr. Patrique Fiedler (Promotion am BMTI): Die Vorbereitungsarbeiten für die in Abschnitt 3.1 verwendeten textilen Stimulationselektroden erfolgten in Zusammenarbeit mit Dr. Fiedler und mündeten in einem gemeinsamen Konferenzbeitrag (Fiedler et al., 2015a).
7. Sophia Wunder: Frau Wunder arbeitete an der bifunktionellen Haube und führte die Studie zur tDCS-Stimulation des visuellen Systems für den Abschnitt 3.1 im Rahmen ihrer Masterarbeit unter meiner Ko-Betreuung durch, diese Zusammenarbeit führte zu einer gemeinsamen Publikation (Wunder et al., 2018).

8. Paul Zwinscher: Herr Zwinscher führte Impedanz- und Eigenpotentialmessungen an additiv gefertigten Elektroden aus kohlenstoffdotierten Filamenten im Rahmen seiner Masterarbeit unter meiner Ko-Betreuung durch, die in Abschnitt 3.2 verwendet wurden.
9. Yongna Fu: Frau Fu arbeitete an der adaptierten bifunktionellen Haube und führte die Studie zur tACS-Stimulation des visuellen Systems für Abschnitt 3.2 im Rahmen ihrer Bachelorarbeit unter meiner Ko-Betreuung durch.
10. Dr. René Machts (Promotion am BMTI): Designs, Konstruktionen und Teile von Gussformen für Elektroden und Phantomkomponenten, die in den Abschnitten 3.2, 4.1 und 4.2 entwickelt wurden, sind in Zusammenarbeit mit Dr. Machts (Masterarbeit unter meiner Ko-Betreuung) entstanden.
11. Dirk Gutkelch (Physikalisch Technische Bundesanstalt): Entwürfe und Konstruktionen der in Abschnitt 4.2 verwendeten Phantomkomponenten wurden in Zusammenarbeit mit Herrn Gutkelch entwickelt.
12. Theresa Stephan: Frau Stephan baute die 3D-Messanordnung zusammen und führte die TES-Messungen im Aquarium und im Kopfphantom für die Abschnitte 4.1 und 4.2 im Rahmen ihrer Bachelorarbeit, einer wissenschaftlichen Assistenzstelle und ihrer Masterarbeit unter meiner Ko-Betreuung durch.

Ich habe die Studienparadigmen und Messaufbauten konzipiert, Pilotmessungen durchgeführt, Mess- und Studienreihen betreut und die Daten analysiert.

Weitere Personen waren an der inhaltlich-materiellen Erstellung der vorliegenden Arbeit nicht beteiligt. Insbesondere habe ich hierfür nicht die entgeltliche Hilfe von Vermittlungs- bzw. Beratungsdiensten (Promotionsberater oder anderer Personen) in Anspruch genommen. Niemand hat von mir unmittelbar oder mittelbar geldwerte Leistungen für Arbeiten erhalten, die im Zusammenhang mit dem Inhalt der vorgelegten Dissertation stehen.

Die Arbeit wurde bisher weder im In- noch im Ausland in gleicher oder ähnlicher Form einer Prüfungsbehörde vorgelegt.

Ich bin darauf hingewiesen worden, dass die Unrichtigkeit der vorstehenden Erklärung als Täuschungsversuch bewertet wird und gemäß § 7 Abs. 10 der Promotionsordnung den Abbruch des Promotionsverfahrens zur Folge hat.

Ilmenau, den 26. November 2020



Alexander Hunold

A homogeneous volume conductor and a realistically shaped three-compartment head phantom have been physically implemented for technical verification experiments. Metrological experiments in these phantoms demonstrated feasibility of multi-electrode stimulation configurations, especially the approach of temporal interference, and verified the stable performance of new electrode concepts.

The present thesis addresses current flow modeling for targeted stimulation, electrode developments for current administration and measurement approaches verifying stimulation configurations.

Simulated transorbital stimulation gave rise to current density distributions in the retina demonstrating distinct hot spots depending on the electrode montage. Similarly, simulations of multi-electrode configurations on the head addressed location and orientation specific targets in the cortex. These simulations indicate the feasibility of specific stimulation configurations for targets in the retina and the cortex.

For stimulation application, new concepts for stimulation application based on textile electrodes with integrated electrolyte reservoir and additive manufactured dry electrodes embodied in a textile cap have been introduced. These newly developed electrodes demonstrated functionality by replicating previously described effects of current stimulation and increased stimulation precision, reproducibility and lowered the preparation effort.

Electric manipulation of neuronal activity gathered interest in neuroscientific research and showed therapeutic effects throughout past centuries. The non-invasive application of weak currents with a few milliamperes to the head, called transcranial electric stimulation (tES), captured manifold applications in neuroscience and clinical research in the last decades. The conventionally cumbersome and rather unspecific administration of the stimulation current with respect to its distribution for targeting and the electrode interface desire further innovation and verification.

Concluding, the present thesis contributes innovations in the field of tES with a new approach for targeting cortical areas by multi-electrode stimulation, new compliant electrode concepts and physical phantoms for metrological verification.